Ingenieurfakultät Bau Geo Umwelt
Fachgebiet für Tektonik und Gefügekunde

Quantification of Impact-Induced Brittle Structures: An Analysis of Stress- and Scale-Dependence of Brittle Deformation Processes

Md. Sakawat Hossain

Vollständiger Abdruck der von die Ingenieurfakultät Bau Geo Umwelt der Technischen Universität München zur Erlangung des akademischen Grades eines Doktors der Naturwissenschaften genehmigten Dissertation.

Vorsitzender: Univ.-Prof. Dr.-Ing. Detlef Heinz

Prüfer der Dissertation

1. Univ.-Prof. Dr. rer. nat. habil. Jörn H. Kruhl
2. Univ.-Prof. Dr. rer. nat. Claudia Trepmann
   Ludwig-Maximilians-Universität München
3. Univ.-Prof. Dr. rer. nat. habil. Jürgen Scheurle

Die Dissertation wurde am 17.06.2015 bei der Technischen Universität München eingereicht und durch die Ingenieurfakultät Bau Geo Unwelt am 08.09.2015 angenommen.

Abstract

Impact craters display a large variety of brittle structures, such as fracture patterns, fragment size distribution, fragmentation structures in the upper parts of the Earth's crust. Some questions regarding the characteristics and spatial distribution of these structures in the target rock are as yet to be answered in detail. Impact-induced brittle structures of basement rocks and their limestone cover in and around the Ries impact crater (Germany) were recorded, measured and quantified. Quantification was performed mainly using methods based on structural geology, classical spatial statistics and fractal geometry. The possible influences of the fragmentation structures on karstification and cave formation in the Eastern Swabian Alb are also investigated. Structures related to 'suevite' (Stac Fada Member) emplacement and 'suevite' textures are studied as well at the Stoer impact, Ullapool (NW Scotland).

Shock-induced fracture patterns and fragment size distribution (FSD) of the Malm limestone and lower basement rock in and around the Ries carter are recorded on outcrop, hand sample, and thin section scale, and quantified mainly by fractal-geometry methods. Quantification is performed by automated procedures and in areas of square-centimetres to square-decametres with a maximum resolution of a few micrometres. On all scales, the rock fragmentation forms complex, statistically self-similar patterns (fractals) with specific characteristics: (i) The pattern fractality is scale-dependent. (ii) Three different power-law relationships exist, which reflect the effect of three fragmentation processes. (iii) The fracture patterns are anisotropic and inhomogeneous over larger areas. (iv) Complexity and anisotropy of the fracture patterns vary systematically with distance from the impact site. Such systematic variations appear typical for impact-induced dynamic fragmentation.

Prominent fractures, zones of intense fragmentation, fracture branching and near-surface target-rock delamination are identified as typical impact-induced fragmentation structures. Characteristics of these structures as well as impact-related orientation of prominent fractures show systematic changes with distance from the impact centre. Beyond ~1.3 times crater diameter away from the Ries outer crater rim, these structures are no longer observed, and the orientation of prominent fractures is mainly controlled by the pre-existing regional tectonic structures. Zones of intense fragmentation are observed both in horizontal and vertical direction, and show systematic repetition of their occurrence. The geometry of the fracture branching structure reveals symmetry together with strong anisotropy and preferred fracture orientation. Near-surface delamination is indicated by a variety of brittle-plastic structures (e.g., thrusting, folding) in the upper layers of the target rocks, and decreases exponentially with depth and distance from the impact centre. Such systematic changes of the characteristics and spatial distribution of fragmentation structures are not observed in the regional tectonic deformation, and are probably related to weakening of impact-induced shock and subsequent rarefaction waves with distance from the impact point.

Observations which indicate the possible influence of the Ries and Steinheim impact on the development of some of the Eastern Swabian Alb caves include: (i) the geometry and orientation of straight cave sections on the horizontal plane, (ii) spatial distribution, i.e. lateral extent of the fragmentation structures of the Ries and Steinheim impact, (iii) approximately Mid-Miocene origin of the caves as well as (iv) presence of magnetic spherules with elevated nickel and cobalt concentration in cave sediments. In the Stoer impact area, structures related to the strong horizontal component of fluidized flow as well as ballistic flow derived ejecta and subsequent air fall component, suggest that the 'suevite' is a double layer ejecta blanket deposit. High abundance of melt clasts, delicate shape lumps of glassy material, and degassing structures in the 'suevite' possibly imply extensive melting which in turn indicates a water saturated target rock.

These characteristic fracture patterns, FSD, and fragmentation structures are not observed in regional tectonic deformation and have previously not been quantitatively well demonstrated.

Acknowledgements

First I would like to thank my supervisor, Professor Dr. Jörn H. Kruhl. He has always been available and welcoming whenever I needed him and offered support, guidance, inspiration and scientific help throughout my PhD research. A special thanks also goes to my mentor (second supervisor) Professor Dr. Claudia Trepmann (University of Munich). Prof. Trepmann not only gave me enlightening scientific discussion; but also provided her support in writing recommendation letters related to my study. I am also grateful to my external supervisors Thomas Kenkmann, Tom Blenkinsop, and Giacomo Prosser for their valuable scientific advice and guidance. My stay in Germany, specifically in Munich is as enjoyable as it is productive, and for that I owe thanks to all the wonderful people at TUM and LMU with whom I am in contact.

During my time at the TUM I have been helped out of one difficulty or another by numerous people; if I mentioned them all by name I am sure I would leave someone out, so I thank them all collectively. I must, however, extend specific gratitude to several people. First, my two office mates for the last three years, Christian Stäb and Tim Yilmaz who have always been ready to assist whatever the problem and have accelerated the writing-up process by racing me to the finish. I would also like to thank Namvar Jahanmehr and Klaus Mayer for sample and thin section preparation. Annette Spengler from TUM Graduate School who helped a lot in dealing with administrative work related to my PhD research.

I have been extremely fortunate during my PhD research to attend several conferences and field works, and discuss my work with many leading voices in the field of impact cratering and fractal geometry. This thesis draws much from these stimulating discussions and I would therefore like to thank Michael H. Poelchau, Alison Ord, Bruce Hobbs, Mark Peternell, Diego Perugini, Ulrich Steiner, Dietmar Jung, Soraya Heuss-Aßbichler, Kai-Uwe Hess, and Donald Fisher. I would also like to thank Lutz Cleemann for cordial help with aerial photography of the quarries by using his personal drone. Parts of this thesis have been published as a paper in Pure and Applied Geophysics. I would like to thank the reviewer for insightful comments and constructive criticism during the review process, which indirectly lead to the improvement of this thesis.

Thanks are also extended to the colleagues from the Centre for Ries Crater Impact Research (ZERIN) in Nördlingen for providing core samples, to Axel Gerik and Mark Peternell for giving access to the AMOCADO and MORFA programs, and to Mr. Ottomar Krentz for kind giving of the SRTM image of the Ries impact area. Appreciation is also extended to all the people associated with the quarries studied around the Ries impact for their support. I would like to gratefully acknowledge the financial support in the form of Scholarship, given by the German Academic Exchange Service DAAD (grant A/11/75209).

Last but by no means least I would like to thank my family members. They have always offered love and support in everything I do. I dedicate my achievements in the last three years, and this PhD thesis, to them.

CONTENTS

CHAPTER ONE

1. Introduction

1.1 Motivation and aim of the study

Most of the landforms of terrestrial planets, moons and asteroids of our solar system are dominated by impact craters. Meteorite impacts producing craters are “the most fundamental of all processes that have taken place on the terrestrial planets” (Shoemaker, 1977). Post impact processes, such as tectonics, volcanism, fluvial and aeolian erosion and sedimentation have significantly obliterated, eroded, and/or buried the record of the impact craters and associated structures on different terrestrial planets, especially on the Earth (French, 1998; Kenkmann et al., 2014). The number of impact craters, their distribution and state of preservation reflects the geologic history of the Earth. The Earth was struck by a large number of meteorites during its long history. Most of them are probably still unnoticed due to their poor state of morphological preservation. To date, the number of confirmed impact craters discovered on Earth is 188 and is projected to increase over time (Earth impact data base: www.passc.net/EarthImpactDatabase). A substantial number of craters that are yet to be discovered, together with confirmed crater structures may significantly contribute to the overall morphology and structure of the Earth’s crust.

Meteorite impact craters and associated small- to large-scale deformation structures can reveal physical properties of the target material, as well as the mechanics of the cratering process (Wood and Andersson, 1978; Kenkmann and Ivanov, 2006; Kenkmann et al., 2014). Impact craters display a large variety of deformation structures (Kenkmann et al., 2014) that are mainly caused by rapidly changing primary shock (e.g., planar deformation features, fracture branching) and subsequent rarefaction waves (e.g., target-rock delamination). Other causes include elastic or seismic waves (final modification of shock wave approximately at crater rim), elastic rebound of the transient crater floor and gravitational collapse of the transient crater wall (Melosh, 1989; French, 1998; Osinski and Pierazzo, 2013). Micro- to kilometre-scale deformation related to shattering and fracturing of the target rocks produce a variety of brittle deformation structures including complex fragmentation patterns. The intensity (density as well as spacing) of these deformation structures rapidly decreases from the point of impact outwards (von Dalwigk, 2003; Kenkmann et al., 2014). Although impact research was shifted into focus of international research during the last years, open questions which are related to characteristics and spatial distribution of brittle deformation structures of the target rock remain. Therefore, major goals of this PhD study are the quantification of impact-induced fracture patterns and fragment size distribution (FSD), characterization of typical impact-related fragmentation structures, and determination of the spatial distribution of brittle deformation structures around an impact crater.

Small-scale fractures of vertical to sub-vertical orientations, with little or no displacement, are dominant mainly inside the crater and on its rim (Hossain and Kruhl, 2014a). The irregular to parallel networks of these small-scale fractures form complex patterns that can only be analysed by fractal-geometry methods (Kruhl, 2013). Besides, dynamic fragmentation of the target rock influences FSD which can be properly described by a fractal size distribution (Buhl et al., 2013). Quantification of fracture patterns as well as FSD are important tools for getting deeper insight into impact-related fragmentation processes and their interaction (Buhl et al., 2013; Hossain and Kruhl, 2014a). Such quantification of dynamic fragmentation would allow us to compare them with the quasi-static tectonic fragmentation (Blenkinsop, 1991; Volland and Kruhl, 2004; Keulen et al., 2007; Park et al., 2010; Melosh et al., 2014).

Large-scale vertical to sub-vertical fractures in contrast to small-scale fractures are dominant mainly on and outside the crater rim. Detailed studies of these large-scale fractures will help to distinguish impact brittle deformation from regional tectonic deformation, and to determine the spatial distribution of brittle deformation around an impact crater (Hossain and Kruhl, 2014b). In addition, the speed of fracture tip propagation influences the development of fracture geometry, networks, and hierarchical bifurcations or branching similar to surfaces of shatter cones (Sagy et al., 2001, 2004). However, in case of natural dynamic fragmentation, the scale of fracture branching structures, their structural complexity, orientation and lateral distance of their occurrence with respect to impact centre are yet to be described and quantified. Moreover, the horizontal and vertical extent of near-surface target-rock delamination around an impact crater (Kenkmann and Ivanov, 2006) are needed to be demarcated more precisely.

In order to study all these aspects of brittle deformation in and outside the crater, this PhD research focuses on the Ries meteorite impact (Nördlingen, Germany), where the Ries Research Borehole 1973 (Graup, 1977; Gudden, 1974) and numerous quarries around the crater allow the study of impact-related fragmentation structures in the thin sedimentary target rock and underlying basement. Moreover, the Ries crater is one of the best preserved craters in the world and so can be used to produce a comprehensive data base of impact fragmentation structures (Hossain and Kruhl, 2014a). Micro- to kilometre-scale brittle deformation structures related to the impact crater are recorded, measured and quantified by using structural, classical spatial statistics and fractal geometry methods, and the results are discussed in detail. Lateral extent of the brittle deformation structures of the Ries impact and its possible influence on the development of the Eastern Swabian Alb caves (Strasser et al., 2009a; Strasser, 2011) are also discussed. In addition, field investigation has been carried out to study a recently reported Precambrian proximal ejecta blanket deposit (‘suevite’) near Ullapool, NW Scotland (Amor et al., 2008, 2011). The impact crater related to this ejecta blanket deposit is currently completely obscured probably due to burial or erosion. The results of the field observation are discussed to provide an assessment of the fabric and texture of the ‘suevite’, structures related to ‘suevite’ emplacement, and possible location of the currently obscured ‘impact centre’.

1.2 Introduction to meteorite impact

Over the last few decades, hypervelocity impact cratering has emerged as a significant geological process that has played an important role in the formation and subsequent evolution of all terrestrial planetary bodies and satellites (Osinski and Pierazzo, 2013). This ubiquitous geological process brought material from depth to the surface in the form of ejecta deposits and central uplifts, and thus, provides a unique opportunity to examine the subsurface on planetary bodies where drilling more than a few metres is not yet a viable option. On the Earth, impacts of meteoritic objects have not only affected the evolution of life (Schulte et al., 2010) but also created large- to small-scale structures in the upper parts of the Earth's crust which in turn lead to major ore deposits (Donofrio, 1998; French, 1998; Grieve, 2005; Ames and Farrow, 2007). Hypervelocity impacts of a large meteorite also pose a threat to human civilization on Earth. Evidence for a major impact as the cause of the mass extinction event at the Cretaceous–Paleogene (K–Pg) boundary ~65 Ma ago is already proven (Alvarez et al., 1980; Hildebrand et al., 1991; Schulte et al., 2010). When a small meteor exploded in the atmosphere near Chelyabinsk in Russia on 15th February, 2013 it caused wide spread anxiety (Popova et al., 2013). Therefore, it is not surprising that impact craters have been, and remain, high-priority targets for planetary exploration missions to the Earth, Moon and Mars as well as other solid planetary objects.

Knowledge of the impact cratering process has significantly improved in the last few decades, but several fundamental aspects related to the processes and resultant products is yet to be well understood (Osinski and Pierazzo, 2013). The impact cratering process starts with micro-seconds of shock loading and terminates with gravity-driven collapse over a period of a few minutes (Melosh, 1989). Pressures, temperatures and strain rates related to this process are all several orders of magnitude higher than in ordinary geologic processes. In addition, impact-induced shock and subsequent rarefaction waves are different from the normal seismic waves (Ahrens and O'Keefe, 1972, 1987; Melosh, 1989). At the beginning of a kilometre-sized asteroid impact, pressure reaches up to several hundred gigapascals (GPa), temperature up to several ten-thousand degrees, and strain rate more than ~10^{+6} s^{-1} at the point of impact (O'Keefe and Ahrens, 1975; Huffman and Reimold, 1996; Collins et al., 2005) (Fig. 1.1). Whereas, under normal static load condition, rock in the Earth's crust is subjected to pressure less than a few GPa which generates relatively low strain rates of ~10^{-3} s^{-1} to 10^{-13} s^{-1}, and builds up over a much longer time period. Such extreme differences in physical parameters, time duration, and the nature of the energy release make the cratering process difficult to understand (Osinski and Pierazzo, 2013). As magnitudes of pressure and strain rates are enormously high and the duration of deformation is extremely short, characteristics of impact deformation differ from those of tectonic deformation (Fig. 1.1). Within a few minutes of impact cratering, a large variety of deformation features are formed under rapidly changing stress, temperature and strain-rate conditions (Kenkmann et al., 2014). Target rocks affected by shock are subjected to melting, vaporization, shock metamorphism, brecciation, and fracturing, depending on the intensity of shock compression and subsequent rarefaction waves.

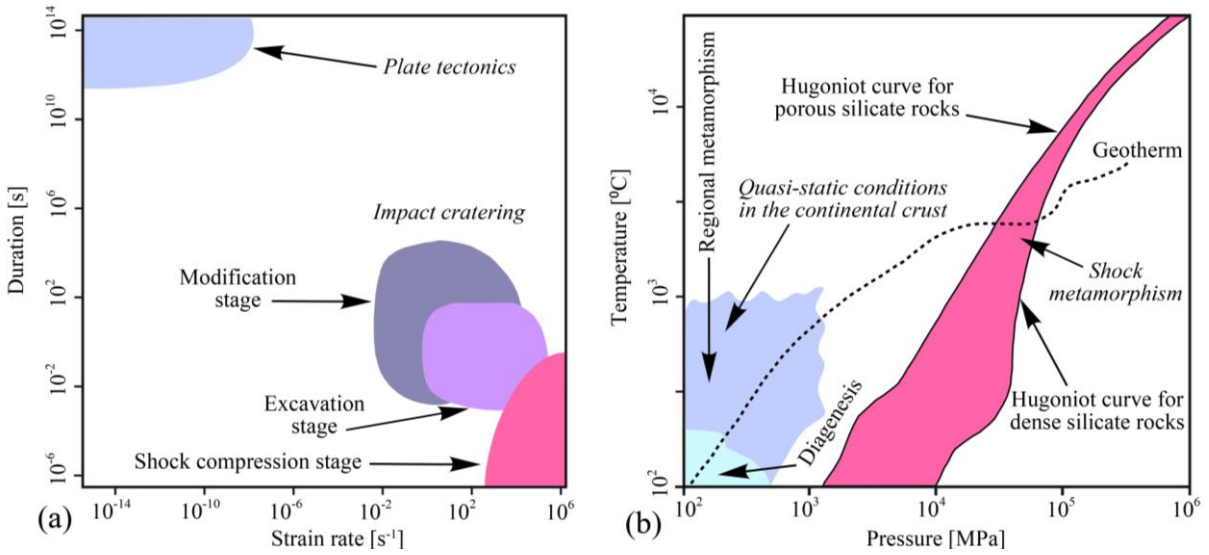

Figure 1.1: Comparison of pressure, temperature, strain rate, and duration between dynamic impact cratering and quasi-static tectonic processes. (a) Strain rate versus duration of tectonic and impact cratering processes. Maximum strain rates occur during impact within the shock wave but the duration is a fraction of a second even for large-scale impacts. The cratering process is generally finished within a few tens of seconds to minutes, whereas tectonic processes have much longer duration. (b) Pressure (P) – temperature (T) diagram of tectonic metamorphism and shock metamorphism. At the point of impact, pressure reaches up to several hundred gigapascals, and temperature reaches up to tens of thousands of degrees during shock compression. Boundaries of the Hugoniot elastic limit (Hugoniot curves) are based on the shock behaviour of single-crystal quartz and porous sandstone. Shock metamorphic features can be used as diagnostic characteristics to identify the impact crater structures as there is no overlap between regional and shock metamorphism (modified after Kenkmann et al., 2014).

As Earth is a dynamic planet, few craters are well preserved (e.g., Barringer crater, USA; Matt Wilson crater, Australia; Ries crater, Germany; Serra da Cangalha crater, Brazil; Upheaval Dome crater, USA) and can be explored to study the impact-induced fragmentation structures (Kenkmann and Poelchau, 2009; Kenkmann et al., 2014; Hossain and Kruhl, 2014a). Fragmentation characteristics of these well-preserved impact craters (Kumar, 2005; Kumar and Kring, 2008; Hossain and Kruhl, 2014a; Kenkmann et al., 2014) are also needed to compare with the fragmentation reported from the micrometeoroid impact on the solar panels of spacecraft (Graham et al., 2004), the nuclear test site in the Yucca Flat region of Nevada (Barosh, 1968; Allen et al., 1997; Grasso, 2001), and laboratory impact experiments (Lange and Ahrens, 1987; Polanskey and Ahrens, 1990; Kenkmann et al., 2011; Buhl et al., 2013) for a better understanding of the cratering processes. One should keep in mind that cratering experiments are often very difficult, and their reliability is hampered due to them being scaled down from the natural phenomena under scrutiny. On the other hand, although numerical modelling and simulations of impact phenomena (Holsapple, 1993; Camacho and Ortiz, 1996; Anderson et al., 2003; Leone et al., 2014; Jutzi et al., 2015) provide useful quantitative data for particular impact events, they do not lead to an intuitive understanding of the process itself. Currently, the hydrocode modelling and simulation seems to be capable of accounting for 3D- geometries, multi-layer targets, strength, strain localization, fragmentation and particle-atmosphere interactions (Melosh et al., 1992; Wünnemann and Ivanov, 2003; Collins et al., 2004; Pierazzo et al., 2008; Elbeshausen et al., 2009; Artemieva and Pierazzo, 2011; Johnson and Melosh, 2014) but still a lot of improvement needs to be made.

However, it is not the purpose of this PhD thesis to provide a comprehensive introduction to meteoritic impact process and resultant products. Only a brief outline of impact process and resultant products are given here. For various aspects of impact cratering, interested readers are referred to the excellent works by Melosh (1989), French (1998) and Osinski and Pierazzo (2013), and to the numerous classic papers compiled in French and Short (1968), Roddy et al. (1977) and Koeberl and Henkel (2005). In addition, the excellent review papers by French (1972), Barlow (2004), French and Koeberl (2010), Kenkmann et al. (2014) and references therein would be great resources.

1.3 Stages of impact cratering

Hypervelocity impact crater formation is a continuous process that begins when the meteorite first hits the terrestrial planetary surface and ends with the final movements of the debris and rock mass (Melosh, 1989). In order to enhance the ability to comprehend the vast array of processes that occurs within a very short time, Gault et al. (1968) grouped similar phenomena together and divided the processes into three main stages: (i) contact and compression; (ii) excavation; and (iii) modification (Fig. 1.2). However, in nature, these three stages grade into one another and it is very difficult to define accurately when one stage ends and the next stage begins (Melosh, 2013).

1.3.1 Contact and compression stage

This stage of impact cratering begins when a cosmic projectile, be it an asteroid or comet, which is large and stable enough to penetrate the Earth's atmosphere, makes contact with the target surface (Melosh, 1989; French, 1998). The projectile with cosmic velocity (average is ~17 km/sec) then compresses the target material before its immense kinetic energy is transferred to compressional supersonic shock waves at the interface between projectile and target (Fig. 1.2a). If the target material is solid, the projectile penetrates approximately one or two times its own diameter within a fraction of second and then stops (Kieffer and Simonds, 1980; O'Keefe and Ahrens, 1982).

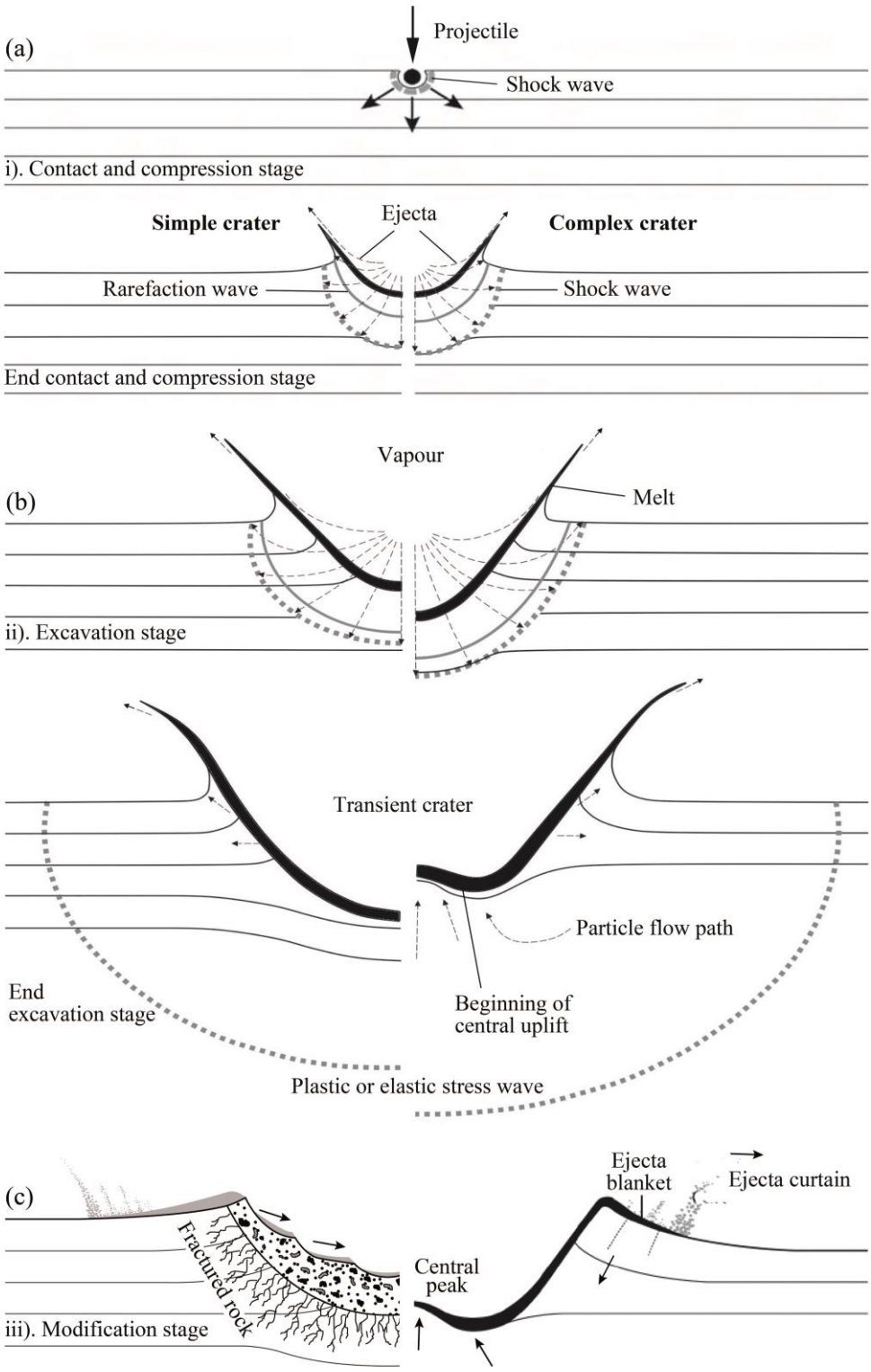

Figure 1.2: Schematic sketches (not to scale) illustrating the three progressive stages (i–iii) of simple and complex crater formation. First two stages (i and ii) are divided into progressive sub-stages for better representation. The left and right panels (except top one) are for simple and complex craters, respectively. (a) Contact and compression stage (i). In this stage, a projectile penetrates into target rock, generates shock wave at the projectile target interface, and parts of the projectile and target material may be melted depending on the size of the projectile. At the end of this stage, the shock wave continues expanding hemispherically into the target material, and a rarefaction wave develops behind the shock wave at the free surface. Due to interaction of the rarefaction wave with the shock wave, near-surface material is accelerated upward and outward. (b) Excavation

stage (ii). In this intermediate stage, both waves penetrate further into the target rock, and the crater cavity continues expanding due to further excavation of material outward as ejecta flow or ejecta curtain. At the end of this stage, the rarefaction wave reduces the strength of the shock wave, hence the transient crater cannot develop further, i.e. it reaches its maximum extent, and the crater rim starts to uplift. In case of the complex crater, the central uplift starts to form. (c) Modification stage (iii). During this end stage of cratering, the transient crater rim is subjected to gravitational collapse, and near-crater ejecta start to fall back into the crater cavity. In case of the complex crater, a reverse particle flow path beneath the central cavity leads to further development of the central uplift. Central uplift may start to collapse due to its own weight (modified after French, 1998, Buhl, 2013 and Osinski and Pierazzo, 2013).

Shock waves originate at the point where the projectile first hits the target surface and is characterized by a rapid, nearly discontinuous change in pressure, temperature and density. The expanding shock wave interacts with the projectile as well as the target, and develops peak shock pressure generally reaching hundreds of GPa. This peak shock pressure decreases exponentially with distance from the crater centre for two reasons: (i) the hemispherically expanding shock front covers an increasingly larger area with increasing radial distance, thus reducing the overall energy density, and (ii) additional energy is lost by heating, deformation, and displacement of the target material (Robertson and Grieve, 1977; Holsapple, 1987; Melosh, 1989; French, 1998). The contact and compression stage is the fastest among all three stages of the cratering process, and it ends when the shock wave has reached the free trailing surface of the projectile (Gault et al., 1968; Melosh, 1989; French, 1998).

1.3.1.1 Physical consequences of contact and compression stage in target rocks

As the shock pressure far exceeds the yield strength of the projectile and target material, both materials may either completely melt or vaporize (Melosh, 1989). The maximum stress a rock can resist under shock compression without plastic deformation and internal rearrangement is known as the Hugoniot elastic limit (HEL). Rock undergoes shock-metamorphic overprint above HEL, and dominance brittle deformation below HEL (Kenkmann et al., 2014). Physical consequences of the shock waves can be observed as the irreversible deformations in the rock-forming minerals such as planar deformation features (PDFs), high pressure polymorphs, complete amorphization, and melting (Stöffler and Langenhorst, 1994; Grieve et al., 1996; Osinski and Pierazzo, 2013). Other physical consequences of the shock waves in the target include shatter cones (Dietz, 1947, 1960; Sagy et al., 2002, 2004), and narrow spaced fracture networks (Kenkmann et al., 2014). Well recognized shock stages (S0 to SV), their corresponding pressures and the resulting effects in non-porous rocks is given in Table 1.1. As soon as the shock wave reaches a free unconfined surface or the rear surface of the projectile, a tensile rarefaction wave is formed. As the material has already attained higher density due to shock compression, the rarefaction wave is actually moving faster than the shock front continues forward into the target material and begins to decompress the material. When the rarefaction wave reaches the front of the projectile and begins to enter the adjacent compressed target, this marks the end of contact and compression stage and the beginning of the excavation stage (Melosh, 1989; French, 1998). The first stage of impact cratering lasts no more than a few seconds, even for impacts of very large projectile.

1.3.2 Excavation stage

The transition from the brief contact and compression stage into the longer excavation stage is a continuum. The target material at the contact of the projectile is compressed and accelerated as it is engulfed by the more or less hemispherically propagating shock wave (Fig. 1.2b). Upon unloading by

the first moving rarefaction wave the target material cannot be completely decelerated and a residual velocity remains (Melosh, 1989). This residual velocity, resulting from the outward-directed shock waves and the downward-directed rarefaction waves, sets the target material in motion with an initial outward radial trajectory, initiating a sub-sonic excavation flow of the material that ultimately opens the crater (French, 1998; Osinski and Pierazzo, 2013). The kinematics of the excavation flow result in an approximately bowl-shaped crater cavity, and the maximum extent of the cavity is known as the transient crater which is very different from the final crater. The resultant transient carter diameter is many times larger than the projectile diameter, and has a depth/diameter (*d/D*) ratio of about 1/4–1/3, apparently regardless of the size of the crater (Osinski and Spray, 2003; Sharpton and Dressler, 2003). This is one of the most important characteristics that differentiate hypervelocity impacts from low velocity penetration-type impacts (Melosh, 1989).

The transient crater is divided vertically into two zones, namely upper excavated zone and lower displaced zone (Osinski and Pierazzo, 2013). The material from the upper zone which is one-third to half of the transient crater is subjected to upward and outward ballistic ejection. This ballistic ejection of the materials forms an upwards rising ejecta plume which extends hemispherically outwards exceeding the rim of the final crater, and deposited as allochthonous ejecta (Grieve et al., 1977; Kieffer and Simonds, 1980; Melosh, 1989). At the lower zone of the transient crater, the rarefaction wave is not strong enough to eject material, therefore the target material dominantly moves downwards and outwards. Both zones propagate further and are accompanied by structurally uplifted near-surface target rock to form the transient crater rim. The excavation flow is halted, and the formation of the transient crater cavity is finished when the gravity forces or cohesive strength of the target material supersedes the remaining kinetic energy of the excavation flow (French, 1998; Kenkmann et al., 2012). In the case of a simple crater, the transient cavity rim is approximately equal to the final crater rim. In the case of a complex crater, the transient cavity rim is typically destroyed during the final stage of cratering, and getting bigger (Osinski and Pierazzo, 2013). Defining the transient crater is crucial in determining critical characteristics of an impact structure such as the size and velocity of the projectile, the amount of material melted and ejected, original depth and diameter of the carter, and the amount of structural uplift of the central peak in case of a complex crater (French, 1998).

1.3.2.1 Impact lithologies and macroscopic structures

The excavation stage produces mainly two different types of lithological products which include allochthonous impact breccias, and impact melt rocks (Fig. 1.3). These products are found mainly in the ejecta curtain around the transient crater cavity and in the crater walls and floor. Close to the crater rim (~2–3 times the crater radius), ejecta deposition is continuous and forms a blanket, but with increasing radial distance ejecta deposition becomes discontinuous. Impact lithic breccias within the ejecta deposits are generally two types: polymict and monomict. Monomict breccia is mainly observed as proximal ejecta deposits near the edge of the transient crater. In general, allochthonous lithic breccias are polymict in nature and may contain fragments of various degrees of deformation and shock metamorphism. Bunte Breccia is a local term for variegated colour polymict lithic breccia of the ejecta blanket deposit at the Ries impact crater, Germany (Fig. 1.3a) (Stöffler and Grieve, 2007). The term ‘suevite’ is used if the matrix of the polymict impact lithic breccias is truly clastic, and consists of lithic and mineral clasts in all stages of shock metamorphism including cogenetic impact melt particles which are in a glassy or crystallised state (Fig. 1.3b) (Stöffler and Grieve, 2007; Stöffler et al., 2013). Suevite also contain lumps of glassy material or ‘glass-bombs’ (Fig. 1.3c) and degassing pipes (Fig. 1.3d). On the other hand, if the solidified rock from an impact melt containing variable

amounts of clastic debris of different degrees of shock metamorphism then it is known as impact melt breccia or impact melt rock (Fig. 1.3e). The sharp contact between the melt-bearing breccias (suevites) and minor impact melt-bearing rocks (Bunte Breccia) of the Ries ejecta layers indicates that there is a clear temporal hiatus between emplacement of the ballistic Bunte Breccia and the overlying suevites (Fig. 1.3f) (Hörz, 1983). According to Kenkmann et al. (2014), impact breccia fragments are formed through five successive processes: (i) tensile failure due to shock pressure release, (ii) shear and tensile failure plus abrasion during the material flow within the transient cavity, (iii) tensile break-up during ballistic ejection by aerodynamic drag forces and inter-fragment collision, plus by the release of elastic strain, (iv) fragmentation during the first deposition of the ejecta and (v) further fragmentation by the entrainment of the ejecta debris flow moving radially outward.

Table 1.1: Shock classification scheme and the physical consequences of shock waves in non-porous rocks (modified after Kenkmann et al., 2014). Data from Stöffler (1984), Stöffler and Langenhorst (1994) and French (1998).

Shock Stage	Shock pressure [GPa]	Post-shock temperature [°C]	Physical effects and related features
S 0	0–8		Fracturing: Narrow space fracture networks, shatter cones, fracture branching, planar fractures, breccia formation Twinning: Basal twinning in quartz
S Ia	8–20	>100	Fracturing: Shatter cones, planar fractures Localized amorphization: Planar deformation features High pressure polymorphs: Stishovite
S Ib	20–35	>170	Localized amorphization (Bulk reduction of refractive indices and birefringence): Planar deformation features High pressure polymorphs: Coesite
S II	35–45	>300	Complete amorphization: Diaplectic quartz and feldspar glasses
S III	45–60	>900	Complete amorphization: Diaplectic quartz glasses Melting: Vesiculated feldspar melt
S IV	60–80	>1500	Bulk melting: Melted quartz and feldspar
S V	>80–100	>2500	Bulk vaporization: Condensed glass

The height of the crater rim crest is a result of equal (approx.) contributions by: (i) ejecta debris deposits, and (ii) structural uplift of the pre-impact target rocks. Maximum uplift is observed beneath the rim crest, decreases with increasing distance, and diminishes to zero at ~1.3–1.7 times of crater radius (Melosh, 1989). Structural uplift is caused by strong horizontal compressive force acting on the rocks underneath the crater cavity, pushing outward from the crater centre, fracturing the rock and squeezing it upward. Signs of outward movement are preserved as shear sense indicators at the crater sub-surface and wall rock (Roddy, 1977; Shoemaker et al., 2005). Shear sense indicators are concentrically striking drag folds and/or asymmetric folds with inclined fold planes and top-outward vergencies. The horizontal compressive force also produces inward- and outward-dipping thrust faults, and sub-horizontal material injection into the crater wall. Relative to the crater, thrust faults are concentrically striking, and parallel to steeply dipping (Pilon et al., 1991). Injection into the wall rock can either occur as breccia dike or by the emplacement of intact target materials (Melosh, 1989; Kenkmann et al., 2014) (Fig. 1.4). Dikes generally have sharp contacts with the host rock, mainly consisting of intensively fragmented and fluidized rock debris with or without contribution of melted

material. In some cases, dikes may display several branching points (Wittmann et al., 2004). The other form of injection, known as interthrust wedges, is developed when coherent blocks of target rock are injected into the crater cavity wall (Poelchau et al., 2009). In addition, when the ejecta debris is thrown out at very low velocity, target materials often form coherent and intact rock units with inverted stratigraphy. This inverted stratigraphy is known as overturned flap (Fig. 1.4) (Melosh, 1989). However, due to the collapse of the transient crater rim into the carter cavity, such structures may not always be present.

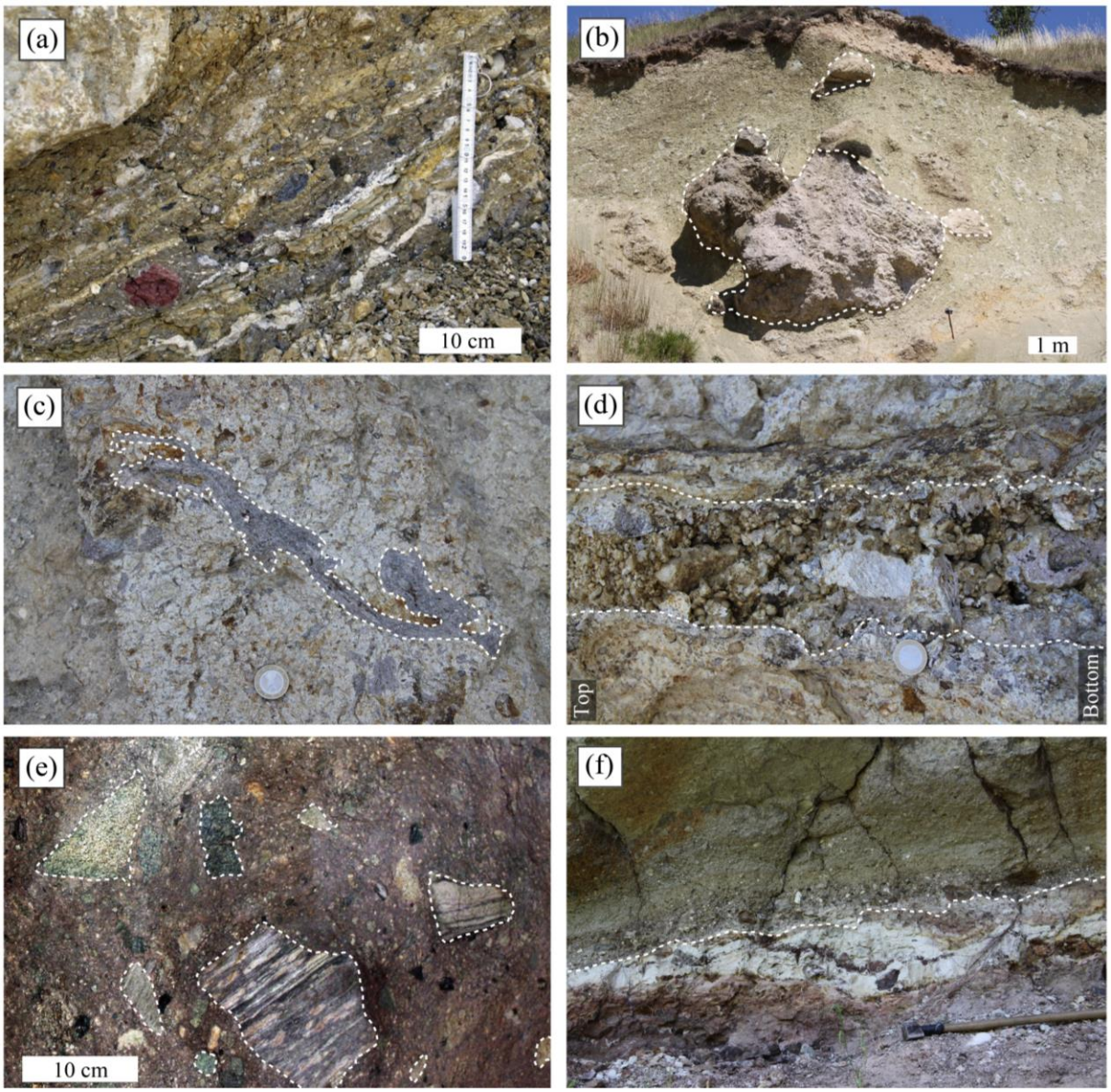

Figure 1.3: Impact breccia lithologies of the Ries crater. (a) Variegated colour polymict lithic breccia ('Bunte breccia') of the continuous ejecta blanket deposits at Gundelsheim quarry, ~20.5 km E of crater centre. Mechanically abraded lithic clasts are embedded in a clay-rich matrix that displays fluid-assisted ductile and/or granular flow. The flow of the clay-rich matrix leads to compositional banding and small-scale disharmonic folding. (b) Monomictly brecciated allochthonous granite blocks (broken outline) of the crystalline basement rock is embedded in suevite at the Unterwilfingen quarry, in the megablock zone, ~8.5 km WNW of the crater centre. The whitish-grey elongated particles in the suevite are melt lumps (glass-bombs) altered to phyllosilicates (hydrothermally altered). (c) Centimetre- to decimetre size delicate-shape S IV-type melt lumps ('glass-bombs', black-ash colour) are embedded in suevite at Aumühle quarry. The largest glass-bomb on the image is marked

by a broken outline. A two euro coin on the image (diameter 25.75 mm) is used as scale. (d) Metre-long and centimetre-wide sub-vertical degassing pipe or 'degassing structure' within suevite at Aumühle quarry, contains millimetre- to 1 centimetre-large loosely 'dumped' angular suevite fragments. A two euro coin on the image (diameter 25.75 mm) is used as scale. (e) Impact melt rock consisting of crystalline fragments is embedded in a melt-rich matrix at Polsingen area. Most of these crystalline fragments (broken outline) are subjected to shock deformation of various intensity. (f) Contact (broken outline) between suevite at top and Bunte Breccia at bottom, on the eastern quarry face (Aumühle). Hammer in the image is 0.60 m long. Aumühle quarry is located ~11 km NNE of the crater centre. Fig. (a and e) modified after Kenkmann et al., 2014; photographs b to d and f taken by Jörn H. Kruhl.

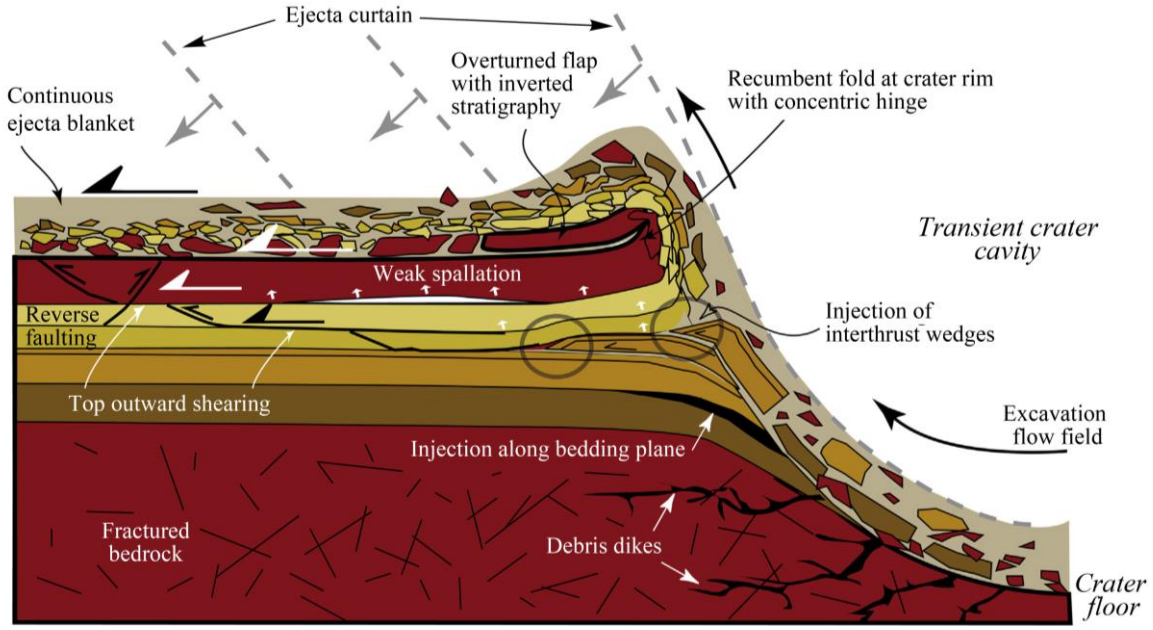

Figure 1.4: Schematic cross-section of an impact crater rim illustrating structures formed during excavation stage. Outwards and upwards directed excavation flow leads to the ballistic ejection of target material, forms an ejecta blanket that is deposited mainly outside the crater. At the crater rim, the slow movement of the proximal ejecta forms an overturned flap of coherent to semi-coherent overturned target layers. At greater distance from the rim, the ejecta is sheared and brecciated upon initial deposition due to the horizontal dragging of the oblique impact shower. In the crater wall, spallation induces horizontal zones of weakness creating small gaps in the target rock. The outward excavation flow material can be injected into the target rock either in the form of dike breccias, melt or as coherent blocks, known as interthrust wedges. Injections lead to an uplift of the target surface at the crater wall. Displacements are also observed in top outwards and bottom outwards thrusting generally away from the crater rim (modified after Kenkmann et al., 2014 and Melosh, 1989).

1.3.2.2 Near-surface target-rock delamination

During the excavation stage, target rocks are subjected to another important deformation process known as spallation, which is restricted only in the surficial part of the waves interference zone (Melosh, 1989). When the rarefaction wave starts travelling downward and outward, the rocks are subjected to deformation (e.g., fracturing, folding) as it moves forward (Melosh, 1989; Bäckström, 2005). At distance, the interference shock and rarefaction waves near the target surface cause spallation, producing highly variable deformation at a given range from the impact centre (Fig. 1.5). Thickness of the interference zone depends on the rise time in the shock wave front, which is controlled by the structures and physical properties of the target rock (Melosh, 1989). However, Kenkmann and Ivanob (2006) proposed two separate mechanisms for near-surface deformation based on numerical modelling: (i) weak spallation caused upward and outward directed motion leading to decoupling of the target materials, and (ii) subsequent dragging by the oblique impact shower delivers

a horizontal momentum to the uppermost target area. Dragging causes striations on these detachment planes or top layer of the target rock indicate top-outward shearing with radial slip vectors ranging from metres to decametres (Kenkmann and Schönian, 2006). Kenkmann and Ivanob (2006) suggested lateral extent of the spallation zone up to a distance of ~1.8 times crater radius. However, during this research, the lateral extent of this zone is observed up to ~3 times of the Ries crater radius. Therefore, to understand the clear extent of spallation and dragging effect, further field observation and numerical modelling is required.

Figure 1.5: Ries impact-induced near-surface deformation of the bedded Malm limestone is associated with target delamination of different intensity at Eireiner quarry, ~13 km E of the crater centre. Out of ~40 - 60 m of total thickness, only the upper few metres of delamination are visible in this image. The target rock is dismembered into different thrust and tilted blocks. For clarification some bedding planes are traced as dotted lines, and thrust as well as detachment planes are traced as solid lines. In this upper part of the target-rock delamination, strata undulation (1), high-angle strata cut-offs at the detachment (2), large-scale thrusting (3), thrust wedge (4), bedding parallel detachment plane (5), and related brittle deformation are visible. Locally, the uppermost several metre thick layers are strongly fragmented (photograph taken by Christian Stäb).

1.3.3 Modification stage

The final stage of the cratering process begins when the fully excavated unstable transient crater is generally subjected to collapse under gravity (Fig. 1.2c). The modification stage lasts a little bit longer than the excavation stage, generally less than a minute for a small crater, and a few minutes for a large crater (Melosh, 1989). The crater modification process is governed by the size of the transient cavity and the physical properties of the target rocks (Melosh and Ivanov, 1999). Under the Earth's gravitational field, the diameter at which the transition from simple to complex craters occurs is ~2 km for craters developed in sedimentary targets and ~4 km for those in crystalline target rock (Osinski and Pierazzo, 2013). The transient cavity of the small crater undergoes only minor modification and produces a simple bowl-shaped crater. Modification is mainly restricted to debris sliding down along the steep transient crater rim and walls, and leads to an increase in cavity diameter by 10–20%. The depth-to-diameter ratios of a simple crater is ~1:5 to 1:7 (Melosh, 1989). The carter cavity is filled by a thin layer of allochthonous unshocked and shocked brecciated materials of the target rock (Grieve, 1987; Kenkmann et al., 2014). However, as the modification of the transient crater depends mainly on the gravity (Melosh, 1989), simple to complex crater transition occurs at ~5–10 km on Mars, and at ~15–27 km on the Moon (Pike, 1980; Osinski and Pierazzo, 2013).

The transient cavity of a large crater on Earth is quite unstable and undergoes strong modification

due to gravity, producing a complex crater of significantly different shape from its transient cavity (Kenkmann et al., 2014). Strong modification of a large transient crater has to compensate gravitational instability and its collapse includes the slumping of the transient cavity walls and the elastic rebound of the crater floor. The collapse first initiates at the deepest point of the transient cavity floor. As the cavity floor starts to rise upward and inward, it causes a rotational flow field underneath the cavity, pushing the cavity floor upward at the central part. This also results in a mass deficit in the subsurface beneath the cavity rim, which ultimately produces slumping of the steep crater walls and causes an extension of the transient carter rim (Kenkmann et al., 2012). The central peak which brought deep subsurface material to the surface may become gravitationally unstable in the case of a larger carter and can collapse due to its own weight, producing annular ridges inside the crater. Therefore, the resultant shape of the complex crater is characterized by various macroscopic structures such as terraced rims, uplifted central peak, peak ring, crater moat or annular trough of the crater floor, and multi ring basins (see details in Kenkmann et al., 2014). Due to late-stage strong modification, complex craters are shallower than simple craters, with depth-to-diameter ratios of ~1:10 to 1:20 (Melosh, 1989). Overall, with increasing crater diameter, complex crater structures may be of three different types: (i) central-peak structures, (ii) central-peak-basin structures, and (iii) peak ring basin structures (Grieve at al., 1981; Melosh, 1989; French 1998). The crater cavities are filled with a variety of impact generated lithologies known as impactites. According to French (1998), the modification stage has no clearly marked end of complex cratering process. Processes such as the crater floor uplift and wall rock collapse merge into more familiar exogenous geological processes, such as mass movement, erosion and so on.

1.3.3.1 Brittle deformation at modification stage

The intensity of late-stage impact-induced brittle deformation increases from the crater rim to the centre, with accumulated material strain of ~0.25 at the carter rim to ~1 underneath the crater centre (Collins et al., 2004; Kenkmann et al., 2012, 2014). This is related to a transition from localized brittle deformation to a more pervasive cataclasis and granular flow. Hence, large-scale displacements occur on localized fault planes within the crater rim with large blocks sustaining only weak internal damage. On the other hand, an increased brittle deformation occur in the inner crater with small blocks with more internal damage. Between blocks, pervasive cataclasis and granular flow are observed down to the grain scale (Kenkmann, 2003). It is also observed that the target underneath the crater floor, particularly at the central uplift is disintegrated into blocks. The size of the blocks are controlled by lithology of the target rock and distance from the crater centre (Kenkmann et al., 2010). In addition, the peak shock pressures eventually drop to about 1–2 GPa at greater distances from the impact point (Kieffer and Simonds, 1980). Therefore, at the final crater rim, the shock waves become regular elastic or seismic waves, and their velocity drops to that of the velocity of sound in the target rocks. These low pressure seismic waves are not able to produce any permanent deformation of the rocks through which they pass, rather they may produce fracturing, brecciation and faulting (French, 1998).

1.4 Fractures related to impact cratering

During the early stage of cratering when the strain rate is enormously high, closely spaced fractures develop due to passage of the shock wave through the target rock. These fractures tend to be less than 1 cm long with displacements of less than 1 mm, and assemble as irregular to parallel fracture networks (Kenkmann et al., 2014). Together, these small-scale fractures form complex patterns that are not observed in normal tectonic deformation, and can be quantified by fractal-geometry methods

(Hossain and Kruhl, 2014a) (Figs. App. 1.1–1.2). During the excavation stage fractures coalesce and become longer. Inherent flaws as sites of weakness are important for nucleation and coalescence of fractures (Griffith, 1920) resulting in localization of deformation along specific fracture systems (Faulkner et al., 2003; Wilson et al., 2003). The development of narrow-spaced fracture networks on the millimetre- to decimetre-scale to more localized large-scale facture zones on the metre- to decametre-scale indicates the shift from homogeneous to heterogeneous strain distribution (Kenkmann et al., 2014). Besides speed of fracture tip propagation influences the development of fracture geometry. The Rayleigh wave speed of the host rock is the theoretical speed limit for tensile fracture propagation (Sagy et al., 2006), and the fracture propagate at this limit is termed as 'dynamic fracture' (Sagy et al., 2001). According to Sagy et al. (2006), fractures that propagate at high speed, reaching about half of the Raleigh wave velocity, tend to become unstable in brittle materials and bifurcate when velocity excursions occur. In that case, fracture networks are characterized by hierarchical bifurcations or branching as observed on the surfaces of shatter cones (Sagy et al., 2002, 2004). In this study, dynamic fracture branching structures are identified, quantified and successfully used as an indicator of the impact centre location (Hossain and Kruhl, 2015). On the other hand, faults of hundreds of metres to even kilometres length with single-slip offsets of up to several kilometres (Spray, 1997) are always formed during the final stage of cratering, the modification stage.

Ahrens and O'Keefe (1987) divided the peak shock pressure around impact crater into three different pressure regimes: regime 1 is the planar impedance match regime, regime 2 is the pressure decay regime, and regime 3 is the elastic decay regime (Fig. 1.6). Regime 1 extends to few projectile radius into the target rock where planar impedance match pressure exists (McQueen et al., 1970). Much of the target material which is in Regime 1 is thrown out of the resulting crater. Regime 2 extends up to a distance where shock pressure equals the Hugoniot elastic limit (Ai and Ahrens, 2004). Target material is intensely compressed and transformed into fine rock powder by brittle deformation. Except the smaller impact crater, the target material in these two regimes does not remain in the crater but is ejected and may fall back into the crater. At greater distance, intense shear failure of the target rock occurs in the form of concentric and radial fractures. The zone of shear failure is called Grady-Kipp region (Melosh, 1989). Regime 3 begins at a radius beyond the Hugoniot elastic limit. At this regime, the compressional radial stress related to shock wave and tensional circumferential stress related to the rarefaction wave are perpendicular and parallel to the shock front, respectively (Shibuya and Nakahara, 1968; Ai and Ahrens, 2004). When the circumferential stress exceeds the tensile strength of the target materials, it generates radial fractures, i.e. Mode I tensional fractures. As the tensile strength is much less than the compressive strength for a given material, radial fractures extend further than the concentric fractures (Ai and Ahrens, 2004), possibly up to a distance of several times the crater diameter or depth (Melosh, 1989). Tangential (concentric) fractures are formed either by direct shock wave compression, or upon relaxation due to elastic rebound of the rocks after the impact shock wave has passed. They may also be developed by differential movement of the free boundary as the rock is forced outward from the centre of the impact along shear planes intersecting the ground surface (Fulmer and Roberts, 1963). According to Melosh and Mckinnon (1978) and Croft (1981), circumferential tensional fracture or normal fault is produced due to flows of deformable material into the transient crater.

The fracture patterns surrounding the impact crater stem from the impact itself (mainly during the modification stage) as well as the post-impact loading and subsequent crater modification (Melosh, 1989; Freed et al., 2001). In the case of pre-impact fractures of the target rock, impact events generally transformed these fractures into tear faults, and motions along those faults appear to have controlled the geometry of the impact-induced fragmentation structures (Kumar and Kring, 2008). Impact-

induced fractures in terrestrial craters and their adjacent areas have been observed on different scales and using different methods, including direct counting and measuring from outcrops (Bischoff and Oskierski, 1988; Brandt and Reimold, 1995; Bäckström, 2005; Kumar, 2005; Kumar and Kring, 2008; Hossain and Kruhl, 2014a, 2014b, 2015), remote sensing studies (Gurov and Gurova, 1982; Brandt and Reimold, 1995; Gurov et al., 2007; Wright et al., 2013; Sturm et al., 2015), and geophysical and petrophysical methods (Pilkington and Grieve, 1992; Brandt et al., 1998; Bäckström, 2005; Morgan and Rebolledo-Vieyra, 2013). It is generally accepted that the zone of impact-induced fracturing may extend up to one crater diameter away from the crater rim (Gurov and Gurova, 1982; Pilkington and Grieve, 1992; Brandt et al., 1998). However, Hossain and Kruhl (2015) reported that impact-induced fracturing extended up to ~1.3 times crater diameter away from the Ries crater rim.

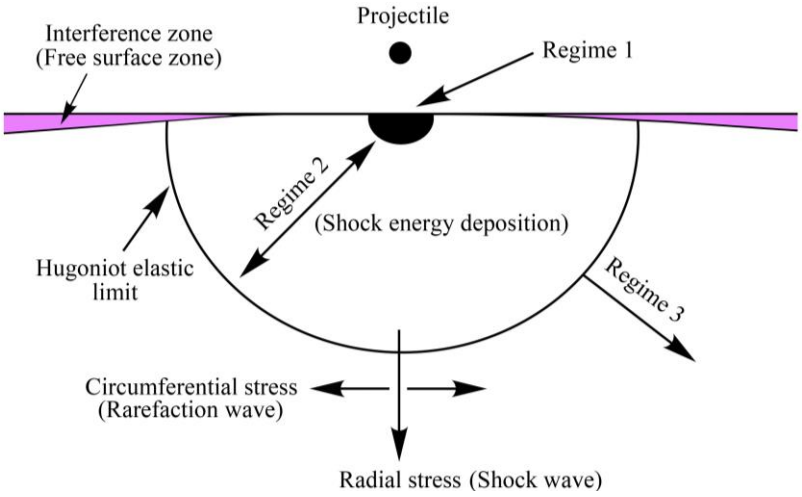

Figure 1.6: Schematic sketch illustrating three shock pressure regimes beneath the impact crater. Regime 1 is the impedance match regime from where much of the target material is thrown out of the resulting crater. Regime 2 is the pressure decay regime, zone of shock energy deposition. Target rock is subjected to mainly shock metamorphism, and intense shear deformation (at periphery). Regime 3 is the elastic decay regime, it begins at a radius beyond the Hugoniot elastic limit. Target rock is subjected to mainly brittle deformation in this regime. Interference zone is developed at the free surface of the target rock (modified after Ahrens and O'Keefe, 1987 and Ai and Ahrens, 2004).

Moreover, the fracture patterns surrounding impact craters are generally quite variable due to local and regional differences of the target rock. Common fracture patterns seen in most cases are radial and concentric (tangential) fracture patterns (Fig. 1.7) (Bischoff and Oskierski, 1988; Hode et al., 2003; Gurov et al., 2007; Kumar and Kring, 2008; Hossain and Kruhl, 2015). These fracture patterns are comparable with the fractures reported from laboratory impact experiments (Fig. 1.7a) (Lange and Ahrens, 1987; Polanskey and Ahrens, 1990; Buhl et al., 2013), micrometeoroid impacts on the solar panels of spacecraft (Graham et al., 2004), and nuclear test sites in the Yucca flat region of Nevada, USA (Fig. 1.7b) (Barosh, 1968; Allen et al., 1997; Grasso, 2001). Overall, five different types of fractures have been reported based on impact cratering experiments (Fig. 1.7a): spall, concentric, radial, vertical, and near-surface fractures (Fulmer and Roberts, 1963; Roddy et al., 1977; Polanskey and Ahrens, 1990). However, in natural impact craters (e.g., Ries crater) it is difficult to distiguish all these fractures. During this study, Ries impact fractures are divided into two sets: radial and tangential (Hossain and Kruhl, 2015). It is most likely that the tangetial set is equivalent to the concentric, conical and vertical fractures, and the radial set is equivalent to the radial as well as so called near-surface fracture reported by Polanskey and Ahrens (1990), and Ahrens and Rubin (1993).

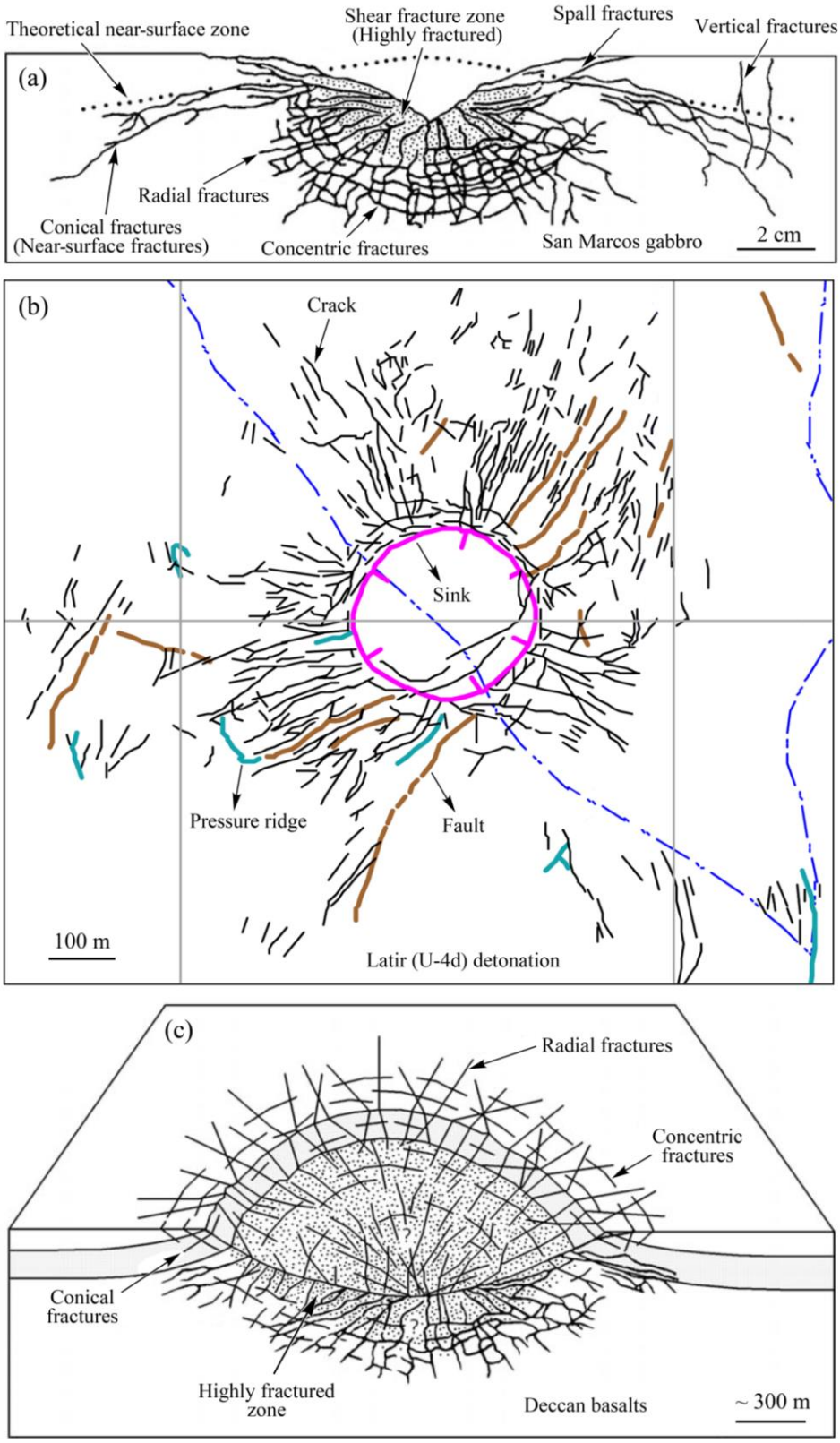

Figure 1.7: Fracture patterns related to different types of dynamic deformation. (a) Cross-section of laboratory impact crater in San Marcos gabbro. Overall, fractures are classified into five types including the highly fractured zone at the centre (modified after Polanskey and Ahrens, 1990). (b) Fractures around a nuclear test site (U-4d, detonated on 2/27/1974) in the Yucca Flat region of Nevada. This is a classic example for surface fracture patterns formed by a nuclear shock explosion (modified after Grasso, 2001). (c) A schematic sketch shows the crater wall fractures of the Lonar crater, India (modified after Kumar, 2005).

1.5 Fragment size distribution related to impact cratering

Impact-induced fragmentation of the target rock is related to a reduction of fragment or particle size. The cumulative frequency curve of the resultant fragment size distribution (FSD) can be properly quantified and described by power-law relationship in which the exponent is referred to as the fractal dimension or *D*-value (Buhl et al., 2013; Hossain and Kruhl, 2014a). Studies on natural impacts provide a wide range of *D*-values within 1.2–2.99 (Rousell et al., 2003; Key and Schultz, 2011; Hossain and Kruhl, 2014a). Impact experiments show an increase of *D*-values with increasing impact energy (Lange et al., 1984), and cratering as well as shock-recovery experiments suggest a correlation with strain rate (Buhl et al., 2013). High values are reported to be related to increasing strain or strain localization (Monzawa and Otsuki, 2003; Billi and Storti, 2004; Dyer et al., 2012). The wide range of fractal dimensions in the literature as well as in this research argues against shock-induced fragmentation being the only or dominant process during impact and suggests that different parameters, such as rock type and pre-impact rock structures, and their interaction have to be considered. In addition, the influence of the latter two stages of impact cratering (the excavation and modification stages) versus other parameters is expected to vary with time and distance from the point of impact and may produce a wide range of *D*-values (Hossain and Kruhl, 2014a).

Quantification of FSD related to quasi-static as well as dynamic fragmentation are increasingly used in investigations of stress fields (Leterrier et al., 2001; Chao and Kaneko, 2004; Kaushik, 2007; Zhao et al., 2009; Quinta et al., 2012), rock strength and deformability (Feng et al., 2009) and strain rate of deformation (Buhl et al., 2013). FSD may originate from different processes of fragmentation, for example, ballistic fragmentation or fragmentation in a slowly increasing stress field (Kaye, 1989; Buhl et al., 2013). Shock experiments demonstrate that dynamic fragmentation influences the FSD and can be expressed as fractal (Buhl et al., 2013). On the other hand, FSD in fault rocks show variations in *D*-values, interpreted as resulting from different fragmentation processes, the number of events, energy input, confining pressure, selective fracturing of larger particles and, in certain situations, alteration of particles (Blenkinsop, 1991). Therefore, *D*-value quantification of FSD related to dynamic fragmentation and their comparison with the *D*-value of the fault rock FSD can be used as important tools for getting deeper insight into impact-related fragmentation processes and their interaction (Table App. 1.1).

Even though international research has focused on impact research in recent years, more detailed investigations are still necessary for deeper understanding of impact-induced fracture patterns, FSD and fragmentation structures in the target rock. In this PhD research, Ries impact-induced fracture patterns and FSD are recorded, measured and quantified (chapter three), and characteristics as well as the spatial distribution of the fragmentation structures around the carter rim (chapter four) and their possible influence on the development of karstification (chapter five) are investigated. Structures related to ‘suevite’ emplacement and ‘suevite’ internal textures are also studied from the ‘Stoer impact’ area, NW Scotland (chapter six). Chapter three has been published in Pure and Applied Geophysics and chapter four is submitted to Earth and Planetary Science Letters. Thus, chapters three and four have their own abstract. Chapters five and six are the preliminary result of the ongoing investigation. In addition, most of the processed data, supplementary figures and computer script are given in appendix one to six.

CHAPTER TWO

2. Quantification of impact-induced fragmentation - Methods

Characteristics of the impact-induced fragmentation structures and resultant complex patterns are mainly quantified by methods based on structural geology, classical spatial statistics and fractal geometry. Fragmentation structures and complex fracture patterns are mainly quantified by using fractal-geometry methods. Methods based on classical spatial statistics are used for quantification of the zones of intense fragmentation. Methods based on structural geology are used for the analysis of prominent fractures, and cave phase orientations. A brief description of all the methods is given here.

2.1 Fractal-geometry methods

Fractures occur in any material and at all scales. Generally, they form complex patterns, i.e. are statistically self-similar over a certain range of scale ('fractal') (Mandelbrot, 1982; Kruhl, 2013). Such patterns cannot be analysed by conventional methods but are suitable for application of fractal-geometry techniques (Mandelbrot, 1982). Since fragmentation patterns, i.e. the purely geometric aspects of fractures and fragments, bear most information, pattern analysis represents the 'core' of investigation of fractured matter and fracture-forming processes. Fragmentation patterns are generally different (i) in different directions (anisotropy), (ii) in different areas (inhomogeneity), and (iii) on different scales (scaling) (Kruhl, 2013). Anisotropy of fracture patterns results from direction-related processes. Depending on orientation and differences of the principal stress components, fractures tend to follow certain orientations and thus fracture patterns tend to have an azimuthal anisotropy (Velde et al., 1990). Inhomogeneity of fractures mostly results from inhomogeneity of the material fabrics in different areas, inhomogeneous distribution of pre-given fractures, stress distribution pattern, as well as fabric-forming processes. Consequently, the analyses of fracture patterns provide information about these parameters and processes (Kaye, 1993; Kruhl, 2013). Fracture patterns may be self-similar over several orders of scale. However, self-similarity may also change from one range of scale to the next, as a result of different material fabrics and deformation behaviour on different scales (Kruhl, 2013).

Various fractal-geometry methods are established, which lead to successful quantification of complex patterns of various types and in a wide range of materials (Kaye, 1989; Kruhl, 2013). The basic concept of all fractal analysis methods is that a pattern will be repeated on different scales in the same manner, the major variable being the fractal dimension which is used as a measure of the nature of the pattern (Velde et al., 1990). The fractal relation can be expressed as $N = d^{-D}$, where N is the number of events, d is the measurement dimension (e.g., 1D, 2D, 3D), and *D* is the fractal dimension. The methods discussed here are organised so that they proceed in a logical order and each method builds on the previous one.

2.1.1 Fragment size distribution

Fragment sizes form a common type of data set related to brittle failure of the rock or rock fragmentation. The cumulative frequency curve of the resultant fragment size distribution (FSD) can be properly quantified and described by power-law relationship in which the exponent is referred to as the fractal dimension or *D*-value (Sammis and Biegel, 1989; Blenkinsop, 1991; Keulen et al., 2007). Buhl et al. (2013) reported fragment size distribution as fractal for impact-loaded rocks based on impact cratering experiments. In this PhD study, grinded and polished cuts of the boulders and core samples (Ries Research Borehole 1973) of the Ries impact crater is prepared and scanned with a

resolution of 1200 dpi. In addition, thin sections from the core samples, and 'suevite' (Stoer impact, NW Scotland) are scanned with 4200 dpi resolution. Outline of the fragments from all cuts and thin sections are manually digitized using ArcMap10 and converted into binary images of two scale ranges (i) decimetre- to millimetre-scale (sample-scale), and (ii) millimetre- to micrometre-scale (thin-section-scale) (Fig. 2.1). These scales allow analysis of the fragments within the statistically reliable range of over one order of magnitude. The computer program Crack Image Analysis System (CIAS) has been used to extract FSD data from the binary images of boulder and core samples. CIAS is an automated system for the quantification of cracks and fragments (Liu et al., 2011, 2013). Quantification of different geometrical parameters of the fragments using CIAS has three steps: (i) image segmentation, (ii) crack network identification, and (iii) measurement of the geometrical parameters of crack and fragment. Area, perimeter, length, and width of the fragments are calculated in the final step of CIAS analysis. The lower limit of the CIAS resolution is about five pixels, which includes about 98.5% of the total number of fragments. After extracting geometrical parameters from CIAS and processing FSD data in spreadsheet, size-cumulative frequency in double logarithmic plots are prepared. The exponent of the power-law relationship is referred to as the *D*-value of the FSD.

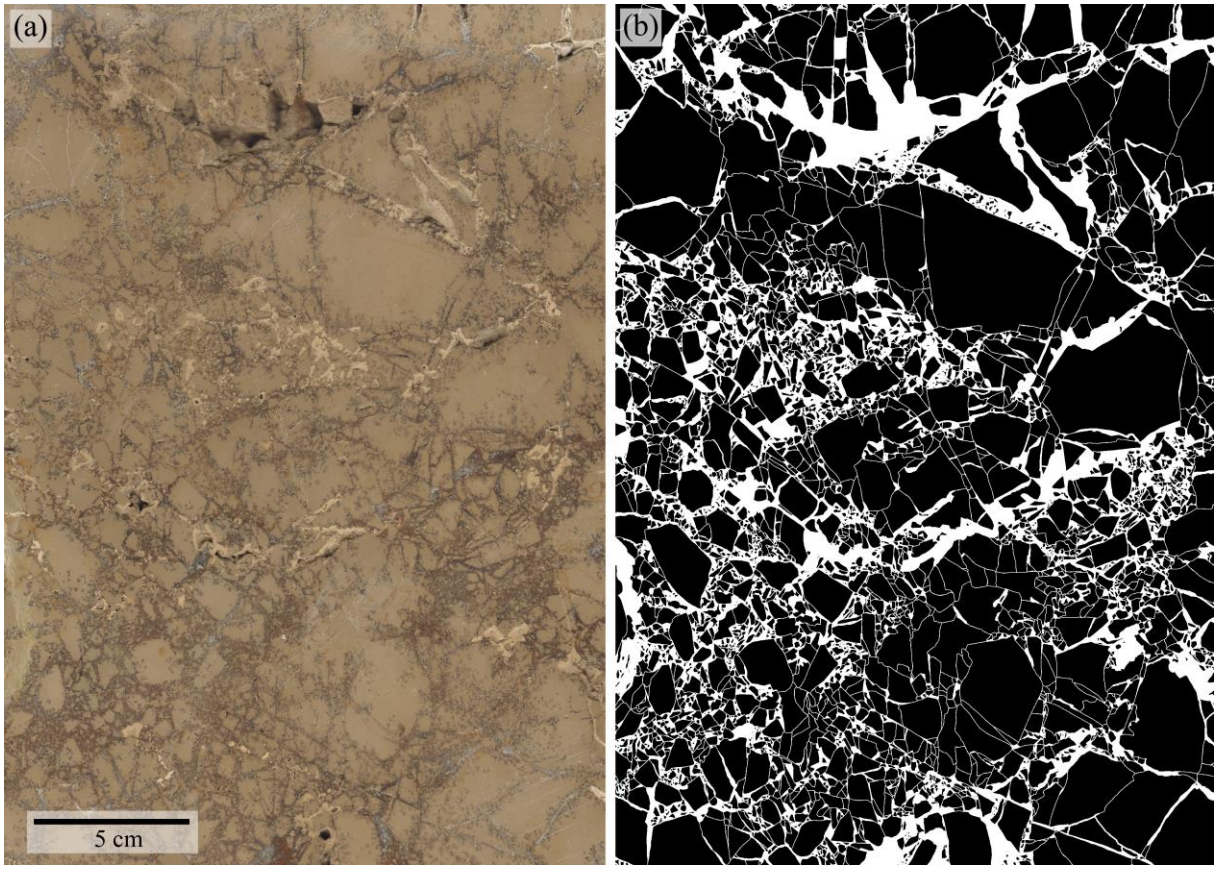

Figure 2.1: Manual digitization of fragments outline from a limestone boulder collected from the Unterwilfingen quarry, in the megablock zone, ~8.5 km WNW of the Ries crater centre (see location in Fig. 3.1, chapter three). (a) Sample cut of a monomict limestone breccia (allochthonous boulder). The sample is ground, polished and scanned with a resolution of 1,200 dpi. (b) Binary image of fractures (white lines) and regions of sub-microscopically fragmented material (small white areas). One pixel = 0.065 mm on the rock surface.

However, during FSD analysis, deviation of the data points from the regression line is observed at the upper and lower limit. The lower limit of the resolution is about 0.1 mm for the core samples and

boulder rock samples and about 0.01 mm for the thin sections. The upper limit of the resolution is about 10–20 cm for the core samples and boulder rock samples and about 10–20 mm for the thin sections. Deviation at the lower limit is most likely due to the fact that some of the small fragments are poorly visible and, therefore, not fully recorded during the digitization of the fragmentation pattern from scan image. This under-sampling or truncation effect influences the result and is omitted from the analysis (Ackermann et al., 2001; Volland and Kruhl, 2004; Ford and Blenkinsop, 2008; Kruhl, 2013). This is perhaps also true for the deviated data points at the upper limit as some of the larger fragments are partially cut due to rectangular image selection for the analysis, or that larger fragments do not occur in a statistically suitable number. However, fragments in the thin section do not show such effect as the thin section provides more or less 100% outcrop view.

2.1.2 2D box counting

Fractures and fragments often form complex structures characterized by the arrangement of smaller fractions of the structure. During quantification of the structure, it is necessary to take into consideration this arrangement and the internal geometry of sub-structures. This is very important because the less information about the geometry of the structure i.e. the orientation of pattern fractions relative to each other gets lost, the more information about structure-forming processes is preserved (Kruhl, 2013). The box-counting method (Mandelbrot, 1977; Kaye, 1989) is a powerful tool to quantify the degree of complexity in object distribution patterns, i.e. the ability of a pattern to fill the space (Mandelbrot, 1982). This method is widely used to quantify fracture patterns on the micro- to mega-scale and to various materials (Castaing et al., 1996; Cello, 1997; Ayunova et al., 2007; Park et al., 2010).

To calculate fractal dimension using the box-counting method, a grid of square boxes of side length S is superimposed on the binary image which contains line pattern of fracture and/or fragment. The number of boxes that contain fracture line N(S) is plotted against S (box side length) on double logarithmic scale. The procedure is repeated by decreasing the box side length in each step. If the plot is linear then it shows a power-law relationship in which the exponent is referred to as the fractal dimension or *D*-value (Turcotte, 1989; Roy et al., 2007). In this study, 2D box-counting analysis of the fracture pattern has been performed by using the software Benoit 1.3 (Seffens, 1999). During analysis using Benoit, it is necessary to use lower coefficient value (1.1), and lower incremental grid rotation value (~1–5°) to get a statistically robust data set. Fractal dimension limit for a 2D natural data set is in between 1 and 2. Outside this limit, the measured fractal dimension would return a trivial value of 1 for time series data or 2 for image data.

2.1.3 Map counting

In the case of large fragmentation images with significant pattern variation (Hossain and Kruhl, 2014a), box-counting method does not catch the variation of the patterns in different parts, i.e. inhomogeneity of the pattern. In order to receive information about this property, combinations of methods are required (Kruhl, 2013). Inhomogeneity of pattern complexity is best quantified by applying box counting to systematically selected sub-patterns. Peternell et al. (2010) developed a method known as Map counting which is able to quantify the inhomogeneity of the pattern. This method is a combination of the box-counting method and gliding window procedure. At first, the image has been divided into a number of rectangular sub-images with certain overlap. Then a rectangular gliding window of the sub-image size has been used as analysis window (Peternell et al., 2010, 2011). The rectangular window passes over the image and generates fractal dimensions of the

pattern within the window. Each value is converted to a colour code and plotted as a single coloured pixel at the centre of the window (sub-image) (Fig. 2.2). Eventually, a colour-coded map is produced based on the distribution of all pixels. However, before applying the map-counting method, individual analyses of several sub-images is required to fix the analysis interval and other parameters (e.g., base, threshold distance). In addition, the size of the rectangular window and the gliding distance in each step need to be adjusted based on the size of binary pattern, overall pattern complexity, and computational power and time. On top of that, constant fractality of the pattern over the entire range of scale may not exist. For example, patterns may show two different fractalities on two different scales: structural fractality on large-scale and textural fractality on smaller-scale (Kaye, 1989; Kruhl, 2013). Therefore, the inhomogeneities of the pattern with respect to these two fractalities need to be quantified and presented independently.

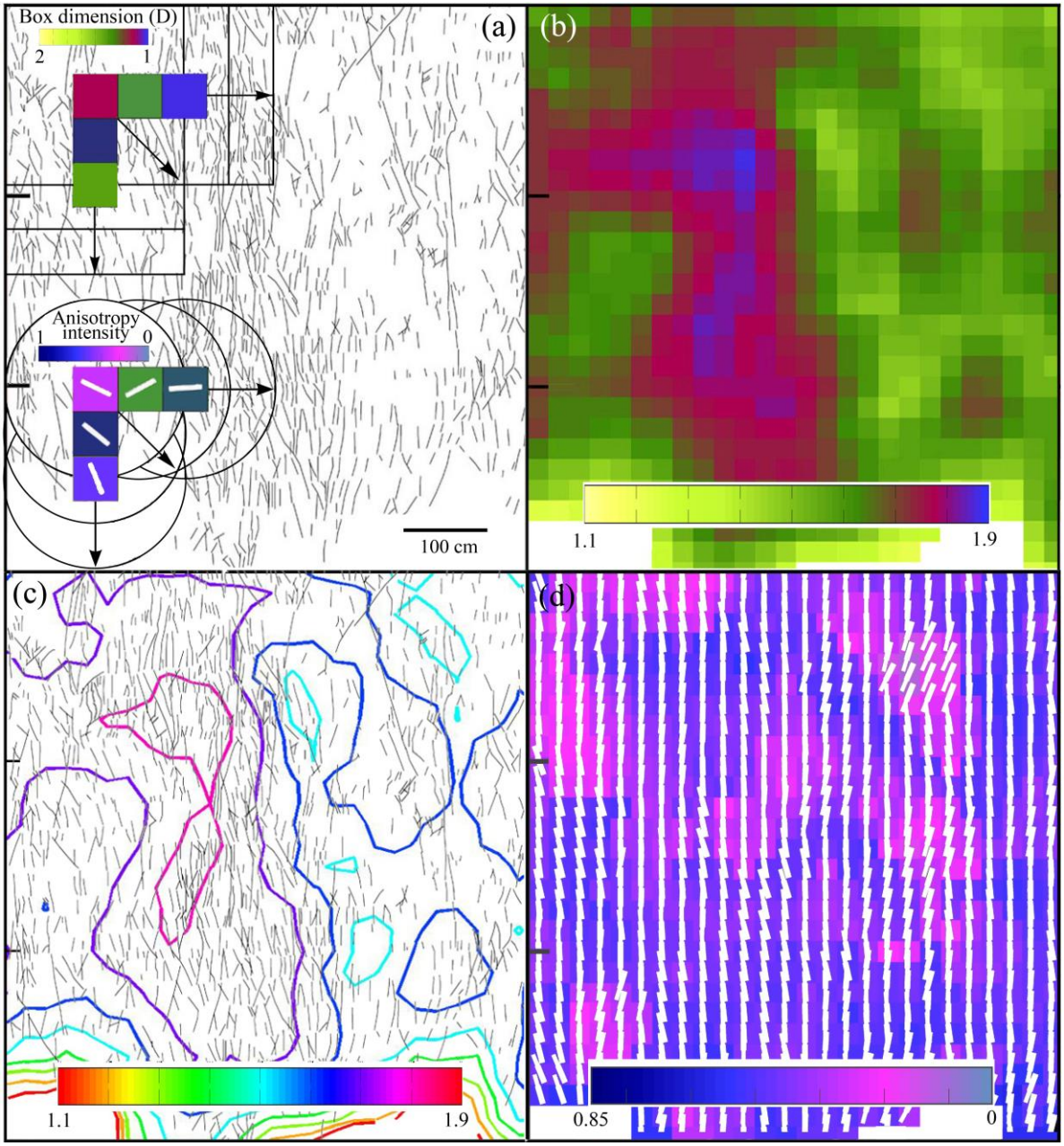

Figure 2.2: Map counting (Peternell et al., 2010) and MORFA (Peternell et al., 2011) exemplified by a fracture distribution pattern (black lines). (a) Map counting (upper left corner): An initial rectangular window (solid-line

box) of specific size is shifted in two orthogonal directions (arrows) over the pattern, with certain steps of lengths (overlap). For each of the rectangles the fractal dimension *D* is determined by box counting. The *D*-value is then plotted in the centre of each related window as a colour-coded pixel with a size equal to the step length. MORFA method (lower left corner): An initial circular window (black circle) of specific size is shifted in two orthogonal directions (arrows) over the pattern, with certain steps of lengths (overlap). The pattern within each circle is analysed by the modified Cantor's-dust method (Volland and Kruhl, 2004) using AMOCADO (Gerik and Kruhl, 2009) and resulting anisotropy value is plotted in the centre of each circle as a colour-coded pixel with size equal to step length. Each coloured pixel represents the anisotropy intensity (ratio *a*/*b* of a fit ellipse) of the analysed pattern. The white bar represents the direction of the short axis *b* from a fit ellipse, i.e. the short axis of anisotropy. (b) Colour map of the box-counting dimension is based on the rectangular grid arrangement of *D*-value. Rectangular measurement window: 100 × 100 cm with 75% overlap. (c) Contour map of the box-counting dimension based on the rectangular grid arrangement of *D*-value. (d) Colour map of anisotropy intensity is superimposed with the direction of anisotropy of pattern complexity (i.e. short axis *b*). Circular measurement window: 100 cm diameter with 75% overlap.

2.1.4 Cantor's dust

In structural geology, three major aspects of fractures (fault, joints) are commonly analysed and quantified on a given surface area of a rock which influence fragmentation: fracture length, fracture spacing, and fracture thickness (Turcotte, 1986; Velde et al., 1990; Kruhl, 2013). But, it is well recognized that fractures follow specific directions according to the stress tensor which has been applied to the material in question (Velde et al., 1991). Therefore, one would expect that a fracture pattern would be disposed differently in different directions in response to the forces which produced it. As a consequence of this situation, anisotropy of the fracture patterns is expected. Quantification of such 2D anisotropic patterns can be easily performed by 1D Cantor's-dust method. In order to identify the self-similarity of fracture spacing on a given fracture pattern, two different approaches of the Cantor's-dust method are generally used: (i) the spacing-population method (Harris et al., 1991; Merceron and Velde, 1991), and (ii) the interval-counting method (Velde et al., 1990, 1991). The former method counts the number of segments N, which contains at least one intercept point, vs. the segment length S in the direction of measurements. The latter method is basically a 1D version of box counting (Kruhl, 2013). In this study, the concept of self-similarity of the impact-induced fracture patterns has been checked by using both the interval-counting method (Velde et al., 1990) and the spacing-population method (Merceron and Velde, 1991) (Figs. App. 2.1–2.2).

2.1.5 Modified Cantor-dust method

Volland and Kruhl (2004) modified the spacing-population technique (Harris et al., 1991) of the Cantor's-dust method for analysing the 1D distribution of structures in relation to directions in 2D. Parallel lines at specific intervals are superimposed on the pattern's binary image and oriented in different directions with certain degree intervals in each step to cover 0 to 180°. Subsequently, their cumulative frequency distribution in each direction is presented in a double-logarithmic plot, and the exponent of the power-law relationship is referred to as the fractal dimension or *D*-value. This holds for all other directions. Then the fractal dimensions in all measured directions are plotted in a single diagram with respect to the centre of a sphere. Finally, a fractal Dimension Orientation Diagram (DOD) is generated from the sphere based on the best fit ellipse of the measured data (Velde et al., 1990; Volland and Kruhl, 2004). Anisotropy intensity (AI) is quantified based on the ratio of short (*b*) and long (*a*) ellipse axes representing the orientations of minimum and maximum fractal dimension, and the diagram is known as the azimuthal anisotropy of fractal dimension (AAD) (Volland and Kruhl, 2004). The total process is known as modified Cantor-dust Method (MCDM).

2.1.6 Automated modified Cantor-dust method

Due to manual analysis, the MCDM is particularly time consuming. To overcome this problem, Gerik and Kruhl (2009) automated the process for fast and efficient analysis by developing a Matlab based software tool known as automated modified Cantor-dust method (AMOCADO). As this software tool considers the slope value *m* of the double logarithmic plot as size-distribution coefficients, it can be used to perform quantifications of both fractal and non-fractal patterns. To facilitate the interpretation of the data sets, logarithms with 10 base are used in this software. The set of parallel scan lines is successively rotated counter-clock-wise from initial horizontal position around a fixed centre point on a binary pattern. The total rotational angle is 0–180° with a constant successive increment of rotation angle. The angular resolution of 1° or even less is possible by this software. After calculating the slope values, they are plotted in a direction vs. slope diagram known as DOD (Volland and Kruhl, 2004) with a best-fit ellipse that represents most of the data points. Anisotropy intensity (AI) is quantified based on the ratio of short (*b*) and long (*a*) ellipse axes as in MCDM. In order to minimize the occurrence of edge effects due to cut off along the periphery of the binary pattern, the first and/or last segment of the scan line, which is only partly covering the pattern phase is eliminated (Gerik and Kruhl, 2009). The number of scan lines and their spacing depend on the size and complexity of the pattern as well as available computation time.

2.1.7 Mapping of rock fabric anisotropy

For a pattern with significant variation in different parts, MCDM based AMOCADO does not catch the variation of the patterns anisotropy in different parts, i.e. inhomogeneity of pattern anisotropy. This technical problem is overcome by the method known as mapping of rock fabric anisotropy (MORFA), developed by Peternell et al. (2011). MORFA combines AMOCADO with a gliding-window procedure and thus quantifies the inhomogeneity of the anisotropy of the pattern complexity (Fig. 2.2d). Measurements are carried out in circular windows and results are plotted as pixels at the centre of each circle. Pixel colour intensity indicates anisotropy intensity represented by the axial ratio of a fit ellipse. A bar at the centre of each pixel is equivalent to the orientation of the short axis (*b*) of the fit ellipse which is known as the short axis anisotropy (SAA). This short axis represents the general direction of minimum pattern complexity. However, before applying MORFA method, individual analysis of several sub-images using AMOCADO is required to fix the analysis interval and other parameters (e.g., base, threshold distance). In addition, the size of the circular window and the gliding distance in each step are needed to be adjusted based on the size of binary pattern, overall pattern complexity, and computational time. Moreover, as mentioned before in Map counting, inhomogeneity of the pattern anisotropy with respect to structural, and textural fractality (Kaye, 1989; Kruhl, 2013) may need to be quantified and presented separately if the pattern shows two different fractalities on two different scales.

2.2 Time-series analysis

Impact-induced fragmentation produces zones of high deformation (Hossain and Kruhl, 2014a). Fracture frequency within these intensely fragmented zones is much higher than their neighbouring regions. Moreover, these zones seem to occur repeatedly both in vertical and horizontal direction but at different intervals (Hossain and Kruhl, 2015). The time-series analysis aims to understand the spatial behaviour of fracture frequency (y) in space (x), i.e. to detect possible repetition interval (cyclicities) of the zones of high deformation. In this study, basis of quantification in horizontal

direction is high resolution field photographs from the vertical sections of two different quarries (see details in Hossain and Kruhl, 2015), and basis of quantification in vertical direction along the drill core of the Ries Research Borehole 1973 is the geophysical well-log data of fragmentation taken from Ernstson and Pohl (1974). The raw data sets are smoothed and linear trends are removed by using 'lowess' and 'detrend' function respectively, available in the Matlab Curve Fitting Toolbox™. 'Lowess' smooths scatterplots by robust locally weighted regression (Cleveland, 1981), and 'detrend' removes any linear trend hidden in the data vector. Time-series analysis (Vere-Jones and Davies, 1966; Trauth, 2010) of the fracture frequency data is performed by using Fourier transform (Bracewell, 2000) and Wavelet transform (Morlet, 1983; Mackenzie et al., 2001) methods to understand spatial fracture frequency distribution in horizontal and vertical direction.

2.2.1 Autospectral

In autospectrum analysis (Hegge and Masselink, 1996), powerspectra (Frigo and Johnson, 1998) is estimated by using fast Fourier transformation (FFT) algorithm. As the data set used in this study is discontinuous, the FFT method computes a discrete Fourier transform (DFT) with reduced execution time. The DFT is very important in the area of frequency (spectrum) analysis because it takes a discrete signal in the time domain and transforms that signal into its discrete frequency domain representation (see details in Trauth, 2010). In addition, variations of the spectral peaks amplitude with distance are determined by Evolutionary powerspectra (Oppenheim et al., 1999). The Matlab based script written for this analysis is given in Appendix 2.3a. However, as the time series data is divided into overlapping segments and computes the Fourier transform of these segments, the Fourier transform method has some disadvantages, such as spectral leakage and underrepresentation of the low-frequency cycles (Trauth, 2010).

2.2.2 Wavelet transform

To overcome the problem of spectral leakage and underrepresentation of the low-frequency cycles, Wavelet transform (Morlet, 1983; Lau and Weng, 1995; Mackenzie et al., 2001) has been used. Wavelet transform is an excellent tool well suited to analyse multistate, non-stationary processes occurring over finite spatial domain. Although this method can easily map changes in the time or spatial-frequency domain with a flexible standard resolution, it is underused and underexplored for geological research, specifically fracture frequency studies. For wavelet power spectrum analysis, different wavelets are used that can be grouped into two categories: continuous and orthogonal wavelets. In this study we have used complex Morlet wavelet (Torrence and Compo, 1998), which is a continuous wavelet and consists of a plane wave modified by a Gaussian envelope. This wavelet is widely used in geophysics and best suited for our data set. The wavelet transform is computed in 120 different scales between 1 and 120. The Matlab based script written for this analysis is given in Appendix 2.3b.

2.3 Structural geology methods

Orientation analysis of fractures, folds and bedding is done using Stereo32 software. Besides, a number of digital field photographs of each vertical section is taken from approximately the same distance with ca. 35% overlap. Photographs of each section are subsequently merged to a single image using Photoshop CS4. Individual fracture in the image is then digitized manually using ArcMap10 and Photoshop CS4, and converted into a binary pattern. All visible fractures in the field photographs are

digitized with a lower limit of resolution up to 3 mm, irrespective of being impact related or not. At the time of digitization, careful attention has been given to keep the zooming levels same for all parts of the image. During digitization of the fracture surface, core and thin-section images, only fractures that passed through several grains or extended across more than one grain are digitized. However, small fractures restricted in a single grain but connected with larger fractures are also digitized. Lower limit of digitization resolution is 0.2 mm for the surface and core samples, and 0.01 mm for thin section.

Digitization and subsequent processing with Photoshop have left a few isolated, randomly distributed pixels inside the pattern ('salt and pepper noise'), which are removed by using a Matlab image processing algorithm. In addition, we have used a remotely controlled drone for photographs to produce a panorama image of the Gundelsheim quarry. During photographs, drone altitude is maintained at the same level, camera focal length and exposure is not changed, and sufficient overlap is maintained between neighbouring photographs. In post processing, Lightroom 5.7 software is used for removing lens distortion and vertical correction, and Photoshop CS4 is used to merge individual photographs to produce a panorama image.

2.3.1 Intercept-counting method

The anisotropy of the fabric distribution patterns can also be determined by using the intercept-counting method (Underwood, 1970; Launeau and Cruden, 1998; Launeau et al., 2010). The set of parallel scan lines is successively rotated from initial vertical position around a fixed centre point of a circular area on a binary pattern. The total rotational angle is 0–180° with a constant successive increment of rotation angle (Launeau et al., 2010). Mean length of the intercepts in each direction is counted by dividing the total area of the fragments in the analysis window by the number of its intercepts on that specific direction (Launeau and Cruden, 1998). The resultant rose diagram of the mean intercept length is a measure of 2D shape anisotropy, degree of preferred orientation and size of the fragments. The anisotropy orientation is given by the direction ψ of the second component of its Fourier series (Launeau and Robin, 1996), and its intensity is given by the ratio of the mean intercept lengths of the fragment counted in directions ψ and $\psi+\pi/2$, i.e. ratio of the length of long (a) and short axis (b), respectively, of the rose diagram (inertia tensor) (Launeau et al., 2010). A population of circular or randomly oriented fragments will give anisotropy intensity $a/b = 1$. However, to keep consistency between intercept and AMOCADO analysis, anisotropy direction (a-axis) is counted clock-wise from the horizontal direction and anisotropy intensity is measured as b/a in this study.

However, data generated from a two dimensional surface do not necessarily reflect the true sizes of the fragment in three dimensions. They can underestimate fragment size because a surface that randomly cuts spherical or equant fragments is more likely to intersect a section that does not include the true maximum diameter. This is called the intersection-probability effect (Cashman and Mangan, 1994; Higgins, 2000; Sahagian and Proussevitch, 1998). In addition, random planes cut through rocks with similarly-shaped, but differently-sized populations of fragments are more likely to intersect larger fragments, hence creating a bias in fragment size distributions towards coarser fragments, known as the cut-section effect (Higgins, 2000). Moreover, selective and insufficient sampling, low number of data points, and incorrect set of the analysis area in relation to the pattern may lead to a considerable bias of the pattern quantification results (Kruhl, 2013). Therefore, careful attention is needed during pattern recording, measurement and quantification.

CHAPTER THREE

3. Fractal geometry-based quantification of shock-induced rock fragmentation in and around an impact crater

Published in Pure and Applied Geophysics: Hossain, M.S., and Kruhl, J.H., 2014. Fractal Geometry-Based Quantification of Shock-Induced Rock Fragmentation in and around an Impact Crater. Pure and Applied Geophysics, doi:10.1007/s00024-014-0922-8.

Abstract

Shock-induced fragmentation structures of basement rocks and their limestone cover in and around the Ries impact crater (Germany) were recorded on outcrop, sample and thin-section scale and quantified mainly by fractal-geometry methods. Quantification was performed by automated procedures and in areas of square-centimetres to square-decametres with maximum resolution of micrometre scale. In 2D and on all scales, the fragmentation structures form complex, statistically self-similar patterns (fractals) with specific characteristics: (i) The pattern fractality is scale dependent. (ii) Three different power-law relationships exist, which reflect the effect of three fragmentation processes. (iii) The fracture patterns are anisotropic and inhomogeneous over larger areas. (iv) Complexity and anisotropy of the fracture patterns vary systematically. Such systematic variation appears typical for impact-related fragmentation.

3.1 Introduction

Impact fragmentation is mainly caused by a primary shock and secondary refraction waves propagating through the rocks. Other causes include elastic rebound of the transient crater floor and gravitational collapse of the transient crater wall. Different fracture patterns have been recorded based on (i) field observations (von Dalwigk, 2003; Kumar and Kring, 2008), (ii) cratering experiments (Polanskey and Ahrens, 1990; Buhl et al., 2013) and (iii) numerical modelling (Melosh and Ivanov, 1999; Wünnemann and Ivanov, 2003; Collins et al., 2004). These studies show that stress, strain and strain rate are highest near the impact site and decrease with radial distance. Thus, shock-related shattering and fracturing of the target rocks rapidly decrease from the impact site outwards. The target rocks are intensively fractured from a micro- to a kilometre-scale. Large-scale fractures with vertical to sub-vertical orientations and little or no displacement are dominant. Overall, the fractures form complex patterns, statistically self-similar (fractal) over a range of scales that can be best analysed by fractal-geometry techniques (Mandelbrot, 1982; Kaye, 1993). The quantitative aspects of such patterns are mostly represented by pattern anisotropy, inhomogeneity and scaling behaviour (Kruhl, 2013).

Quantification of fracture patterns and fragment size distributions (FSD) are increasingly important in investigations of stress fields (Leterrier et al., 2001; Chao and Kaneko, 2004; Kaushik, 2007; Zhao et al., 2009; Quinta et al., 2012), rock strength and deformability (Feng et al., 2009) and strain rate of deformation (Buhl et al., 2013). Fracture patterns may originate from different processes of fragmentation, for example, ballistic fragmentation or fragmentation in a slowly increasing stress field (Kaye, 1989). FSD in fault rocks show variations in fractal dimensions, interpreted as resulting from different fragmentation processes, the number of events, energy input, confining pressure, selective fracturing of larger particles and, in certain situations, alteration of particles (Blenkinsop, 1991). Shock experiments demonstrate that dynamic fragmentation influences the FSD and can be expressed as fractal (Buhl et al., 2013). Therefore, quantification of fracture patterns as well as fragment sizes are

an important tools for getting deeper insight into impact-related fragmentation processes and their interaction.

The Ries meteorite crater (Nördlingen, Germany; Fig. 3.1) is one of the best preserved craters in the world and has been studied from various geological and geophysical perspectives. At 14.6 ± 0.1 million years ago (Schwarz and Lippolt, 2013), an oblique impact of an approximately 1.5 km diameter achondritic meteorite (Stöffler et al., 2002) formed a crater of approximately 25 km diameter. The meteorite impacted a terrane that consisted of a 620–750 m thick sub-horizontally layered sequence of water-saturated sedimentary rocks of Triassic to Jurassic age, resting on basement rocks that experienced their last deformation and metamorphism about 320 million years ago (Graup, 1977; Hüttner and Schmidt-Kaler, 1999). Prior to the impact, the sedimentary rocks did not undergo any deformation except for late-Eocene subsidence and mid-Miocene gentle uplift (Plant et al., 2003; Strasser et al., 2009a).

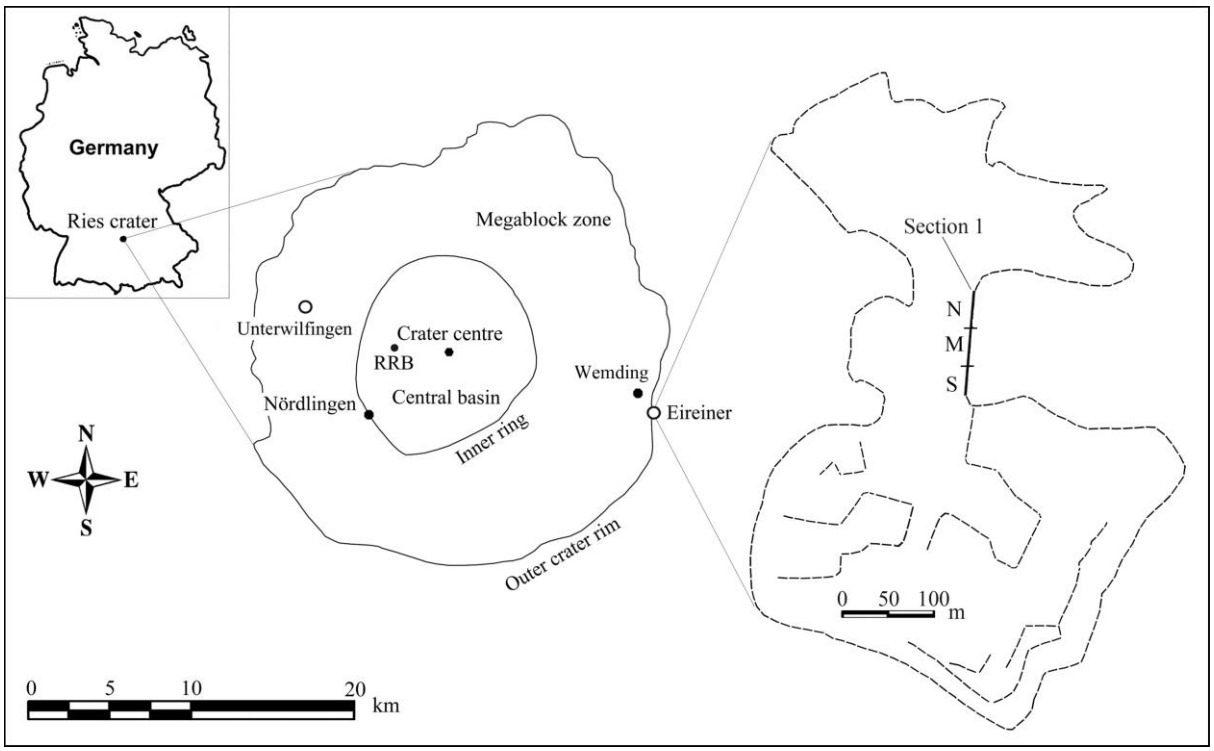

Figure 3.1: Ries impact area with crater outline, crater centre, location of Ries Research Borehole RRB, boulder sample location (Unterwilfingen) and position of Eireiner quarry. The dashed line indicates the boundary of the quarry. Total length of section-1 (quarry wall): 114.03 m; average height: 9 m. N, M and S: north, middle, and south parts of the section, used for quantification.

The Ries meteorite crater is a complex impact crater with three distinct parts: centre, inner crater ring and outer crater rim (Stöffler, 1977). The inner ring boundary (Fig. 3.1) is mostly formed by up- and outward displacement of the crystalline basement. Between the inner ring and the outer crater rim is a megablock zone characterized by concentrically faulted separate blocks. The boundary of the outer rim is the structural margin of the Ries crater. Based on different fractal-geometry methods, our paper presents quantification of the inhomogeneity and anisotropy of shock-induced fracture patterns and their FSD. The results of FSD are discussed and compared with tectonically and experimentally produced FSD from other studies.

3.2 Materials, methods and measurements

For fracture-pattern quantification, we photographed a vertical face in a quarry at the outer crater rim ESE of the crater centre (Fig. 3.1; the Eireiner quarry, section-1, approximately 45 m below surface). The quarry is located in the 140–150 Ma old Upper Malm limestone (Hüttner and Schmidt-Kaler, 1999). We also quantified fracture patterns in core samples from the 1973 Ries Research Borehole (RRB) and patterns in two strongly fragmented boulders from the Unterwilfingen quarry (Fig. 3.1).

In the Eireiner quarry, 40 digital photographs of section-1 were taken from approximately the same distance and subsequently merged to an image representing a 117.35 m length of the quarry face. When taking the photographs, we used a medium focal length in order to minimize distortion. Other steps taken to minimize distortion, included overlapping the vertical sides of the photographs by approximately 35% and cutting 5%–10% off the top and bottom of each photograph. Partly covered fractures at the base of the section and incomplete fractures close to the edges of the photographs were not digitized, except for a few (<15) large fractures that went out of the photographs. Some edge effects are present because of the uneven rock surface and fractures that were not fully exposed on the photographs. The full range of fractures in all orientations can only be measured in three orthogonal sections, with additional statistical corrections, which was not possible in this study owing to the limited rock exposures.

Individual fractures in the image were digitized manually using ArcMap10 and converted into a binary pattern representing a 114.03 m length (Fig. 3.2). Digitization and subsequent processing with Photoshop left a few isolated, randomly distributed pixels inside the pattern (‘salt and pepper noise’), which were removed by a Matlab image processing algorithm (low pass and median filtering). Binary images of the boulder and core samples were processed in the same manner. Subsequently, the binary pattern from the quarry wall photographs was divided into 27 smaller parts for more convenient application of fractal-geometry methods. The minimum resolution of the analysis was about 5 mm. The steps undertaken from image acquisition to final processing are illustrated in Fig. App. 3.1.

As mentioned, we also examined two boulders and six core samples. The two non-oriented boulders (limestone and granite) are each about 60 cm × 50 cm × 45 cm in size. Based on their lithology and location in the megablock zone, we infer that they are from that zone. The six core samples were obtained from the granitoid parts of the RRB core (Gudden, 1974; Graup, 1977), each 10 cm in diameters and 10 to 45 cm long. Two saw cuts parallel and perpendicular to the long-axes of the boulders and core samples were ground, polished and scanned with a resolution of 1200 dpi. In addition, thin sections from the core samples were scanned with 4200 dpi resolution. The fracture patterns from all saw cuts and thin sections were manually digitized using ArcMap10 and converted into binary images. The lower limit of the resolution is about 0.1 mm for the core samples and boulder rock samples and about 0.01 mm for the thin sections. In the boulder and core samples, fracture width is about 0.1 mm. In core thin sections, the fracture width is about 0.015 mm.

Fractality of the fracture patterns of all the 27 sub-sections was tested by 2D box counting (Mandelbrot, 1982), using the Benoit® software. Because box counting is sensitive with respect to both the lower limit of resolution and the total area of analysis, larger and smaller box sides in a range of 150–0.6 cm were chosen, clearly far from the upper and lower limits of pattern resolution.

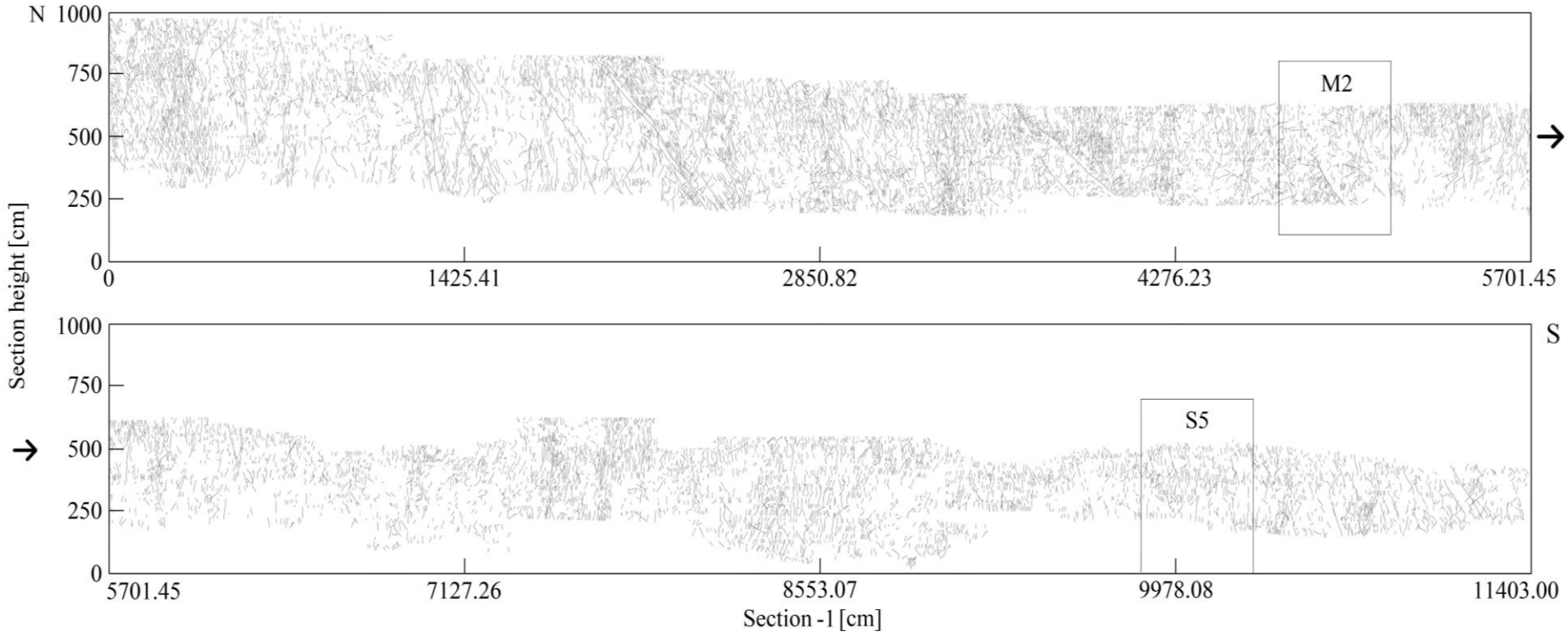

Figure 3.2: Binary image of fractures in section-1 of the Eireiner quarry after merging, digitizing and processing 40 high-resolution digital photographs. Each photograph imaged an area of roughly 4.6 m × 6.9 m. One pixel in the binary image = 1.98 mm on the ground. The fractures were manually drawn on the basis of the photographs. The N, M and S areas (Fig. 3.1) were divided into 10, 9 and 8 sub-sections, respectively. A total of 27 sub-sections (called N1, M2, S5 etc.) were produced. M2 and S5: locations of two sub-sections.

The possible inhomogeneity of the fracture pattern of section-1 was investigated by map counting (Peternell et al., 2010), where box counting is applied to a rectangular window that passes over the image and generates fractal box-counting dimensions for each window. These values are plotted as colour pixels in the centre of the windows. When counting is completed, a colour-coded map is produced on the basis of the distribution of all pixels. In this study, a window of 100 cm × 100 cm was used with a gliding distance of 25 cm in each step (i.e. with 75% overlap).

The possible anisotropy of the fracture pattern and its spatial variation were explored by the modified Cantor dust method (MCDM) (Velde et al., 1990; Volland and Kruhl, 2004) and by mapping of rock fabric anisotropy (MORFA) (Peternell et al., 2011). MCDM was performed with the AMOCADO software (Gerik and Kruhl, 2009), an automated procedure that measures the 1D complexity of a pattern in different directions (i.e. the anisotropy of pattern complexity). MORFA combines MCDM with a gliding-window procedure and thus quantifies the inhomogeneity of the anisotropy of the pattern complexity. Details of the method can be found in Peternell et al. (2011).

In boulders and core samples, fracture patterns analysed by box counting and FSD were determined and presented as cumulative frequencies on log-log plots. The slopes of the linear point arrangements are taken as fractal dimensions of the FSD. The computer program Crack Image Analysis System (CIAS) (Liu et al., 2013) was used to calculate the geometric parameters and statistical analysis of the fragments in the binary image of boulders and core samples. The lower limit of the CIAS resolution is about five pixels, which includes about 98.5% of the total number of fragments.

3.3 Results

3.3.1 Large-scale fracture patterns

The larger fractures exposed in the Eireiner Quarry are dominantly ESE–WNW and NNE–SSW fractures, i.e. fractures oriented radially and tangentially to the centre of the Ries crater. These two orientations also determine the partly rectangular plan of the quarry (Fig. 3.1). Based on the outcrop conditions, the fractures could be recorded in sufficient numbers and with sufficient quality only on a roughly N–S oriented quarry face (section-1); therefore, the analysed fractures are generally radial to the crater centre. They are typically visible over distances of centimetre to decimetres. The few fractures of more than 1 m in length usually extend beyond the section-1 boundary. The fracture patterns were analysed by four fractal-geometry methods in order to identify pattern fractality and its inhomogeneity as well as inhomogeneity of anisotropy.

3.3.1.1 Fractality of fracture pattern

Application of the box-counting method resulted in two linear groups of data point whose regression lines clearly have different slopes (Fig. 3.3). For all 27 sub-sections, the switch from one regression line to the other occurs between the 10 and 20 cm box sizes. The slopes of the two regression lines, i.e. the fractal dimensions D_1 and D_2, of all sub-sections are 1.03–1.15 and 1.40–1.85, respectively. Along the section, D_2 varies strongly and systematically (Fig. 3.4). The same is true for D_1 (shown in Fig. App. 3.2).

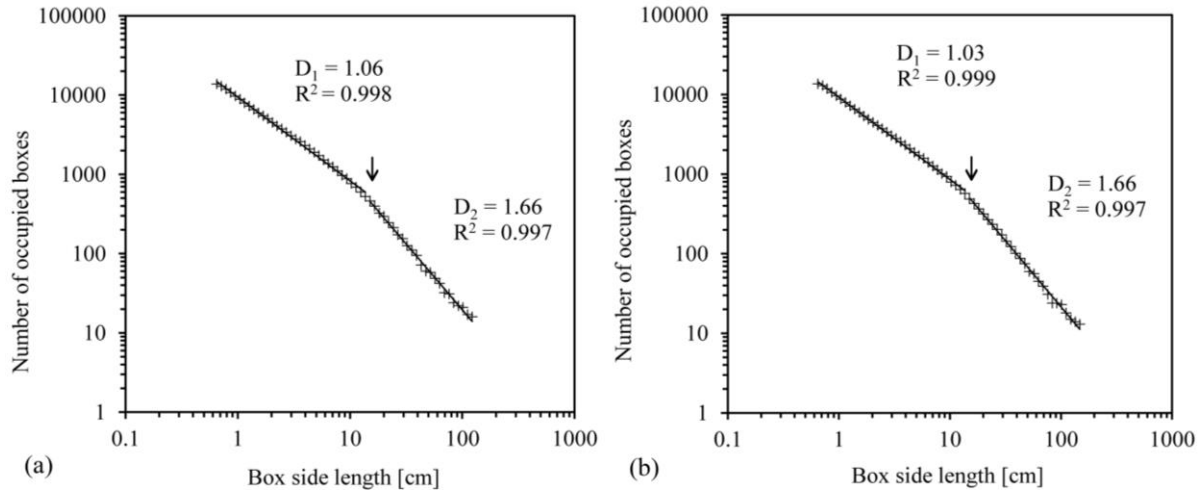

Figure 3.3: Box counting applied to sub-sections M2 (a) and S5 (b); locations shown in Fig. 3.2. For each sub-section, the cumulative frequency distribution shows two linear groups of points representing two fractal dimensions, D_1 and D_2. Arrows indicate the switch from one group to the other. R^2: correlation coefficient.

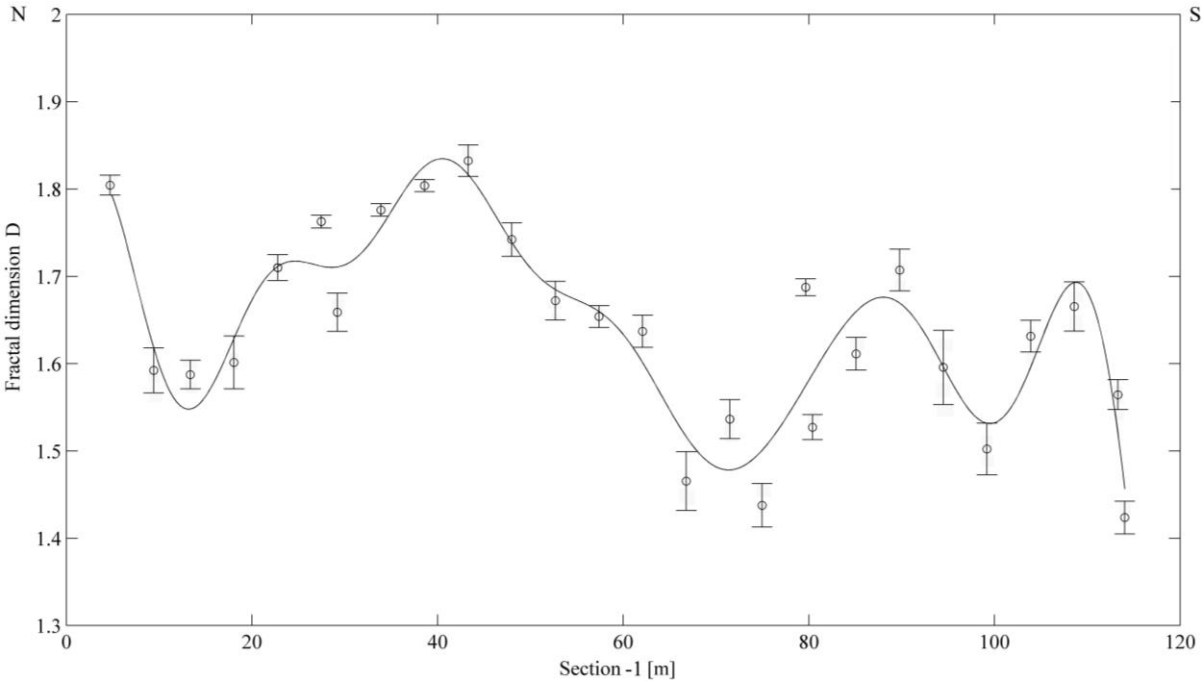

Figure 3.4: Variation of fractal box-counting dimension D along section-1 (summation of 27 sub-sections). The fractal dimension D_2 of each sub-section (Fig. 3.3) and its mean value is calculated by four initial and final box sizes. Error bar: 95% confidence interval of the mean value. Solid curve: 7th order Fourier fit.

3.3.1.2 Inhomogeneity of fracture-pattern fractality

The binary fracture pattern, based on digital outcrop photographs of section-1, already reveals complexity and variation (Fig. 3.2). Map counting applied to this pattern produced a colour-coded map of box-counting dimensions D (Fig. 3.5). On the map, the D-values of 1.10–1.87 represents the variation in fracture pattern complexity over the analysed area, i.e. pattern inhomogeneity. The D-values do not differ randomly but exhibit some regularity with several vertical to sub-vertical elongate areas of high values of 1.7–1.87. The high-D areas are surrounded by more diffuse regions with low D-values of 1.15–1.55.

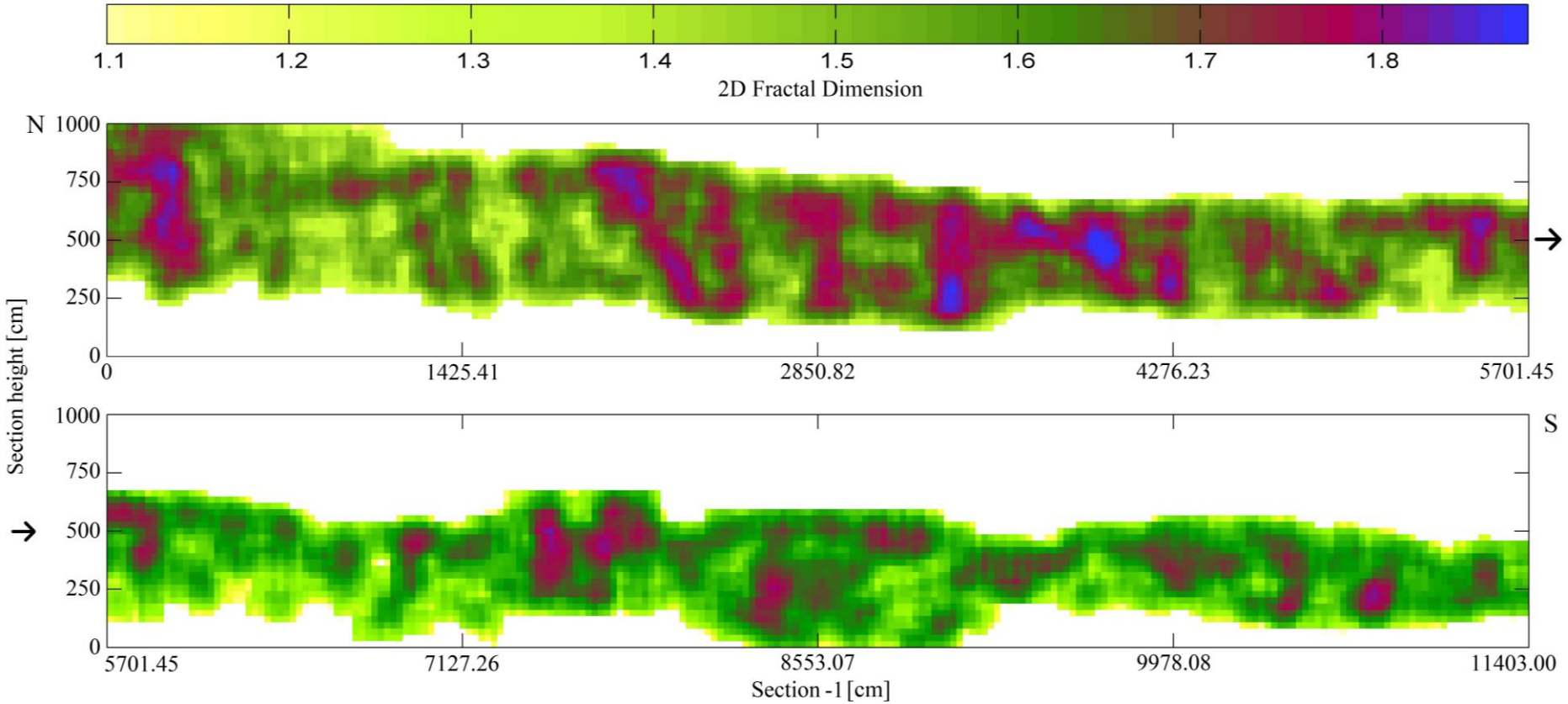

Figure 3.5: High-resolution map-counting method (Peternell et al., 2010) applied to the fracture pattern of section-1. See text for description of the method. Rectangular measurement window: 100 cm × 100 cm with 75% overlap. The box-counting dimension is scaled by colour index. Each pixel is equivalent to an area of 25 cm × 25 cm. The colour index represents the intensity of inhomogeneity of the fracture pattern complexity, with 1.1 = low complexity (light yellow) and 1.87 = high complexity (blue).

3.3.1.3 Inhomogeneity of anisotropy of pattern complexity

Application of the MORFA method to the binary fracture pattern of section-1 resulted in a colour-coded map of anisotropy intensity (Fig. 3.6). The values 0.2–0.8 represents the variation in fracture pattern complexity in different directions over the analysed area. High values of around 0.45–0.75 are dominant, while low values of 0.25–0.10 are observed only in diffuse areas. MORFA also performs an elliptical fit of the data points, whose short axis represents statistically the direction of lowest *D*-value or the short axis of anisotropy. This short axis is relatively constant and vertical to sub-vertical over the entire pattern, mostly in combination with relatively high anisotropy intensity (>0.45).

3.3.2 Small-scale fracture patterns and fragments

FSD and fracture patterns were also determined and quantified in boulders and core samples.

3.3.2.1 Boulders

Application of the box-counting method on fracture patterns of granitoid and limestone boulders (Figs. 3.7a and 3.8a) revealed that the fracture patterns are fractal in the range 0.9–20 mm (Figs. 3.7b and 3.8b). The slopes of the regression lines, i.e. the fractal dimensions *D*, of 1.70 and 1.75 are in the range given for granite and carbonate rocks from fault zones (Keulen et al., 2007).

FSD of the two boulders shows a power-law distribution in 20–100 mm^2 (Figs. 3.7c and 3.8c). Because the number of larger fragments is not statistically significant, these data points were excluded from the analysis. The smaller fragments were also excluded as the number of fragments is biased by low observability (because many fragments were too small to count). The slopes of the regression lines are 1.40 and 1.11 for the granitoid and limestone boulder, respectively, and those fractal dimensions are far below the range of values given in the literature (Blenkinsop, 1991).

3.3.2.2 Core sample

Box counting applied to the fracture patterns of the six hand-specimen-scale core samples (Fig. 3.9a) shows two linear groups of data points with fractal dimensions D_1 and D_2 in the range 1.36–1.44 and 1.63–1.85, respectively (Fig. 3.9b). For all six analysed core samples, the switch from one interval to the other is between 1 and 2.5 mm. FSD of all core samples also show two linear groups of data points with slopes 0.67–0.97 and 1.20–2.98, respectively (Fig. 3.9c). For all core samples, the switch from one regression line to the other occurs between 45 and 65 mm^2 fragment area.

Application of box counting to the fracture pattern of the thin sections from the core samples (Fig. 3.10a) results in two linear groups of data points with fractal dimensions D_1 and D_2 1.29–1.35 and 1.80–1.88, respectively (Fig. 3.10b). For all thin sections, the switch from one interval to the other is between 0.4 and 0.5 mm. FSD of the core thin section also leads to two groups of points with clearly different regression line slopes (fractal dimensions D_1 and D_2) of 0.63–0.68 and 2.08–2.15 (Fig. 3.10c). For all core thin sections the switch from one regression line to the other occurs between 2.5 and 3.5 mm^2 fragment area.

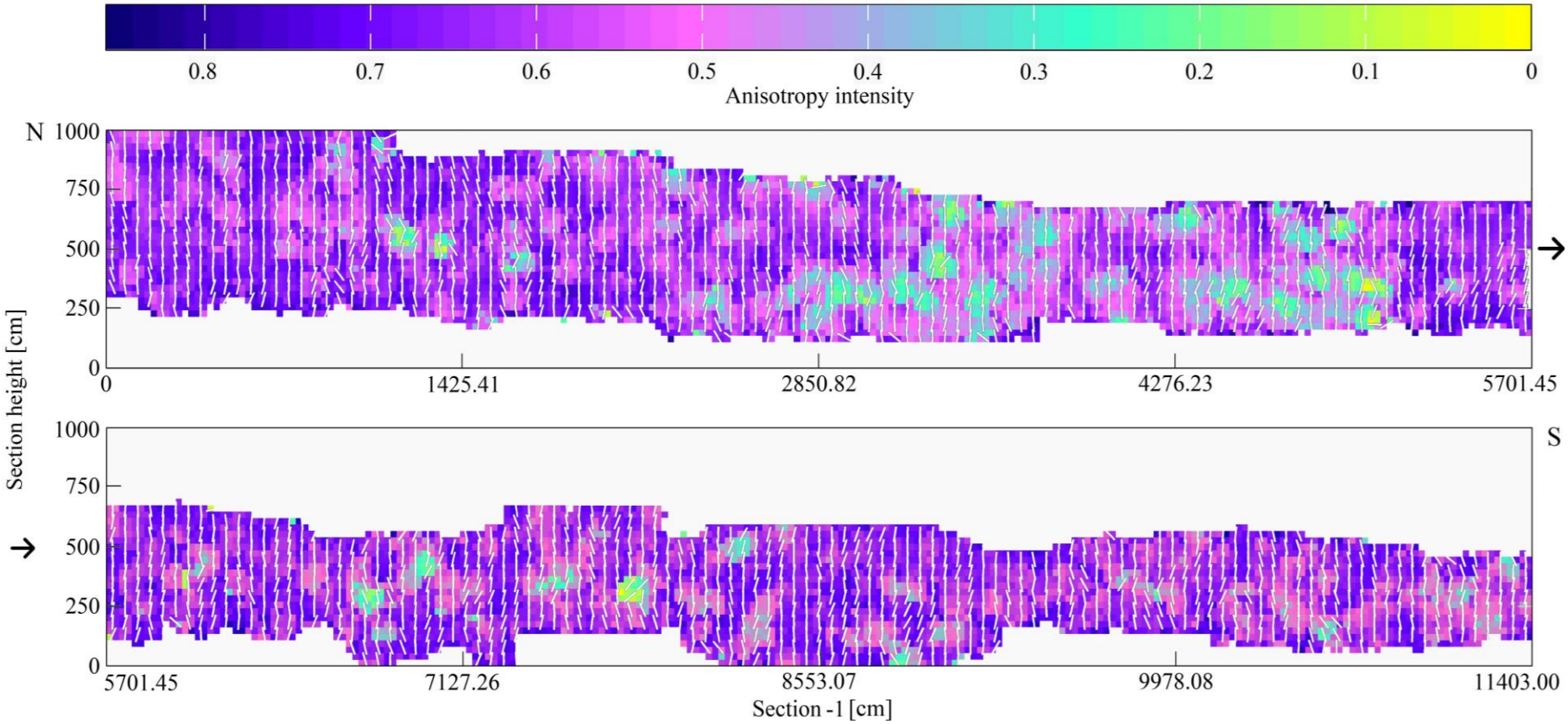

Figure 3.6: High-resolution mapping of rock fabric anisotropy (MORFA) method (Peternell et al., 2011) applied to the fracture pattern of section-1. Circular measurement window for MORFA: 100 cm diameter with 75% overlap. The colour index represents the anisotropy intensity of pattern complexity, with 0 = isotropic (yellow) and 0.75 = high anisotropy (blue). Each colour pixel represents 25 cm × 25 cm. The short white bars represent the short axis of the fit ellipse, i.e. the general direction of the minimum pattern complexity.

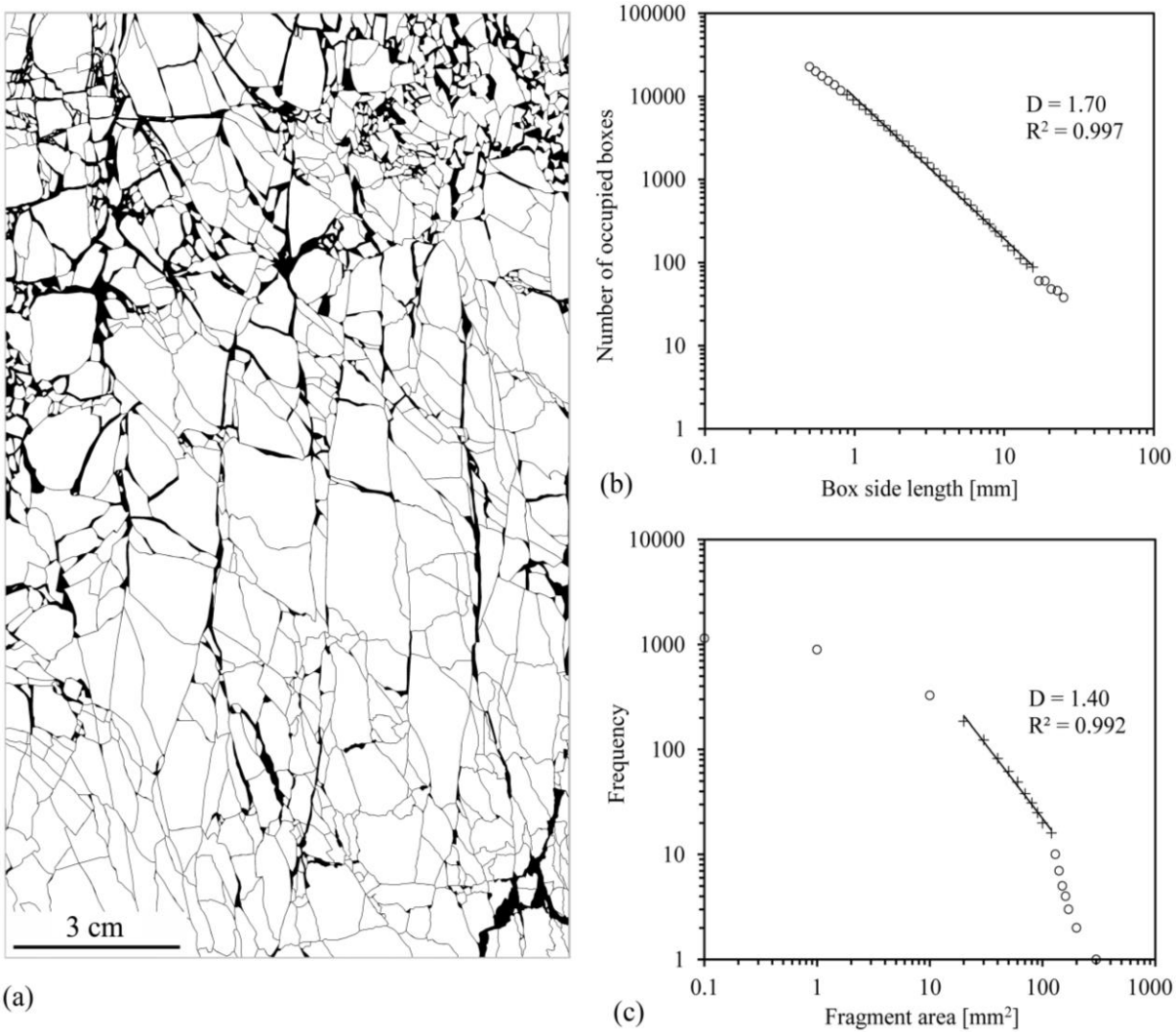

Figure 3.7: Analysis of fracture pattern from a granitic basement rock boulder collected in the Unterwilfingen quarry (Fig. 3.1). (a) Binary image of fractures (black lines) and regions of sub-microscopically fragmented material (small black areas). One pixel = 0.065 mm on the rock surface. (b) Box counting applied to the fracture pattern shown in (a). A power-law relationship (solid line) over more than one order of magnitude with a fractal dimension of 1.70 is indicated. Open circles: measurements excluded from analysis. R^2: correlation coefficient. (c) Cumulative size frequency distribution of fragment areas from (a). The areas are calculated by counting the number of pixels inside the fragments (Liu et al., 2011). A power-law relationship (solid line) over less than one order of magnitude with a fractal dimension of 1.40 is indicated. Measurements with low statistics (large fragments) or with truncation effects (Blenkinsop, 1991) because of small size and low observability (open circles) were excluded from the analysis. R^2: correlation coefficient.

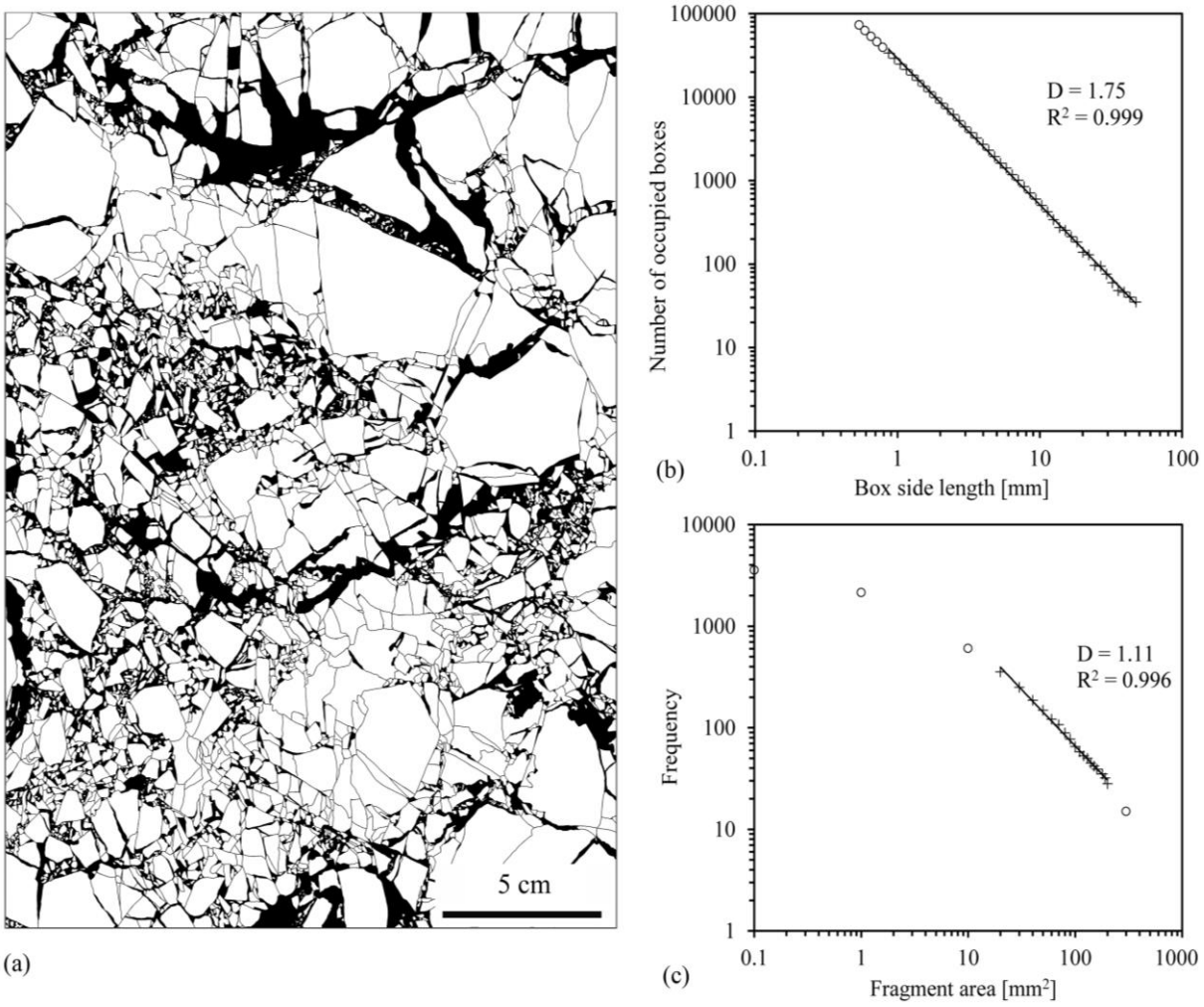

Figure 3.8: Analysis of fracture pattern from a limestone boulder collected from the Unterwilfingen quarry (location in Fig. 3.1). (a) Binary image of fractures (black lines) and regions of sub-microscopically fragmented material (small black areas). One pixel = 0.065 mm on the rock surface. (b) Box counting applied to the fracture pattern shown in (a). A power-law relationship (solid line) over more than one order of magnitude with a fractal dimension of 1.75 is indicated. Measurements with low statistics (large boxes) or with truncation effects (Blenkinsop, 1991) because of small size and low observability (open circles) were excluded from the analysis. R^2: correlation coefficient. (c) Cumulative size frequency distribution of fragment areas from (a). Area is calculated by counting the number of pixels inside the fragments (Liu et al., 2011). A power-law relationship (solid line) over less than one order of magnitude and a fractal dimension of 1.11 is indicated. Measurements with low statistics (large fragments) or with truncation effects (Blenkinsop, 1991) because of small size and low observability (open circles) were excluded from the analysis. R^2: correlation coefficient.

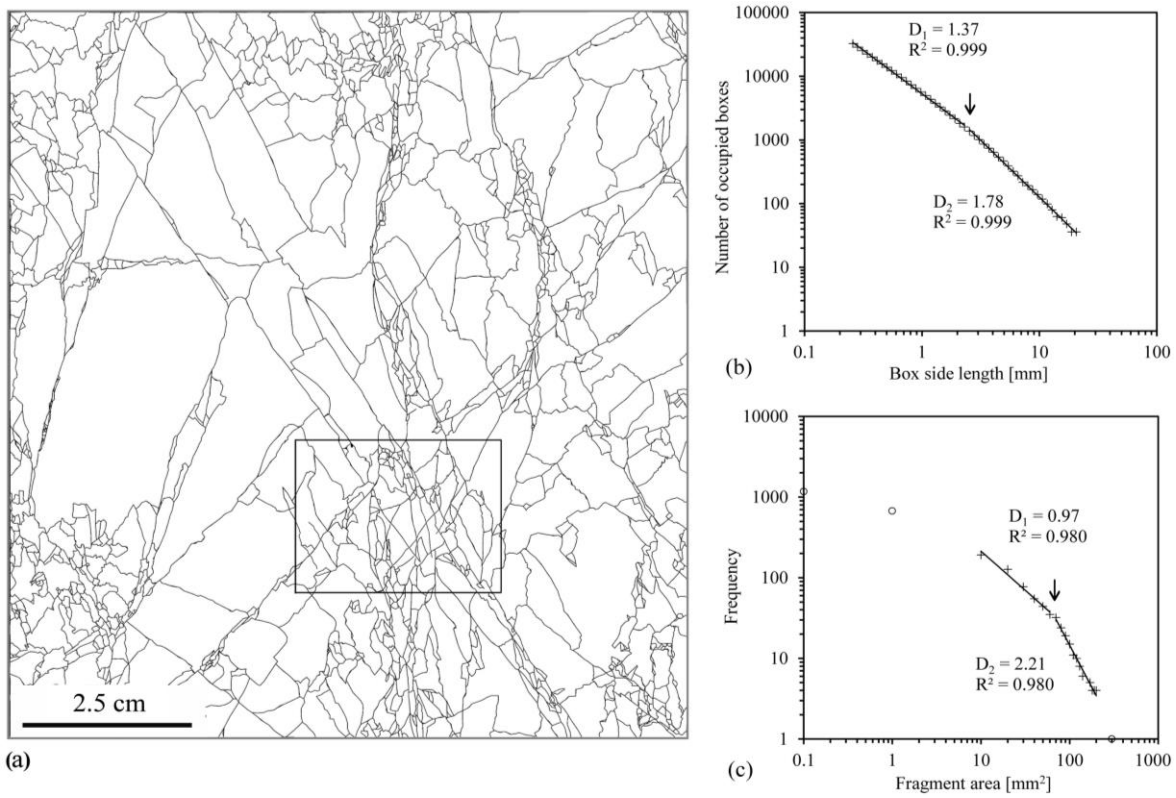

Figure 3.9: Analysis of the hand-sample-scale fracture patterns from the drill core of the Ries Research Borehole (RRB)-1973 (Centre for Ries Crater Impact Research, ZERIN); location shown in Fig. 3.1. (a) Binary image of fractures (black lines) from a vertical cut of a granitoid rock sample from a depth of 510.5 m. This image is an example of the six images analysed for this study (Fig. App. 3.3). The rectangle outlines the area shown in thin section (Fig. 3.10a). One pixel = 0.025 mm on the rock surface. (b) Box counting applied to the fracture pattern shown in (a). The arrangement of measurement points shows two power-law relationships (solid lines) with fractal dimensions D_1 and D_2. The arrow indicates the switch from one linear point arrangement to the other. R^2: correlation coefficient. (c) Cumulative size frequency distribution of fragment areas from (a). The areas are calculated by counting the number of pixels inside the fragments (Liu et al., 2011). Two power-law relationships (solid lines) over less than one order of magnitude and fractal dimensions D_1 and D_2 are indicated. Because the number of larger fragments is not statistically significant and small fragments have low observability, those data points (open circles) were excluded from the analysis. The arrow indicates the switch from one linear point arrangement to the other. R^2: correlation coefficient.

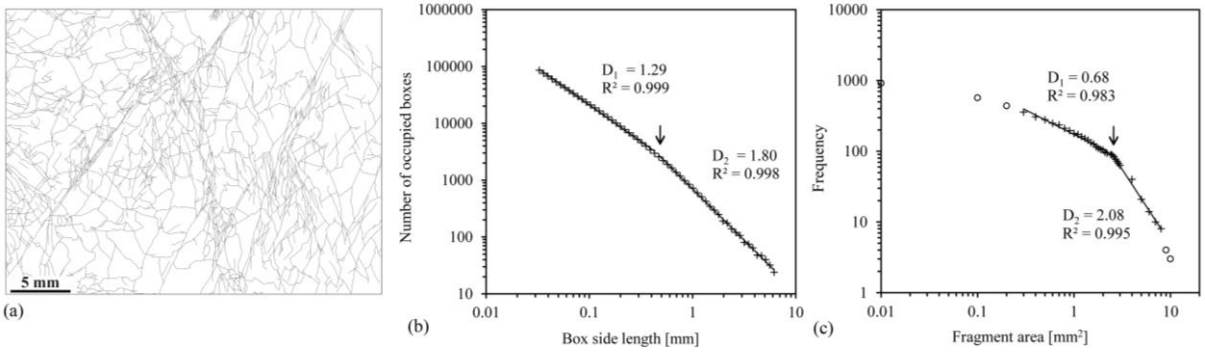

Figure 3.10: Analysis of thin-section-scale fracture pattern from drill core of the Ries Research Borehole (RRB)-1973; location shown in Fig. 3.1. (a) Binary image of fractures (black lines) from a thin section of a granitoid rock from a depth of 510.5 m. This image is an example of the three images analysed for this study. The area from which the thin-section was taken is shown in Fig. 3.9a. One pixel = 0.006 mm in the thin section. (b) Box counting applied to the fracture pattern shown in (a). The arrangement of measurement points show two power-

law relationships (solid lines) with fractal dimensions D_1 and D_2. The arrow indicates the switch from one linear point arrangement to the other. R^2: correlation coefficient. (c) Cumulative size frequency distribution of fragment areas from (a). The areas are calculated by counting the number of pixels inside the fragments (Liu et al., 2011). Two power-law relationships (solid lines) over less than one order of magnitude and fractal dimensions D_1 and D_2 are indicated. Because the number of larger fragments is not statistically significant and small fragments show low observability, those data points (open circles) were excluded from the analysis. The arrow indicates the switch from one linear point arrangement to the other. R^2: correlation coefficient.

3.4 Discussion

Outcrop images in and around the Ries crater clarify that the country rocks are intensively fractured far beyond the range and style typical for regional brittle deformation (Suppe, 1985; Ramsay and Huber, 1987). In particular, brittle structures are locally highly varied and form complex patterns. In order to characterize this type of deformation and understand its correlation with scale, pattern quantification is necessary. For this purpose, fractal geometry methods are useful, which can quantify the inhomogeneity and anisotropy of patterns as well as the combination of both (Velde et al., 1991; Volland and Kruhl, 2004; Peternell et al., 2010, 2011). This study applies fractal methods that are designed for automated analysis and thus can record patterns over large areas with high precision (Gerik and Kruhl, 2009; Peternell et al., 2010, 2011). In general, fragmentation largely follows power laws but to different extents on different scales and at different locations. In addition, fragmentation patterns may be inhomogeneous and anisotropic.

Box counting applied to approximately 114 m long, N–S oriented vertical section of Malm limestone, exposed about 13 km ESE of the crater centre (Eireiner quarry, Fig. 3.1), indicates fractality of the 2D fragmentation pattern in all parts of the section (Fig. 3.3), but with different fractal dimensions D_1 and D_2 on two different scales. The ranges of D_1 and D_2 values of 1.03–1.15 and 1.40–1.85 in the 27 sub-sections analysed are clearly differentiable (Fig. 3.4). Two different power-law relationships are usually interpreted as resulting from two different or two combined pattern-forming processes (Kaye, 1989; Kruhl, 2013). We also consider our D_1 and D_2 values to have been produced by two processes.

We interpret one process to be the result of the contact and compression stage at the first phase of impact cratering. During this stage of cratering, strain rates are very high and small and closely spaced fractures develop (Kenkmann et al., 2014). Small, vertical to sub-vertical networks of parallel fractures, mainly restricted to single sedimentary beds (Fig. 3.2), are closely related to the contact and compression stage of deformation. We interpret the second process to be the result of the excavation stage during the intermediate phase of impact cratering. In this stage, individual fractures merge to form more complex fracture networks that lead to the second range of *D*-values.

The two different ranges of *D*-values can be interpreted as follows. The release wave related to the excavation stage fragments the rocks around the impact, which were earlier subjected to the shock wave. Consequently, the excavation stage increases the density of the fracture pattern within the early stage shock-wave-related centimetre-scale fragmented limestone. Preferentially in the more intensively fragmented regions, existing shock-related fractures were possibly partly reactivated, leading to a relatively smaller number of new fractures compared with less densely fractured regions. Thus, the fracture pattern is intensified at larger scales than at smaller scales, with increased *D*-values at the larger scale and decreased *D*-values at the smaller scale. The switch from one power-law relationship to the other at 10–20 cm (Fig. 3.3), which is the same for all of our sub-sections, represents the scale on which the impact-related fragmentations have transformed from early stage contact and compression to intermediate stage excavation. However, the third and final phase of impact cratering (crater modification) is not reflected in our box-counting analysis of the sub-sections.

This is possibly due to scaling limitation. In the final stage of impact cratering, faults and fractures of hundreds of metres or even kilometres in length are formed (Spray, 1997), and therefore they are not visible on the scale of this study.

The 7th order Fourier fit with residual fractal dimensions ≤0.10 (Fig. 3.4) for the box-counting D_2 indicates a systematic variation of pattern fractality along the N–S section. The set of different D_2 fractal dimensions that occur at the scale larger than 20–30 cm is possibly related to the high deformation strain and inherent flaws in the rock. Inherent flaws are important as sites of weakness for the nucleation and coalescence of fractures (Griffith, 1920). These sites result in localization of deformation along specific fracture systems (Faulkner et al., 2003; Wilson et al., 2003). Moreover, beyond a certain threshold limit of strain rate ($\sim 10^1$–10^3 s^{-1}) material inertia begins to affect the nucleation and propagation of the fractures (Kipp et al., 1980). Transition from narrow-spaced fracture networks to more localized large-scale fractures indicates the degree of strain localization shifting from a relatively homogeneous to a strongly heterogeneous distribution (Kenkmann et al., 2014).

More detailed quantification of the pattern variation with high-precession Map Counting (Peternell et al., 2010) revealed multiple vertical to sub-vertical elongate areas, dominated by high box-counting dimensions. The values of 1.7–1.85 correspond to more intensely fractured areas (Fig. 3.5). These elongated areas are regularly spaced at intervals of 2.5–3.5 m. They are also observed in other parts of the Eireiner quarry. Similar *D*-values are reported from fault zones and larger-scale tectonic regions (Hirata, 1989; Bour and Davy, 1997; Volland and Kruhl, 2004). Even though the fractality of 2D patterns increases with increasing filling of the plane (Mandelbrot, 1982), increasing fractality is also related to the geometric arrangement of the fracture pattern (Peternell et al., 2011). Hence, it can be argued that the high *D*-value of the presented fracture pattern indicates higher complexity as well as a higher degree of fragmentation. The overlay of the Map-counting *D*-value contours on the fracture map revealed the correlation between fracture density and fractal dimension values (Fig. App. 3.4).

The regular variation in the fracture pattern complexity in section-1 seems to be typical for impact-related fragmentation. Moreover, based on fracture lengths, spacing, and location and depth of section-1, it can be assumed that these fractures are related to the transition zones between Grady-Kipp (below) and spall fragmentations (above) (Melosh, 1984, 1989).

Application of MORFA (Peternell et al., 2011) to the fracture pattern in section-1 leads to generally similar but locally different results (Fig. 3.6). The directions of minimum pattern complexity are parallel to the vertical to sub-vertical fracture orientation in some parts of the section, whereas in other parts they differ. Mostly these differing orientations are not related to regions of low anisotropy, and therefore, are not an artefact of the method. They occur in numerous areas of up to 50 cm wide and 150 cm high, each of which shows a dominant direction of minimum pattern complexity with 15–20° angle to the vertical either to the north or to the south (Fig. 3.6). This indicates a strong and regularly oriented anisotropy of the pattern fractality, which is in agreement with the generally steep orientation of the single fractures. Because these directions roughly correlate with the main fracture orientation, a systematic change of fracture orientation is indicated. This might be correlated with shatter-cone style fractures on the decimetre to metre scale. Shatter cones of such size have been reported in the literature (Osinski and Pierazzo, 2013). In addition, these results show that MORFA is able to detect and quantify diffuse patterns of rock structures, patterns not measurable with conventional methods.

For each sample, fracture patterns and FSD of the boulders lead to a power-law relationship over one order of magnitude scale (Figs. 3.7 and 3.8) and, therefore, indicate one single fragmentation process. This process is represented by material excavation through non-ballistic ejection during the impact (Chao and Minkin, 1977; Chao et al., 1978). The boulders we studied are assumed to be parts of larger highly fragmented blocks, which are transported over a short distance towards the crater

centre. This conclusion is supported by their location inside the crater (Fig. 3.1). Because these blocks were only subjected to the shock-related fragmentation during non-ballistic ejection, only one single process is imprinted on the boulders, thus resulting in only one power-law relationship.

Analysis of the core samples leads to two distinct box-counting D-values (D_1 and D_2) of the fracture patterns and two values of FSD (Figs. 3.9 and 3.10). The switch from D_2 to D_1 occurs at different scales for box counting and for FSD. As for the fracture pattern in the Malm limestone at the Eireiner quarry, the two different *D*-values are interpreted as resulting from two subsequent pattern-forming processes during the Ries impact. The first one is related to shock-wave fragmentation and the second to elastic rebound of the transient crater floor from a depth of 4.5–5 km to its current level of 500–600 m depth (Gudden, 1974; Wünnemann et al., 2005). In this stage, shear fracturing leads to additional diminution of the shock-wave fragments. Their re-fragmentation leads to a relatively higher number of small fragments (Keulen et al., 2007) and, consequently, to two different *D*-values.

The box-counting D_1- and D_2-values of six analysed core samples are 1.36–1.44 and 1.63–1.85 (Fig. 3.9b) and those of the three analysed thin sections from the core samples are 1.29–1.35 and 1.80–1.88, respectively (Fig. 3.10b). These values are similar to the values of the fragmented Malm limestone of Section-1 and of fragmentation elsewhere (Hirata, 1989; Castaing et al., 1996; Cello, 1997; Ayunova et al., 2007; Park et al., 2010). In addition, the D_1- and D_2-values are similar or show slight overlap. However, the values on the same scale in thin section and sample are different. Even though this is possibly related to the different resolutions of both patterns, the variation in *D*-values on different scales suggest scale-dependence of the fragmentation processes (Kruhl, 2013).

The FSD of core samples also show two different fractal dimensions of 0.67–0.97 and 1.20–2.98, respectively (Fig. 3.9c). Specifically the higher values fall into the wide range of values given for rock fragmentation (Blenkinsop, 1991; An and Sammis, 1994; Storti et al., 2003; Chester et al., 2005). Impact experiments show an increase of *D*-values with increasing impact energy (Lange et al., 1984), and cratering and shock-recovery experiments suggest a correlation with strain rate (Buhl et al., 2013). Studies on natural impacts provide *D*-values within 1.2–1.8 (Rousell et al., 2003; Key and Schultz, 2011). High values are reported to be related to increasing strain or strain localization (Monzawa and Otsuki, 2003; Billi and Storti, 2004; Dyer et al., 2012). The wide range of fractal dimensions in the literature as well as in our investigations argues against shock-induced fragmentation being the only or dominant process during impact and suggests that different parameters, such as rock type and pre-existing rock structures, and their interaction have to be considered. In addition, the influence of the latter two stages of impact cratering (the excavation and modification stages) versus other parameters is expected to vary with time and distance from the point of impact and may produce a wide range of *D*-values.

In the core samples the D_2-values of the fracture patterns do not change with depth (Fig. 3.11a). The D_2-values of FSD, however, decrease from a depth of 510.5 m to 773.3 m but are higher at a depth of 1169.5 m (Fig. 3.11b). The decrease in *D* with increasing depth below the crater floor has also been observed in impact experiments and is related to a zone of 'pervasive crushing and compaction' (Buhl et al., 2013). The same authors observed a zone of localized deformation, at a farther distance from the impact, with increased *D*-values. They related this increase to enhanced comminution due to stress localization, which leads to reduced fragment sizes. In our data, the high *D*-value at greater depth can possibly be ascribed to the same effect- localized deformation. The zones of increased fragmentation, observed in limestone outcrops at the surface (Fig. 3.2), might correspond to zones of localized deformation. However, *D*-values from FSD are sensitive to truncation effects (Kruhl, 2013) and should be interpreted carefully. FSD provides information about different fragmentation processes (Keulen et al., 2007; Kruhl, 2013), but not about the fragmentation pattern.

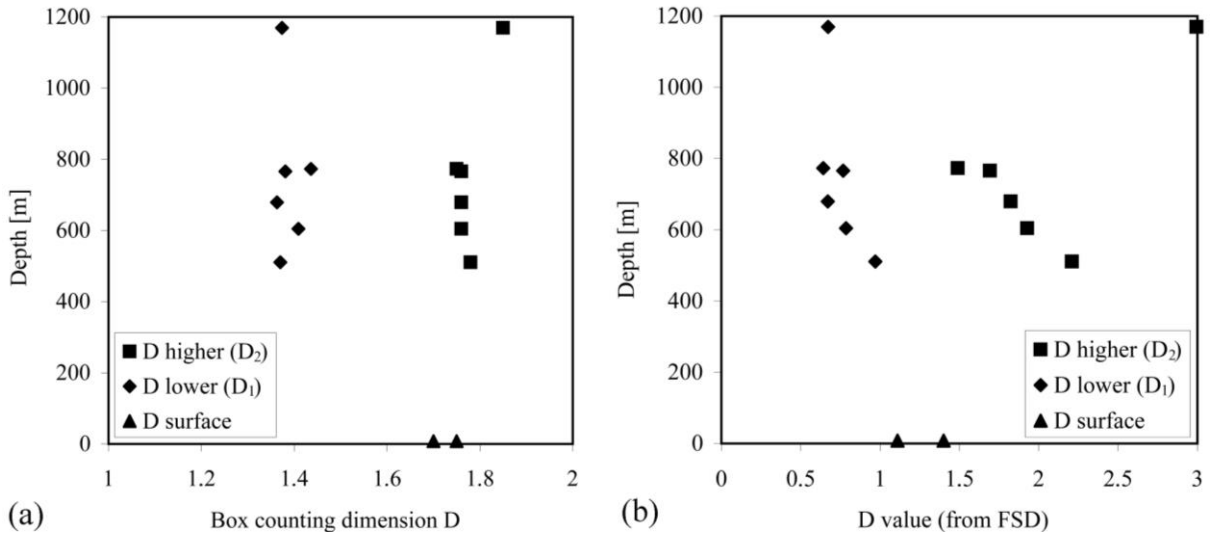

Figure 3.11: Variation of fracture pattern and fragment size distribution for boulders and core samples from the surface to a depth of 1169.5 m. (a) Depth vs. *D*-value obtained from box-counting analysis of fracture patterns (Figs. 3.7b, 3.8b and 3.9b). (b) Depth vs. *D*-value obtained from fragment size distributions (Figs. 3.7c, 3.8c and 3.9c).

Summarizing, fractal-geometry-based quantification of fragmentation structures in and around the Ries impact crater reveals (i) the general complexity, i.e. fractality, of these structures, (ii) the variation in complexity on different scales and in relation to distance from the impact centre, (iii) partly the effect of three different fragmentation processes, and (iv) the inhomogeneity of the fragmentation pattern over larger areas. A systematic variation in fracture orientation is indicated by the short axis of the anisotropy of the pattern, which might be correlated with shatter-cone style fractures on the decimetre- to metre-scale. The absence of a narrow range of fractal dimensions for FSD of the Ries core samples argues against shock-induced fragmentation being the only or dominant process during impact. The high *D*-value for FSD at greater depth can possibly be related to enhanced comminution due to stress localization and might correspond to the zones of localized deformation. Fractal geometry, specifically when based on automated procedures, proves a powerful tool for quantifying and thus analysing complex rock structures.

Acknowledgements

We are grateful to the colleagues from the Centre for Ries Crater Impact Research (ZERIN) in Nördlingen for providing core samples, to Mark Peternell for giving access to the map-counting and MORFA program system and to Christian Stäb, Tim Yilmaz, Thomas Kenkmann, Alison Ord, and Tom Blenkinsop for helpful discussions. Reviews by Mark Peternell and an anonymous reviewer greatly improved the manuscript. We also express our gratitude to Namvar Jahanmehr and Klaus Mayer for sample and thin-section preparation. Md.S.H. gratefully acknowledges financial support by the German Academic Exchange Service DAAD (grant A/11/75209).

CHAPTER FOUR

4. Characteristics and spatial distribution of fragmentation structures around an impact crater

Submitted to Earth and Planetary Science Letters (EPSL): Hossain, M.S., and Kruhl, J.H., 2015. Characteristics and spatial distribution of fragmentation structures around an impact crater.

Abstract

Impact craters display a large variety of fragmentation structures in the upper parts of the Earth's crust. Some questions regarding the characteristics and spatial distribution of these fragmentation structures in the target rock are as yet to unanswered. In this study, impact-induced brittle deformation structures within the Malm limestone and lower basement rock in and around the Ries crater, located in Germany, were recorded, measured and quantified. Quantification was performed mainly using methods based on structural geology, classical spatial statistics and fractal geometry. A variety of deformation structures were observed, including (i) prominent fractures, (ii) zones of intense fragmentation, (iii) fracture branching and (iv) near-surface target-rock delamination. The characteristics of the prominent fractures as well as their impact-related orientations show systematic changes with distance from the impact centre. Beyond a certain distance, their characteristics are not easily recognizable and their orientations are mainly controlled by the pre-existing regional tectonic structure. Decimetre- to metre-wide zones of intense fragmentation are present as systematic repetitions in the horizontal direction and in the vertical Ries Research Borehole. The repetition interval is ~3–4 m horizontally and ~34 m vertically. The fracture branching structures on the centimetre- to decimetre-scale are symmetrical as well as strongly anisotropic with the preferred fracture orientation roughly parallel to the symmetry plane. The structures show unimodal distribution of branching angles and unequivocally indicate the direction of fracture opening away from the impact centre. The near-surface delamination is evident from the variety of brittle-plastic structures in the upper layers of the target rocks. Displacements within the delamination zone range from decimetres to decametres and decrease with increasing depth and distance from the crater centre. The thickness of this zone exponentially decreases as the distance from the impact centre increases. The distance-related presence of fragmentation structures and changes in their characteristics most likely result from the interaction of rapidly varying impact-induced shock and rarefaction waves that spread horizontally and vertically from the point of impact. In general, the fragmentation structures developed during this type of dynamic deformation are different from those generated during quasi-static regional tectonic deformation.

Key words: fracture frequency; fracture branching; target delamination; pattern quantification

4.1 Introduction

Formation of an impact crater is an extremely complicated and dynamic process, beginning with micro-seconds of shock loading and terminating with gravity-driven collapse during a period of a few minutes (Melosh, 1989). At the beginning of a kilometre-sized asteroid impact, the pressure increases to several hundred gigapascals, the temperature to several tens of thousands of degrees and the strain rate to more than 10^{+6} s^{-1} (Huffman and Reimold, 1996; Kenkmann et al., 2014). Within a few minutes, a large variety of deformation features are formed under conditions of highly different and rapidly changing stress, temperature and strain rate (Kenkmann et al., 2014). The initial impulse of the

impact is carried to the target rock by stress waves of varying strength and propagation direction. Because the magnitudes of the pressure and strain rates are enormously high and the duration of deformation is extremely short, the characteristics of impact deformation differ from those of tectonic deformation.

Impact-induced micro- to kilometre-scale shattering and fracturing of the target rocks rapidly decrease from the point of impact outwards (von Dalwigk, 2003). During the early stage of cratering, closely spaced fractures develop. These fractures tend to be less than 1 cm long with displacements of less than 1 mm (Kenkmann et al., 2014). This type of fracture is predominant up to the transient crater rim. During the intermediate stage of cratering, fractures coalesce and increase in length. Large-scale fractures/faults usually develop during the final stage of cratering (Spray, 1997). At the crater rim and beyond, large-scale, vertically to sub-vertically oriented fractures with little or no displacement are generally dominant. Inherent flaws, which are sites of weakness, are important for nucleation and coalescence of fractures (Griffith, 1920) resulting in localization of deformation along specific fracture systems (Faulkner et al., 2003; Wilson et al., 2003). Beyond a certain threshold of strain rate (~10^1 to 10^3 s^{-1}), material inertia begins to affect the nucleation and propagation of the fractures (Kipp et al., 1980). The development of narrowly spaced fracture networks on the millimetre- to decimetre-scale to more localized large-scale factures zones on the metre- to ten-metre-scale indicates the shift from homogeneous to heterogeneous strain distribution (Kenkmann et al., 2014). Detailed studies of these large-scale fractures may help to differentiate impact-induced brittle deformation from tectonic brittle deformation and to determine the spatial distribution of brittle deformation around impact craters that have not yet been studied.

The speed of fracture tip propagation influences the development of fracture geometry. The Rayleigh wave speed of the host rock is the theoretical speed limit for tensile fracture propagation, and the fracture propagation at this limit is termed the ‘dynamic fracture’ (Sagy et al., 2001). According to Sagy et al. (2006), fractures that propagate at high speed, reaching about half of the Rayleigh wave velocity, tend to become unstable in brittle materials and bifurcate when velocity excursions occur. In that case, the fracture network is characterized by hierarchical bifurcations, as observed in the surfaces of shatter cones (Sagy et al., 2002, 2004). However, in the case of impact-induced dynamic deformation, the distribution of fracture bifurcations, structural complexity and orientation with the parent fracture have yet to be well described and quantified. Moreover, the horizontal and vertical distribution (i.e. extent) of target delamination (Kenkmann and Ivanov, 2006) of the Ries impact has not been fully studied.

In order to study these aspects of brittle deformation inside and outside the crater, we choose the Ries meteorite impact (Nördlingen, Germany) (Fig. App. 4.1), where numerous quarries around the crater and the Ries Research Borehole allow study of impact-related brittle deformation and structural features in the target sedimentary cover and lower basement rock. The 25-km-diameter crater was formed 14.6 ± 0.1 (0.2) million years ago (Schwarz and Lippolt, 2013) by the oblique impact of a ca. 1.5-km large meteorite (Stöffler et al., 2013) on a target terrain that consisted of 620–750 m thickness of sub-horizontally layered sedimentary rocks of Triassic to Jurassic age resting on a Variscan basement (Stöffler et al., 2001). Outside the inner crater ring, the upper sedimentary layer, consisting of Malm limestone, was subjected to brittle deformation far beyond the range and style of the typical regional brittle deformation (Hossain and Kruhl, 2014a).

The present study focuses on a more intense investigation of these structures, using quantitative analyses of fracture orientation, fracture frequency distribution, complexity of fracture bifurcation pattern and horizontal and vertical distribution of target delamination. In order to understand impact-induced brittle deformation, field work was carried out in 16 different quarries around the Ries impact

crater (Table App. 4.1). During field investigation, (i) vertical and horizontal sections in quarry outcrops were photographed; (ii) prominent fracture orientation data were collected in conjunction with the section orientation and (iii) high-resolution field photographs were taken of a branching fracture structure in the Gundelsheim quarry.

4.2 Impact-induced fragmentation structures

Four different kinds of impact-induced deformation structures were observed during the field investigations: (i) prominent fractures; (ii) zones of intense fragmentation; (iii) fracture branching and (iv) near-surface target-rock delamination. Partly open fractures longer than ~2 m, which are generally orientated perpendicular to bedding and have a characteristic spacing of a few metres, are defined as 'prominent fractures' in this study (Figs. 4.1 and 4.2). In general, these fractures start and terminate at specific bedding planes at a shallow depth of approximately several metres. In horizontal sections, most of the fractures are straight to curvilinear (Fig. 4.1); in vertical sections they are typically straight with vertical to sub-vertical dips (Fig. 4.2). Some of the open fractures are partly filled by calcite. In contrast, the fractures and faults of the regional tectonic system form conjugate systems that are symmetrical to a vertical plane and at a moderate to high angle to bedding and always transect entire quarry faces. The prominent fractures are atypical for regional tectonics and are, therefore, interpreted as impact-generated.

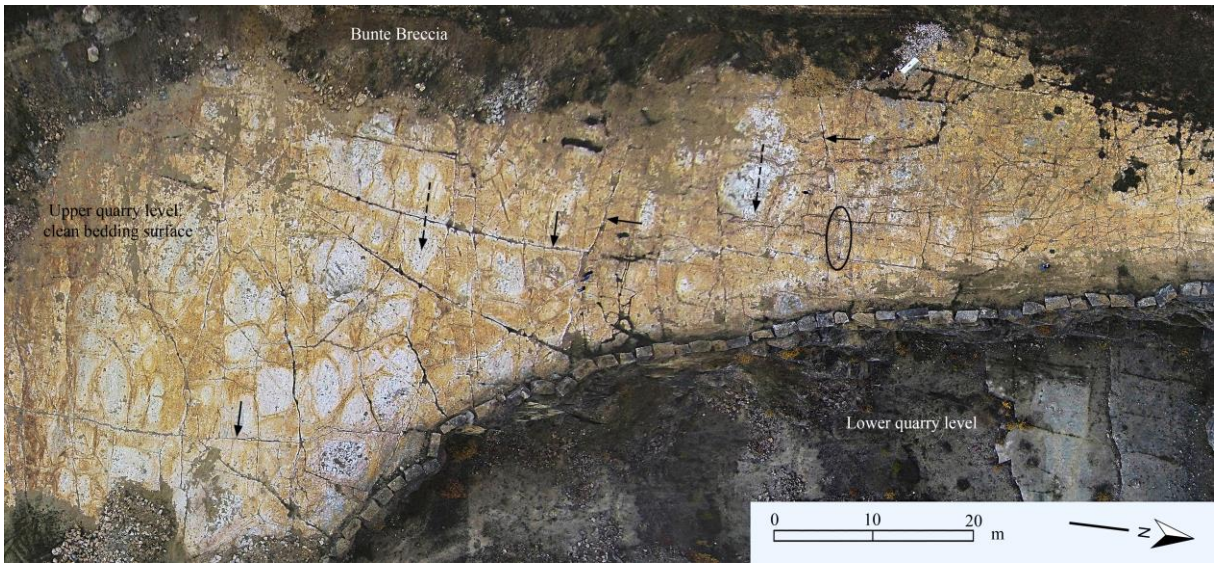

Figure 4.1: Large-scale panorama image of the western part of the Gundelsheim quarry (location in Fig. 4.4) showing overall fracture orientation on a horizontal bedding surface of Malm limestone. Photographs were taken by a drone at an altitude of 150 m from ground level and merged. The effects of peripheral distortion were minimized by using 30% overlap of photographs. For post-processing, Lightroom 5.7 software was used for vertical correction and to remove lens distortion. Photoshop CS4 was applied to merge individual photos to produce the panorama image. Short black arrows: prominent fractures (see text for description); long broken arrows: striation on top of limestone bedding surface caused by the impact-induced outward-directed flow of the Bunte Breccia; ellipse: location of the branching structure illustrated in Fig. 4.8(a).

Zones of intense fragmentation were observed in outcrops relatively close to the impact and in the drill core of the Ries Research Borehole. In quarry outcrops (Fig. 4.3), these zones are not spatially related to drill core blasting, relics of which are locally visible. The zones of intense fragmentation are not typical of the regional tectonics and, therefore, most likely of impact origin. Moreover, locally

some of the open fractures form decimetre-wide fracture branching structures. Single fractures with a clear network of offspring developed along the direction of propagation with a convex, concave or linear geometric shape are termed ‘branching structures’ herein. These fracture branching structures are visible on different scales on vertical faces in the Eireiner quarry, on a horizontal face in the Gundelsheim quarry and in core samples of the Ries Research Borehole. Additionally, decimetre- to decametre-scale near-surface target-rock delamination can be observed in the upper Malm limestone in five different quarries situated at various distances from the impact centre. The near-surface target-rock delamination is characterized by ramp-and-flat geometries of the detachment plane with visible offset and metre- to decametre-scale intense deformation (thrust wedges, thrust and normal faults and various types of folding). All these structures were analysed using methods based on structural geology, classical spatial statistics and fractal geometry.

Figure 4.2: Impact-induced prominent fractures in the Gundelsheim quarry (visible on the bedding plane in Fig. 4.1) subjected to post-impact healing and/or widening. (a) Horizontal view of a vertical open fracture partly filled/healed by precipitated calcite (Cc). Coin (2.5 cm diameter) for scale; long broken arrow: striation, caused by flow of the Bunte Breccia; white arrow points to caps of euhedral calcite crystals. (b) Vertical view of open fractures (black arrows) extending over several metres. The fractures clearly originate and terminate at specific bedding planes and widen towards the bottom. Md. Sakawat Hossain for scale.

Figure 4.3: Approximately N–S oriented vertical section in the Eireiner quarry (location in Fig. 4.4) with centimetre- to 1-decimetre-thick bedding in Malm limestone, slightly inclined to the south. Zones of intense fragmentation (dashed lines) transect the bedding. These zones are typically several metres long and decimetres-wide and composed of shorter, irregular, centimetre-spaced fractures. In general, the zones are perpendicular to the bedding, regardless of bedding inclination. Locally, fractures show cm-wide opening (arrows).

4.2.1 Orientation of prominent fractures and regional tectonic structures

Orientation analysis of the prominent fractures in various quarries around the Ries impact crater reveals two approximately orthogonal sets (Fig. 4.4). On the basis of cluster arrangement of the pole-point density contours, the two fracture-sets are clearly distinguishable in most of the quarries. However, in some quarries (4, 9–13) it is difficult to separate the two fracture-sets due to diffuse clustering of the pole points. To overcome this problem, data points within the areas of the two lowest contours were excluded. The remaining pole points and their contours define two clearly distinguishable fracture-sets. One set can be regarded as radial and the other as tangential with respect to the Ries impact centre (Tables App. 4.2–4.3).

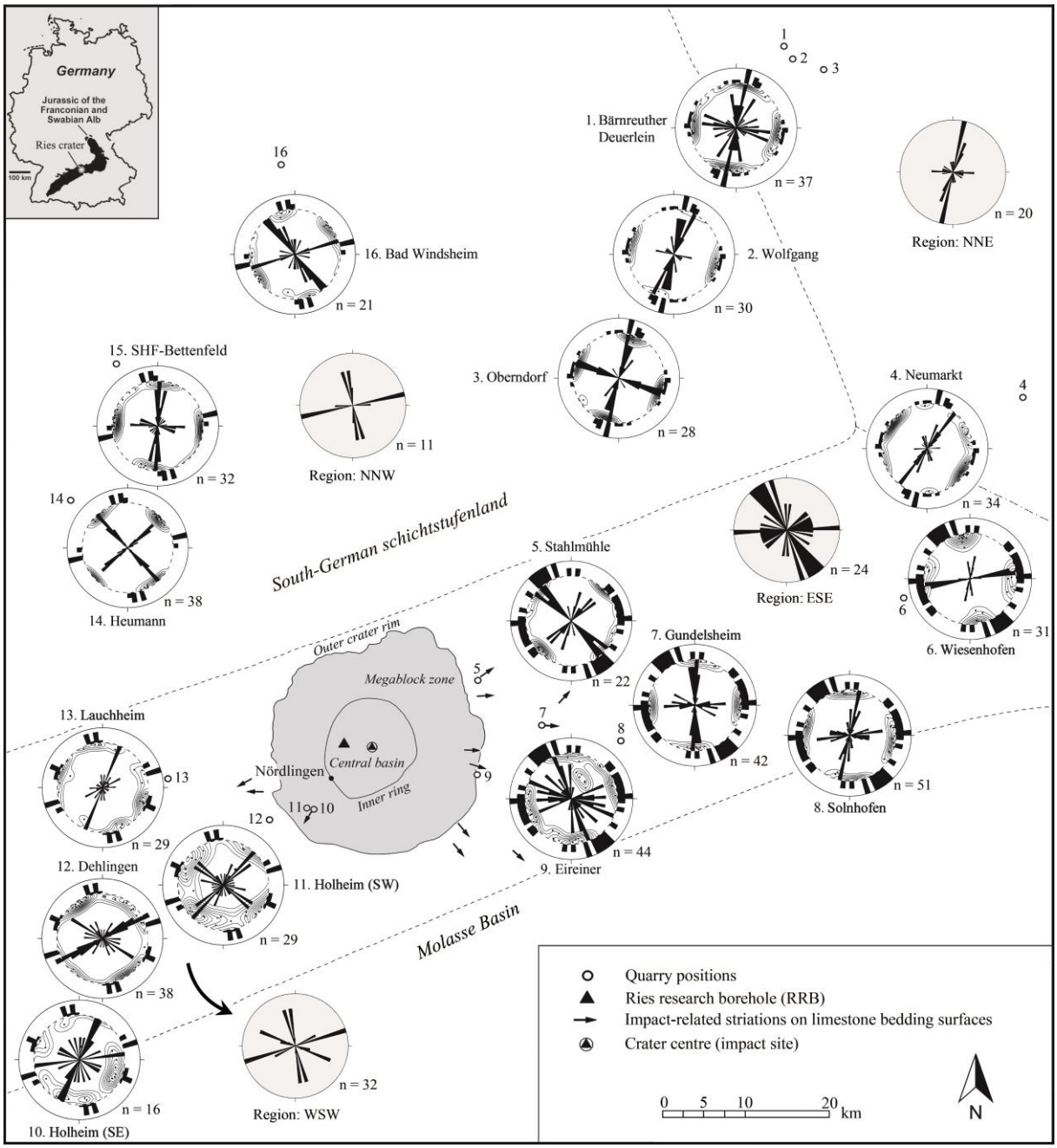

Figure 4.4: Strike of prominent vertical to sub-vertical fractures, measured in outcrops around the Ries impact crater, and their relation to regional deformation structures around the Ries impact crater (see text for details). Indicated are crater outlines and positions and names of the quarries from which fracture orientation data were collected. Quarry numbers 1 to 16 are based on increasing azimuth values with respect to geographic N. Orientations of prominent fractures from each quarry (as shown in Figs. 4.1 and 4.2) are presented in contoured pole-point diagrams (equal-area projection, lower hemisphere, contours based on Fisher distribution) with superimposed rose diagrams of fracture strike (inside broken circle). The number of these measurements is given by n. The strikes of lineaments, fractures and faults related to regional tectonics in four different regions (NNE, ESE, WSW and NNW) around the Ries impact are presented in four rose diagrams with light grey backgrounds. NNE region: northern part of Fränkische Alb, quarry 1–4; ESE region: southeastern part of Fränkische Alb, quarry 5–9; WSW region: eastern part of Schwäbische Alb, quarry 10–13; NNW region: south-German Schichtstufenland, quarry 14–16 (Henningsen and Katzung, 2006; Strasser, 2011). For better comparison, these four rose diagrams have been added as outer rings to the rose diagrams of the respective quarries. Broken lines: boundaries of the four different regions; short black arrows: impact-related striations on bedding surfaces, obtained from Schmidt-Kaler (2004).

The strikes of the fractures and faults related to regional tectonics in the four different regions show similarities as well as differences in their orientation (see four rose diagrams with light grey background in Fig. 4.4). In total, four dominant sets of planes of regional tectonics are observed in the study area. Their mean strike directions are ~15°, ~75°, ~115° and ~340°. The set with ~15° strike is observed in the NNE region only. In the ESE, WSW and NNW regions, the dominant sets have strikes of ~75° and ~340°. The set with ~115° strike is present only in the WSW region. In addition, a very weak set with ~95° strike was observed in the NNE region. In quarries 1–4, the radial fracture set shows a similar orientation to the dominant set (~15°) of the regional tectonic planes. Of these four quarries, the tangential fracture set in quarries 2 and 4 is not well developed; in quarries 1 and 3, the fracture set has a similar orientation to the very weak set (~95°) of the regional tectonics. The tangential fracture set in quarry 5 and the radial fracture set in quarry 6 have nearly the same orientation as the dominant regional tectonic set, with strikes of ~340° and ~75°, respectively. The radial and tangential fracture sets in quarries 7 and 8 exhibit differences in orientation with respect to the regional tectonic planes. In quarries 9–12, the orientation of the prominent fracture sets is diffuse; however, this fracture set has a different orientation from the planes of regional tectonics. In quarry 13, only the tangential fracture set is well developed and its orientation is different from the planes of regional tectonics. In quarry 14, the orientations of both sets of prominent fractures are different from the planes of regional tectonics. In quarries 15 and 16, the strikes of the prominent fracture sets have an approximately similar orientation to that of the regional tectonics, with the exception of the radial fracture set in quarry 16.

Although there is some overlap of the orientation of the prominent fracture sets with the planes of regional tectonics in some quarries; in general, the fracture sets show systematic variation with distance from the impact centre (Fig. 4.5a, b). Within ~10–15 km, i.e. mostly within the crater margin, the orientations of the prominent fracture sets generally differ from those of the planes of regional tectonics. The only exception is the tangential fracture set in quarry 5, the orientation of which is similar to that of the regional tectonic planes. At a distance of ~15–47 km, the orientations of impact-induced prominent fractures and regional ones are also different. At distances greater than ~47 km, the orientations of prominent fracture sets and planes of regional tectonics are similar, except in quarries 4 and 6. In quarry 4, both fracture sets display large variation, in quarry 6 only the tangential set is different.

The angular deviation of the mean strike of the two fracture sets to the Ries impact centre reveals important information in terms of their respective quarry distance (Fig. 4.5c, d). Within the crater margin, i.e. at a distance of ~10–15 km from the impact centre, the angular deviation is highly variable and does not show any systematic relationship with distance. At a distance of ~15–47 km, the mean angular deviations of the radial and tangential fracture sets are less than ca. 10° and 15°, respectively. One exception is the ~20° deviation of the tangential fracture set at a distance of ~25 km. Beyond ~47 km distance, the angular deviation of both fracture sets has a higher variation except for the radial set in quarry 6 and the tangential in quarries 2 and 4. The maximum angular deviation for both sets was observed in quarry 15 at a distance of ~59 km. In general, the tangential fracture sets show higher deviation than the radial ones. In addition, the striations and mean radial strike azimuths in four different quarries within ~10–20 km of the impact centre have similar orientations (Fig. App. 4.2).

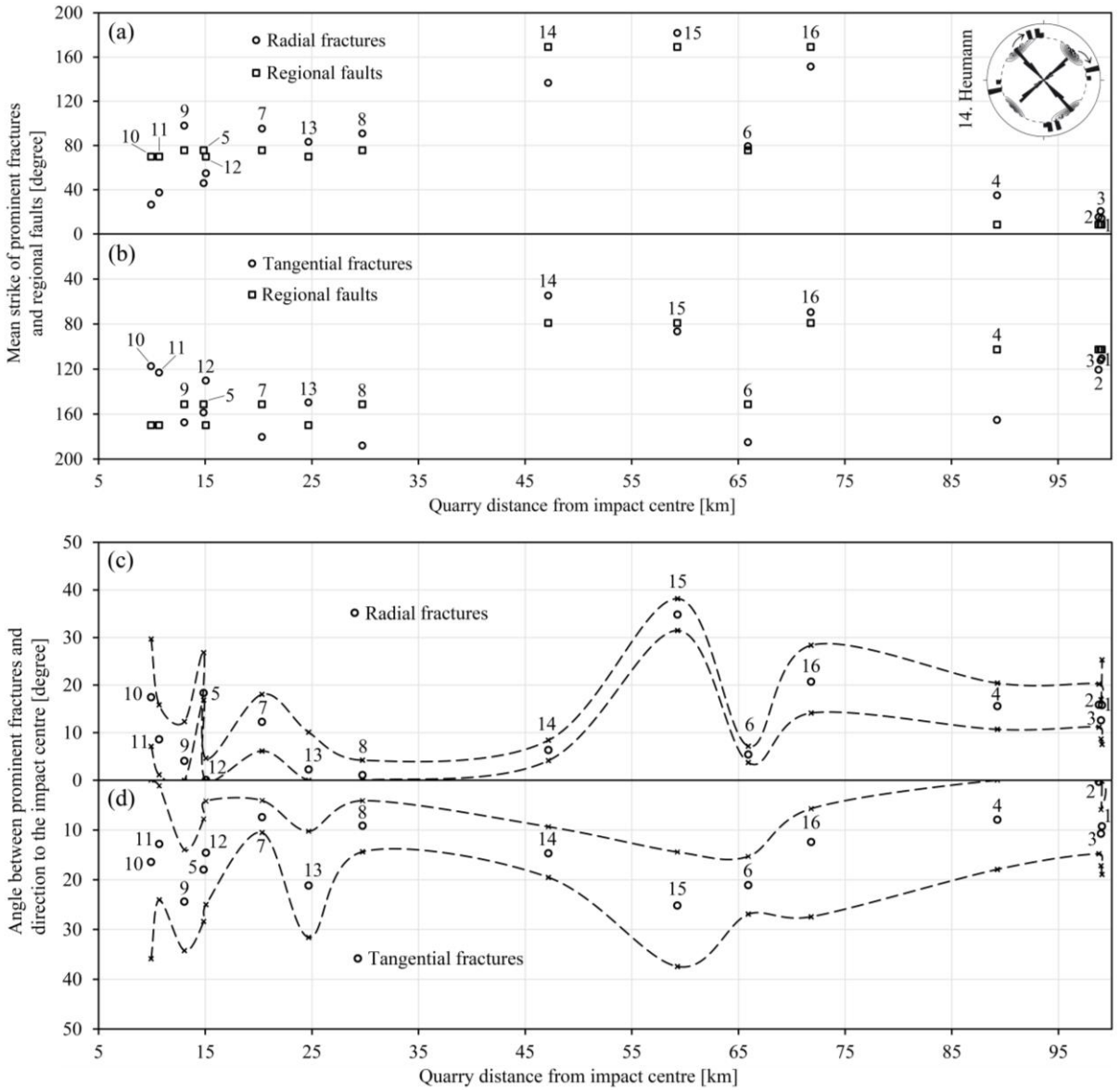

Figure 4.5: Relationship between the strikes of fracture planes induced by impact and by regional tectonics. (a–b) Variation of angle between the strike of the impact-induced fractures and fractures of regional tectonics (as shown in Fig. 4.4). Illustrated are the mean strike directions of two prominent fracture sets in each quarry, roughly radial (a) and tangential (b) to the impact centre, and their respective nearest regional deformation orientation. The angles between these directions are plotted against distance of the respective quarry to the impact centre. The determination of the angle, based on mean directions, is shown in the rose diagram (upper right corner). (c–d) Variation of angle between the strike of the impact-induced radial and tangential fractures (c and d, respectively) and the direction of the respective quarry relative to the Ries impact centre. The strikes of the fractures are given as mean values, taken from figure (a–b). The difference between this value and the quarry-impact centre direction is plotted against the distance of the respective quarry from the impact centre (open circles with quarry numbers). Broken lines indicate the 95% confidence interval. For the tangential fracture set the angle complementary to 90° is given. The zero–degree line represents the direction to the impact centre. As the data show a non-Gaussian distribution, the upper and lower parts of the confidence interval were calculated based on bootstrap method using the PAST software (Hammer et al., 2001). Numbers are those of quarries in Fig. 4.3.

4.2.2 Fracture frequency in zones of intense fragmentation

The fracture frequency in zones of intense fragmentation was quantified in both the horizontal and the vertical direction. Quantification in the horizontal direction was based on high-resolution field photographs from two vertical sections of two different quarries: one approximately N–S-oriented section in the Eireiner quarry and one 20°-oriented section in the Solnhofen quarry. The fracture frequency in the vertical direction was quantified along the drill core of the Ries Research Borehole 1973, based on geophysical well-log data of fragmentation (Ernstson and Pohl, 1974). Distance-related variations of fracture frequency in the quarry sections as well as in the drill core are best matched by a seventh to eighth order Fourier fit. The residual data indicate that additional cycles may be present (Fig. App. 4.3).

The autospectrum of the horizontal fracture frequency data from the Eireiner quarry (Fig. 4.6a) reveals two main peaks at frequencies of ~0.00125 and ~0.00375 cm^{-1}, corresponding to periods of ~800 and ~267 cm, respectively (Fig. 4.6b). Similarly, the horizontal fracture frequency data from the Solnhofen quarry (Fig. 4.6c) show two peaks at frequencies of ~0.0025 and ~0.00375 cm^{-1}, corresponding to periods of ~400 and ~267 cm, respectively (Fig. 4.6d), and a weak peak at 0.00562 cm^{-1}, corresponding to a period of 178 cm. However, the autospectrum analysis using Fourier transform methods has some disadvantages, such as spectral leakage and underrepresented low-frequency cycles. To overcome this problem, we used a wavelet power spectrum (Lau and Weng, 1995; Mackenzie et al., 2001), which can easily map changes in the time- or spatial-frequency domain with a flexible standard resolution. The wavelet power spectrum of the Eireiner section (Fig. 4.6e) shows continuity of the ~270 cm cycle along the entire section but does not contain the ~800 cm cycle. This cycle is probably an artefact of the autospectrum analysis. Similarly, in the Solnhofen quarry (Fig. 4.6f), the ~400 cm cycle occurs through the entire section, but the ~267 and ~170 cm cycles are present only in parts of the section. In addition, the autospectrum of degree of fragmentation in the core (Fig. 4.7a) reveals two main peaks at frequencies of ~0.0031 and ~0.029 m^{-1}, corresponding to periods of ~320 and ~34 m, respectively (Fig. 4.7b). The wavelet power spectrum of the degree-of-fragmentation data exhibits discontinuity of the ~320 m cycle and continuity of the relatively weak ~34 m cycle along the vertical direction within the depth range 605–1200 m beneath the centre of the crater. The wavelet power spectrum of the degree of core fragmentation (Fig. 4.7c) reveals continuity of the ~34 m weak cycle along the sections, but does not display the ~320 m cycle. The ~320 m cycle is probably an artefact of the autospectrum analysis.

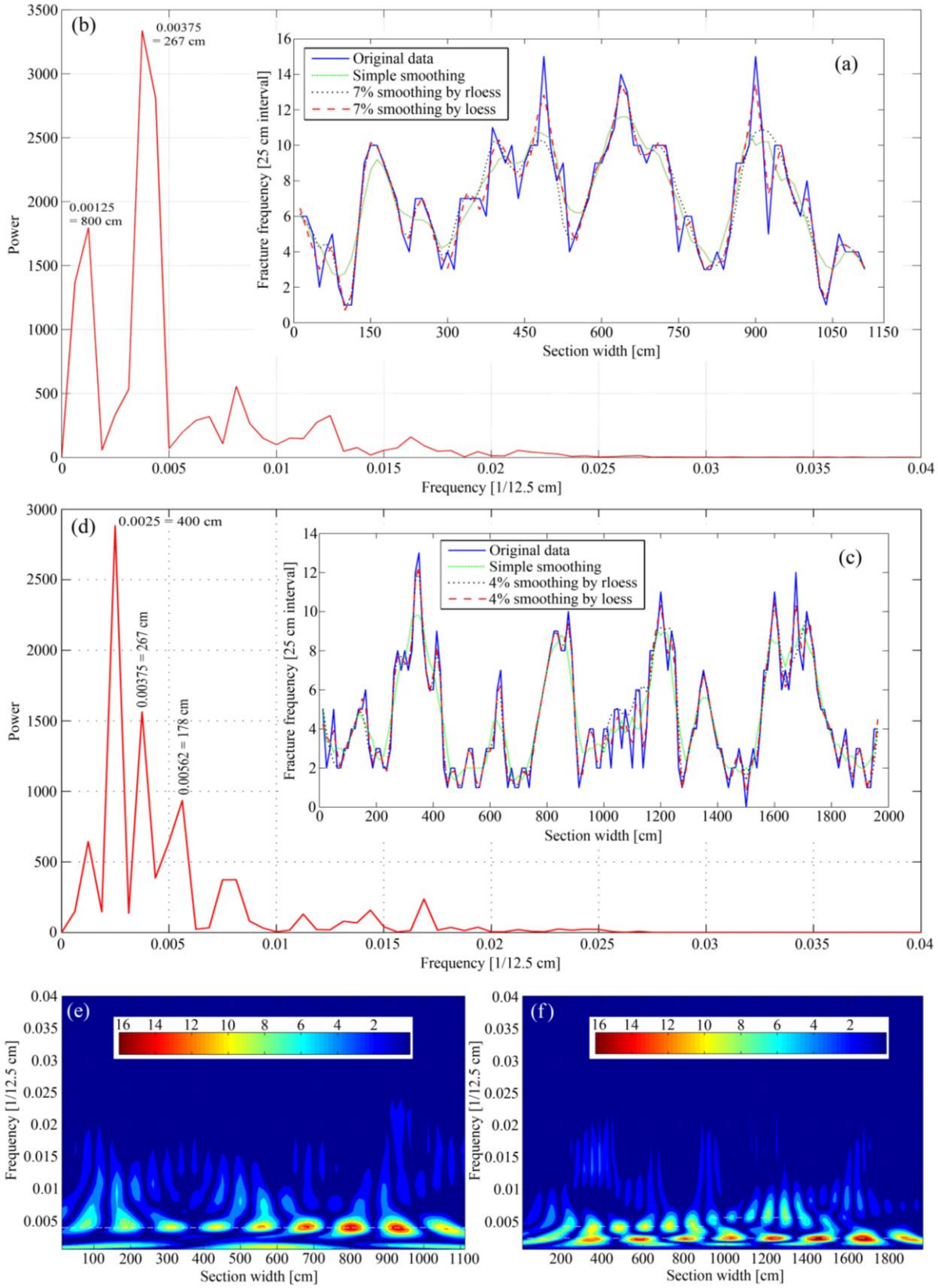

Figure 4.6: Time-series analysis of fracture frequency along an approximately N–S oriented 1120 cm vertical section in the Eireiner quarry and a 20° oriented 1965 cm vertical section in the Solnhofen quarry. The analysed fracture pattern is based on (i) field photographs of the section, merged to give a single image, (ii) manual digitization and (iii) conversion into binary images. For details see Hossain and Kruhl (2014a). Along a horizontal scan-line approximately at a medium altitude of the section, the number of fracture intercepts was

recorded for each 25-cm interval, with 50% overlap, and plotted against the section length (see Fig. App. 4.3). (a) Histogram of smoothed fracture frequencies of the Eireiner section, based on three different smoothing functions, available in the Matlab Curve Fitting Toolbox™. The best match to the original data was achieved using the Lowess/Loess smoothing function with 7% smoothing (broken red line). (b) Autospectrum using Fourier transform on best-match smoothed data of the Eireiner section, after removal of the linear trend using the 'detrend' function. Similarly, a histogram and autospectrum for the Solnhofen section are provided in figures (c) and (d), respectively. (e–f) Wavelet power spectrum (Lau and Weng, 1995; Mackenzie et al., 2001) using Morlet wavelet, applied to the same data used for (b and d). The wavelet transform was computed at 120 different scales between 1 and 120 to map changes in the spatial-frequency domain with a flexible standard resolution.

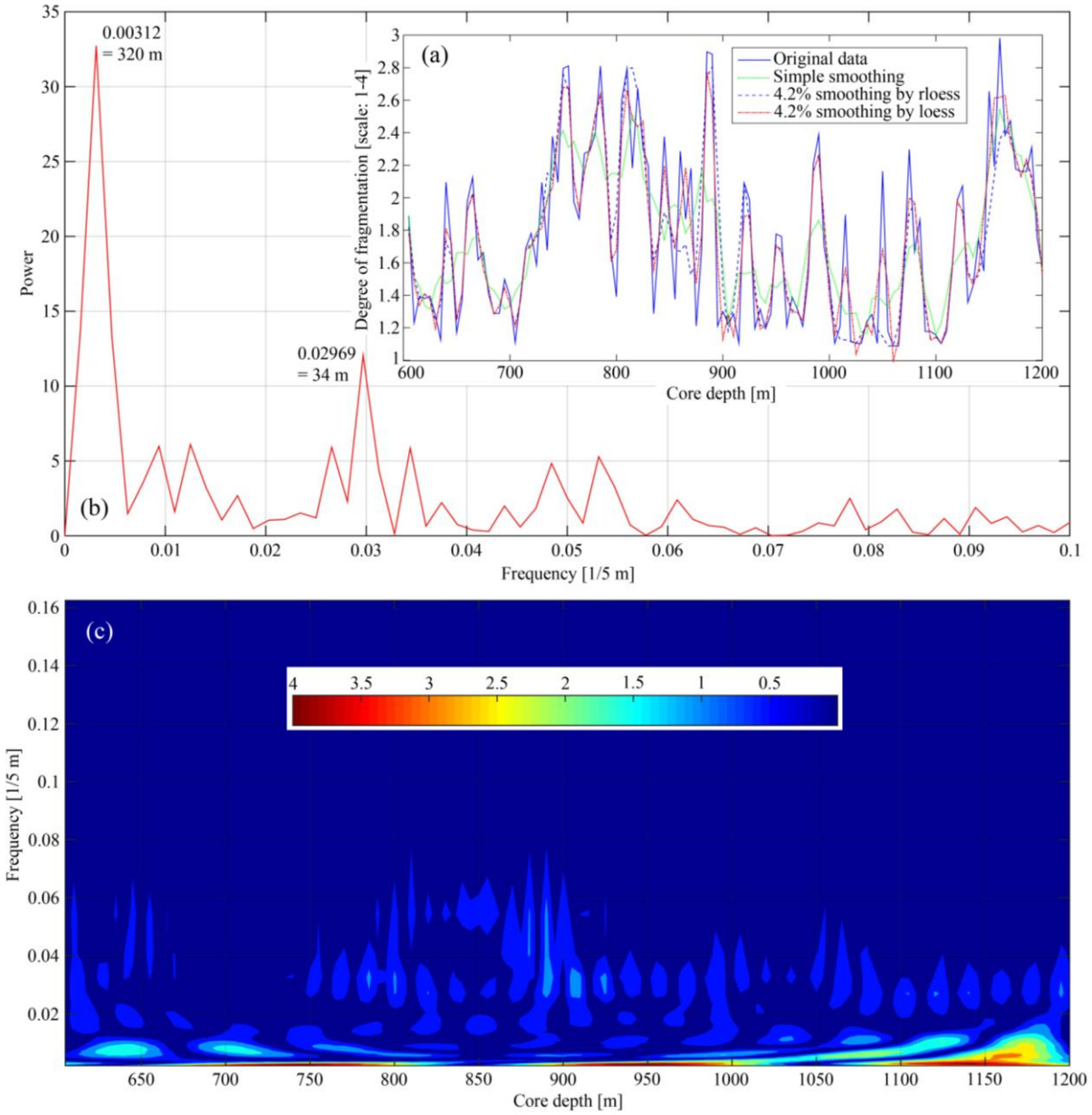

Figure 4.7: Time-series analysis of degree of drill core fragmentation of the basement rock at a depth of 605 to 1200 m beneath the Ries crater centre (position marked in Fig. 4.4). This vertical quantification of core fragmentation is based on measurements within core samples and geophysical logging data for the Ries Research Borehole obtained from Ernstson and Pohl (1974). The degree of fragmentation was measured at 5 m intervals. (a) Histogram of smoothed degree of fragmentation, based on three different smoothing functions available in the Matlab Curve Fitting Toolbox™. The best match was achieved by the Lowess/Loess smoothing function with 4.2% smoothing (broken red line). (b) Autospectrum using Fourier transform on best-match smoothed data,

after removal of the linear trend using the 'detrend' function. (c) Wavelet power spectrum (Lau and Weng, 1995; Mackenzie et al., 2001) using Morlet wavelet, applied to the same data used for (b). The wavelet transform was computed at 120 different scales between 1 and 120 to map changes in the spatial-frequency domain with a flexible standard resolution.

4.2.3 Fracture branching structure

Fracture branching structures, combined with dominant single fractures, are visible at different scales on vertical faces in quarry 9, on a horizontal face in quarry 7 and also in core samples. The propagation direction of the fracture system can be determined using the offspring direction (Fig. 4.8a, b). This direction exactly points away from the Ries impact centre. Three primary fractures are present at the beginning of the branching structure. One main primary fracture diverges into dominant first- and second-order offspring fractures, developing into an increasingly complex branching structure (Fig. 4.8b). The branching segments range from a few millimetres to several decimetres, but only those longer than 1 cm were sketched and analysed. Up to 15th-order branching or offspring levels were counted beginning from a single primary fracture. The frequency distribution of the branching angles β is unimodal and roughly symmetric (Fig. 4.8c); however, very weak asymmetry with slightly positive skewness and low kurtosis is present. The angles do not vary systematically with distance parallel to the propagation direction. The fracture branching pattern shows a preferred fracture orientation roughly parallel to the symmetry axis.

Quantification of the pattern complexity of the structures provides information about the processes responsible for these structures (Kruhl, 2013). Although qualitative analysis is meaningful, there is still a need for quantitative analyses, as only these will allow comparison between natural and experimental processes (Gerik and Kruhl, 2009; Buhl et al., 2013). Specifically, fractures generally form complex patterns that are often different in different directions (anisotropy) and in different areas (inhomogeneity) (Kruhl, 2013). We applied the modified Cantor-dust method (MCDM) using AMOCADO software (Gerik and Kruhl, 2009) to quantify the intensity of pattern anisotropy of the branching structures. Anisotropy intensity is measured using the ratio of short (*b*) and long axis (*a*) of the fit ellipse (Fig. 4.8e). In addition, to understand the pattern variation in different parts, i.e. the inhomogeneity of anisotropy, MORFA (Peternell et al., 2011) was applied. MORFA is a combination of AMOCADO and a gliding window procedure. A circular window passes over the image and generates fractal dimensions in a particular direction related to the respective position of the window. The resulting anisotropy direction is then plotted as a black bar at the centre of analysis window that represents the orientation of the short-axis anisotropy parallel to the orientation of the short axis (*b*) of the ellipse (Fig. 4.8f). This study used a circular window of 300 pixels and a gliding distance of 50% in each step.

As the width of the fracture branching structure is different from its length and the structure has significant pattern variation in its different parts (Fig. 4.8b), the MCDM was applied to three different parts (left, middle, right) of the pattern. Because the results of the analyses for the three parts are the same (or at least similar), only the result for the middle part is presented, as the segment-length-frequency relation for a single direction (Fig. 4.8d) and as the direction-dependence of the pattern's fractality (Fig. 4.8e). The fractality, i.e. the *m*-value (slope of the linear arrangement of the data points), is between 6.95 and 2.37, with the highest fractality related to the 100°-direction. This direction is roughly orthogonal to the fracture propagation direction. The direction dependence is strongly anisotropic, with an axial ratio of 0.41 of the best-fit ellipse through the data points. A detailed description of the analysis is provided in the figure caption. Application of the MORFA method to the same pattern results in a map of the short axis of the fit ellipse (Fig. 4.8f), which

represents the direction of minimum pattern complexity. Over the entire fracture pattern, this short axis show a relatively constantly orientation, parallel to sub- parallel to the fracture propagation direction. Local disturbances are caused by variation in the orientation and density of branches.

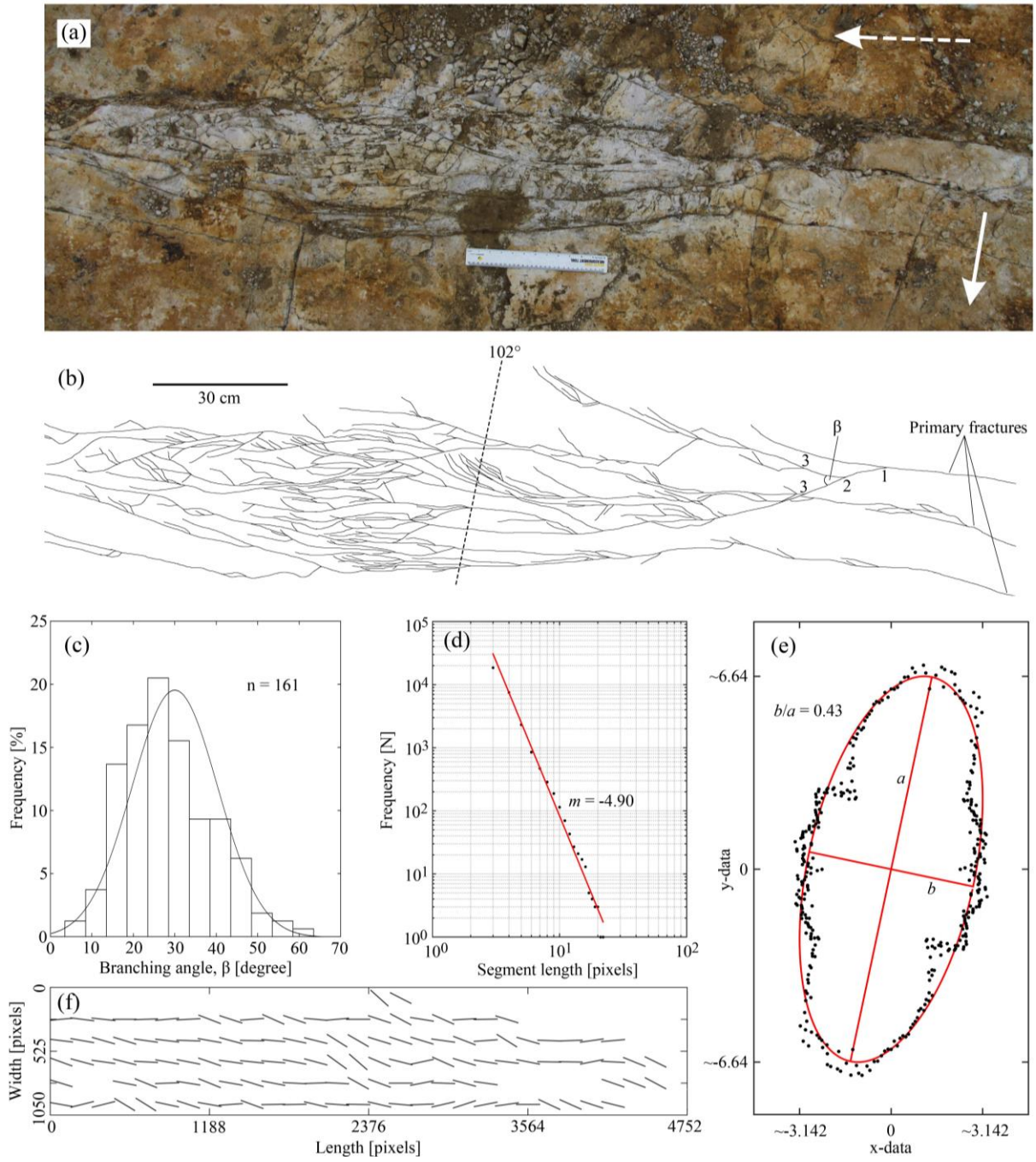

Figure 4.8: 2D image perpendicular to a 3D branching structure from the Gundelsheim quarry. (a) The structure is exposed on a specific bedding plane of Malm limestone, which was covered by Bunte Breccia during the impact. The scale in the image is 31.5 cm long. Solid white arrow: north direction. Broken white arrow: direction away from the impact centre. (b) Binary pattern of the branching structure that was manually generated based on Fig. 4.8a. Single parts of the fracture network with minimum lengths of 1 cm were digitized. The pattern contains three primary fractures, which develop from right to left into a cascade of 'sub-fractures'. Starting with the 'upper' primary fracture, the increasing order of branching is numbered 1, 2, 3, etc. The branching angle (β) was measured at 1 cm distance from each branching point. (c) Histogram of branching angle β measured in Fig. 4.8b, represented in 5° classes. Solid line: normal distribution fit. (d) Basic diagram of the modified Cantor-dust

method (AMOCADO software, Gerik and Kruhl, 2009), exemplified for the 102° direction (figure b). The linear arrangement of segment length vs. cumulative frequency data points in the double logarithmic plot indicates self-similarity, i.e. fractality, of the pattern over the entire range of measurement, characterized by the slope value *m*. (e) Representation of *m*-values for all 180 directions (with 1° angular distance) through the branching structure. The values are plotted from the centre to the outside. The best-fit ellipse highlights the geometry of the data point arrangement and serves as a measure for the anisotropy of the structure, given by the ratio of the ellipse axes *b* and *a*. (f) Anisotropy of the branching structure, quantified by high-resolution mapping of rock fabric anisotropy (MORFA) (Peternell et al., 2011). MORFA produced black bars, each of them representative for sub-images of 300 × 300 pixels. Each bar represents the short axis of the fit ellipse, i.e. the general direction of the minimum pattern complexity.

4.2.4 Near-surface target-rock delamination

Near-surface delamination of the upper Malm limestone (target rock) was observed in five different quarries situated at different distances from the Ries impact centre in an east to north–northeast direction. Multiple detachment horizons with visible offset and metre- to decametre-scale faulting and folding were observed in quarry 9 (see Fig. 4.4 for location). The occurrence of intense deformation is evident here from the ramp-and-flat geometries of the detachment plane, the thrust wedge, thrust and normal faulting and various types of folding. The vertical extent of this deformation is ca. 40–60 m from the lowermost visible detachment plane. In quarry 7, a possible detachment plane was observed ca. 12 m beneath thickly bedded Malm limestone. However, no other visible deformation was observed except the prominent fractures perpendicular to limestone bedding and striation and grooves at the top surface that was covered by Bunte Breccia. In quarry 8, small-scale ramp-and-flat thrusts are observed in the upper blocks of thinly bedded Malm limestone separated by multi-level, layer-parallel, low angle strata cut-off detachment plane (Fig. 4.9a). In another section (Fig. 4.9b), the hanging wall block is decoupled from the foot wall along a layer-parallel detachment plane that leads to small-scale asymmetric drag folding. The depth of the lowest visible detachment plane is ca. 6–7 m. At a distance of ca. 46 km east of the Ries impact centre (~10 km north of Eichstätt), small-scale thrust-propagating folds in the hanging wall block were observed in a quarry, separated by a layer-parallel detachment plane at a depth of 2–3 m below the ground surface. Within a distance of ~47–90 km of the impact centre, near-surface delamination was not observed in the studied quarries. However, ca. 99 km from the impact centre, there are three quarries close to each other (quarries 1, 2 and 3, see locations in Fig. 4.4): of these three quarries, evidence of possible near-surface delamination is only observed in quarry 1. In quarry 1, an upper unit of thickly bedded limestone is decoupled from a basal unit along a flat-lying bedding-parallel shear plane at a depth of ca. 16–18 m. The upper unit is partly folded with estimated fold axes oriented at ca. 100° (Fig. 4.10a). Along the detachment plane, sub-angular to sub-rounded fragments with systematic preferential alignment of their long axes were observed in the southern part of the section, indicating bedding-parallel movement and the sense of shear (Fig. 4.10b). These fragments are coated with thin argillaceous matrix, which may have enhanced the movement by locally lubricating the plane.

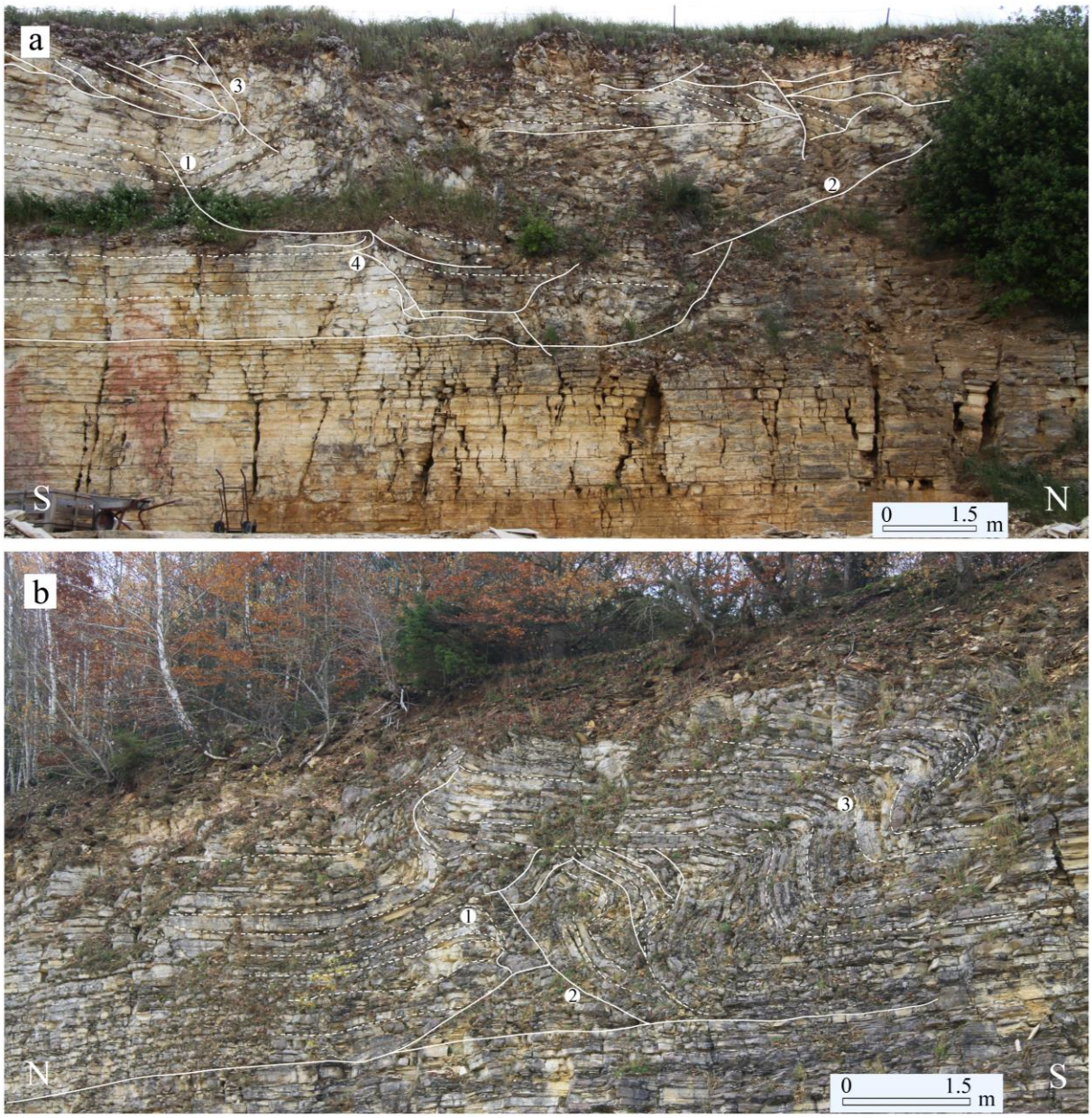

Figure 4.9: Impact-induced near-surface deformation of thinly bedded Malm limestone associated with target delamination of different intensities at the Solnhofen quarry (for the location see Fig. 4.4). (a) The uppermost several-metre-thick layer is dismembered into different thrust and tilted blocks and separated by several thrust planes (solid lines) from a lower layer of less deformed limestone. For clarification, some bedding planes are indicated by dashed lines. In the upper part of the undulating strata (1), low-angle strata cut-offs at the detachment (2), small-scale thrusting (3), thrust wedges (4) and related brittle deformation are visible. In the lower part numerous up to decimetre-scale open fissures cut vertically through the bedding planes. These are typically up to several metres long and start and terminate at specific bedding planes. Their orientation perpendicular to the S–N oriented quarry face identifies them as radial fractures with respect to the impact centre. Clearly there is no specific 'detachment plane' that controls the extension of these open fissures. (b) Locally, the uppermost several-metres-thick layer is strongly folded on the metre-scale and partly detached from the lower undisturbed layers of Malm limestone. The deformed layers show strata undulation (1), low-angle strata cut-offs at places (2) and asymmetric overturned drag folds (3).

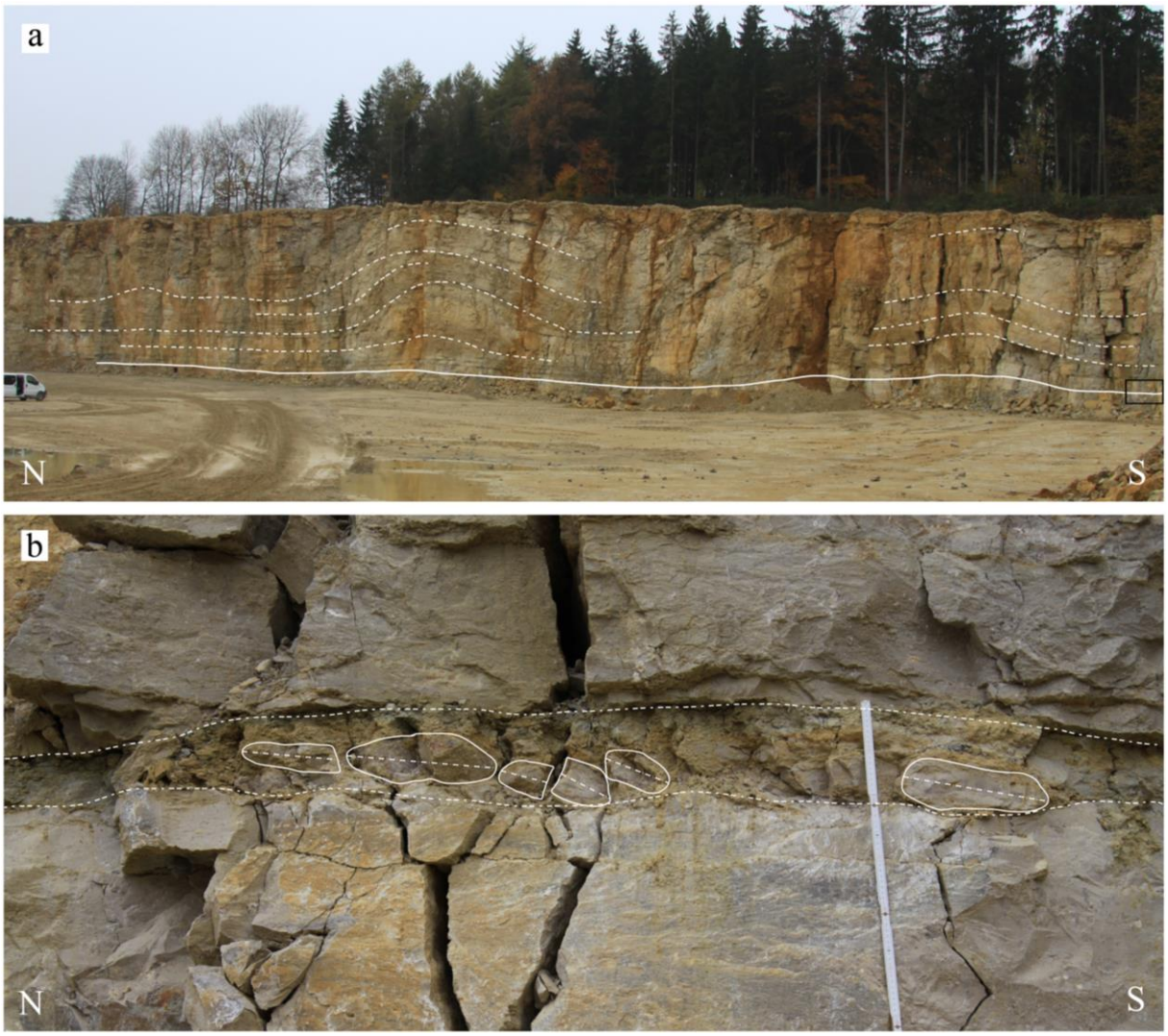

Figure 4.10: Deformation structures associated with target delamination in Bärnreuther-Deuerlein quarry (for location see Fig. 4.4). (a) Decametre-scale folds in the bedded Malm limestone (dotted lines) above a bedding-parallel detachment plane (solid line), separating the lower undeformed part. Estimation of fold axes in the outcrop gave a result of ca. 100°, i.e. roughly perpendicular to the quarry face. The black box indicates the location of figure b. (b) Close-up of the detachment plane. This represents a ca. 20 cm thick gouge-like zone with sub-angular to sub-rounded fragments in an argillaceous matrix. The long axes of the fragments are marked by broken lines inside the fragments. The systematic inclination of these axes indicates top-to-the-left movement.

4.3 Discussion

Our study of fragmentation structures indicates that impact-induced structures can in general be distinguished from regional tectonic structures. Four typical impact fragmentation structures have been identified: (i) prominent fractures; (ii) zones of intense fragmentation; (iii) fracture branching and (iv) near-surface target-rock delamination. The characteristics and spatial distribution of these structures around the Ries impact crater have been determined. After a short discussion of the characteristics of each fragmentation structure, we will briefly outline their physical background followed by their spatial distribution around the impact crater.

4.3.1 Prominent Fractures

These fractures (i) are partly open, (ii) start and terminate at specific bedding planes at shallow depth, (iii) are generally orientated perpendicular to bedding and (iv) show characteristic spacing of a few metres. Locally some of the open fractures show branching, which is clear evidence of dynamic fragmentation (Sharon et al., 1995; Sagy et al., 2006). On the basis of their orientation with respect to the Ries impact centre, these prominent fractures can be broadly classified into two sets: radial and tangential (Figs. 4.4 and 4.5). The characteristics of these two fracture sets (Figs. 4.1–3) are comparable with the fracture characteristics reported from laboratory impact experiments (Lange and Ahrens, 1987; Polanskey and Ahrens, 1990), micrometeoroid impacts on the solar panels of spacecraft (Graham et al., 2004), the nuclear test site in the Yucca Flat region of Nevada (Barosh, 1968; Grasso, 2001) and other natural impact craters (Kumar, 2005; Kumar and Kring, 2008; Kenkmann et al., 2014). Although Polanskey and Ahrens (1990) reported five different types of fractures from their impact-cratering experiments, it is difficult to distinguish them separately in the field. It is most likely that our tangential set is equivalent to the concentric, conical and vertical (at distance) fractures, and the radial set is equivalent to the radial as well the near-surface fractures reported by Polanskey and Ahrens (1990) and Ahrens and Rubin (1993). As most of the prominent fractures are open, the limestone wall rock will have been subjected to chemical weathering resulting from water percolation and leaching from the top along the fractures in some places. This will have caused the distinctive characteristic of widening at the bottom and closing at the top of some of the Ries prominent fractures (Fig. 4.2).

4.3.1.1 Physical background of prominent fractures

The two prominent fracture sets, radial and tangential, are attributed to the rising and falling of the ground surface in response to the passage of impact-induced shock and rarefaction waves (Melosh, 1989). Ahrens and O'Keefe (1987) reported three successive regimes of peak shock pressure around the impact crater: regime 1 (impedance match), regime 2 (pressure decay) and regime 3 (elastic decay). The transition from Regime 2 to Regime 3 is characterized by a gradual reduction of localized intense deformation or fracture localization to gradual emergence of homogeneous fracturing (Qian et al., 2009). From the evidence of deformation, it is probable that the studied quarries (Fig. 4.4) are situated at the boundary of Regimes 2 and 3 and in Regime 3. When the high-pressure shock wave and the opposite but equal tensional rarefaction wave reached these regimes (wall rock), prominent fractures started to develop. The compressional radial stress related to the shock wave and tensional circumferential stress related to the rarefaction wave is perpendicular and parallel to the shock front, respectively, in these regimes (Ai and Ahrens, 2004). The circumferential stress would have generated radial fractures, which is a Mode I tensional fracture when it exceeds the tensile strength of the body. As the tensile strength is much less than the compressive strength for a given material, radial cracks extend further than concentric cracks (Ai and Ahrens, 2004). This explains the observation of fewer anomalous orientations of radial fractures compared to tangential fractures (Fig. 4.5). Tangential fractures are formed either by direct shock wave compression or upon relaxation due to elastic rebound of the rocks after the impact shock wave has passed. They may also be developed by differential movement of the free boundary as the rock is forced outwards from the centre of the impact along shear planes intersecting the ground surface (Fulmer and Roberts, 1963). According to Croft (1981), a circumferential tensional fracture or normal fault is produced as a result of flow of deformable material into the transient crater.

4.3.1.2 Spatial distribution of prominent fractures

Up to ~30 km from the impact centre, most of the characteristics of prominent fractures as well as their proper orientation are observed. Within a distance of ~30–47 km, some of the characteristics of prominent fractures are absent, the fracture sets show large orientation variation with faults or fractures induced by regional tectonics (Fig. 4.5a–b) and low angular deviation of their mean strike orientation with respect to impact centre (Fig. 4.5c–d). Further than ~47 km from the impact centre, most of the characteristics of prominent fractures are absent, the fractures show high angular deviation of their mean strike orientation with respect to the impact centre, and their orientation coincides with faults or fractures induced by regional tectonics. These systematic changes are probably related to weakening of the impact-induced shock wave and subsequent rarefaction waves with distance from the impact centre. The gradual weakening of the shock and rarefaction waves resulted in two possible scenarios beyond ~47 km distance. The first scenario is that prominent fracture sets could not develop in their proper orientation, but their orientation was instead largely controlled by the pre-existing regional tectonic structure (Fig. 4.4). Fracture patterns around nuclear explosion craters provide evidence in support of such reactivation of pre-existing weak zones (Barosh, 1968). The second scenario is that the waves were already weak and, therefore, could not deform the target rock any further. Nevertheless, in the megablock zone (Sturm et al., 2015), i.e. within a distance of ~10–15 km from the impact centre, fracture planes are diffusely clustered, with weakly anomalous orientations (Fig. 4.5). In this zone, the initial orientation of large blocks has been altered by gravitational slumping (crater modification stage). Therefore, the prominent fractures within these blocks were also subjected to these changes.

4.3.2 Zones of intense fragmentation

Time-series analysis revealed systematic repetitions of the decimetre-wide zones of intense fragmentation in the horizontal direction (Fig. 4.6) and metre-wide zones of intense fragmentation in the vertical Ries Research Borehole (Fig. 4.7). The repetition interval is ~3–4 m horizontally, and ~34 m vertically. In the horizontal direction, a high-amplitude power spectrum with a period of ~267 cm adjacent to the crater rim (ca. 13 km) are weakened to half of its amplitude at a distance of ca. 30 km. In addition, the appearance of a very-high-amplitude power spectrum with a period of ~400 cm at distance of ca. 30 km probably indicates further modification of the impact-induced stress waves away from the point of impact. Conversely, the large periodic interval (~34 m) of the core degree of fragmentation may indicate that the impact-induced stress waves evolved differently in the vertical direction. The different periodicities of these zones in two different directions appear typical of impact fragmentation. Buhl et al. (2013) reported small-scale zones of intense fragmentation in cratering experiments.

4.3.2.1 Physical background of zones of intense fragmentation

According to Melosh (1989), the thickness of the shock wave in solid rocks is up to a few metres, and the shock front is discontinuous. After generation, as the shock wave expands, it weakens, first being converted into a plastic stress wave and then entirely into an elastic wave. This elastic wave continues to travel through the target rock and is further weakened only by normal seismic attenuation (Melosh, 1989). Conversely, close to the surface, the rarefaction wave produced by the reflection of shock wave energy from the free surface reduced the stress caused by the shock wave. However, at a greater distance from the free surface, the difference in speed between the shock wave and the tensile rarefaction wave causes tensile stress (Ai and Ahrens, 2004). When this stress reaches the tensile

strength of the target materials, it generates fractures in the target materials (Bäckström, 2005). The impact also excites a surface wave, which attenuates less rapidly than a body wave. The surface wave may be also important for brittle deformation at large distances. Therefore, it can be argued that the systematic repetitions of intensely fragmented zones most likely results from the interaction of rapidly changing impact-induced shock and rarefaction waves.

Observations in the horizontal and vertical directions indicate different repetition intervals of these fragmentation zones. In addition, inherent flaws as sites of weakness are important for nucleation and coalescence of fractures (Griffith, 1920), resulting in localization of deformation along specific fracture systems (Faulkner et al., 2003; Wilson et al., 2003). However, in order to make a reasonable correlation of the systematic repetition of the zones of intense fragmentation with the shock, rarefaction and seismic waves, further field observations, numerical modelling and simulations are required.

4.3.2.2 Spatial distribution of zones of intense fragmentation

In the horizontal direction, zones of intense fragmentation were observed at a distance of up to ~1.2 times the crater diameter, i.e. ~ 30 km, away from the Ries impact centre. Beyond this distance, no clear evidence of these zones was found in the studied quarries. Throughout the roughly vertical Ries Research drill core, zones of intense fragmentation were observed. However, information on the distribution of these zones is limited by the drilling depth of 1206 m (Ernstson and Pohl, 1974).

4.3.3 Branching structures

Quantitative analysis of the branching structure geometry on the centimetre- to decimetre-scale reveals symmetry together with strong anisotropy and a preferred fracture orientation roughly parallel to the symmetry axis (Fig. 4.8). The opening of the branching angles unequivocally indicates the direction of fracture opening, pointing away from the impact centre. The value of the anisotropy intensity of the branching fracture patterns of 0.41 is relatively high compared to those of the anisotropy intensity of impact-induced fractures in near-surface layered limestone (Hossain and Kruhl, 2014a) and those of fracture patterns in regional brittle shear zones (Volland and Kruhl, 2004; Pérez-López and Paredes, 2006). Moreover, irrespective of scale, the branching fracture surfaces do not show any evidence of slip or measurable shear displacements. Instead, the fracture surfaces display diverging pairs of grooves that are not geometrically consistent with fracture-parallel shear. This indicates the extensional nature of these fractures. Sagy et al. (2004) also reported a similar geometry of dynamic tensile fractures from laboratory experiments.

4.3.3.1 Physical background of branching structures

According to Qian et al. (2009), the crack propagation velocity is often limited to 0.2–0.5 of the shear wave velocity. At this velocity, single fractures tend to bifurcate in order to minimize the energy of the system (Meyers, 1994). Inherent micro-flaws in limestone and granitoid rocks serve as points of weakness for the nucleation and coalescence of fractures, as described by the Griffith theory (Griffith, 1920). In addition, Sagy et al. (2004) suggested that branching is driven by the tensile stresses that develop in the tail of the shock wave. The presence of weak heterogeneities in the rock further amplifies tensile stress by scattering. This later amplification of tensile stress triggers branching. According to Baratoux and Melosh (2003), the intensity of the tensile stresses could be as high as 0.5 of the compressive pressure of the shock front, thus could exceed a few gigapascals—sufficient to produce shatter cones. The intensity of this tensile stress decreases further with distance from the

impact point. When the fracture propagation velocity is < 90% and > 30–40% of the Rayleigh wave velocity (VR), dynamic fractures spontaneously spawn both large-scale and small-scale branching fractures (Sharon et al., 1995; Sagy et al., 2006). Therefore, on the basis of our field observations and previously reported laboratory experiments, it can be concluded that the observed branching structures are most likely tensional fractures (mode I). The direction of fracture propagation, marked by the complex forking structure, points away from the impact centre (Fig. 4.8a, b). In addition, the higher order of branching (up to 15th-order for the primary fracture) indicates high-stress conditions (Ono and Allaire, 2000). Consequently, it can be argued that branching structures occur up to the distance from the point of impact at which the propagation velocity reaches values of ~0.9–0.3 VR (Sagy et al., 2006).

4.3.3.2 Spatial distribution of branching structures

In the horizontal direction, branching structures are only observed up to a distance of 20 km from the impact centre. Beyond this distance, the fracture propagation velocity was probably lower than ~0.3–0.4 VR. Branching structures are present throughout the approximately vertical Ries Research drill core; although no information on the distribution of these structures is available below the core drilling depth of 1206 m (Ernstson and Pohl, 1974).

4.3.4 Target-rock delamination

At the crater rim and outside the crater, impact-induced near-surface deformation associated with target delamination of different intensities is indicated by the presence of various deformation structures, mostly in the hanging wall blocks separated by lower detachment planes (Figs. 4.9, 4.10). Kenkmann and Ivanob (2006) also reported target-rock delamination of the Ries impact. In general, the lowermost detachment planes exposed in the quarries are observed at depth from a few to tens of metres beneath the target surface. The displacements along these planes range from decimetres to decametres and decrease with increasing depth and distance from the centre of the crater. With increasing distance, the detachment horizons generally ascend to shallower levels except in quarry 1 (Fig. App. 4.4).

4.3.4.1 Physical background of target-rock delamination

All these near-surface deformation features probably represent the surficial part of the impact-induced interference zone (Melosh, 1989). In this zone, strong shock waves impinge in the surface from below, producing a rarefaction wave that is equal in strength but opposite in sign to the shock wave. This rarefaction wave starts travelling downwards and outwards for many times the crater depth and diameter, fracturing the rock as it moves forwards (Melosh, 1989; Bäckström, 2005). At distance, the interference shock and rarefaction waves near the target surface cause spallation, resulting in highly variable deformation at a given range from the impact centre. The spallation effect decreases rapidly with distance due to exponential decrease of the impact-induced stress (Ai and Ahrens, 2004). The thickness of the interference zone depends on the rise time of the shock-wave front, which is controlled by the structure and physical properties of the target rock (Melosh, 1989). On the other hand, Kenkmann and Ivanob (2006) proposed two separate mechanisms for near-surface deformation, based on numerical modelling. First, weak spallation causes upwards- and outwards-directed motion, and also leads to decoupling of the target materials, which increases in magnitude towards the target surface. Second, subsequent dragging by the oblique impact shower delivers horizontal momentum to the uppermost target area and results in a second horizontal displacement increment by dragging.

4.3.4.2 Spatial distribution of target-rock delamination

The thickness of the near-surface target-rock delamination at the crater rim is more than 40–60 m and decreases exponentially to less than a few metres at a distance of ~46 km from the crater centre (Fig. App. 4.4). Nevertheless, the horizontal extent of target delamination observed in our study is ~46 km, which is approximately twice as much as that reported by Kenkmann and Ivanob (2006) (~20 km or 1.8 times crater radius). Conversely, the absence of near-surface deformation beyond ~46 km could suggest that the stress waves were too weak to produce any spallation effect at this distance. However, target delamination appears to have occurred down to a depth of ca. 16–18 m in quarry 1, i.e. at a distance of ca. 99 km from the impact centre (approximately in the downrange direction, ENE). This finding contrasts with the observed absence of delamination closer to the impact (~47–90 km from the impact centre). A spallation mechanism for this delamination is unlikely for two reasons: (i) absence of spallation-related brittle deformation and (ii) absence of any near-surface delamination in the adjacent quarries. On the other hand, the effect of horizontal dragging by the oblique impact shower for this delamination is only indicated by the presence of bedding-parallel horizontal shear movement. Notwithstanding, the local presence of a strong dragging effect simply due to an oblique impact shower at such a long distance is inconceivable. Therefore, to understand fully the mechanisms of near-surface target-rock delamination and spatial distribution of delamination structures, further field observations and numerical modelling are required.

4.4 Conclusions

This study yields a number of insights into the characteristics and spatial distribution of fragmentation structures around an impact crater. Prominent fractures, zones of intense fragmentation, fracture branching, and near-surface target-rock delamination appear as typical impact-induced brittle deformation structures. These structures, in addition to impact-related orientations of the prominent fractures, are observed at a distance of up to ~1.6 times the crater radius from the impact centre. Beyond this distance, branching structures were not observed. On the other hand, within the distance of ~2.4–3.8 times crater radius from the impact centre, prominent fracture sets show large variations in orientation, with faults or fractures induced by regional tectonics and low angular deviation of their mean strike orientation with respect to the impact centre. Zones of intense fragmentation are also absent beyond a distance of ~2.4 times crater radius. Finally, at distances greater than ~3.8 times crater radius from the impact centre, most of the characteristics of brittle deformation structures are absent. Fracture sets show high angular deviation of their mean strike orientation with respect to the impact centre, and their orientations coincide with faults or fractures induced by regional tectonics. Such systematic changes of the characteristics and spatial distribution of fragmentation structures are not observed in the regional tectonic deformation and are probably related to weakening of impact-induced shock and subsequent rarefaction waves with distance from the impact point. Therefore, it can be concluded that impact-induced dynamic fragmentation structures are different from those of quasi-static tectonic deformation.

Acknowledgements

We are grateful to Thomas Kenkmann, Alison Ord, Tom Blenkinsop, Michael H. Poelchau, Christian Stäb and Tim Yilmaz for helpful discussions. We are also thankful to Axel Gerik and Mark Peternell for giving access to the AMOCADO and MORFA programs. SRTM image of the Ries impact area was kindly provided by Ottomar Krentz. Lutz Cleemann cordially provided help with aerial photography of the quarries by using his personal drone. Support by people from the studied

quarries is gratefully acknowledged: Frank Eichler, Peter Iberl, Lein Felder, Hubert Lederer, Uwe Schneider, Mr. Kahr and Mr. Schumm. Md.S.H. gratefully acknowledges financial support by the German Academic Exchange Service DAAD (grant A/11/75209).

CHAPTER FIVE

5. Eastern Swabian Alb caves and their possible relationship with the Ries and Steinheim impact

5.1 Introduction

The Swabian Alb is the central part of a ridge, comprising mostly of Jurassic rocks that stretches right across South-West Germany over a length of approx. 220 km and a width of up to 80 km (Fig. 5.1). It is bordered by North-Alpine Molasse Basin in the south, Black Forest in the south-west, South-German Schichtstufenland in the north, and the Ries impact crater to the east (Berger et al., 1977; Henningsen and Katzung, 2006; Strasser et al., 2009a). The river Danube flows along the southern boundary of the Swabian Alb. The Swabian Alb is generally subdivided into three parts: western, central and eastern Swabian Alb (Strasser et al., 2009a). The karstified plateau of these parts of the Swabian Alb consists of Upper Jurassic limestones and hosts numerous caves, sinkholes (dolines), and dry valleys. The presence of strath terraces, cut-and-fill terrace (Hancock and Anderson, 2002), conglomerates, and impact craters within this area has provided important time steps for reconstructing the landscape history and cave development. It is well established that uplift related to tectonic movements at the northern rim of the Northern Alpine Foreland Basin and east of the Rhine Graben valley plays a significant role in the cave development in the Swabian Alb (Strasser et al., 2009b; Strasser, 2011). The spatial distribution of most karst features in relation to the palaeo-water-table and its discontinuous lowering over time is the result of uplift and/or incision. The Eastern Swabian Alb that was affected by the Ries and Steinheim meteoritic impacts (twin impact) ca. 14.6 ± 0.1 Ma ago has at least nine caves (Schwarz and Lippolt, 2013). It is most likely that the twin impact had influence on speleogenesis of the Eastern Swabian Alb caves, specifically those that are located close to the impact craters, and are yet to be studied.

Correlation of speleogenesis with dated geomorphic features can reveal the chronology of karstification events. Strasser et al. (2009a) proposed that the Laierhöhle is created in phases, broadly consisting of three horizontal levels: the upper (level 1), middle (level 2) and lower (level 3), covering the time-span from late Middle Miocene to Pliocene/Pleistocene. Based on the available absolute (Buchner et al., 2003) and relative (Strasser et al., 2009a) age dating, it is thought that the oldest phase of karstification event is represented by the level 1 (Mid-Late Miocene age, ~14 million years) (Dongus, 2000; Strasser, 2011). Remarkably, the oldest age of this karstification is similar to that of the Ries and Steinheim meteorite impact (~14.6 million years, Schwarz and Lippolt, 2013), indicates that the twin impact may possibly have some influence on cave initiation and/or development. Karstification or speleogenesis is likely to start at impact-induced weak zones such as fractures and faults, and/or pre-impact weak zone which is reactivated by the twin impact. These kind of weak zones in rock act as fluid pathways and hence their influence on karstification (Connors et al., 1996). However, vertical cave section orientation on the horizontal plane available from Laierhöhle (Strasser, 2011) is discussed so far only in terms of regional tectonics, not from the possibility of impact origin.

Caves are natural archives for karst landscape and their historical events. Examinations of cave sediments in the Laierhöhle, Laichinger Tiefenhöhle, and Mordloch indicate the presence of micrometre-scale spherical metallic particles (Strasser et al., 2009b; Strasser, 2011). Magnetic spherules in the sediments provide information on geological environments through geological time (Taylor et al., 1996; Colombetti et al., 1998; Marini et al., 2004; Mathur et al., 2005; Stankowski et al., 2006). Several models are considered to explain the origin of magnetic spherules in the sediments (Taylor et al., 1996; Stankowski et al., 2006). Presence of magnetic spherules in the Eastern Swabian

Alb caves and their possible association with the nearby Ries and Steinheim impact event are discussed by Strasser et al. (2009b) and Strasser (2011). However, spatial distribution and accumulation of the possible Ries and Steinheim impact-induced magnetic spherules in the cave sediments need further discussion.

Therefore, in order to understand the possible influence of the Ries and Steinheim impact on the development of the Eastern Swabian Alb caves, primary orientation data of the cave vertical section on the horizontal plane from Charlottenhöhle, and secondary data from Laierhöhle have been analysed. Brittle deformation features and their spatial distribution associated with the Ries impact (Hossain and Kruhl, 2015) are particularly considered for this study. The 25 km diameter Ries and ~4 km diameter Steinheim crater were formed ca. 14.6 ± 0.1 million years ago (Schwarz and Lippolt, 2013) by an oblique twin impact (Artemieva et al., 2013) on a target terrain that consisted of 620–750 m thick sub-horizontally layered sedimentary rocks of Triassic to Jurassic age, resting on Variscan basement (Hüttner and Schmidt, 1999; Graup, 1977). This study focuses on the analysis of orientation of the almost straight sections of the caves in the horizontal plane and their possible relationship to large-scale impact-induced prominent fractures orientation (Hossain and Kruhl, 2015). Moreover, secondary data of cave sediments and the age of the earliest karstification events of Eastern Swabian Alb are discussed to understand their possible association with the Ries and Steinheim meteorite impact event.

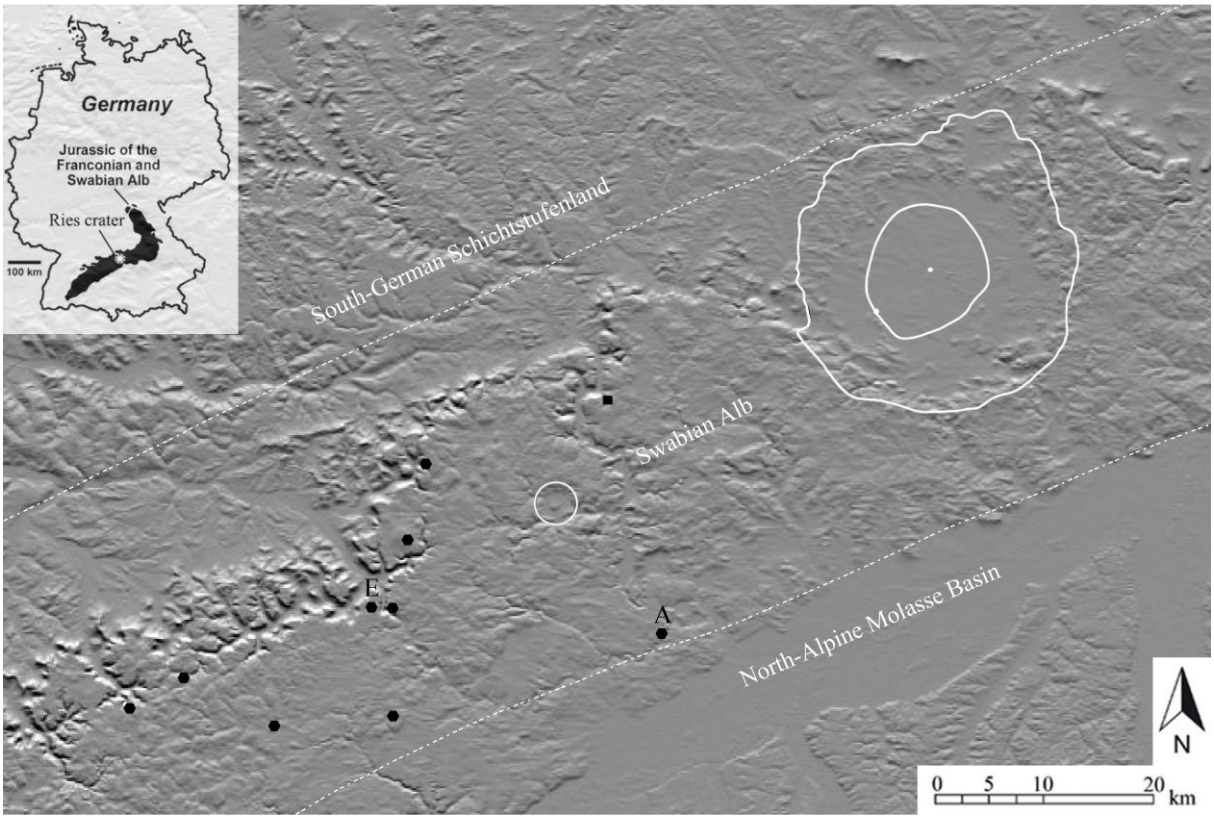

Figure 5.1: Topographic relief image of the Ries and Steinheim impact area. Image is based on Shuttle Radar Topography Mission (SRTM) data with grid resolution ca. 60 m (east illumination, magnification 1:5). Ries crater outlines are marked by white lines (outer line: outer crater rim; inner line: inner crystalline ring) at the top right of the image. Small white circle (approximately at the centre of the image): Steinheim crater. Black square: location of Ochsenberg area. Black hexagons: locations of the Eastern Swabian Alb caves. The Charlottenhöhle and Laierhöhle are marked as A and E, respectively. Broken lines: boundaries between three different tectonic regions (Berger et al., 1977; Henningsen and Katzung, 2006). Image is provided by Ottomar Krentz.

5.2 Studied caves

5.2.1 Charlottenhöhle

This cave is located in the Eastern Swabian Alb at Hürben (between Ulm and Nördlingen), and the geographic position is 48° 35′ 04″ latitude and 10° 12′ 27″ longitude. It is situated ~42 km (~218° azimuth) from the Ries crater and ~15 km (~137° azimuth) from the Steinheim crater (A in Fig. 5.1). The cave was discovered by forester Hermann Emil Sihler in 1893, and named as Charlotten cave in honour of Queen Charlotte of Württemberg. Total length of the cave is 587 m, and its entrance is located at 487.5 m above sea level (Adam et al., 1968) (Fig. 5.2a). On average, the cave passage is 25 to 30 m below the surface. With a total length of 532 m the Charlotten cave, and its prime stalactite inventory is used as one of the finest show caves in Germany (Adam et al., 1968). The cave developed in dolomite and consists of a narrow tube-like cave passage, generally of keyhole-shape (Binder et al., 1993). The cave has nicely developed vertical sections on the horizontal plane which show two main orientations, providing a good opportunity to understand the possible influence of the twin impact on its development.

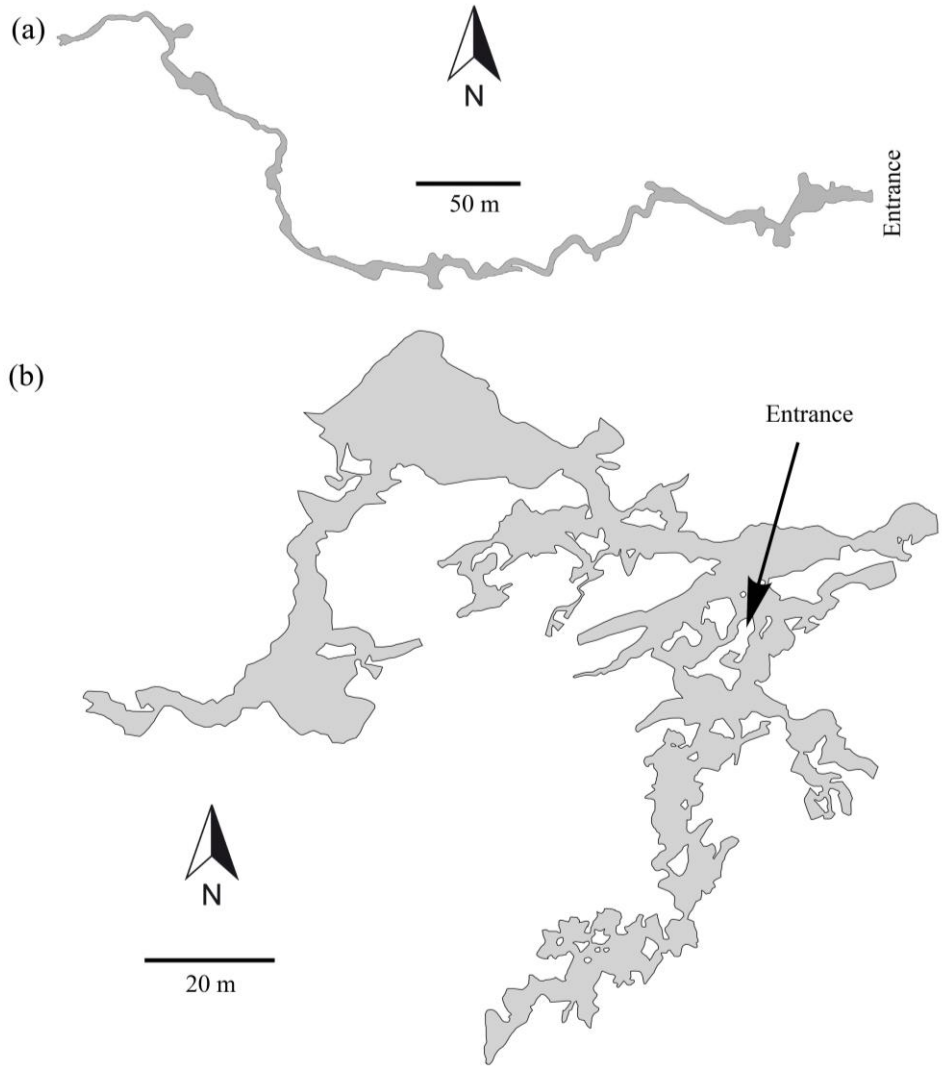

Figure 5.2: Plan view of the two studied caves of the Eastern Schwäbische Alb. (a) Charlottenhöhle: ~42 km SW of the Ries crater centre. (b) Laierhöhle: ~60 km WSW of the Ries crater centre.

5.2.2 Laierhöhle

This cave is located in the Eastern Swabian Alb, 1.5 km east of Geislingen, and is one of the deepest caves of the southwest German Swabian Alb. The geographic location of the cave is 48° 36′ 54″ latitude and 9° 51′ 41″ longitude, situated ~60 km (~240° azimuth) from the Ries crater and ~17 km (~242° azimuth) from the Steinheim crater (E in Fig. 5.1). Total length mapped is approximately 2200 m, and currently explored depth is 127 m (Fig. 5.2b). The entrance situated 685 m above present sea level, coincides with the highest point in the surroundings. To preserve the pristine state of the cave, access is only permitted for scientific purposes. The cave is developed within top units (Late Kimmeridgian) of the Upper Jurassic limestone plateau. Only a little east of the cave is the Battenau, the largest karst depression of the Alb. The Laierhöhle is supposed to be created in phases, consisting of three groups of horizontal levels and four vertical shafts (Strasser et al., 2009a). Among the upper (level 1), middle (level 2) and lower (level 3) horizontal levels, the oldest cave phase is represented by the level 1. Cave age has been determined based on the local correlation between speleogenesis and morphology. Strath terraces of the Ur-Lone valley (Levy, 1922; Dongus, 1977) precisely correlate with the level 1 and level 2a, over horizontal distances of less than 400 m. In SE direction (at the Klifflinie), these two sets of terraces gradually merge into one. Their Mid-Late Miocene age (~14 million years) (Dongus, 2000; Strasser et al., 2009a; Strasser, 2011), indicates that the Laierhöhle is probably the oldest cave in the Swabian Alb.

5.3 Methods, measurements and results

To understand the possible influence of the Ries and Steinheim meteorite impact on the development of the Eastern Swabian Alb caves, field work was carried out in the Charlottenhöhle (A) to record and measure the orientation data of the almost straight cave section on the horizontal plane. In addition, secondary orientation data of almost straight sections of the Laierhöhle (E) in horizontal plane (Strasser, 2011), and lineaments/fractures in Ochsenberg area (Bayer and Groschope, 1993) are analysed. All these orientation data are also compared with the orientation data of the Ries impact-induced prominent fractures (Hossain and Kruhl, 2015).

In Charlottenhöhle, only the almost straight section which is at least a few meters long and controlled by fracture is measured. The fracture controlled cave section is clearly evident by the presence of fracture at the roof, and inverted V-shaped geometry of the cave vertical section (Fig. 5.3a). Ries impact-induced prominent fractures in a vertical face of Gundelsheim quarry, approximately 20 km away from the Ries impact centre also have similar geometry (Fig. 5.3b). These kinds of cavities are generally observed where a prominent fracture terminates at an un-fractured bedding plane. But, as the cave floor is mostly covered by carbonate precipitation and clay-rich soil, it hard to observe any possible pre-given fractures at the bottom of the cave passage (Fig. 5.3a). It is also observed that the transition of the fracture controlled cave section from one to the next is approximately orthogonal. However, it is not confirmed whether the measured orientation of the Laierhöhle are controlled by fracture or not. Analysis reveals approximately orthogonal arrangements of the almost straight sections orientation of the cave A and E on the horizontal plane (rose diagram inside the broken circle, Fig. 5.4). Lineaments orientation of the Ochsenberg area also shows two sets orthogonal to each other.

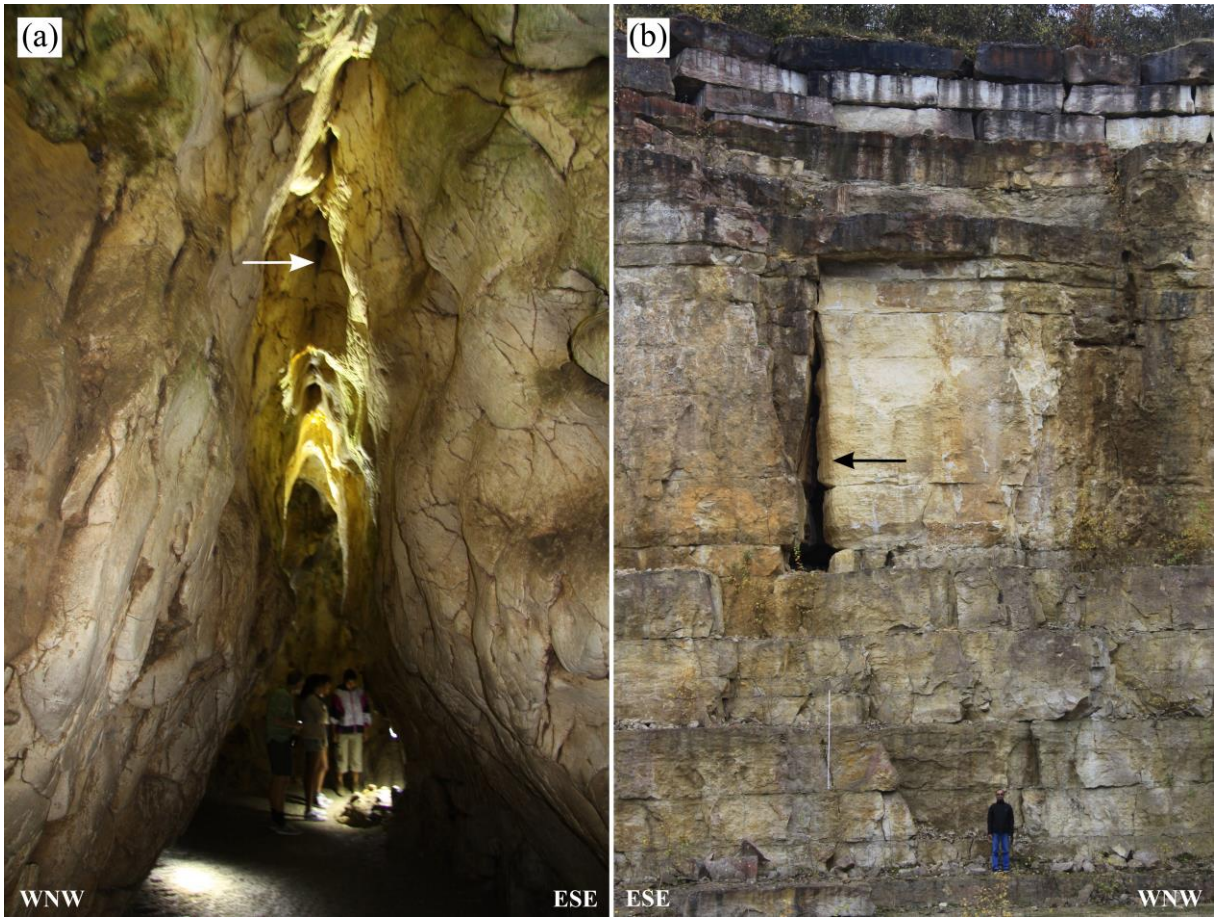

Figure 5.3: Comparison of the fracture controlled, almost straight cave section geometry of the Charlottenhöhle, with the geometry of the prominent fracture related to the Ries impact. (a) Inverted V-shape geometry of the almost straight cave section on horizontal plane at the Charlottenhöhle. White arrow: approximately vertical fracture visible at the roof. Length of this almost straight section of the cave is ~10 m. (b) Vertical view of large-scale open fractures (black arrows) is extending over several metres at the Gundelsheim quarry. The fractures clearly start and terminate at specific bedding planes and widen towards the bottom. White stick: 2 m long, used for scale (photographs taken by Jörn H. Kruhl).

On the other hand, strikes of the fractures and faults related to regional tectonics in the Eastern Swabian Alb show three dominant sets (see rose diagram with light grey background in Fig. 5.4). Their mean strike directions are ~82°, ~115°, and ~345°. Comparison of the mean orientation of the two sets of cave section on the horizontal plane with their nearest regional tectonic lineaments orientation (rose diagram outside the broken circle) (Fig. 5.4) reveals important information. In Charlottenhöhle (~42 km from the Ries impact centre), one set (NE) shows completely different orientation and the other set (NW) shows slightly different orientation to the nearest regional tectonic deformation. In Laierhöhle (~60 km from the Ries impact centre), both sets show slightly different orientation to the nearest regional structures. However, among the two sets of lineaments in Ochsenberg area, one set shows slightly different orientation and other set shows almost similar orientation to the nearest regional structures. In addition, the prominent fractures of the Ries impact reveal two approximately orthogonal sets (exemplified for the quarry 1 in Fig. 5.4). With respect to the Ries impact centre, one set is regarded as radial and the other set as tangential (Hossain and Kruhl, 2015). Interestingly, nearly orthogonal arrangements of the cave section orientation on the horizontal plane roughly coincide with the orientations of the two fracture sets of the Ries impact (Fig. 5.4).

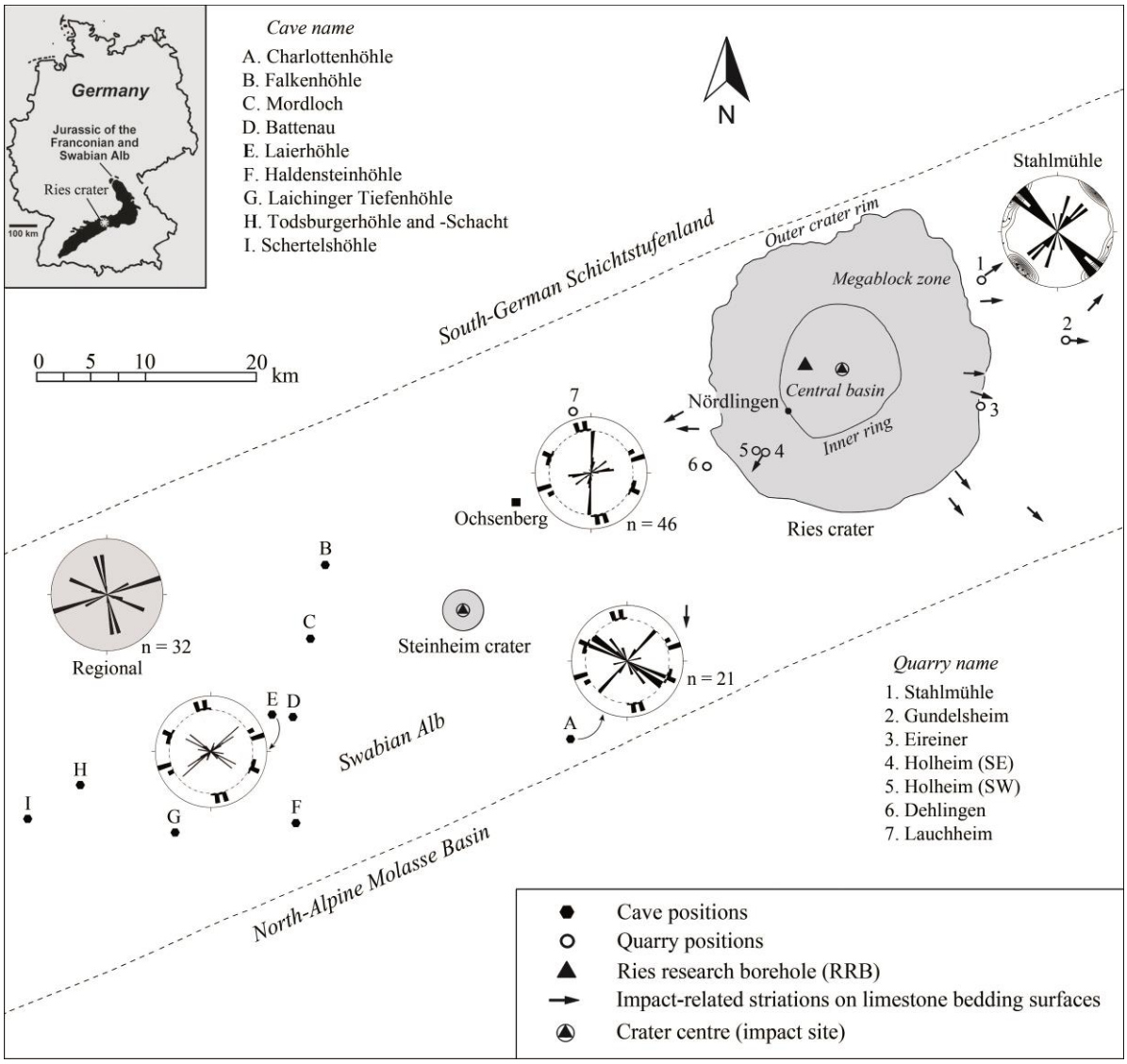

Figure 5.4: Positions of the Eastern Schwäbische Alb cave (A to I), and some of the studied quarries (1–7) around the Ries impact crater. Cave numbers A to I are based on increasing distance with respect to the Ries impact centre. Quarry numbers 1 to 7 are based on increasing azimuth values with respect to geographic N. Broken lines: boundaries between three different tectonic regions (Berger et al., 1977; Henningsen and Katzung, 2006); short black arrows: impact-related striations on bedding surfaces are taken from Schmidt-Kaler (2004). Filled rectangle (Ochsenberg): location of the lineation data. Orientation data of the almost straight sections of the two caves (A and E) in the horizontal plane, and lineaments/fractures orientation of the Ochsenberg are presented as rose diagrams (inside broken circle). Orientation data of Level 2a in cave E is taken from Strasser (2011) and lineaments/fractures data of the Ochsenberg is taken from Bayer and Groschope (1993). The number of the orientation measurement is given by n. Lineaments strike related to regional tectonics in the Eastern Swabian Alb is presented as rose diagrams with grey background (data taken from Strasser, 2011). For better comparison, this rose diagram is added as an outer ring to the rose diagrams of the caves and Ochsenberg lineament/fracture. Decametre-scale Ries impact-induced fracture is represented as pole density contour superimposed with rose diagram (at top right corner) and is exemplified for the quarry 1 (Stahlmühle).

To calculate the angular concentric deviation (CD) of the almost straight cave section, the position of each cave is converted from its original geographic reference system to its azimuth on the basis of the Ries crater centre, giving angular values from 0 to 360° (0° toward north) (Fig. 5.5). In the next step, mean orientation of the almost straight section on the horizontal plane relative to the Ries crater centre is determined and given an angular value that is referred to as concentric deviation (Poelchau

and Kenkmann, 2008). Cave section orientation that is tangential to a hypothetical circle around the crater centre is defined as concentric and has a CD value of 0°. Orientation that is rotated clockwise relative to the circle has positive CD values, while anticlockwise rotation produces negative values (Fig. 5.5). Concentric deviation (CD) of the tangential cave section orientation of the two caves reveals important information in terms of their respective cave distance. Charlottenhöhle which is situated at a distance of ~42 km from the Ries impact centre shows CD only 3°. On the other hand, Laierhöhle which is situated at a distance of ~60 km from the Ries impact centre shows CD of 11°.

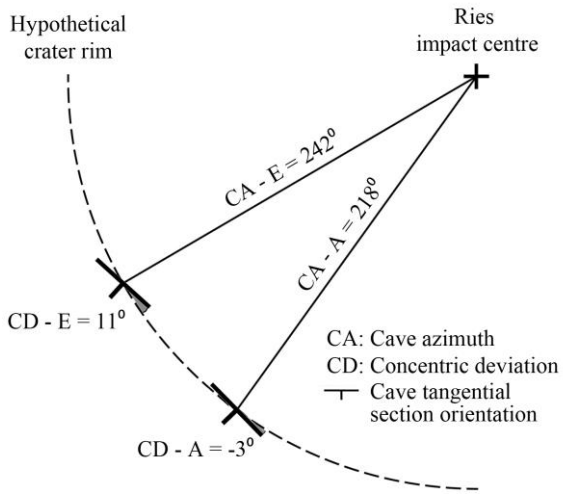

Figure 5.5: Determination of the azimuth and concentric deviation of the almost straight tangential cave section on the horizontal plane based on their orientation and the location of the cave (see text for details). The azimuth is the position of the caves relative to the Ries impact centre. Concentric deviation (CD) defines the orientation of the straight section of the cave relative to the crater centre, with cave tangential section lying tangential to a hypothetical crater rim (dashed curve) around the crater centre. CA-A and CA-E are the cave azimuth for the Charlottenhöhle and Laierhöhle, respectively. CD-A and CD-E are the concentric deviation of the tangential section for the Charlottenhöhle and Laierhöhle, respectively.

Near-surface target-rock delamination data associated with the Ries meteorite impact is taken from Kenkmann and Ivanov (2006), and Hossain and Kruhl (2015). They reported detachment plane and associated hanging wall deformation of the target rock in quarries situated mainly at a distance of ca. 13–45 km from the Ries impact centre. In general, detachment planes are observed at depths between a few meters to more than 50–70 m beneath the target surface. The displacements along these planes range from decimetres- to decametres and decrease with increasing depth and distance from the crater centre (Fig. 5.6). Clear evidence of multiple detachment horizons with visible offset, and decimetre- to decametre-scale faulting and folding are observed in different quarries mainly situated within ~45 km from the Ries impact centre. This radial distance covers the Charlottenhöhle which is situated ~42 km from the Ries impact centre. With increasing distance from the crater centre, detachment horizons climb to shallower levels and intensity of deformation decreases in the hanging wall. Therefore, it is clear that development of the caves which are situated within the distance of ~45 km from the Ries impact centre are most likely influenced by the impact.

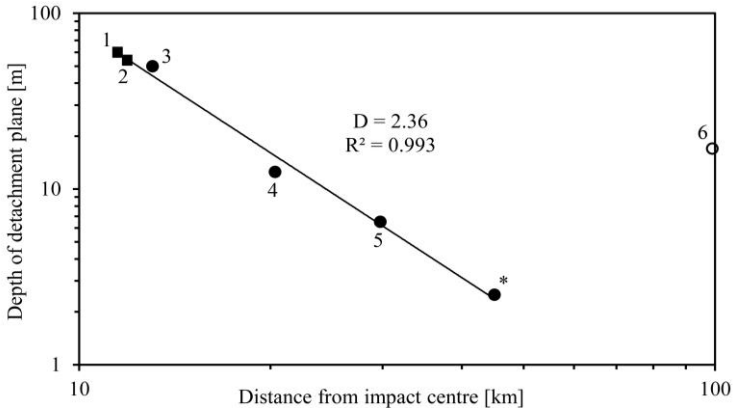

Figure 5.6: Relationship of the depth of near-surface deformation to distance from the impact centre in five different quarries. Double logarithmic plot of quarry distance versus depth of near-surface deformation (target delamination) in each quarry shows a power-law relationship, i.e. fractality (D = 2.36) for the six nearest quarries. Six quarries are numbered 1–6 based on their increasing distance from the Ries crater centre. Data for quarry 1 and 2, i.e. Heroldingen and Grosssorheim, respectively is taken from Kenkmann and Ivanov (2006). Data for quarry 3 to 6 (3: Eireiner, 4: Gundelheim, 5: Solnhofen, and 6: Bärnereuther) is taken from Hossain and Kruhl (2015). The quarry marked with an asterisk [*] is located ~10 km north of Eichstätt, i.e. ~46 km E of the Ries impact centre (the quarry name is unknown).

5.4 Discussion and conclusions

5.4.1 Geometry and orientation of cave vertical section

Geometry and orientation of the Ries impact-induced large-scale fracture sets (prominent fractures) are comparable to the geometry and orientation of the almost straight cave section on the horizontal plane, specifically in the Charlottenhöhle (Figs. 5.3 and 5.4). In some places, impact-induced open fractures in limestone wall rock is most likely subjected to chemical weathering due to water percolation and leaching from the top along the fractures (Hossain and Kruhl, 2015). This leads to a distinct characteristic of inverted V-shape geometry with widening at the bottom and closing at the top (Fig. 5.3b). Similar geometry is observed for the fracture controlled almost straight cave section on the horizontal plane in the Charlottenhöhle (Fig. 5.3a).

Vertical cave section orientation on the horizontal plane in the Charlottenhöhle, and in level 2a of the Laierhöhle show two preferred almost straight sets of sections (Fig. 5.4) roughly coincide with the orientations of the two prominent fracture sets of the Ries impact (Hossain and Kruhl, 2015). Hossain and Kruhl (2015) reported that within a distance of ~30–47 km from the Ries impact centre, fracture sets show low angular deviation of their mean strike orientation with respect to the impact centre and large orientation variation with faults caused by regional tectonics. Beyond ~47 km, fracture sets show high angular deviation of their mean strike orientation, and this mean orientation is more or less in accordance with faults caused by regional tectonics. Remarkably, the almost straight cave section on the horizontal plane (NE set) of the Charlottenhöhle which is situated to WSW direction at a distance of ~42 km, shows large orientation variation with lineaments/faults caused by regional tectonics, and very low angular deviation of the section orientation with respect to the impact centre (A in Fig. 5.4). On the other hand, Laierhöhle which is situated ~60 km from the Ries impact centre, shows small orientation variation of the cave section (both set) with faults/lineaments caused by regional tectonics, and high angular deviation of the section orientation with respect to the impact centre (E in Fig. 5.4). This is also true for another cave which is situated ~62 km away from the Ries impact (see Fig. App. 5.1). Moreover, the exponential decrease of near-surface deformation (Melosh, 1989) up to distance of

~3–3.5 times the crater radius (~45 km) is caused by the spallation and ejecta dragging mechanisms (Kenkmann and Ivanob, 2006). This lateral extent of near-surface deformation covers the distance of the Charlottenhöhle. But, the near-surface deformation associated with the Steinheim impact may only extend up to ~7–8 km (crater radius is ~2 km, Ivanov and Stöffler, 2005; Buchner and Schmieder, 2013) from the impact centre and, hence, does not reach the studied cave.

Therefore, based on the geometry of the straight cave section on the horizontal plane, their orientation with respect to the Ries impact centre, and the lateral extent of the near-surface deformation related to the Ries impact, it is possible to argue that development of some of the Eastern Swabian Alb caves is probably influenced by the twin impact. However, distance from the Ries crater centre, and pre-impact tectonic structures of the target rocks probably played a significant role in the orientation of the almost straight cave section on the horizontal plane.

5.4.2 Cave sediments and relative cave age

Fine grained sediments mainly consisted of Upper Jurassic limestone weathering residues (silicified skeletal elements of echinoderms, chert and goethite grains), mud (mostly pure clay) as well as considerable amounts of quartz grains are common in the Laierhöhle (Strasser, 2011). A group of particles related to these cave sediments are called spherules (Fig. 5.7a–d). In the deeper level of the Laierhöhle and Laichinger Tiefenhöhle, these spherical particles in the ~20 to 200 µm range exist together with the amorphous silicates (Glassphärulen) and/or metal (oxides) (Strasser et al., 2009b). Four types of metallic or magnetic spherules are reported based on their surface structures: absolutely smooth, micro-crystalline skelettoidale, ‘fiederförmige’ (Spinifex, pennate structure) and coarsely crystalline of pseudo-hexagonal and octahedral crystals. These magnetic spherules in the cave sediments are thought to be the product of ablation from meteorites during impact (Strasser, 2011). In addition, elevated nickel and cobalt levels of the spherules (Fig. 5.7e–f), and their (Ni/Co) ratio are affirming a cosmic origin or a direct indication of an impact (Taylor et al., 1996; Colombetti et al., 1998; Stankowski et al., 2006). Therefore, a possibility of their association with the nearby Ries and Steinheim impact events are most likely.

The Ries and Steinheim impacts occurred ca. 14.6 ± 0.1 Ma ago (Schwarz and Lippolt, 2013). The magnetic spherules which are produced through ablation during this twin impact probably fell out and mixed with distinctive layers of impact ejecta blanket. Later flushing of the magnetic spherules from the ejecta blanket is archived into the karstic voids (possibly initiated by the impact) which are only a few steps away. It is highly likely that most cave sediments are accumulated during the final vadose phases of active cave-forming episodes as a result of flooding events, reaching areas above the normal groundwater table. Flooding also washes material from outside into the cave and re-deposits the eroded older cave sediments (Strasser et al., 2009a). Within most of the cave sediments, spherules are accompanied by crystals of titano-magnetite. Both spherules and titano-magnetites are proxies for re-deposited Mid-Miocene sediments. The stratified cave sediments are specifically well-preserved in level 1 and 2b of the Laierhöhle (Strasser, 2011). On the other hand, different horizontal levels of the Laierhöhle are considered to be the product of a stationary paleo-water table associated with the crustal tilting and isostatic uplift of the southwest German crust from late Mid Miocene to earliest Pleistocene (Strasser et al., 2009a). A chronology of events is determined based on the correlation of speleogenesis with dated geomorphic features. The oldest episodes of karstification (upper levels: horizontal level 1 and 2a) are dated to the late Middle Miocene and Late Miocene (Dongus, 2000; Strasser et al., 2009a; Strasser, 2011). This is similar in age to the Ries and Steinheim impact events.

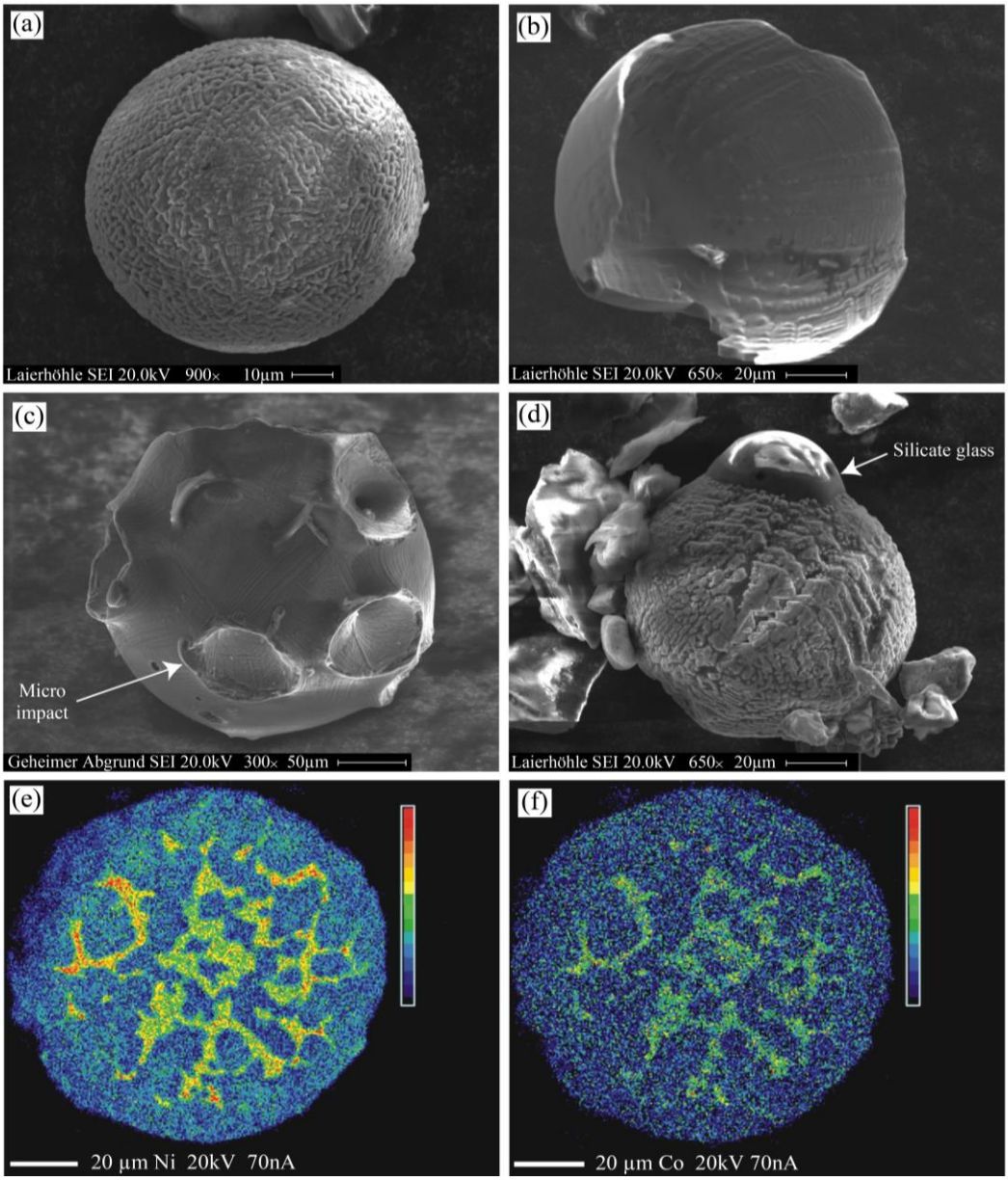

Figure 5.7: High resolution images of spherules from the cave sediments of Laierhöhle. (a to d) Raster Electron Microscope (REM) images. (a) Microcrystalline surface with spinifex texture. (b) Broken hollow spherule; the thinned out walls indicate a fragmentation already during formation. (c) Large spherule with several funnel-shape micro impacts. (d) Spinifex-spherule with silicate glass-material welded to the surface. (e and f) Electron microprobe backscattered electron images with element mapping of (e) nickel (yellow-orange: up to 7.8 weight %) and (f) cobalt (green-yellow: up to 0.6 weight %) (modified after Strasser et al., 2009b).

Finally, (i) the geometry and orientation of the straight cave section on the horizontal plane, (ii) spatial distribution of the fragmentation structures of the Ries and Steinheim impact, (iii) approximately Mid-Miocene origin of the caves (Strasser et al., 2009a) as well as (iv) presence of magnetic spherules in cave sediments (Strasser et al., 2009b), suggest the highly probable influence of the twin impact on the development of some of the Eastern Swabian Alb caves. The influence of the Ries impact-induced brittle deformation on the cave development is presumably restricted within ~45 km from the impact centre. However, in order to fully understand the actual effect of the twin impact, still much more extensive field work including systematic sampling campaigns and section orientation measurements in other caves of the Eastern Swabian Alb is required.

Chapter Six

6. Stoer impact – NW Scotland

6.1 Introduction

The geologic structures and macro-deformation features associated with most of the larger, complex impact craters are too deeply eroded to allow detailed structural analysis of their crater rims. One exception is the well preserved, complex impact structure of the Ries crater, Germany whose structure (Kenkmann and Ivanov, 2006; Sturm et al., 2015; Hossain and Kruhl, 2015) and proximal ejecta (Meyer et al., 2011; Artemieva et al., 2013; Stöffler et al., 2013) have been studied comprehensively. Amor et al. (2008, 2011) recently reported, well preserved and one of the oldest ejecta blanket deposits (1177 ± 5 Ma, Parnell et al., 2011) from the Ullapool area of NW Scotland. The name of the deposit is the Stac Fada Member (SFM) preserved within the Mesoproterozoic Stoer Group of the Torridonian Supergroup in NW Scotland (Young, 2002). It is believed that rapid burial has preserved the SFM in almost pristine condition (Amor et al., 2008). Type area of the SFM is located just NNW of Ullapool a harbour town on Loch Broom in the Ross and Cromarty district of the Highland council, about 73 km north-west of Inverness (Fig. 6.1). For decades, the anomalous origin of the SFM has been debated and unsatisfactorily credited to an isolated instance of volcanism in the region (Lawson, 1972; Young, 2002). Although Amor et al. (2008) suggested its impact origin, the crater structure is currently completely obscured, and the location of the impact centre is unknown.

Crater structure starts to develop when impact-induced shock and subsequent rarefaction waves set target material in motion and initiate a second phase of impact cratering known as the excavation stage (Melosh, 1989). The kinematics of the excavation flow results in parabolically shaped crater cavity the maximum extent of which is known as the transient crater. The end of excavation is reached at the moment when gravity forces stop the outward- and upward-directed motion of non-ejected material at the crater rim (Kenkmann and Ivanov, 2006). Important lithological products of this stage include different types of allochthonous breccias, diamictites and impact melt rocks that are mainly observed in the debris of the ejecta blanket and crater walls and floor (Kenkmann et al., 2014). This ejecta blanket around the transient crater cavity is continuous to a distance of ~2–3 times the crater radius. Near the edge of the transient cavity, the proximal ejecta blanket is either monomict or polymict lithic breccias depending on the target rock types. The polymict lithic breccias are named ‘suevite’ if melted particles are visible with naked eye and are embedded in a fine-grained clastic matrix (Stöffler and Grieve, 2007). Moreover, the microscopic planar deformation features (PDFs) as a result of shock effects in major rock-forming minerals (quartz, feldspar, and olivine) and diaplectic glasses as a result of solid-state amorphization are also observed in the ejecta deposits (Stöffler and Langenhorst, 1994; French, 1998). Based on the above features, Amor et al. (2008, 2011) suggested the SFM as impact originated ejecta blanket deposits or ‘suevite’. However, detailed macroscopic characterization of the ‘suevite’ and its emplacement in water saturated environments are yet to be described.

The position of the crater rim is indicated by the presence of shear sense indicators such as concentrically striking drag folds or asymmetric folds with inclined fold planes and top-outward vergencies related to upward and outward movement of ejecta (Roddy, 1977; Shoemaker et al., 2005). Also, due to horizontal outward movement, a notably large amount of rock material becomes injected into the walls of the crater subsurface in two forms: (i) as sub-horizontal dike breccia and/or (ii) by the emplacement of intact rock masses as interthrust wedges (Melosh, 1989). Dikes have sharp contacts with target rock, and generally consist of intensively cataclastically deformed and fluidized rock debris (Wittmann et al., 2004). On the other hand, injection of coherent blocks into the cavity walls are known

as interthrust wedges (Poelchau et al., 2009). These two forms of injections result in thickening and uplift of the transient crater rim (Melosh, 1989; Kenkmann et al., 2014). Moreover, the proximal ejecta sometimes forms an overturned flap of the coherent and intact target rock mass with inverted stratigraphy during outward movement. Nevertheless, this structure is not always present, as the crater wall collapse frequently carries it downward into the crater cavity (Melosh, 1989). In general, the presence of shear features, injections, and overturned flaps characterizes the crater rim. On top of that, target rock below the ejecta blanket locally shows zones of intense fragmentation and decimetre wide fracture branching structures, specifically at crater rim (Hossain and Kruhl, 2015). However, no such parautochthonous structural geological data associated with emplacement of proximal ejecta blanket deposits of the SFM ('suevite') have been available so far.

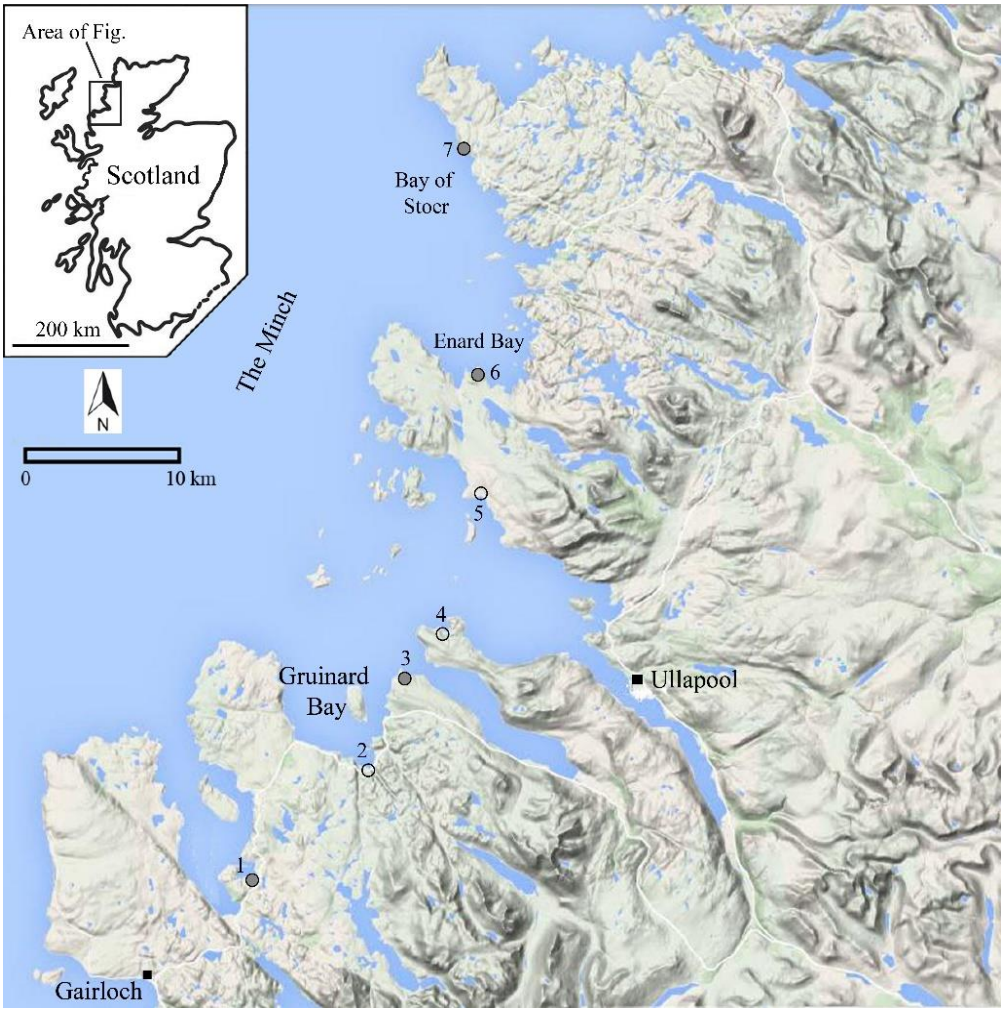

Figure 6.1: Terrain map of the Ullapool area, NW Scotland (based on Google Earth terrain image). Circle: Location of the exposed Stac Fada Member. The exposure locations are marked by numbers from south to north as 1 to 7 (1: Loch Thùrnaig, 2: Second Coast, 3: Static Point, 4: Cailleach Head, 5: Achilitibuie, 6: Enard Bay and 7: Bay of Stoer). We have studied four exposures which are marked as filled circles.

Therefore, this study focuses on the field observation of the parautochthonous structures above and below the SFM as well as macroscopic observation of the SFM itself. The SFM is reported to be exposed in seven different locations along an N–S-aligned outcrop from Gairloch in the south to Stoer in the north as a chord section (Fig. 6.1). Four of these exposures have been studied and representative samples collected. The results discussed here are based on the field observations and light microscope study of

the ‘suevite’. The study provides a primary assessment of (i) the fabric and texture of the ‘suevite’, (ii) structure related to ‘suevite’ emplacement and (iii) approximate location of the centre of the ‘Stoer impact crater’.

6.2 Geological settings of the study area

The Stac Fada Member (SFM) is emplaced within the stratified Stoer Group of the Torridonian Supergroup (Young, 2002). The Torridonian Supergroup is unconformably underlain by Archaean ‘Lewisian’ Basement Complex of predominately gneisses (Fig. 6.2a) (Young, 2002; Parnell et al., 2011). The Stoer Group represents the lowest rock package of the Torridonian Supergroup derived from the adjacent Lewisian basement (Stewart, 2002). In general, bedding of the northerly striking Stoer Group sediments dips with ~20° to the west, and is assumed to underlie the Mesozoic Minch Basin. In the type locality (Bay of Stoer area), the Group is divided into the gradually younger Clachtoll, Bay of Stoer and Meall Dearg Formations (Young, 2002). Bay of Stoer Formation comprising a sedimentary succession of mainly siliciclastic rocks, consists of basal breccias, conglomerates and sandstones, together with subordinate mudstones and limestones (Fig. 6.2b). The upper part of this formation is subdivided into two key units namely, the SFM, and the overlying Poll a’ Mhuilt Member (Stewart, 2002). The SFM occurs at the transition between the sandstone-dominated part of the Bay of Stoer Formation below and lacustrine black shales, reddish grey mudstones, and limestone of the Poll a’ Mhuilt Member above (Young, 2002; Parnell et al., 2011). The lower sandstone-dominated part comprises more than 500 m of interbedded fluviatile and alluvial sandstones, and ripple-marked lacustrine siltstones and mudstones.

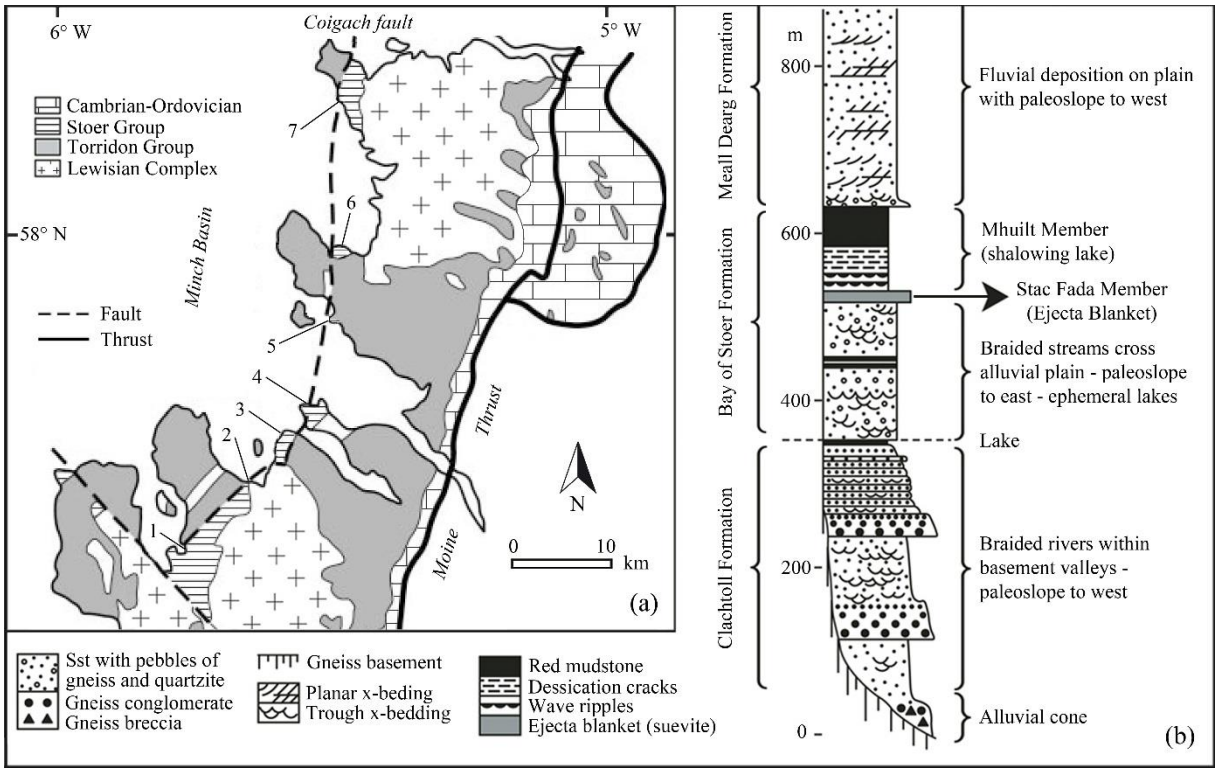

Figure 6.2: Geology and stratigraphy of the study area. (a) Simplified geological map of the study area (modified after Young, 2002, Amor et al., 2008 and Parnell et al., 2011). Outcrops of the Stac Fada Member are marked by numbers as 1 to 7 (see Fig. 6.1 for location names). The exposures are found only along the coast and their western boundary is mostly fault controlled. (b) Lithostratigraphic succession of the Stoer Group at the Bay of Stoer area (location-7) (modified after Amor et al., 2008 and Parnell et al., 2011).

The melt-bearing SFM is traceable over 55 km along ~N–S aligned outcrops starting from Gairloch in the south to Stoer in the north (Young et al., 2002; Parnell et al., 2011). The SFM is unique in the Stoer Group, being characterized by the presence of greenish altered delicate-shape glass lumps, lapilli, and degassing structures (Stewart, 2002; Young, 2002; Amor et al., 2008). Parnell et al. (2011) dated the SFM at 1177 ±5 Ma, based on $^{40}Ar/^{39}Ar$ dating of authigenic K-feldspars precipitated in degassing structures. Its origin has been debated for decades and variably interpreted as an ash flow (Lawson, 1972), a peperitic mudflow (Sanders and Johnston, 1989), a volcanic debris flow above basaltic magma (Young, 2002). All these proposed hypotheses are invoking some connection with volcanic activity in the region, except the recent suggestion of an ejecta deposit from meteorite impact (Amor et al., 2008, 2011). All these models involve emplacement of a hot melt-bearing sandy deposit onto wet sediment. The interpretation of ejecta deposits is based upon field observation, planar deformation features in quartz, and geochemical and mineralogical criteria, including an iridium anomaly, an extra-terrestrial chromium isotope signature (Amor et al., 2008).

6.3 Field observation and measurements

Macroscopic features of the SFM and associated parautochthonous target structures above and below the SFM are observed in 4 separate locations (see studied locations in Fig. 6.1). In the type locality of the Bay of Stoer (location-7), fluviatile siltstone and sandstone below the SFM, and lacustrine siltstone and sandstone above the SFM (Fig. 6.2b) show similar bedding attitude (~270/25) and thickness (~centimetres to decimetre). Decimetre-size ripples with ~206/09 orientation are observed in the lower sandstone layers. Four units of the SFM or so called ‘suevite’ (Amor et al., 2008) have been identified in this location (Fig. 6.3a). Total thickness of the ‘suevite’ is ~14 m, and the thickest unit is laying at top. Folded and heavily deformed rafts of sandstone are observed in ‘suevite’, ranging from decimetre- to decametre-scale, and showing a wide range of fold axis orientation (266/20 to 07/00) (Figs. 6.3a-c and 6.4a). Some of them have a thin ‘felsic’ contact zone with the ‘suevite’ mass. Platy aggregates of suevite clasts show weak preferential alignment around the rafts (Figs. 6.3b and 6.4a). Overturned flaps (Melosh, 1989) of sandstone beddings are observed in the upper part of the ‘suevite’ (Fig. 6.3a). The lower three units of the ‘suevite’ are injected several metres within the sandstone bedding planes of the Bay of Stoer Formation (Figs. 6.3a and 6.4b). Decimetre- to metre-scale drag folds with fold axis orientation of ~290/34 are observed above and below the contact of wedge-shaped ‘suevite’ injection (Fig. 6.4c). Immediately south of this type location, possible zones of intense fragmentation are observed in the sandstone bedding below the ‘suevite’ (Hossain and Kruhl, 2014a). These zones are oriented approximately to 175/82 and 60/82 directions.

Poorly sorted, clay to coarse sand size particles form the ground mass of the ‘suevite’ which also include millimetre- to decimetre-size lithic clasts, lumps of glassy material, and mineral clasts. Lithic clasts are mainly sandstone, gneiss, mudstone and granite, and mineral clasts are mainly quartz and feldspar (Fig. 6.4d). In general, crystalline fragments are more rounded compared to the sedimentary fragments. Few big rounded pebbles of basement rocks are observed in the upper thick unit of ‘suevite’, which were probably rounded before they embedded into the ‘suevite’ ejecta. Besides, centimetre-size approximately vertically aligned degassing structures are observed in the ‘suevite’ mainly consisting of reddish k-feldspar, calcite and millimetre-size un-oriented greenish lump of glassy material (Fig. 6.4e) (Squire and McPhie, 2002; Gernon et al., 2008). In addition, millimetre-size greenish and reddish-grey lumps of devitrified glassy material are observed in ‘suevite’ matrix (Fig. 6.4f–g). Overall, the clasts and lumps of glassy material show weak gradation. On the other hand, in some part, fine grained non-aligned crystals with slightly platy or prismatic habits are observed at the contact between sandstone

and ‘suevite’ (Fig. 6.4h). Thickness of such felsic contact zone ranging from 1 to 3 cm, probably resulted from high heat of ‘suevite’ during its emplacement.

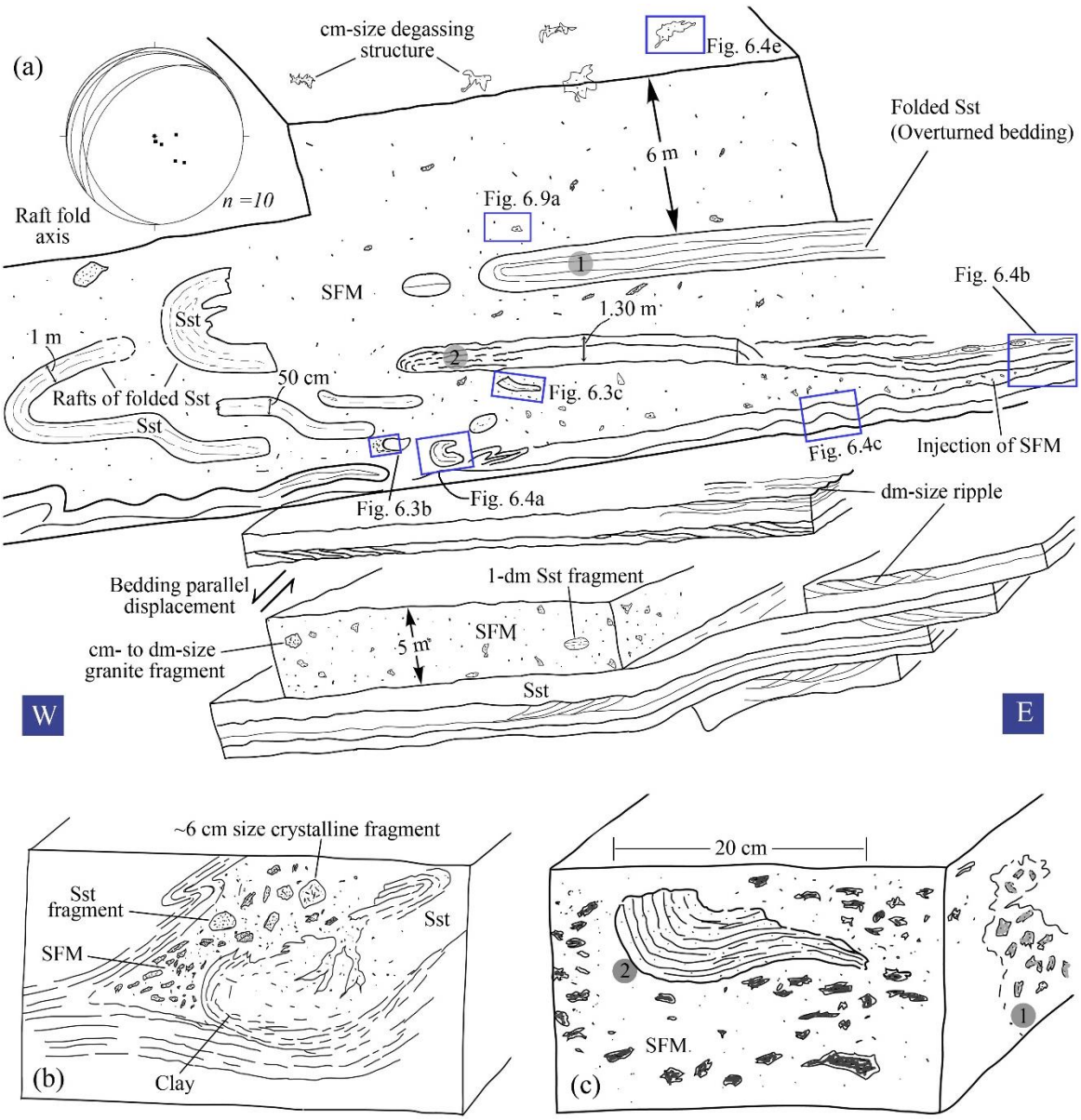

Figure 6.3: Schematic sketch illustrating the exposure details of the Stac Fada Member (SFM) at the type locality Bay of Stoer. (a) Drawing schematically illustrates important structural features related to SFM or ‘suevite’ emplacement (not to scale). Four units of ‘suevite’ are observed in which the upper three are merged in the left. Decimetre- to decametre-large rafts of sandstone have been ripped up and in some instances heavily deformed and folded. Within the ‘suevite’, lithic fragments show very weak gradation. On the right, lower three units of ‘suevite’ are injected within the bedding planes of sandstone of the Bay of Stoer Formation. Folded sandstone layers below the ‘suevite’ injection indicate lateral force and associated movement approximately from left to the right. Centimetre-size degassing structures with irregular outline are mainly observed at the top unit or upper part of the ‘suevite’. The rectangles indicate the position of Figs. 6.3(b–c), 6.4(a–c, e) and 6.9(a). 1 and 2: overturned flap. Sst: sandstone. Rose diagram (top left corner): Orientations of fold axis of the sandstone rafts are presented as great circle and pole point (equal-area projection, lower hemisphere). (b) Contact zone of sandstone raft and ‘suevite’. Within the ‘suevite’ matrix, lithic fragments, mineral clasts, and millimetre-size lumps of glassy material are observed. Sandstone is subjected to bending due to dragging effect possibly related to horizontal movement of ‘suevite’. (c) A ripped up folded sandstone raft (marked as 2) within suevite shows a fold axis oriented to ~312/37. The degassing structure is in the right side (marked as 1) (see text for details).

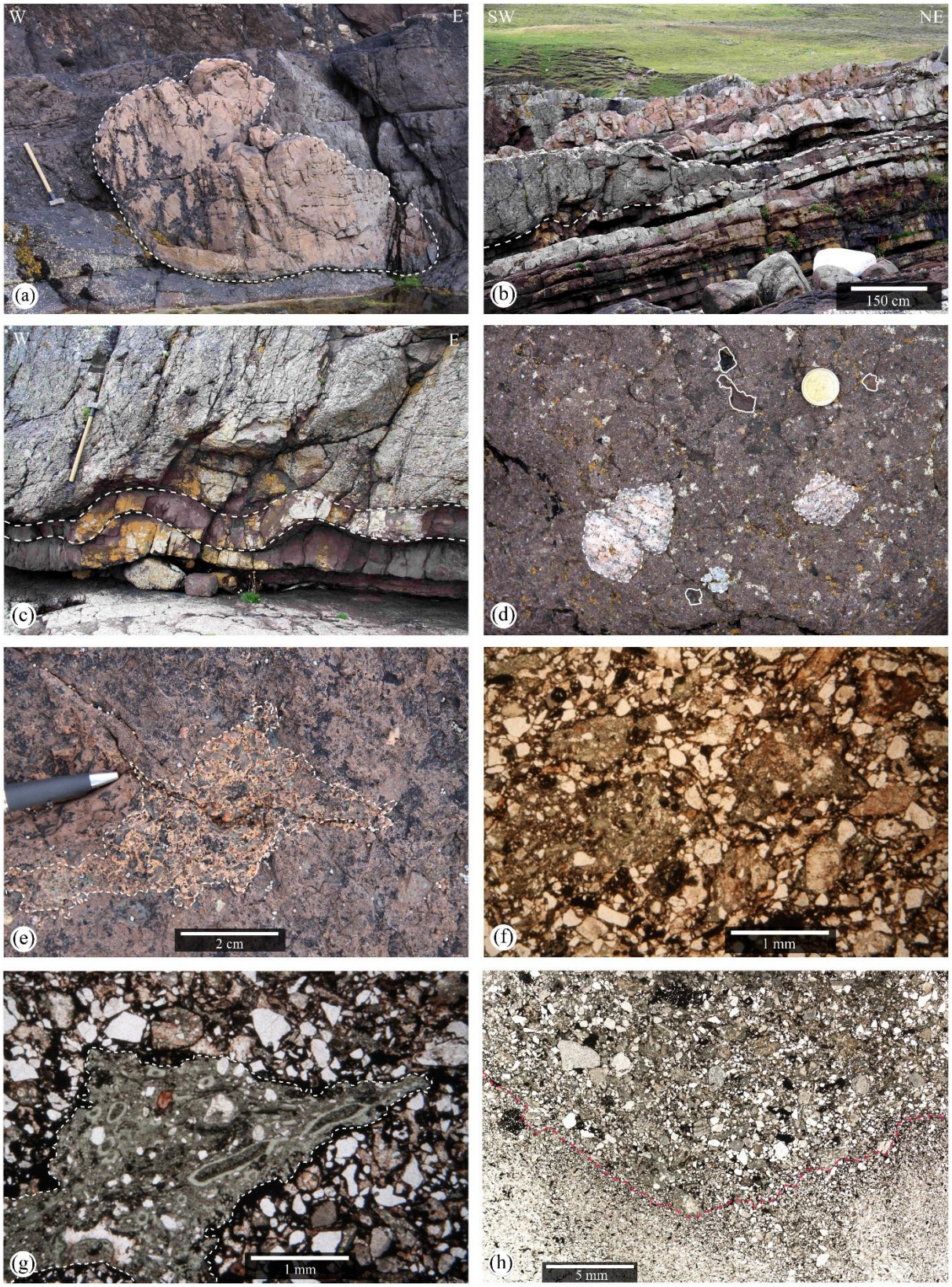

Figure 6.4: Parautochthonous structures associated with the 'suevite' emplacement, and structural as well as textural features of the 'suevite'. (a) A ripped up raft of folded sandstone embedded in 'suevite' (broken outline). Around this sandstone, lithic clasts and lumps of glassy material of the 'suevite' show preferential alignment indicating laminar low viscosity ductile flow that must have been assisted by a fluid phase. Hammer in the image is 0.60 m long. (b) The wedge-shaped 'suevite' injection (broken line) from the left to the right within the bedding

planes of Stoer Group sandstone. The sandstone beds are oriented to ~270/25. (c) Decimetre- to metre-scale asymmetric drag folds (broken line) at the contact of 'suevite' are possibly related to the 'suevite' injection. Fold axis is oriented to ~290/34. Hammer in the image is 0.60 m long. (d) Sedimentary (solid outline) and crystalline fragments (broken outline) within 'suevite' (ca. middle part). Crystalline fragments are mainly gneiss and granite, and are comparatively more rounded than the sedimentary fragments which are mostly sandstone. (e) Centimetre-size degassing structure (broken outline) in the upper part of the 'suevite'. (f) Typical suevite texture consisting of angular lithic and mineral clasts as well as lumps of greenish glass material. Mineral clasts comprised of feldspar and quartz giving an overall arkosic composition. The clasts are also embedded in glassy materials (oriented sample 5176A); microphotograph. (g) Delicate-shape greenish lump of glassy material (broken line) is embedded in quartz and feldspar rich sand matrix of the 'suevite' (oriented sample SI5176A); microphotograph. (h) Thermally altered sandstone (hornfels) at the contact with 'suevite' (broken line: sandstone at bottom and suevite at top) (oriented sample SI5176E); microphotograph.

Maximum thickness of the 'suevite' is observed at the Enard Bay area (location 6). From bottom to top, the 'suevite' unit can be divided into approximately three horizons based on gradation of the 'suevite' clasts (Fig. 6.5a). Lower part is dominated by highly disorganized centimetre- to decimetre-size angular to sub-angular lithic fragments of variegated colour (Fig. 6.5b). Most of them are feldspar-rich sandstone fragments, and only a few of them are crystalline fragments (mainly gneiss, and granite). The assemblage of such polymict lithic clasts are not observed in any other locations. Footwalls (reddish sandstone) of the 'suevite' show intense fragmentation and shearing possibly related to impact-induced shock deformation (Sturm et al., 2013; Hossain and Kruhl, 2014a). In the middle part, millimetre- to centimetre-size sub-angular to sub-rounded lithic clasts are mainly crystalline, only a few are sedimentary (Fig. 6.5c). The crystalline clasts seem to be variously deformed possibly due to impact-induced shock. Millimetre-size greenish lumps of glassy material are observed in the 'suevite' matrix. However, they do not show any preferred orientation.

Upper part of the 'suevite' is distinctly different from the lower and middle part by the presence of accretionary lapilli (Burns et al., 2003; Schulte et al., 2010). Toward the top ~2–3 m, millimetre- to centimetre-size numerous pellets of accretionary lapilli are embedded in 'suevite' matrix (Fig. 6.6a). The lapilli are mainly composed of aggregates of lithic and mineral clasts surrounded by onion skin like shells of clay-grade material (Fig. 6.6b). Some of the lapilli show hematitic coating with well-developed onion skin structure around a core. Most of them exhibit oval-shape in section view, and few of them are broken. The sub-angular to sub-rounded lithic and mineral clasts (mainly quartz and feldspar) of the core show similar composition and texture to the 'suevite' matrix (outside the lapilli). In addition, few armoured lapilli (Fisher and Schmincke, 1984) are also observed (Fig. 6.6c). They result from the accumulation of smaller solid lithic clasts that are coated in a thin layer of clay grade materials around a large solid lithic clast. On top of the lapillistone are some ~20–25 cm thick, normally graded beds of fine sediments.

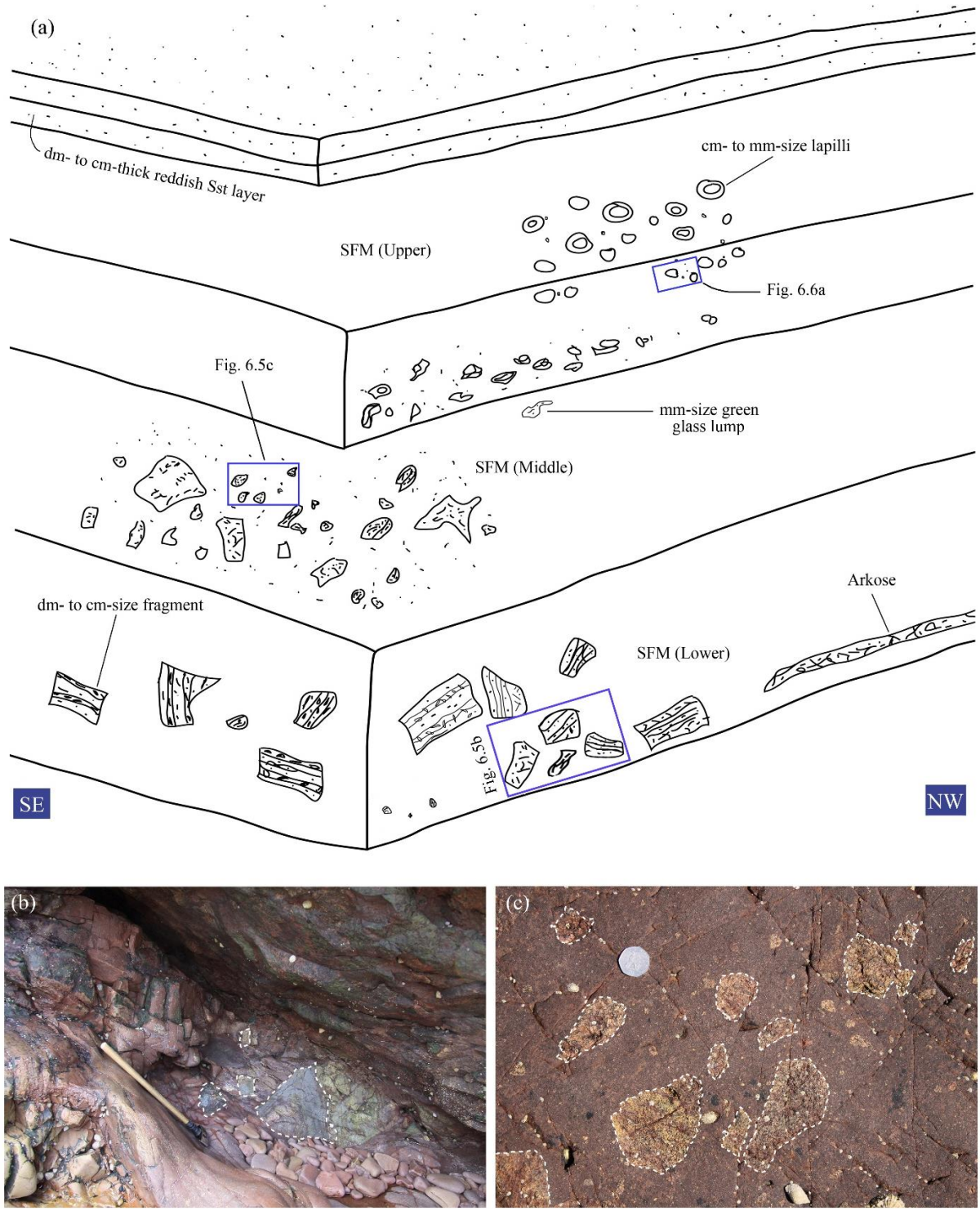

Figure 6.5: Schematic sketch and field photographs illustrating the exposure details of the 'suevite' at the Enard Bay area. (a) A simplified sketch of the 'suevite' from bottom to top shows gradation of the 'suevite' clasts. Lower part is dominated by centimetre- to decimetre-size lithic fragments. In the middle part, 'suevite' consists of millimetre- to centimetre-size sub-angular to sub-rounded lithic fragments and mineral clasts. Millimetre-size greenish lumps of glassy material are also present in this part. In the upper part of 'suevite' matrix, millimetre- to centimetre-size rounded lapilli are observed. The rectangles indicate the position of Figs. 6.5(b–c) and 6.6a. The arkose occurs as dike-like features within the basal part of the 'suevite'. (b) Highly disorganized angular to sub-angular lithic fragments of variegated colour (broken outline) at the base of the 'suevite'. Hammer in the image is 0.60 m long. (c) Sub-angular to sub-rounded crystalline lithic clasts (broken outline) in the middle part of the 'suevite'. A fifty pence coin on the image (diameter 27.3 mm) is used as scale.

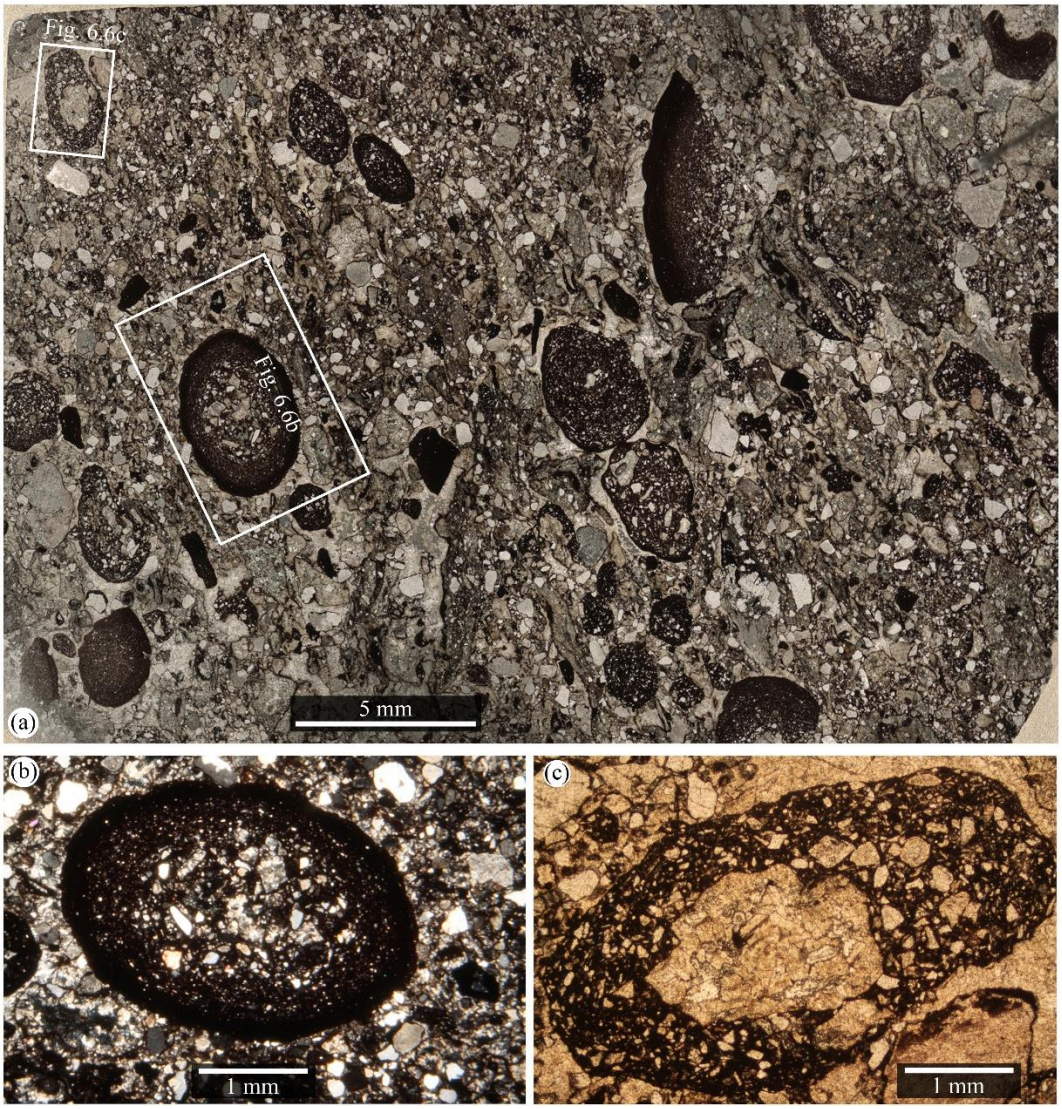

Figure 6.6: Accretionary lapilli in the upper part of the 'suevite' at the Enard Bay area (oriented sample SI5242B). (a) A polished uncovered thin section scan (cross-polarized) shows multiple pellets of accretionary lapilli embedded in lithic and mineral clasts of 'suevite' matrix. Some of the lapilli have well developed onion structure around the core, and few of them are broken. Rectangles are the position of Fig. 6.6(b–c). (b) A well-developed accretionary lapillus (Allaby, 2008) shows typical onion skin structure (mantle) around a core of lithic and mineral clasts. (c) An armored lapillus (see text for details) (Fisher and Schmincke, 1984).

Longest continuous exposure of the 'suevite' with ~N–S orientation is observed at the Static Point (location 3) having maximum thickness at the centre of ~12 m and general wanes of thickness both to the north (~8–10 m) and south (~5–6 m) (Fig. 6.7a). The top and bottom contact of the 'suevite' with the Stoer Group sediment is observed here. The bottom contact of the 'suevite' shows clear disconformity with the lower Stoer Group sandstone. The geometry of the lower contact and its disconformity nature possibly suggests a pre-impact channel (Fig. 6.7a). On top of the 'suevite', an approximately 10 cm thick fine-grained sandstone layer is observed along the contact and has the orientation of ~273/20 (Fig. 6.7b). Above this layer, an approximately 60 cm thick zone of highly deformed and folded sandstone-claystone interlayering of Stoer Group sediments is observed. General alignment of their fold axis orientation is ~298/33. Within this zone, claystone layers are comparatively thicker than the centimetre-thick sandstone layers. Sharp increase of the layer thickness and decrease of folding intensity are observed above the interlayered zone (Fig. 6.7c). In some part, sandstone layer on

top of the ‘suevite’ shows fragmentation similar to desiccation crack (Fig. 6.7d). Lithic clasts and lumps of glassy material in the fine-grained sandy matrix of the ‘suevite’ show weak gradation. Centimetre- to millimetre-size sub-angular to sub-rounded clasts with centimetre-size lumps of greenish glass material are dominant in the lower part. Long axis of the large clasts show weak preferred azimuth of ~102°. Sandstone clasts are seem to be comparatively more rounded than the other clasts. The upper part of the ‘suevite’ is slightly clay rich and the lithic clasts are also comparatively smaller than the lower part.

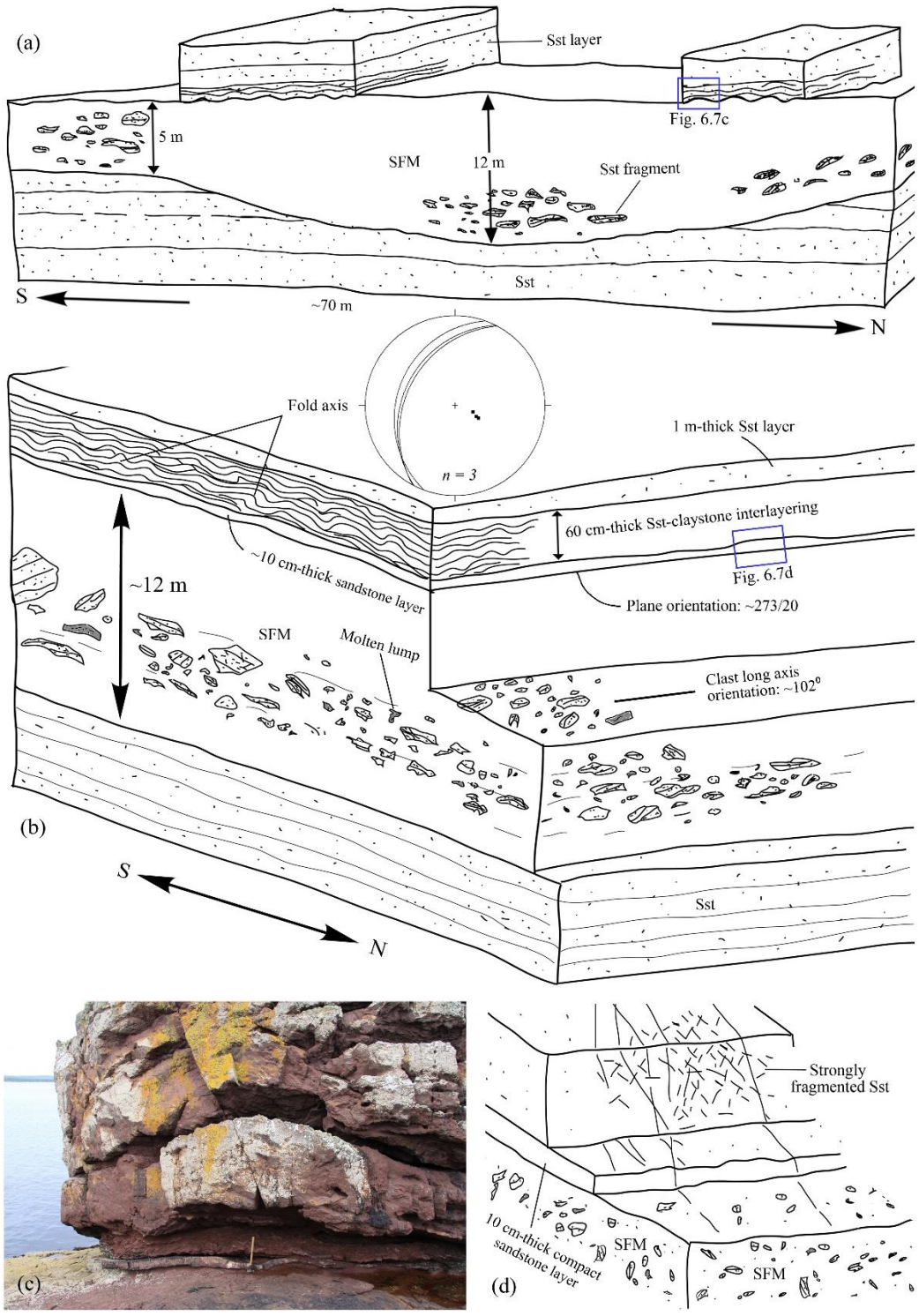

Figure 6.7: Schematic sketch and field photograph illustrating the ‘suevite’ and associated structures at the Static Point area (Longest exposure of the SFM or ‘suevite’). (a) A simplified sketch exhibits the vertical extent of the

‘suevite’ and its lateral thickness variation. The ‘suevite’ at the base shows disconformities with lower Stoer Group sandstone. Rectangles are the location for Fig. 6.7(c–d). (b) More detail sketch of the central part of the figure (a) shows weak gradation of the lithic clasts and lumps of glassy material. At the upper part, a thin compacted sandstone layer developed at the top of ‘suevite’. Above the sandstone layer, thin interlayering of sandstone-claystone is subjected to bending with preferential alignment. Rose diagram: Orientations of fold axis of the bended interlayered sandstone claystone are presented as great circle and pole point (equal-area projection, lower hemisphere). (c) Centimetre- to decimetre-scale folding of the Stoer Group sediments above the upper contact of the ‘suevite’. Intensity of the folding decreases and dimension of the fold increases from bottom to top. Hammer in the image is 0.60 m long (photograph taken by Jörn H. Kruhl). (d) Fragmented Stoer Group sandstone at the upper contact of the ‘suevite’. Fragmentation diminishes within a short distance from the contact.

The southernmost extent of the ‘suevite’ is exposed at the Loch Thùrnaig area (location 1). Although the exposure is observed on both sides of the Loch Thùrnaig, the southern part is better exposed, and therefore mainly investigated for this study. The length of the outcrop is approximately 18 m (perpendicular to the strike), and the thickness is approximately 7–8 m (Fig. 6.8). Locally coarse-grained reddish sandstone with bedding orientation of ~355/21 is observed below the ‘suevite’. In some parts, this sandstone shows zones of intense fragmentation with orientation of ~110/87, and spacing of about 2–3 m. Weak gradation is observed from bottom to top in terms of lithic clasts and matrix grain size of the ‘suevite’. Lithic clasts mainly consist of sandstone and gneiss. Lower part of the ‘suevite’ consists of decimetre-size sub-angular to sub-rounded clasts, centimetre-size lumps of greenish glass material, and sand-size matrix materials. Size and number of the lithic clasts as well as lumps of glassy material gradually decrease towards the top. A weak preferred orientation of the clasts long axis are observed towards ~290° on a plane which is oriented ~290/25. Upper part contains small amount of clasts of smaller size compared to lower part with the fine sand to clay-size matrix. However, on top of the ‘suevite’ unit, highly compacted reddish claystone layers with quartz lenses are observed. Flattened clasts and greenish lumps of former glass are embedded within the claystone.

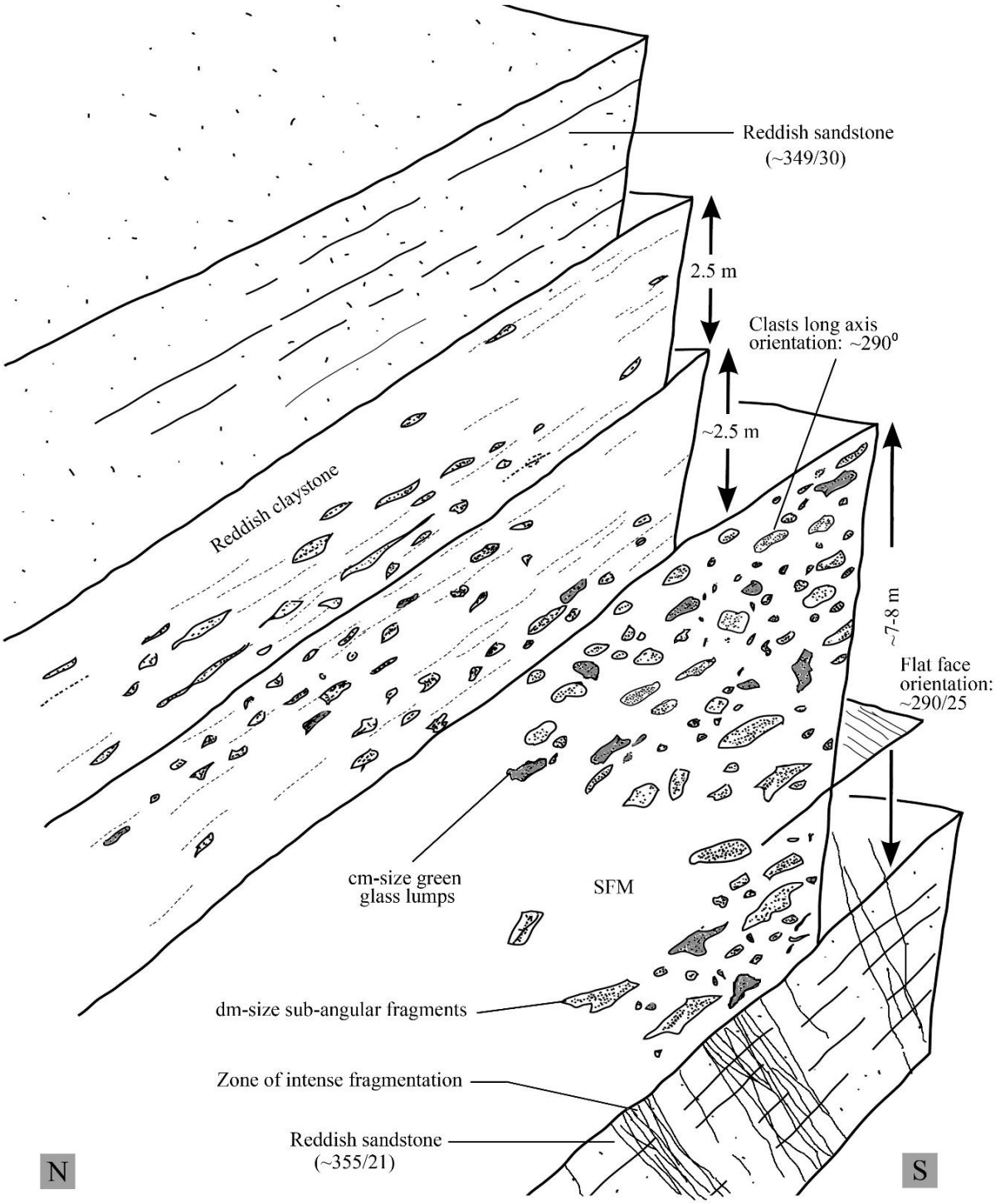

Figure 6.8: Schematic sketch illustrating the exposure of the 'suevite' at the Loch Thùrnaig (location 1). The 'suevite' from bottom to top shows weak gradation. Below the 'suevite', the reddish sandstone shows zones of intense fragmentation in a few places. Above the reddish sandstone, lower part of the 'suevite' is dominated by centimetre- to decimetre-size sub-angular to sub-rounded lithic fragments, lumps of greenish glass material, and sand-size matrix materials. Number and size of the lithic clasts as well as glass lumps gradually decrease towards the top. Lithic clasts are smaller in size at the upper part and are embedded in fine sand to clay-size matrix. At the top of the 'suevite', highly compacted reddish claystone shows similar orientation as of the lower reddish sandstone beds.

6.4 Suevite analysis – preliminary result

A thin section of the 'suevite' sample from Bay of Stoer area is scanned with 4,200 dpi resolution (Fig. 6.9a). The lithic fragments are manually digitized with 1 pixel boundary line using Photoshop CS4 and converted into binary images (Fig. 6.9b). The lower limit of the resolution is about 0.01 mm. The lithic clasts fragmentation pattern is analysed by box counting and fragment size distribution (FSD) is determined and presented as cumulative frequencies on log-log plots. The slopes of the linear point arrangements are taken as fractal dimensions (*D*) of the FSD. The computer program crack image analysis system (CIAS) (Liu et al., 2013) is used to calculate the geometric parameters and statistical analysis of the fragments in the binary image of boulders and core samples. FSD of the 'suevite' lithic clasts (Fig. 6.9b) leads to two points arrangements with clearly different regression line slopes (fractal dimensions D_1 and D_2) of 2.02 and 5.11 (Fig. 6.9c). The switch from one regression line to the other occurs at ~0.1–0.2 mm fragment diameter. Application of box counting to the fragmentation pattern of the lithic clasts from the 'suevite' sample (Fig. 6.9b) also results in two linear data points arrangement with fractal dimensions D_1 and D_2 of 1.25 and 1.83, respectively (Fig. 6.9d). The switch from one interval to the other occurs at 0.2 mm.

Analysis of the 'suevite' clasts (Fig. 6.9b) leads to two distinct box counting *D*-values (D_1 and D_2) of the fragmentation patterns and two values of FSD. The switch from D_2 to D_1 occurs at similar scales for FSD, and for box counting. The two different *D*-values of the FSD and fragmentation patterns of the lithic clasts in the 'suevite' are interpreted as resulting from two subsequent pattern-forming processes during the impact. The first one is related to shock-wave fragmentation before ejection and the second ejected lithic clasts subjected to further fragmentation processes (Kaminski and Jaupart, 1998; Burgisser and Gardner, 2006; Meyer, 2012). The later re-fragmentation of the ejected clasts through abrasion leads to a relatively higher number of small fragments (Hossain and Kruhl, 2014a) and, consequently, to two different *D*-values. The fractal dimensions of both processes are different, resulting in a shape turned fragment size distribution with a lower *D*-value in the first stage than in the second (Bashkirov and Vityazev, 1996). For fragmentation after ejection, a gas-dominated suspension is required for transport in which fragment-fragment interactions can occur. These interactions affect the fragment size of the lithic clasts from the beginning of ejection till the end of final deposition (Kaminski and Jaupart, 1998).

Modified Cantor-dust method (MCDM) using AMOCADO software (Gerik and Kruhl, 2009), and intercept method (Launeau et al., 2010) are applied to quantify the intensity of pattern anisotropy of the 'suevite' clasts (for detailed description of the methods see chapter two). Anisotropy intensity is measured based on the ratio of short (*b*) and long axis (*a*) of the fit ellipse (Fig. 6.9e–f). In intercept analysis, the direction dependence of the lithic clasts arrangements shows very weak anisotropy, with an axial ratio of 0.96 of the best-fit ellipse through the data points. This very weak anisotropy observes in the direction 84° (along *a*-axis, in Fig. 6.9e). Interestingly, AMOCADO analysis also gives the same result, i.e. very weak anisotropy (0.96). However, anisotropy direction (along *a*-axis, in Fig. 6.9f) in the MCDM method deviate 9° clock-wise (i.e. 93°) than that of the intercept. The value of the anisotropic intensity of the 'suevite' lithic clasts (Fig. 6.9e–f) is extremely low (0.96) compared to anisotropic intensity of the impact (Hossain and Kruhl, 2014a) and tectonic fracture patterns (Volland and Kruhl, 2004; Pérez-López and Paredes, 2006). Such extremely low anisotropic values indicate absence of any direction related processes.

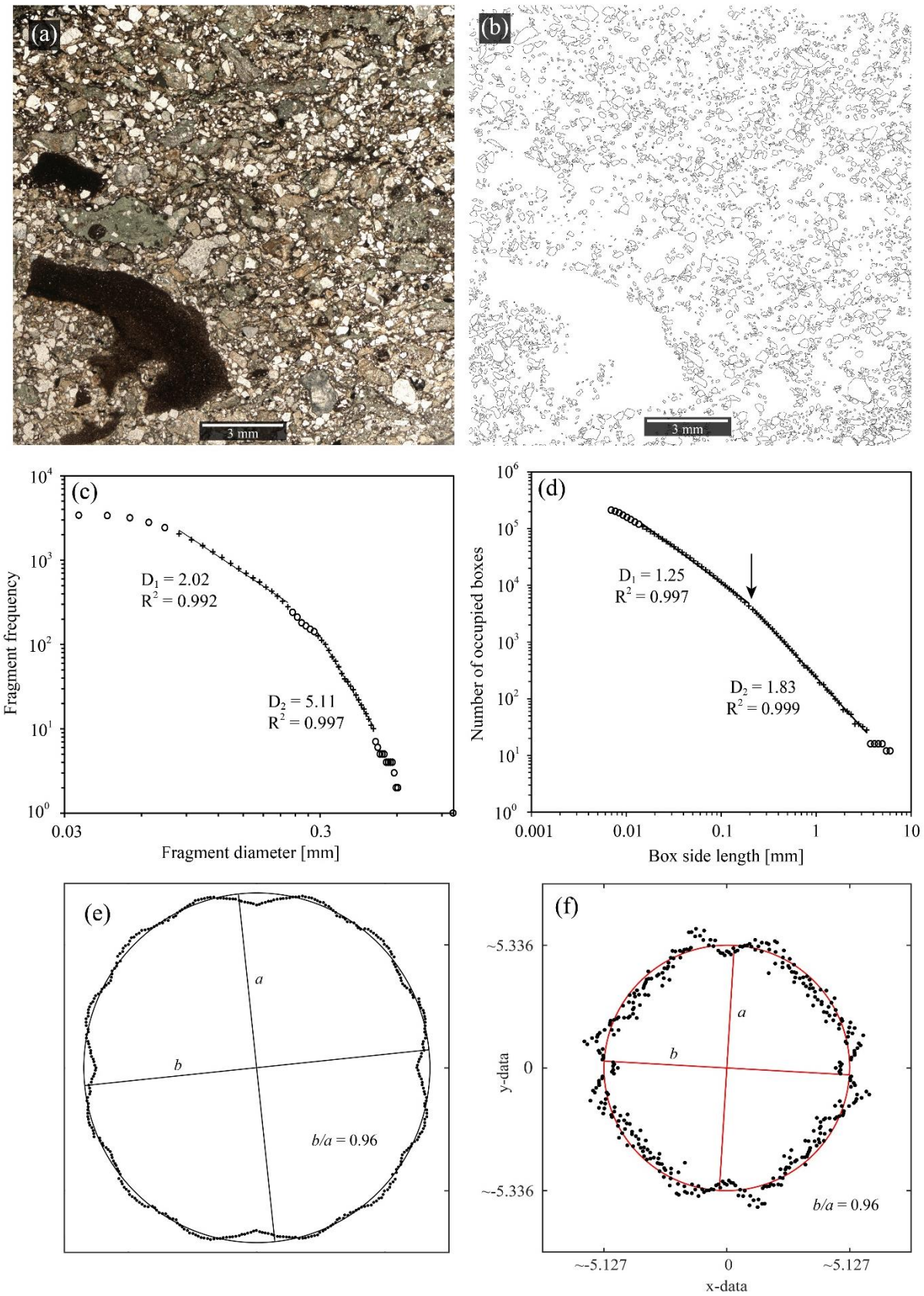

Figure 6.9: Analysis of lithic and mineral clasts within 'suevite' of the Bay of Stoer area; location shown in Fig. 6.3a (oriented sample SI5176A). (a) Plane-polarized image of clasts and matrix from a 'suevite' thin section. (b) Binary image of lithic and mineral clasts (black lines) from the 'suevite' thin section. One pixel = 0.0067 mm (6.7 µm) in the thin section. (c) Cumulative size frequency distribution of fragment diameter shown in (b). Two power-law relationships (solid lines) over less than one order of magnitude and fractal dimensions D_1 and D_2 are indicated.

Measurements with low statistics (large fragments) or with truncation effects (Blenkinsop, 1991) because of small size and low observability (open circles) are excluded from the analysis. In addition, few data points at the central part show little curvature and are therefore excluded from the analysis (switch from one linear point arrangement to the other occurred in this location). R^2: correlation coefficient. (d) Box counting applied to the outline of the lithic and mineral clasts shown in (b). The arrangement of measurement points shows two power-law relationships (solid lines) with fractal dimensions D_1 and D_2. The arrow indicates the switch from one linear point arrangement to the other. R^2: correlation coefficient. Measurements with low statistics (large boxes) or with truncation effects (Blenkinsop, 1991) because of small size and low observability (open circles) are excluded from the analysis. (e) Intensity of pattern anisotropy of the 'suevite' clasts are analysed using intercept method (Launeau et al., 2010): Very weak anisotropy (0.96) is observed in the direction 84°. (f) Intensity of pattern anisotropy of the 'suevite' clasts are analysed using modified Cantor-dust method (AMOCADO software, Gerik and Kruhl, 2009): Very weak anisotropy (0.96) is observed in the direction 93°. In both anisotropy analyses, angles are counted clock-wise from the horizontal position. For details of intercept and AMOCADO see chapter two.

6.5 Discussion and conclusions

Thickness of the Stac Fada Member (SFM) or the 'suevite' unit (Amor et al., 2008; Amor et al., 2011) is variable at different outcrop locations (Fig. 6.10). Significant lateral variation of the thickness is observed only at the Static point (Fig. 6.7a). Different thickness of the 'suevite' in different locations probably resulted from pre-impact topographic variation of the flow ground (target surface), distance from the possible 'impact centre', as well as variation of post-impact erosion in different localities. Overall, the texture of the 'suevite' is not fully homogeneous, and a weak vertical gradation is observed. The matrix is poorly sorted, ranging in grain size from clay to coarse sand, and includes angular to sub-rounded lithic and mineral clasts. However, some sub-rounded to rounded lithic clasts are also observed in the 'suevite' which are probably incorporated from the top unconsolidated sedimentary surface during viscous flow of the 'suevite' or SFM (Sanders and Johnston, 1989; Stewart; 1991; Young, 2002). Presence of millimetre- to decimetre-size lithic clasts of sandstone, mudstone, gneiss and granite, and micrometre- to millimetre-size minerals clasts of mainly quartz and feldspar indicate double or multi-layer target rocks (Meyer et al., 2011; Stöffler et al., 2013). Existence of millimetres to more than 1 centimetre-size delicate-shape greenish lumps of former glassy materials (Fig. 6.4g) as well as degassing structures (Fig. 6.4e) rule out reworking or re-deposition of the 'suevite' (Fig. 6.4f). Moreover, in places of 'suevite' injection, presence of decimetre-to millimetres-thick fine-grained hornfels zone (Bucher and Grapes, 2011) at the upper and lower contact (part of the under and over-laying lithologies, respectively) suggest hot 'suevite' mass during its emplacement (Fig. 6.4h).

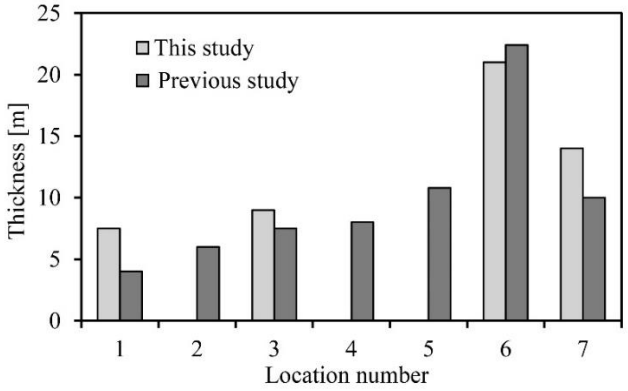

Figure 6.10: Thickness comparison of the 'suevite' in different locations. Bar diagram shows the maximum thickness at location 6 and general wanes of thickness both to north and south. During this study, data is collected from four different locations (1, 3, 6 and 7). Previous study data is taken from Amor et al., 2008. For location name see Fig. 6.1.

Besides, the presence of variously shock-deformed polymict lithic clasts, lumps of greenish glassy material, and approximately vertical orientation of degassing structures within the characteristically coarse- to fine-grained matrix suggest overall similarities with the Ries impact 'suevite' (Meyer et al., 2011; Stöffler et al., 2013). However, in the lower part of the 'suevite' at the Enard Bay, presence of highly disorganized centimetre- to decimetre-size angular to sub-angular lithic fragments of variegated colour (Fig. 6.5a–b) suggest very strong energy conditions probably related to shock fragmentation. This typical assemblage of polymict lithic clasts is more likely equivalent to the Ries 'Bunte Breccia' (Hörz et al., 1983; Sturm et al., 2013) which is generally observed below the 'suevite' (Schmidt-Kaler, 2004; Frank et al., 2005). Alternatively, viscous flowing ejecta debris has probably engulfed these pre-impact polymict clasts from the target surface during its short distance movements along a pre-impact channel. At the Static Point exposure, the geometry of the lower disconformity contact of the 'suevite' possibly suggests the presence of such pre-impact channels (Fig. 6.7a).

Evidence of ballistic flow derived ejecta and subsequent air fall components are only observed at the top 2–3 m of the 'suevite' unit at the Enard Bay area (Figs. 6.5a, 6.6a–c). This top part is characterized by the presences of lapilli (Allaby, 2008), absence of larger lithic clasts, and gradual transition from clasts rich 'suevite' to lapilli rich 'suevite'. Due to its high concentration of lapilli the uppermost part resembles a lapillistone (Morgan and Warme, 2002). Both accretionary and armoured lapilli (Fisher and Schmincke, 1984) are observed at Enard Bay. In general, the lapilli appear to be indistinguishable from pyroclastic lapilli derived from volcanic eruption plume (Gilbert and Lane, 1994). Amor et al. (2008) reported only intact lapilli and suggest water saturated plume cloud (Gilbert and Lane, 1994) for their formation. However, broken lapilli are also observed during this study which are supposed to be formed from a dry cloud and are more likely to have broken later when they come in contact with the ground (Fig. 6.6a). Johnson and Melosh (2014) model the formation of hypervelocity impact lapilli, and suggest that in well preserved ejecta curtain layers, accretionary impact lapilli, melt droplets and melt fragments should be found together. At the top part of the Enard Bay 'suevite', presence of lapilli together with melt droplets and melt fragments suggest their impact origin. Hence, the Enard Bay lapilli can be termed as accretionary impact lapilli. Such lapilli are also observed in other well established impact deposits, such as the Ries ejecta (Graup, 1981; Newsom et al., 1990; Kenkmann and Schönian, 2006), Chicxulub ejecta (Pope et al., 1999; Burns et al., 2003; Schulte et al., 2010), and Alamo impact breccia (Morgan et al., 2002; Warme et al., 2002).

Injection of the 'suevite' within the bedding planes of dominantly fluviatile sandstone (Stewart and Parker, 1979; Stewart, 2002) at the Bay of Stoer area suggest bedding parallel lateral movement approximately from the ~W or WSW (Figs. 6.3a, 6.4b). Preferential alignment of the folded and heavily deformed rafts of sandstone in 'suevite' also suggest a strong horizontal component of fluidized flow from approximately W to the E (Fig. 6.3a). In addition, deformation structures above and below the 'suevite' (Fig. 6.4c) also indicate violent emplacement of the 'suevite'. Amor et al. (2008) also suggested such strong fluidized lateral flow of the 'suevite' mass. In general, it can be reasonably argued that during impact excavation stage (Melosh, 1989), the horizontal outward movement of the impact ejecta from approximately W to the E produce the strong fluidized flow (Figs. 6.3a, 6.4b). Moreover, presence of injection dykes, and overturned flaps at the Stoer Bay area suggest not only the crater rim position of the possible impact but also the upper surface of the target rock (Melosh, 1989; Kenkmann et al., 214). On the other hand, at the Static Point, deformation structures in claystone-sandstones above the 'suevite' probably indicate contemporaneous seismic activity (Lawson, 1972; Young, 2002) as well as differential compaction which result in the ~W vergence of deformation structures (Fig. 6.7b). Besides, presence of flat purple mudstone clasts, and desiccation crack like fragmentation in the upper surface of a sandstone

bed, ~60 cm above the 'suevite', suggests exposure and desiccation of the sandstone bed (Young, 2002). Such desiccation cracks indicate a shallow water to sub-aerial post impact lake depositional setting.

Based on the structures related to strong horizontal component of fluidized flow as well as ballistic flow derived ejecta and subsequent air fall component, a reasonable proposition can be made that the 'suevite' is a double layer ejecta blanket deposit (Boyce and Mouginis-Mark, 2006; Kenkmann and Schönian, 2006; Sturm et al., 2013). The melt-clast rich lower layer is possibly emplaced by a turbulent, vapour-borne, ground flow. On the other hand, a melt-clast poor upper layer containing abundant lapilli probably indicates an air fall component. Besides, the high abundance of melt clasts, delicate-shape lumps of glassy material, and degassing structures in the 'suevite' possibly imply extensive melting which in turn indicates water saturated target rock (Amor et al., 2008; Parnell et al., 2011).

Amor et al. (2008, 2011) proposed possible 'impact centre' in the middle of the North Minch Basin between Stornoway and the Stoer Peninsula based on the injection direction and anisotropy of magnetic susceptibility (AMS) of the 'suevite'. This study complements four more additional data sets from field observation to get a further idea about the possible impact crater centre. Preferential axial plane orientation of the folded rafts and overturned flaps embedded in 'suevite', and folded sandstone beddings beneath the 'suevite' suggest strong horizontal lateral surge of impact ejecta from ~W to E. The mean orientation of the intensely fragmented zones (Hossain and Kruhl, 2014a) in sandstone beneath the 'suevite' also suggests a crater centre west of the outcrops. The chord like distribution of 'suevite' ejecta deposits and the convexity of the chord facing to the west may indicate possible crater centre location to the west (Fig. App. 6.1). Preferential alignments of the lithic clasts and lumps of glassy material towards ~290/25 (~102°) may indicate lateral flow of the 'suevite' mass towards the possible carter cavity during modification stage. These observations are in agreement with the implications of Amor et al. (2008, 2011), and hence it can be more reasonably presumed that the impact crater centre lies under the Minch Basin (Fig. 6.2), the waterway that separates the Isle of Lewis in the Outer Hebrides from the north-west Highlands of Scotland. Finally, the field observations mentioned here provide only few constrains of impact lithologies and associated deformation features. Therefore, there is need for extensive field investigation, detailed laboratory analysis of the 'suevite', geophysical study of the Minch Basin, as well as computer modelling and simulation. Results from such combined studies may provide concrete evidence of impact cratering and will help to accurately describe the possible crater structure.

6.6 Outlook

Focus of future studies to gather concrete evidence of impact cratering as well as possible crater centre location should be as follows:

Grain/fragment size analysis can be used to distinguish the different vertical elements in 'suevite' flows (Meyer, 2012). Besides, the 'suevite' deposits may be considered as a type of pyroclastic flow and therefore one might expect to find similar features and textures in both types of sediments. Therefore, it is necessary to perform similar types of analysis (Sparks, 1976) on 'suevite' deposits, mainly using grain size and shape related techniques (Launeau et al., 2010).

Detail analysis of the 'suevite' in terms of chemistry, texture, and fabric orientation and grading are important (Meyer et al., 2011; Stöffler et al., 2013). This analysis may include: (i) The frequency distribution of lithic and mineral clasts of different degrees of shock and of melt particles (Stöffler et al., 2013), (ii) The lateral as well as vertical variations in the lithic and mineral clast populations within the 'suevite', (iii) The nature and provenance of the primary components (lithic and mineral clasts, lumps of glassy material) of the 'suevite', and (iv) Lookout for evidence of reactions of the mineral clasts with

the hot melt of the ‘suevite’ pool is indicated by characteristic shapes such as ‘ballen quartz’ (Ferrière et al., 2009) and ‘checkerboard feldspar’ (Buchanan and Reimold, 2002). All this analysis will assist in understanding water saturation of the pre-impact target rock and its bathymetric depth.

It is necessary to separate the ground flow and air fall component of the ‘suevite’ through visual observation, and geochemical and geophysical methods to classify the ‘suevite’ as a double or multi-layer ejecta blanket (Sturm et al., 2013). These methods may include vertical profile measurements of anisotropy of magnetic susceptibility (Delgadillo-Peralta et al., 2015), electron spin resonance (Griscom and Beltran-Lopez, 2002) and grain size (Meyer et al., 2011; Hossain and Kruhl, 2014a). The thermal history of the ‘suevite’ components, i.e. ground flow (expected to stay warm for a relatively extended period) and air fall components (cooled rapidly during transit through the atmosphere) are also important for above classification. Moreover, study of the thin hornfels zone is also required to understand the heat condition during ‘suevite’ emplacement (Bucher and Grapes, 2011).

In addition, fractal geometry based analysis of the fragmentation (Hossain and Kruhl, 2014a) of large basement clasts within ‘suevite’ as well as basement beneath the Stoer Group sediments is important. Such quantification will allow comparison of fragmentation with other known impact-induced fragmentation (Hossain and Kruhl, 2014a). Furthermore, extensive field search of possible zones of intense fragmentation (Hossain and Kruhl, 2014a) of the Stoer Group sediments and basement rocks beneath the ‘suevite’ is very important. The orientation analysis of such zones will help us to locate the possible impact crater centre.

CHAPTER SEVEN

7. General conclusions

This PhD research yields a number of quantitative and qualitative insights into impact-induced brittle deformation structures and especially into the characteristics and spatial distribution of the fragmentation structures around an impact crater. The Ries is the only large crater where numerous quarries in and around the crater, and a research drill hole within the inner crater ring provide a unique opportunity to study impact-related complex fracture patterns, fragment size distribution (FSD), and a variety of fragmentation structures in the target sedimentary cover and lower basement rock. Closely spaced, irregular to parallel fracture networks are observed mainly inside the crater and on the crater rim. These centimetre- to decimetre-long fractures form complex patterns. Based on different fractal-geometry methods, this study quantifies the fractal behaviour of these patterns as well as the inhomogeneity and anisotropy of the patterns complexity. Quantification of these fracture patterns and FSD reveals (i) the general complexity, i.e. fractality, of these fragmentation patterns, (ii) the variation in complexity on different scales and in relation to distance from the impact centre, (iii) the inhomogeneity of the fragmentation pattern over larger areas, and (iv) the partial effect of three different but successive fragmentation processes (i.e. three stages of impact cratering: contact and compression, excavation, and modification). The absence of a narrow range of fractal dimensions for FSD of the allochthonous boulder and Ries drill core samples argues against shock-induced fragmentation being the only or dominant process during impact. The high D-value for FSD at greater depth can possibly be related to enhanced comminution due to stress localization, and may correspond to the zones of intense fragmentation.

On decimetre- to decametre-scale, a variety of fragmentation structures is observed typical of impact-induced brittle deformation: (i) Prominent fractures, (ii) zones of intense fragmentation, (iii) fracture branching, and (iv) near-surface target-rock delamination appeared as typical impact-induced brittle deformation structures. Analysis of prominent fracture orientations reveals two main sets of sub-vertical to vertical fractures. One set is tangential and the other one radial to the crater centre. Characteristics of the prominent fractures as well as their impact-related orientation show systematic changes with distance from the impact centre. Decimetre- to metre-wide zones of intense fragmentation are observed in horizontally layered upper Malm limestone as well as lower basement rock. These zones show systematic repetition of their occurrence both in horizontal direction (~3-4 m intervals) and vertical direction (~34 m intervals), and most likely result from interaction of rapidly changing impact-induced shock and rarefaction waves. Locally some of the prominent fractures form centimetre- to decimetre-scale branching structures with unimodal distribution of branching angles and unequivocally indicate the direction of the fracture opening. The near-surface delamination is apparent by variety of brittle-plastic structures in the upper layers of the target rocks (e.g., the ramp-and-flat geometries of the detachment plane, the thrust wedge, thrust and normal faulting and various types of folding). The thickness of the target-rock delamination decreases exponentially with distance from the impact centre.

All these fragmentation structures as well as the impact-related orientations of the prominent fractures are observed up to a distance of ~1.6 times the crater radius away from the impact centre. Beyond this distance, branching structures are no longer observed. On the other hand, within the distance of ~2.4-3.8 times crater radius from the impact centre, prominent fracture sets show large orientation variation with faults or fractures induced by regional tectonics and low angular deviation of their mean strike orientation with respect to the impact centre. Zones of intense fragmentation are also

absent beyond the distance of ~2.4 times crater radius. Finally, beyond a distance of ~3.8 times crater radius away from the impact centre, most of the characteristics of brittle deformation structures are absent. Behind this distance, fracture sets show high angular deviation of their mean strike orientation with respect to the impact centre and their orientations coincide with faults or fractures induced by regional tectonics. All these characteristics and the spatial distribution of fragmentation structures are probably related to weakening of impact-induced shock and subsequent rarefaction waves with distance from the impact centre. The gradual weakening of the wave energy resulted in two possible scenarios beyond ~47 km distance: (i) The wave energy was already low and, therefore, could not deform the target rock any further. (ii) Prominent fracture sets could not develop in their proper orientation, but their orientation was instead largely controlled by the pre-existing regional tectonic structure. In general, it is reasonably argued that impact-induced dynamic fragmentation structures are different from that of quasi-static tectonic deformation.

Observation as well as analysis based on the, (i) the geometry and orientation of the straight cave section in horizontal plane, (ii) spatial distribution of the fragmentation structures of the Ries and Steinheim impact, (iii) approximately Mid-Miocene origin of the caves as well as (iv) presence of magnetic spherules in cave sediments suggest an influence of the the Ries and Steinheim impact (twin impact) in the development of some of the Eastern Swabian Alb caves. The lateral extent of the Ries impact influence on the cave development is presumably restricted within ~45 km from the impact centre. Nevertheless, in order to fully understand the actual effect of the twin impact, still much more extensive field work including systematic sampling campaigns and section orientation measurements in other caves of the Eastern Swabian Alb is required.

Field observation of the Stac Fada Member (SFM ‘suevite’) – one of the oldest ejecta blanket deposits from the Ullapool area of NW Scotland provide insights into the mechanisms of the ‘suevite’ emplacement as well as the possible location of the ‘buried or obscured’ impact centre. On the basis of the structures related to a strong horizontal component of fluidized flow as well as ballistic flow derived ejecta and subsequent air fall components, a reasonable proposition is made that the SFM or ‘suevite’ is a double layer ejecta blanket. The melt-clast rich lower layer is possibly emplaced by a turbulent, vapour-borne, ground flow, whereas a melt-clast poor upper layer containing abundant lapilli probably indicates an air fall component. Moreover, the high abundance of melt clasts, delicate shape lumps of glassy material, and degassing structures in the ‘suevite’ possibly implies extensive melting which in turn indicates water saturated target rock. Furthermore, (i) preferential orientation of the structures related to ‘suevite’ emplacement, (ii) alignment of the ‘suevite’ internal textures, and (iii) the orientation of the intensely fragmented zones of the target sandstone beneath the ‘suevite’, suggest the Minch Basin (west of Ullapool) as the possible impact centre. This observation is in agreement with the implications of previous studies. However, the field observations mentioned here provide only a primary assessment. Hence, there is need for extensive field study, detailed laboratory analysis of the ‘suevite’, geophysical study of the Minch Basin, as well as computer modelling and simulation. Results from such combined studies may provide concrete evidence of impact cratering and will help to accurately describe the possible crater structure.

The overall results, from this PhD research, will provide reasonable guidelines of general validity for typical characteristics of impact-induced brittle deformation structures and their quantification. Some of the findings seemingly conflict with certain published results, as detailed in the text. It is these areas of discrepancy and incomplete understanding where future work must be concentrated. We are thoroughly convinced that a combination of theory, field studies, laboratory experiments, and numerical simulation is necessary to fully understand impact-induced brittle deformation around an impact crater structure.

References

Ackermann, R.V., Schlische, R.W., and Withjack, M.O., 2001. The geometric and statistical evolution of normal fault systems: an experimental study of the effects of mechanical layer thickness on scaling laws. Journal of Structural Geology, 23(11), 1803–1819.

Adam, K.D., Binder, H., Bleich, K.-E., and Dobat, K., 1968. Die Charlottenhöhle bei Hürben Abhandlungen zur Karst- und Höhlenkunde. Reihe A, Heft 3, 1. –3. Aufl. München.

Ahrens, T.J., and O'Keefe, J.D., 1987. Impact on the earth, ocean, and atmosphere. International Journal of Impact Engineering, 5(1–4), 13–32.

Ahrens, T.J., and O'Keefe, J.D., 1972. Shock melting and vaporization of lunar rocks and minerals. The Moon, 4(1–2), 214–249.

Ahrens, T.J., and Rubin, A.M., 1993. Impact-induced tensional failure in rock. Journal of Geophysical Research: Planets, 98(E1), 1185–1203.

Ai, H.-A., and Ahrens, T.J., 2004. Dynamic tensile strength of terrestrial rocks and application to impact cratering. Meteoritics & Planetary Science, 39(2), 233–246.

Allaby, M. (ed.), 2008. A Dictionary of Earth Sciences. Oxford University Press, 3rd edition, p. 654.

Allen, B.A., Drellack, S.L.Jr., and Townsend, M.J., 1997. Surface effects of underground nuclear explosions. Geotechnical Services Bechtel Nevada and U.S. Department of Energy Nevada, DE-AC08-96NV11718-122, p. 160.

Alvarez, L.W., Alvarez, W., Asaro, F., and Michel, H.V., 1980. Extraterrestrial Cause for the Cretaceous–Tertiary Extinction. Science, 208(4448), 1095–1108.

Ames, D.E., and Farrow, C.E.G., 2007. Metallogeny of the Sudbury mining camp, Ontario. In: Goodfellow, W.D. (ed.), Mineral Deposits of Canada: A Synthesis of Major Deposit-Types, District Metallogeny, the Evolution of Geologic Provinces, and Exploration Methods. Geological Association of Canada, Mineral Deposits Division, Special Publication 5, pp. 329–350.

Amor, K., Hesselbo, S.P., Porcelli, D., Thackrey, S., and Parnell, J., 2008. A Precambrian proximal ejecta blanket from Scotland. Geology, 36(4), 303–306.

Amor, K., Taylor, J., Hesselbo, S.P., and MacNiocaill, C., 2011. An Anisotropy of Magnetic Susceptibility Study of the Stac Fada Member Suevite: Constraints on the Impact Crater Location. 74th Annual Meeting of the Meteoritical Society, London, UK, id. 5089.

An, L.-J., and Sammis, C., 1994. Particle size distribution of cataclastic fault materials from southern California: A 3-D study. Pure and Applied Geophysics, 143(1–3), 203–227.

Anderson, J.L.B., Schultz, P.H., and Heineck, J.T., 2003. Asymmetry of ejecta flow during oblique impacts using three-dimensional particle image velocimetry. Journal of Geophysical Research, 108(E8), 13–21.

Artemieva, N.A., and Pierazzo, E., 2011. The Canyon Diablo impact event: 2. Projectile fate and target melting upon impact. Meteoritics & Planetary Science, 46(6), 805–829.

Artemieva, N.A., Wünnemann, K., Krien, F., Reimold, W.U., and Stöffler, D., 2013. Ries crater and suevite revisited - Observations and modeling, Part II: Modeling. Meteoritics & Planetary Science, 48(4), 590–627.

Ayunova, O.D., Kalush, Yu.A., and Loginov, V.M., 2007. Relationship of the seismic activity of the Tuvinian and adjacent Mongolian areas with the fractal dimensionality of a fault system. Russian Geology and Geophysics, 48(7), 593–597.

Bäckström, A., 2005. A study of impact fracturing and electric resistivity related to the Lockne impact structure, Sweden. In: Koeberl, C., and Henkel, H. (eds.), Impact Tectonics. Springer-Verlag, Berlin Heidelbrg, pp. 389–404.

Balsamo, F., and Storti, F., 2011. Size-dependent comminution, tectonic mixing, and sealing behavior of a “structurally oversimplified” fault zone in poorly lithified sands: Evidence for a coseismic rupture? Geological Society of America Bulletin, 123(3–4), 601–619.

Baratoux, D., and Melosh, H.J., 2003. The formation of shatter cones by shock wave interference during impacting. Earth and Planetary Science Letters, 216(1–2), 43–54.

Barlow, N.G., 2004. Martian subsurface volatile concentrations as a function of time: Clues from layered ejecta craters. Geophysical Research Letters, 31(5), L05703, doi:10.1029/2003GL019075.

Barosh, P.J., 1968. Relationships of explosion-produced fracture patterns to geologic structure in Yucca Flat, Nevada test site. In: Eckel, E.B. (ed.), Nevada Test Site. Geological Society of America Memoirs, 110, 199–218.

Bashkirov, A.G., and Vityazev, A.V., 1996. Statistical mechanics of fragmentation processes of ice and rock bodies. Planetary and Space Science, 44(9), 909–915.

Bayer, H.-J., and Groschope, P., 1993. Karstwannen auf der Ostalb: Karstlandschaft Schwäbische Ostalb. Karst und Höhle, Verband der deutschen Höhlen- und Karstforscher e.V., München, pp. 295–304.

Berger, K., Haunschild, H., Schmidt-Kaler, H., Wagner, G.H., Hüttner, R., and Zitzmann, A., 1977. Geologische Übersichtskarte 1:200 000 (CC 7126 Nürnberg). Herausgegeben von der Bundesanstalt für Geowissenschaften und Rohstoffe in Zusammenarbeit mit den Geologischen Landesämtern der Bundesrepublik Deutschland, Hannover.

Biegel, R., Sammis, C., and Dietrich, J., 1989. The frictional properties of a simulated gouge having a fractal particle distribution. Journal of Structural Geology, 11(7), 827–846.

Bischoff, L., and Oskierski, W., 1988. The surface structure of the Haughton impact crater, Devon Island, Canada. Meteoritics, 23, 209–220.

Billi, A., and Storti, F., 2004. Fractal distribution of particle size in carbonate cataclastic rocks from the core of a regional strike-slip fault zone. Tectonophysics, 384(1–4), 115–128.

Binder, H., Lutz, A., and Lutz, H.M., 1993. Schauhöhlen in Deutschland. Aegis Verlag, Ulm, ISBN 3-87005-040-3, p. 82.

Blenkinsop, T.G., 1991. Cataclasis and processes of particle size reduction. Pure and Applied Geophysics, 136(1), 59–86.

Bour, O., and Davy, P., 1997. Connectivity of random fault networks following a power law fault length distribution. Water Resources Research, 33(7), 1567–1583.

Boyce, J.M., and Mouginis-Mark, P.J., 2006. Martian craters viewed by the Thermal Emission Imaging System instrument: Double-layered ejecta craters. Journal of Geophysical Research, 111(E10), doi:10.1029/2005JE002638.

Bracewell, R.N., 2000. The Fourier transform and its applications. McGraw Hill, 3rd edition, Boston, USA, p. 616.

Brandt, D., and Reimold, W.U., 1995. The geology of the Pretoria Saltpan impact structure and the surrounding area. South African Journal of Geology, 98(3), 287–303.

Brandt, D., Reimold, W.U., Franzsen, A.J., Koeberl, C., and Wendorff, L., 1998. Geophysical profile of the Roter Kamm impact crater, Namibia. Meteoritics & Planetary Science, 33(3), 447–453.

Buchanan, P.C., and Reimold, W.U., 2002. Planar deformation features and impact glass in inclusions from the Vredefort Granophyre, South Africa. Meteoritics & Planetary Science, 37(6), 807–822.

Bucher, K., and Grapes, R., 2011. Definition, Conditions and Types of Metamorphism. Petrogenesis of Metamorphic Rocks, Springer Berlin Heidelberg, pp. 3–19.

Buchner, E., and Schmieder, M., 2013. Der Steinheimer Suevit – schmelzeführende Impaktite aus dem Steinheimer Becken, Südwestdeutschland. German Journal of Geology, 164(3), 471–490.

Buchner, E., Seyfried, H., and van den Bogaard, P., 2003. $^{40}Ar/^{39}Ar$ laser probe age determination confirms the Ries impact crater as source of glass particles in Graupensand sediments (Grimmelfingen formation, North Alpine Foreland Basin). International Journal of Earth Sciences, 92(1), 1–6.

Buhl, E., 2013. Brittle deformation of porous sandstone in hypervelocity impact experiments. PhD Thesis, Mathematisch-Naturwissenschaftlichen Fakultät, der Universität Potsdam, Potsdam, p. 136.

Buhl, E., Kowitz, A., Elbeshausen, D., Sommer, F., Dresen, G., Poelchau, M.H., Reimold, W.U., Schmitt, R.T., and Kenkmann, T., 2013. Particle size distribution and strain rate attenuation in hypervelocity impact and shock recovery experiments. Journal of Structural Geology, 56, 20–33.

Burgisser, A., and Gardner, J.E., 2006. Using hydraulic equivalences to discriminate transport processes of volcanic flows. Geology, 34(3), 157–160.

Burns, E., Sigurdsson, H., Carey, S., and Hondt, S.D., 2003. Geochemistry of accretionary lapilli from a Cretaceous-Tertiary impact breccia, Guayal, Mexico. Large Meteorite Impacts (2003), Nördlingen, Germany, id. 4113.

Camacho, G.T., and Ortiz, M., 1996. Computational modelling of impact damage in brittle materials. International Journal of Solids and Structures, 33(20–22), 2899–2938.

Cashman, K.V., and Mangan, M.T., 1994. Physical aspects of magma degassing; II, Constraints on vesiculation processes from textural studies of eruptive products. In: Carroll, M.R., and Holloway, J.R. (eds.), Volatiles in Magmas, Reviews in Mineralogy, Mineralogical Society of America, 30(1), 447–478.

Castaing, C., Halawani, M.A., Gervais, F., Chilès, J.P., Genter, A., Bourgine, B., Ouillon, G., Brosse, J.M., Martin, P., Genna, A., and Janjou, D., 1996. Scaling relationships in intraplate fracture systems related to Red Sea rifting. Tectonophysics, 261(4), 291–314.

Cello, G., 1997. Fractal analysis of a Quaternary fault array in the central Apennines, Italy. Journal of Structural Geology, 19(7), 945–953.

Chao, E.C.T., and Minkin, J.A., 1977. Impact cratering phenomenon tor the Ries multiring structure based on constraints of geological, geophysical and petrological studies and the nature of the impacting body. In: Roddy, D.J., Pepin, R.O., and Merrill, R.B. (eds.), Impact and Explosion Cratering: Planetary and terrestrial implications. Pergamon Press, New York, pp. 405–424.

Chao, E.C.T., Schmidt-Kaler, H., and Hüttner, R., 1978. Principal exposures of the Ries meteorite crater in southern Germany. Description, photographic documentation and interpretation. Bayerisches Geologisches Landesamt, München, p. 84.

Chao, S.H., and Kaneko, K., 2004. Rock Fragmentation Control in Blasting. Materials Transactions, 45(5), 1722–1730.

Chester, J., Chester, F., and Kronenberg, A., 2005. Fracture surface energy of the Punchbowl fault, San Andreas system. Nature, 437, 133–136.

Cleveland, W.S., 1981. LOWESS: A program for smoothing scatterplots by robust locally weighted regression. The American Statistician, 35(1), p. 54.

Collins, G.S., Melosh, H.J., and Ivanov, B.A., 2004. Modeling damage and deformation in impact simulations. Meteoritics & Planetary Science, 39(2), 217–231.

Collins, G.S., Melosh, H.J., and Marcus, R.A., 2005. Earth impact effects Program: a web-based computer program for calculating the regional environmental consequences of a meteoroid impact on Earth. Meteoritics & Planetary Science, 40(6), 817–840.

Colombetti, A., Ferrari, G., Nicolodi, F., and Panini, F., 1998. Some metallic spherulen in calcareous-marly sediments of the Romanoro Flysch, Sestola-Vidiciatico tectonic units (Modena district, Northern Apennines, Italy). Planetary and Space Science, 46(2), 329–340.

Connors, M., Hildebrand, A.R., Pilkington, M., Ortiz-Aleman, C., Chavez, R.E., Urrutia-Fucugauchi, J., Graniel-Castro, E., Camara-Zi, A., Vasquez, J., and Halpenny, J.F., 1996. Yucatán karst features and the size of Chicxulub crater. Geophysical Journal International, 127(3), F11–F14.

Croft, S.K., 1981. The modification stage of basin formation: Conditions of ring formation. In: Schultz, P.H., and Merrill, R.B. (eds.), Multi-Ring Basins: Formation and evolution, Proceeding of Lunar and Planetary science, Pergamon press, 12A, pp. 227–257.

Delgadillo-Peralta, M., Urrutia-Fucugauchi, J., Pérez-Cruz, L., and Velasco-Villarreal, M., 2015. Rock magnetic and AMS fabrics characterization of suevitic breccias from the Cretaceous-Paleogene Chicxulub impact crater. Revista Mexicana Ciencias Geológicas, 32(1), 145–155.

Dietz, R.S., 1947. Meteorite impact suggested by the orientation of shatter-cones at the Kentland, Indiana disturbance. Science, 105(2715), 42–43.

Dietz, R.S., 1960. Meteorite impact suggested by shatter cones in rock. Science, 131(3416), 1781–1784.

Dongus, H., 1977. Die Oberflächenformen der Schwäbischen Alb und ihres Vorlandes. Marburger geographische Schriften, 72. Selbstverlag des Geographischen Institutes der Universität Marburg, Marburg/Lahn, p. 487.

Dongus, H., 2000. Die Oberflächenformen Südwestdeutschlands. Gebrüder Borntraeger, Berlin, Stuttgart, p. 189.

Donofrio, R.R., 1998. North American impact structures hold giant field potential. Oil and Gas Journal, 96, 69–83.

Dyer, H., Amitrano, D., and Boullier, A.-M., 2012. Scaling properties of fault rocks. Journal of Structural Geology, 45, 125–136.

Elbeshausen, D., Wünnemann, K., and Collins, G.S., 2009. Scaling of oblique impacts in frictional targets: implications for crater size and formation mechanisms. Icarus, 204(2), 716–731.

Ernstson, V.K., and Pohl, J., 1974. Einige Kommentare zu den bohrlochgeophysikalischen messungen in der Forschungsbohrung Nördlingen 1973. Geologica Bavarica, 72, 81–90.

Faulkner, D., Lewis, A., and Rutter, E., 2003. On the internal structure and mechanics of large strike-slip fault zones: field observations of the Carboneras fault in southeastern Spain. Tectonophysics, 367(3–4), 235–251.

Feng, Z.C., Zhao, Y.S., and Zhao, D., 2009. Investigating the scale effects in strength of fractured rock mass. Chaos, Solitons & Fractals, 41(5), 2377–2386.

Ferrière, L., Koeberl, C., and Reimold, W.U., 2009. Characterisation of ballen quartz and cristobalite in impact breccias: new observations and constraints on ballen formation. European Journal of Mineralog, 21(1), 203–217.

Fisher, R.V., and Schmincke, H.-U., 1984. Pyroclastic Rocks. Springer-Verlag, p. 472.

Fondriest, M., Smith, S.A.F., Di Toro, G., Zampieri, D., and Mittempergher, S., 2012. Fault zone structure and seismic slip localization in dolostones, an example from the Southern Alps, Italy. Journal of Structural Geology, 45, 52–67.

Ford, A., and Blenkinsop, T.G., 2008. Combining fractal analysis of mineral deposit clustering with weights of evidence to evaluate patterns of mineralization: application to copper deposits of the Mount Isa Inlier, NW Queensland, Australia. Ore Geology Reviews, 33(3–4), 435–450.

Frank, H., Märtel, A., and Reichel, R., 2005. Geologische Karte Des Rieses 1:50,000, back cover. Bayersiches Geologisches Landessamt, Bavaria.

Freed, A.M., Melosh, H.J., and Solomon, S.C., 2001. Tectonics of mascon loading: resolution of the strike-slip faulting paradox. Journal of Geophysical Research, 106(E9), 20603–20620.

French, B.M., 1972. Shock-metamorphic features in the Sudbury structure, Ontario: A review. In:

Guy-Bray, J.V. (ed.), New developments in Sudbury Geology. Geological Association of Canada, Special paper 10, 19–28.

French B.M., 1998. Traces of Catastrophe: A Handbook of Shock-Metamorphic Effects in Terrestrial Meteorite Impact Structures. LPI Contribution No. 954, Lunar and Planetary Institute, Houston, TX., Contribution CB-954, p. 120.

French, B.M., and Koeberl, C., 2010. The convincing identification of terrestrial meteorite impact structures: what works, what doesn't, and why. Earth-Science Reviews, 98(1–2), 123–170.

French, B.M., and Short, N.M. (eds.), 1968. Shock Metamorphism of Natural Materials. Baltimore, Mono Book Corp., p. 644.

Frigo, M., and Johnson, S.G., 1998. FFTW: An Adaptive Software Architecture for the FFT. Proceedings of the International Conference on Acoustics, Speech, and Signal Processing, 3, 1381–1384.

Fujiwara, A., Kamimoto, G., and Tsukamoto, A., 1977. Destruction of basaltic bodies by high-velocity impact. Icarus, 31(2), 277–288.

Fulmer, C.V., and Roberts, W.A., 1963. Rock induration and crater shape. Icarus, 2, 452–465.

Gault, D.E., Quaide, W.L., and Oberbeck, V.R., 1968. Impact cratering mechanics and structures. In: French, B.M., and Short, N.M. (eds.), Shock Metamorphism in Natural Materials. Mono Book Corp., Baltimore, pp. 87–99.

Gerik, A., and Kruhl, J.H., 2009. Towards automated pattern quantification: time efficient assessment of anisotropy of 2D pattern with AMOCADO. Computers & Geosciences, 35(6), 1087–1097.

Gernon, T.M., Sparks, R.S.J., and Field, M., 2008. Degassing structures in volcaniclastic kimberlite: Examples from southern African kimberlite pipes. Journal of Volcanology and Geothermal Research, 174(1–3), 186–194.

Gilbert, G.K., 1893. The Moon's face; A study of the origin of its features. Philosophical Society of Washington, 12, 241–292.

Gilbert, J.S., and Lane, S.J., 1994. The origin of accretionary lapilli. Bulletin of Volcanology, 56(5), 398–411.

Graham, G.A., Kearsley, A.T., Drolshagen, G., McDonnell, J.A.M., Wright, I.P., and Grady, M.M., 2004. Mineralogy and microanalysis in the determination of cause of impact damage to spacecraft surfaces. In: Pye, K., and Kroft, D.J. (eds.), Forensic Geoscience: Principles, Techniques and Applications. Geological Society, London, Special Publications, 232, 137–146.

Grasso, D.N., 2001. GIS surface effects archive of underground nuclear detonations conducted at Yucca Flat and Pahute Mesa, Nevada test site, Nevada. U.S. Department of the Interior and U.S. Geological survey, Open-File Report 01-272, p. 34.

Graup, G., 1977. Die Petrographie der kristallinen Gesteine der Forschungsbohrung Nördlingen 1973. Geologica Bavarica, 75, 219–229.

Graup, G., 1981. Terrestrial chondrules, glass spherules and accretionary lapilli from the suevite, Ries crater. Earth and Planetary Science Letters, 55(3), 407–418.

Grieve, R.A.F., 1987. Terrestrial impact structures. Annual Review of Earth and Planetary Sciences, 15, 245–270.

Grieve, R.A.F., 2005. Economic natural resource deposit at terrestrial impact structures. In: McDonald, I., Boyce, A.I., Butler, I.B. et al. (eds.), Mineral Deposits and Earth Evolution, Geological Society, London, Special Publications, 248, 1–29.

Grieve, R.A.F., Dence, M.R., and Robertson, P.B., 1977. Cratering processes: as interpreted from the occurrence of impact melts. In: Roddy, J., Pepin, R.O., and Merill, R.B. (eds.), Impact and Explosion Cratering. Pergamon Press, New York, pp. 791–814.

Grieve, R.A.F., Langenhorst, F., and Stöffler, D., 1996. Shock metamorphism of quartz in nature and experiment: II. Significance in geoscience. Meteoritics & Planetary Science, 31(1), 6–35.

Grieve, R.A.F., Robertson, P.B., and Dence, M.R., 1981. Constraints on the formation of ring impact structures, based on terrestrial data. In: Schultz, P.H., and Merrill, R.B. (eds.), Multi-Ring Basins: Formation and Evolution. Proceeding of the Lunar Planetary Science Conference, Pergamon, New York, 12A, pp. 37–57.

Griffith, A.A., 1920. Phenomena of rupture and flow in solids. Philosophical Transaction Royal Society London, 221A, 163–198.

Griscom, D.L., and Beltran-Lopez, V., 2002. ESR spectra of limestones from the cretaceous-tertiary boundary: Traces of a catastrophe. Adv. ESR Appli., 18, 57–64.

Gudden, H., 1974. Die Forschungsbohrung Nördlingen 1973 - Durchführung und erste Befunde. Geologica Bavarica, 72, 11–31.

Gurov, E.P., and Gurova, E.P., 1982. Some regularities of the areal spreading of fractures around Elgygytgyn impact crater. Lunar and Planetary Science XIII. Lunar and Planetary Institute, Houston, pp. 291–292.

Gurov, E.P., Koeberl, C., and Yamnichenko, A., 2007. El'gygytgyn impact crater, Russia: structure, tectonics, and morphology. Meteoritics & Planetary Science, 42(3), 307–319.

Hadizadeh, J., and Johnson, W., 2003. Estimating local strain due to comminution in experimental cataclastic textures. Journal of Structural Geology, 25(11), 1973–1979.

Hammer, Ø., Harper, D.A.T., and Ryan, P.D., 2001. PAST: Paleontological statistics software package for education and data analysis. Palaeontologia Electronica, 4(1), 1–9.

Hancock, G.S., and Anderson, R.S., 2002. Numerical modeling of fluvial strath-terrace formation in response to oscillating climate. Geological Society of America Bulletin, 114(9), 1131–1142.

Harris, C., Franssen, R., and Loosveld, R., 1991. Fractal analysis of fractures in rocks: the Cantor's Dust method - comment. Tectonophysics, 198(1), 107–111.

Hegge, B.J., and Masselink, G., 1996. Spectral analysis of geomorphic time series: Auto-spectrum. Earth Surface Processes and Landforms, 21(11), 1021–1040.

Heilbronner, R., and Keulen, N., 2006. Grain size and grain shape analysis of fault rocks. Tectonophysics, 427(1–4), 199–216.

Henningsen, D., and Katzung, G., 2006. Einführung in die Geologie Deutschlands. Elsevier, 7. Auflage, p. 215.

Higgins, M.D., 2000. Measurement of crystal size distributions. American Mineralogist, 85(9), 1105–1116.

Hildebrand, A.R., Penfield, G.T., Kring, D.A. et al., 1991. Chicxulub Crater - a possible Cretaceous/Tertiary boundary impact crater on the Yucatán Peninsula, Mexico. Geology, 19(9), 867–871.

Hirata, T., 1989. Fractal dimension of fault systems in Japan: Fractal structure in rock fracture geometry at various scales. Pure and Applied Geophysics, 131(1–2), 157–170.

Hode, T., von Dalwigk, I., and Broman, C., 2003. A hydrothermal system associated with the Siljan impact structure, Sweden - implications for the search for fossil life on Mars. Astrobiology, 3(2), 271–289.

Hörz, F., Ostertag, R., and Rainey, D.A., 1983. Bunte Breccia of the Ries: Continuous Deposits of Large Impact Craters. Review of Geophysics and Space Physics, 21(8), 1667–1725.

Holsapple, K.A., 1993. The scaling of impact processes in planetary sciences. Annual Review of Earth and Planetary Sciences, 21, 333–373.

Holsapple, K.A., 1987. The scaling of impact phenomenon. International Journal of Impact

Engineering, 5(1–4), 343–355.
Hossain, M.S., and Kruhl, J.H., 2014a. Fractal Geometry-Based Quantification of Shock-Induced Rock Fragmentation in and around an Impact Crater. Pure and Applied Geophysics, doi:10.1007/s00024-014-0922-8.
Hossain, M.S., and Kruhl, J.H., 2014b. Small- to large-scale rock fracture patterns as indicators of shock-related fragmentation. In: Raju, N.J. (ed.), Geosstatistical and Geospatial Approaches for the Characterization of Natural Resources in the Environment: Challenges, Processes and Strategies. Capital Publishing Company, New Delhi, India, pp. 280–283.
Hossain, M.S., and Kruhl, J.H., 2015. Characteristics and spatial distribution of fragmentation structures around an impact crater. Earth and Planetary Science Letters (submitted).
Hüttner, R., and Schmidt-Kaler, H., 1999. Geologische Karte 1:50000 Ries mit Kurzerläuterungen auf der Rückseite. Tech. rep. Bayerisches Geologisches Landesamt, scale 1:50000, 1 sheet.
Huffman, A.R., and Reimold, W.U., 1996. Experimental constraints on shock-induced microstructures in naturally deformed silicates. Tectonophysics, 256(1–4), 165–217.
Ivanov, B.A., and Stöffler, D., 2005. The Steinheim impact crater, Germany: Modeling of a complex crater with central uplift. Lunar and Planetary Science XXXVI (2005), id. 1443.
Johnson, B.C., and Melosh, H.J., 2014. Formation of melt droplets, melt fragments, and accretionary impact lapilli during a hypervelocity impact. Icarus, 228, 347–363.
Jutzi, M., Holsapple, K., Wünneman, K., and Michel, P., 2015. Modeling asteroid collisions and impact processes. arXiv preprint arXiv:1502.01844.
Kaminski, E., and Jaupart, C., 1998. The size distribution of pyroclasts and the fragmentation sequence in explosive volcanic eruptions. Journal of Geophysical Research, 103(B12), 759–779.
Kaushik, A.I., 2007. Relationships between multiaxial stress states and internal fracture patterns in sphere-impacted silicon carbide. International Journal of Fracture, 146(1–2), 1–18.
Kaye, B.H., 1989. A random walk through fractal dimensions. Weinheim, VCH Publishers, p. 421.
Kaye, B.H., 1993. Chaos and Complexity. VCH Publishers, Weinheim, p. 593.
Kenkmann, T., 2003. Dike formation, cataclastic flow, and rock fluidization during impact cratering: an example from the Upheaval Dome structure, Utah. Earth and Planetary Science Letters, 214(1–2), 43–58.
Kenkmann, T., Collins, G.S., and Wünnemann, K., 2012. The modification stage of crater formation. In: Osinski, G.R., and Pierazzo, E. (eds.), Impact Cratering: Processes and Products. John Wiley & Sons, Chichester, pp. 60–75.
Kenkmann, T., and Ivanov, B.A., 2006. Target delamination by spallation and ejecta dragging: an example from the Ries Crater's periphery. Earth and Planetary Science Letters, 252(1–2), 15–29.
Kenkmann, T., and Poelchau, M.H., 2009. Low-angle collision with Earth: The elliptical impact crater Matt Wilson, Northern Territory, Australia. Geology, 37(5), 459–462.
Kenkmann, T., Poelchau, M.H., and Wulf, G., 2014. Structural geology of impact craters. Journal of Structural Geology, 62, 156–182.
Kenkmann, T., Reimold, W.U., Khirfan, M., Salameh, E., Konsul, K., and Khoury, H., 2010. The complex impact crater Jebel Waqf as Suwwan in Jordan: effects of target heterogeneity and impact obliquity on central uplift formation. In: Gibson, R.L., and Reimold, W.U. (eds.), Large Meteorite Impacts and Planetary Evolution IV. Geological Society of America Special Paper, 465, 471–487.
Kenkmann, T., and Schönian, F., 2006. Ries and Chicxulub: Impact craters on Earth provide insights for Martian ejecta blankets. Meteoritics & Planetary Science, 41(10), 1587–1603.
Kenkmann, T., Wünnemann, K., Deutsch, A., Poelchau, M.H., Schäfer, F., and Thoma, K., 2011. Impact cratering in sandstone: the MEMIN pilot study on the effect of pore water. Meteoritics &

Planetary Science, 46(6), 890–902.
Keulen, N., Heilbronner, R., Stünitz, H., Boullier, A.-M., and Ito, H., 2007. Grain size distributions of fault rocks: A comparison between experimentally and naturally deformed granitoids. Journal of Structural Geology, 29(8), 1282–1300.
Key, W.R.O., and Schultz, R.A., 2011. Fault formation in porous sedimentary rocks at high strain rates: First results from the Upheaval Dome impact structure, Utah, USA. Geological Society of America Bulletin, 123(5–6), 1161–1170.
Kieffer, S.W., and Simonds, C.H., 1980. The role of volatiles and lithology in the impact cratering process. Reviews of Geophysics, 18(1), 143–181.
Kipp, M.E., Grady, D.E., and Chen, E.P., 1980. Strain-rate dependent fracture initiation. International Journal of Fracture, 16(5), 471–478.
Koeberl, C., and Henkel, H. (eds.), 2005. Impact Tectonics. Springer, p. 552.
Kruhl, J.H., 2013. Fractal-geometry techniques in the quantification of complex rock structures: A special view on scaling regimes, inhomogeneity and anisotropy. Journal of Structural Geology, 46, 2–21.
Kumar, P.S., 2005. Structural effects of meteorite impact on basalt: Evidence from Lonar Crater, India. Journal of Geophysical Research: Solid Earth, 110(B12), doi:10.1029/2005JB003662.
Kumar, P.S., and Kring, D.A., 2008. Impact fracturing and structural modification of sedimentary rocks at Meteor Crater, Arizona. Journal of Geophysical Research: Planet, 113(E9), doi:10.1029/2008JE003115.
Lange, M.A., and Ahrens, T.J., 1987. Impact experiments in low-temperature ice. Icarus, 69(3), 506–518.
Lange, M.A., Ahrens, T.J., and Boslough, M.B., 1984. Impact cratering and spall failure of gabbro. Icarus, 58(3), 383–395.
Lau, K.-M., and Weng, H., 1995. Climate Signal Detection Using Wavelet Transform: How to make a Time Series Sing. Bulletin of the American Meteorological Society, 76(12), 2391–2402.
Launeau, P., Archanjo, C.J., Picard, D., Arbaret, L., and Robin, P.-Y., 2010. Two- and three-dimensional shape fabric analysis by the intercept method in grey levels. Tectonophysics, 492(1–4), 230–239.
Launeau, P., and Cruden, A.R., 1998. Magmatic fabric acquisition mechanisms in a syenite: Results of a combined anisotropy of magnetic susceptibility and image analysis study. Journal of Geophysical Research, 103(B3), 5067–5089.
Launeau, P., and Robin, P.-Y.F., 1996. Fabric analysis using the intercept method. Tectonophysics, 267(1–4), 91–119.
Lawson, D.E., 1972. Torridonian volcanic sediments. Scottish Journal of Geology, 8, 345–362.
Leone, G., Tackley, P.J., Gerya, T.V., May, D.A., and Zhu, G., 2014. Three-dimensional simulations of the southern polar giant impact hypothesis for the origin of the Martian dichotomy. Geophysical Research Letters, 41(24), 8736–8743.
Leterrier, Y., Pellaton, D., Mendels, D., Glauser, R., Andersons, J., and Månson, J.-A.E., 2001. Biaxial fragmentation of thin silicon oxide coatings on poly(ethylene terephthalate). Journal of Materials Science, 36(9), 2213–2225.
Levy, F., 1922. Lonetal und Geislinger Steige. Jahresberichte und Mitteilungen des Oberrheinischen geologischen Vereines N.F., 11, 22–26.
Liu, C., Shi, B., and Tang, C.-S., 2011. Quantification and characterization of microporosity by image processing, geometric measurement and statistical methods: application on SEM images of clay materials. Applied Clay Science, 54(1), 97–106.

Liu, C., Tang, C.-S., Shi, B., and Suo, W.-B., 2013. Automatic quantification of crack patterns by image processing. Computers & Geosciences, 57, 77–80.

Ma, K.-F., Tanaka, H., Song, S.-R., Wang, C.-Y., Hung, J.-H., Tsai, Y.-B., Mori, J., Song, Y.-F., Yeh, E.-C., Soh, W., Sone, H., Kuo, L.-W., and Wu, H.-Y., 2006. Slip zone and energetics of a large earthquake from the Taiwan Chelungpu-fault Drilling Project. Nature, 444, 473–476.

Mackenzie, D., Daubechies, I., Kleppner, D., Mallat, S., Meyer, Y., Ruskai, M.B., and Weiss, G., 2001. Wavelets: Seeing the Forest - and the Trees. Beyond Discovery, National Academy of Sciences, Washington, DC, 1-8.

Mandelbrot, B.B., 1977. Fractals: Form, Chance, & Dimension. W.H. Freeman & Company, San Francisco, CA, p. 365.

Mandelbrot, B.B., 1982. The Fractal Geometry of Nature. W.H. Freeman & Company, New York, p. 468.

Marini, F., Raukas, A., and Tiirmaa, R., 2004. Magnetic fines from the Kaali impact-site (Holocene, Estonia): Preliminary SEM investigation. Geochemical Journal, 38(2), 107–120.

Marone, C., and Scholz, C., 1989. Particle-size distribution and microstructures within simulated gouge. Journal of Structural Geology, 11(7), 799–814.

Mathur, S.C., Gour, S.D., Loyal, R.S., Tripathi, A., and Sisodia, M.S., 2005. Spherules from the Late Cretaceous phosphorite of the Fathehgarh Formation, Barmer Basin, India. Gondwana Research, 8(4), 579–584.

McQueen, R.G., Marsh, S.P., Taylor, J.W., Fritz, J.N., and Carter, W.J., 1970. The equation of state of solids from shock wave studies. In: Kinslow, R. (ed.), High Velocity Impact Phenomena. Academic Press, New York and London, pp. 293–417.

Melosh, H.J., 1984. Impact ejection, spallation, and the origin of meteorites. Icarus, 59(2), 234–260.

Melosh, H.J., 1989. Impact Cratering: A Geological Process. Oxford University Press, New York, p. 245.

Melosh, H.J., 2013. The contact and compression stage of impact cratering. In: Osinski, G.R., and Pierazzo, E. (eds), Impact cratering – Processes and Products. Wiley-Blackwell, UK, pp. 32–42.

Melosh, H.J., and Ivanov, B.A., 1999. Impact Crater Collapse. Annual Review of Earth and Planetary Sciences, 27, 385–415.

Melosh, H.J., and Mckinnon, W.B., 1978. The mechanics of ringed basin formation. Geophysical Research Letter, 5(11), 985–988.

Melosh, H.J., Ryan, E.V., and Asphaug, E., 1992. Dynamic fragmentation in impacts: Hydrocode simulation of laboratory impacts. Journal of Geophysical Research: Planets, 97(E9), 14735–14759.

Melosh, B.L., Rowe, C.D., Smit, L., Groenewald, C., Lambert, C.W., and Macey, P., 2014. Snap, Crackle, Pop: Dilational fault breccias record seismic slip below the brittle-plastic transition. Earth and Planetary Science Letters, 403, 432–445.

Merceron, T., and Velde, B., 1991. Application of Cantor's Method for fractal analysis of fractures in the Toyoha Mine, Hokkaido, Japan. Journal of Geophysical Research, 96(B10), 16641–16650.

Meyer, C., 2012. Sedimentological, Structural and Geochemical Investigations of the Suevite of the Impact Crater Nördlinger Ries, Germany. Department of Earth Sciences. Berlin, Free University of Berlin. PhD Thesis, p. 132.

Meyer, C., Jébrak, M., Stöffler, D., and Riller, U., 2011. Lateral transport of suevite inferred from 3D shape-fabric analysis: Evidence from the Ries impact crater, Germany. Geological Society of America Bulletin, 123(11–12), 2312–2319.

Meyers, M.A., 1994. Dynamic Behavior of Materials. John Wiley & Sons, New York, p. 688.

Monzawa, N., and Otsuki, K., 2003. Comminution and fluidization of granular fault materials: implications for fault slip behavior. Tectonophysics, 367(1–2), 127–143.

Morgan, J., and Rebolledo-Vieyra, M., 2013. Geophysical studies of impact craters. In: Osinski, G.R., and Pierazzo, E. (eds.), Impact cratering – Processes and Products. Wiley-Blackwell, UK, pp. 211–222.

Morgan, M.L., and Warme, J.E., 2002. Carbonate accretionary lapilli in the Late Devonian Alamo Breccia: impact genesis and implications for timing of ejecta emplacement. GSA Denver Annual Meeting, no. 293-3.

Morlet, J., 1983. Sampling Theory and Wave Propagation. In: Chen, C.H. (ed.), Issues in Acoustic Signal - Image Processing and Recognition, NATO ASI Series. Springer Berlin Heidelberg, 1, pp. 233–261.

Newsom, H.E., Graup, G., Iseri, D.A., Geissman, J.W., and Keil, K., 1990. The formation of the Ries Crater, West Germany; Evidence of atmospheric interactions during a large cratering event. In: Sharpton, V.L., and Ward, P.D. (eds.), Global Catastrophes in Earth History, Geological Society of America Special Papers 247, 195–206.

O'Keefe, J.D., and Ahrens, T.J., 1975. Shock effects from a large impact on the moon. In: Lunar and Planetary Science Conference Proceedings, 6, 2831–2844.

O'Keefe, J.D., and Ahrens, T.J., 1982. Cometary and meteorite swarm impact on planetary surfaces. Journal of Geophysical Research: Solid Earth, 87(B8), 6668–6680.

Ono, T., and Allaire, R.A., 2000. Fracture Analysis, a Basic Tool to Solve Breakage Issues. Technical Information Paper, SEMI®FPD Expo Taiwan, TIP 201–209.

Oppenheim, A.V., Schafer, R.W., and Buck J.R., 1999. Discrete-Time Signal Processing. Prentice Hall, Upper Saddle River, N.J., p. 863.

Osinski, G.R., and Pierazzo, E., 2013. Impact cratering - processes and products. In: Osinski, G.R., and Pierazzo, E., (eds.), Impact cratering – Processes and Products. Wiley-Blackwell, UK, pp. 1–20.

Osinski, G.R., and Spray, J.G., 2003. Transient crater formation and collapse: observations at the Haughton impact structure, arctic Canada. Workshop on Impact Cratering: Bridging the Gap Between Modeling and Observations. Lunar and Planetary Institute, Houston, abstract #8010 (CD-ROM).

Park, S.-I., Kim, Y.-S., Ryoo, C.-R., and Sanderson, D.J., 2010. Fractal analysis of the evolution of a fracture network in a granite outcrop, SE Korea. Geosciences Journal, 14(2), 201–215.

Parnell, J., Mark, D., Fallick, A.E., Boyce, A., and Thackrey, S., 2011. The age of the Mesoproterozoic Stoer Group sedimentary and impact deposits, NW Scotland. Journal of the Geological Society, London, 168, 349–358.

Pérez-López, R., and Paredes, C., 2006. On measuring the fractal anisotropy of 2-D geometrical sets: application to the spatial distribution of fractures. Geoderma, 134(3–4), 402–414.

Peternell, M., Bitencourt, M.F., and Kruhl, J.H., 2011. Combined quantification of anisotropy and inhomogeneity of magmatic rock fabrics - an outcrop scale analysis recorded in high resolution. Journal of Structural Geology, 33(4), 609–623.

Peternell, M., Bitencourt, M.F., Kruhl, J.H., and Stäb, C., 2010. Macro and microstructures as indicators of the development of syntectonic granitoids and host rocks in the Camboriú region, Santa Catarina, Brazil. Journal of South American Earth Sciences, 29(3), 738–750.

Pierazzo, E., Artemieva, N.A., Asphaug, E., Baldwin, E.C., Cazamias, J., Coker, R., Collins, G.S., Crawford, D.A., Davison, T., Elbeshausen, D., Holsapple, K.A., Housen, K.R., Korycansky, D.G., and Wünnemann, K., 2008. Validation of numerical codes for impact and explosion cratering: impacts on strengthless and metal targets. Meteoritics & Planetary Science, 43(12), 1917–1938.

Pike, R.J., 1980. Control of crater morphology by gravity and target type – Mars, Earth, Moon. Proceedings of the Lunar and Planetary Science Conference, 11, 2159–2189.

Pilkington, M., and Grieve, R.A.F., 1992. The geophysical signature of terrestrial impact craters. Reviews of Geophysics, 30(2), 161–181.

Pilon, J.A., Grieve, R.A.F., and Sharpton, V.L., 1991. The subsurface character of Meteor Crater, Arizona, as determined by ground-probing radar. Journal of Geophysical Research: Planets, 96(E1), 15563–15576.

Pittarello, L., Di Toro, G., Bizzarri, A., Pennacchioni, G., Hadizadeh, J., and Cocco, M., 2008. Energy partitioning during seismic slip in pseudotachylyte-bearing faults (Gole Larghe Fault, Adamello, Italy). Earth and Planetary Science Letters, 269(1–2), 131–139.

Plant, J.A., Whittaker, A., Demetriades, A., De Vivo, B., and Lexa, J., 2003. The geological and tectonic framework of Europe. A contribution to IUGS/IAGC Global Geochemical Baselines, Geochemical Atlas of Europe, Part 1.

Poelchau, M.H., and Kenkmann, T., 2008. Asymmetric signatures in simple craters as an indicator for an oblique impact direction. Meteoritics & Planetary Science, 43(12), 2059–2072.

Poelchau, M.H., Kenkmann, T., and Kring, D.A., 2009. Rim uplift and crater shape in Meteor Crater: effects of target heterogeneities and trajectory obliquity. Journal of Geophysical Research: Planets, 114, E01006, DOI: 10.1029/2008JE003235.

Polanskey, C.A., and Ahrens, T.J., 1990. Impact spallation experiments: Fracture patterns and spall velocities. Icarus, 87(1), 140–155.

Pope, K.O., Ocampo, A.C., Fischer, A.G. et al., 1999. Chicxulub impact ejecta from Albion Island, Belize. Earth and Planetary Science Letters, 170(4), 351–364.

Popova, O.P., Jenniskens, P., Emelyanenko, V. et al., 2013. Chelyabinsk airburst, damage assessment, meteorite recovery, and characterization. Science, 342(6162), 1069–1073.

Qian, Q., Qi, C., and Wang, M., 2009. Dynamic strength of rocks and physical nature of rock strength. Journal of Rock Mechanics and Geotechnical Engineering, 1(1), 1–10.

Quinta, A., Tavani, S., and Roca, E., 2012. Fracture pattern analysis as a tool for constraining the interaction between regional and diapir-related stress fields: Poza de la Sal Diapir (Basque Pyrenees, Spain). Geological Society, London, Special Publications, 363(1), 521–532.

Ramsay, J.R., and Huber, M., 1987. The Techniques of Modern Structural Geology, Vol. 2: Folds and Fractures. Academic Press, London, p. 391.

Robertson, P.B., and Grieve, R.A.F., 1977. Shock attenuation at terrestrial impact structures. In: Roddy, D.J., Pepin, R.O., and Merrill, R.B. (eds.), Impact and Explosion Cratering: Planetary and Terrestrial Implications. Pergamon, New York, pp. 687–702.

Roddy, D.J., 1977. Large-scale impact and explosion craters: comparisons of morphological and structural analogues. In: Roddy, J., Pepin, R.O., and Merill, R.B. (eds.), Impact and Explosion Cratering. Pergamon Press, New York, pp. 185–246.

Roddy, D.., Pepin, R.O., and Merrill, R.B., (eds.), 1977. Impact and Explosion Cratering. New York, Pergamon Press, p. 1301.

Rousell, D.H., Fedorowich, J.S., and Dressler, B.O., 2003. Sudbury Breccia (Canada): A product of the 1850 Ma Sudbury event and host to footwall Cu-Ni-PGE deposits. Earth-Science Reviews, 60(3–4), 147–174.

Roy, A., Perfect, E., Dunne, W.M., and McKay, L.D., 2007. Fractal characterization of fracture networks: An improved box-counting technique. Journal of Geophysical Research, 112(B12201), 1–9.

Sagy, A., Cohen, G., Reches, Z.E., and Fineberg, J., 2006. Dynamic fracture of granular material

under quasi-static loading. Journal of Geophysical Research: Solid Earth, 111(B4), doi:10.1029/2005JB003948.

Sagy, A., Fineberg, J., and Reches, Z.E., 2004. Shatter cones: branched, rapid fractures formed by shock impact. Journal of Geophysical Research: Solid Earth, 109(B10), doi:10.1029/2004JB003016.

Sagy, A., Reches, Z.E., and Fineberg, J., 2002. Dynamic fracture by large extraterrestrial impacts as the origin of shatter cones. Nature, 418(6895), 310–313.

Sagy, A., Reches, Z., and Roman, I., 2001. Dynamic fracturing; field and experimental observations. Journal of Structural Geology, 23, 1223–1239.

Sahagian, D.L., and Proussevitch, A.A., 1998. 3D particle size distributions from 2D observations: stereology for natural applications. Journal of Volcanology and Geothermal Research, 84(3–4), 173–196.

Sammis, C., and Biegel, R., 1989. Fractals, fault-gouge, and friction. Pure and Applied Geophysics, 131(1–2), 255–271.

Sammis, C., King, G., and Biegel, R., 1987. The kinematics of gouge deformation. Pure and Applied Geophysics, 125(5), 777–812.

Sanders, I.S., and Johnston, J.D., 1989. The Torridonian Stac Fada Member: an extrusion of fluidised peperite? Transactions of the Royal Society of Edinburgh: Earth Sciences, 80(1), 1–4.

Schmidt-Kaler, H., 2004. Geologische Übersichtskarte des Meteoritenkraters Nördlinger Ries 1:100 000. Bayerischen Geologischen Landesamt, München, 5th edition (modified).

Schoutens, J.E., 1979. Empirical analysis of nuclear and high explosive cratering and ejecta. In: Nuclear Geoplosics Sourcebook, vol. 55(2), section 4, Rep. DNA 65 01H4 2, Defence Nuclear Agency, Bethesda, MD.

Schulte, P., Alegret, L., Arenillas, I. et al., 2010. The Chicxulub asteroid impact and mass extinction at the Cretaceous-Paleogene boundary. Science, 327(5970), 1214–1218.

Schwarz, W.H., and Lippolt, H.J., 2013. ^{40}AR-^{39}AR Step heating of Nördlinger Ries Crater impact melts. Meteoritics and Planetary Science Supplement, id. 5191.

Seffens, W., 1999. Order from Chaos. Science magazine, 285(5431), 1228.

Shao, S.-M., and Zou, J.-C., 1996. Fractal research of gouge. Acta Seismologica Sinica, 9(3), 485–491.

Sharon, E., Gross, S.P., and Fineberg, J., 1995. Local crack branching as a mechanism for instability in dynamic fracture. Physical Review Letters, 74(25), 5096–5099.

Shibuya, T., and Nakahara, I., 1968. The semi-infinite body subjected to a concentrated impact load on the surface. Bulletin of the Japan Society of Mechanical Engineers, 11(48), 983–992.

Shoemaker, E.M., 1962. Interpretation of lunar craters. In: Kopal, Z. (ed.), Physics and Astronomy of the Moon. Academic, New York/London, pp. 283–359.

Shoemaker, E.M., 1977. Why study impact craters? In: Roddy, D.J., Pepin, R.O., and Merrill, R.B. (eds.), Impact and Explosion Cratering. Pergamon Press, New York, pp. 1–10.

Shoemaker, E.M., Macdonald, F.A., and Shoemaker, C.S., 2005. Geology of five small Australian impact craters. Australian Journal of Earth Sciences, 52(4–5), 529–544.

Sharpton, V.L., and Dressler, B.O., 2003. Excavation flow and central peak rings: Is there a connection? Workshop on impact cratering: Bridging the Gap Between Modeling and Observations. Lunar and Planetary Institute, Houston, abstract #8059 (CD-ROM).

Sparks, R.S.J., 1976. Grain size variations in ignimbrites and implications for the transport of pyroclastic flows. Sedimentology, 23(2), 147–188.

Spray, J.G., 1997. Superfaults. Geology, 25(7), 579–582.

Squire, R.J., and McPhie, J., 2002. Characteristics and origin of peperite involving coarse-grained host sediment. Journal of Volcanology and Geothermal Research, 114(1–2), 45–61.

Stankowski, W.T.J., Katrusiak, A., and Budzianowski, A., 2006. Crystallographic variety of magnetic spherules from Pleistocene and Holocene sediments in the Northern foreland of Morasko-Meteorite Reserve. Planetary and Space Science, 54(1), 60–70.

Stewart, A.D., 1991. Torridonian. In: Craig, G.Y. (ed.) Geology of Scotland, 3rd edition. Geological Society London, pp. 65–855.

Stewart, A.D. (ed.), 2002. The later Proterozoic Torridonian Rocks of Scotland: their Sedimentology, Geochemistry and Origin. Geological Society London, Memoirs, 24, p. 130.

Stewart, A.D., and Parker, A., 1979. Palaeosalinity and environmental interpretation of red beds from the late Precambrian ('Torridonian') of Scotland. Sedimentary Geology, 22(3–4), 229–241.

Stöffler, D., 1977. Research drilling Nördlingen 1973: Polymict breccias, crater basement, and cratering model of the Ries impact structure. Geologica Bavarica, 75, 443–458.

Stöffler, D., 1984. Glasses formed by hypervelocity impact. Journal of Non-Crystalline Solids, 67(1–3), 465–502.

Stöffler, D., Artemieva, N.A., and Pierazzo, E., 2002. Modeling the Ries-Steinheim impact event and the formation of the moldavite strewn field. Meteoritics & Planetary Science, 37(12), 1893–1907.

Stöffler, D., Artemieva, N.A., Pierazzo, E., and Ivanov, B.A., 2001. Ries carter, Germany: Geology and numerical modelling of impact cratering (abstract). Meteoritics & Planetary Science, 36(Suppl.), A199.

Stöffler, D., Artemieva, N.A., Wünnemann, K., Reimold, W.U., Jacob, J., Hansen, B.K., and Summerson, I.A.T., 2013. Ries crater and suevite revisited - Observations and modeling Part I: Observations. Meteoritics & Planetary Science, 48(4), 515–589.

Stöffler, D., and Grieve, R.A.F., 2007. Impactites. In: Fettes, D., and Desmons, J. (eds.), Metamorphic Rocks: A Classification and Glossary of Terms, Recommendations of the International Union of Geological Sciences. Cambridge University Press, Cambridge, UK, 82–92, 111–125, and 126–242.

Stöffler, D., and Langenhorst, F., 1994. Shock metamorphism of quartz in nature and experiment: I. Basic observation and theory. Meteoritics, 29, 155–181.

Storti, F., Billi, A., and Salvini, F., 2003. Particle size distributions in natural carbonate fault rocks; insights for non-self-similar cataclasis. Earth and Planetary Science Letters, 206(1–2), 173–186.

Strasser, M., 2011. Höhlen der Schwäbischen Alb als Pegelschreiber für Flussgeschichte und Tektonik in Südwestdeutschland seit dem Miozän. Institut für Planetologie, Universität Stuttgart, PhD Thesis, p. 109.

Strasser, M., Strasser, A., Pelz, K., and Seyfried, H., 2009a. A mid Miocene to early Pleistocene multi-level cave as a gauge for tectonic uplift of the Swabian Alb (Southwest Germany). Geomorphology, 106(1–2), 130–141.

Strasser, M., Strasser, A., Schmieder, M., Kröchert, J., and Buchner, E., 2009b. Magnetische Sphärulen in Höhlen der Schwäbischen Alb - Spuren kosmischer Ereignisse. Laichinger Höhlenfreund, 44, 209–222.

Stünitz, H., Keulen, N., Hirose, T., and Heilbronner, R., 2010. Grain size distribution and microstructures of experimentally sheared granitoid gouge at coseismic slip rates - Criteria to distinguish seismic and aseismic faults? Journal of Structural Geology, 32(1), 59–69.

Sturm, S., Wulf, G., Jung, D., and Kenkmann, T., 2013. The Ries impact, a double-layer rampart crater on Earth. Geology, 41(5), 531–534.

Sturm, S., Kenkmann, T., Willmes, M., Pösges, G., and Hiesinger, H., 2015. The distribution of megablocks in the Ries crater, Germany: Remote sensing, field investigation, and statistical analyses. Meteoritics & Planetary Science, 50(1), 141–171.

Suppe, J., 1985. Principles of Structural Geology. Prentice-Hall Inc., Englewood Cliffs, p. 537.

Taylor, P.L., Nusbaum, R.L., Fronabarger, A.K., Katuna, M.P., and Summer, N., 1996. Magnetic spherules in coastal plain sediments, Sullivan's Island, South Carolina, USA. Meteoritics & Planetary Science, 31(1), 77–80.

Torrence, C., and Compo, G.P., 1998. A Practical Guide to Wavelet Analysis. Bulletin of the American Meteorological Society, 79(1), 61–78.

Trauth, M.H., 2010. MATLAB Recipes for Earth Sciences - Third Edition. Springer, Berlin Heidelberg New York, p. 292.

Turcotte, D.L., 1989. Fractals in Geology and Geophysics. Pure and Applied Geophysics, 131(1–2), 171–196.

Turcotte, D.L., 1986. Fractals and fragmentation. Journal of Geophysical Research, 91(B2), 1921–1926.

Underwood, E.E., 1970. Quantitative Stereology. Addison-Wesley series in metallurgy and materials, Addison-Wesley Publishing Company, Menlo Park, California – London – Don Mils, Ontario, p. 274.

Velde, B., Dubois, J., Moore, D., and Touchard, G., 1991. Fractal patterns of fractures in granites. Earth and Planetary Science Letters, 104(1), 25–35.

Velde, B., Dubois, J., Touchard, G., and Badri, A., 1990. Fractal analysis of fractures in rocks: the Cantor's Dust method. Tectonophysics, 179(3–4), 345–352.

Vere-Jones, D., and Davies, R.B., 1966. A Statistical Survey of Earthquakes in the Main Seismic Region of New Zealand. Part 2 - Time series analyses. New Zealand Journal of Geology and Geophysics, 9(3), 251–284.

Volland, S., and Kruhl, J.H., 2004. Anisotropy quantification: the application of fractal geometry methods on tectonic fracture patterns of a Hercynian fault zone in NW Sardinia. Journal of Structural Geology, 26(8), 1499–1510.

Von Dalwigk, I., 2003. Fracture pattern in a complex impact structure - what can it tell us about crater collapse? A new look at the Siljan impact structure. EGS - AGU - EUG Joint Assembly, France, Abstract 10568.

Warme, J.E., Morgan, M., and Kuehner, H.C., 2002. Impact-generated carbonate accretionary lapilli in the Late Devonian Alamo breccia. In: Koeberl, C., and MacLeod, K.G. (eds.), Catastrophic Events and Mass Extinctions: Impacts and Beyond, Geological Society of America Special Papers 356, 489–504.

Wilson, J., Chester, J., and Chester, F., 2003. Microfracture analysis of fault growth and wear processes, Punchbowl Fault, San Andreas system, California. Journal of Structural Geology, 25(11), 1855–1873.

Wittmann, A., Kenkmann, T., Schmitt, R.T., Hecht, L., and Stöffler, D., 2004. Impactrelated dike breccia lithologies in the ICDP drill core Yaxcopoil-1, Chicxulub impact structure, Mexico. Meteoritics & Planetary Science, 39(6), 931–954.

Wood, C.A., and Andersson, L., 1978. New morphometric data for fresh lunar craters. Proceedings of the 9th Lunar and Planetary Science Conference. Lunar and Planetary Institute, Houston, pp. 3669–3689.

Wright, S.P., Tornabene, L.L., and Ramsey, M.S., 2013. Remote sensing of impact craters. In: Osinski, G.R., and Pierazzo, E. (eds.), Impact cratering - Processes and Products. Wiley-Blackwell,

UK, pp. 194–210.

Wünnemann, K., and Ivanov, B.A., 2003. Numerical modelling of impact crater depth-diameter dependence in an acoustically fluidized target. Planetary and Space Science, 51(13), 831–845.

Wünnemann, K., Morgan, J.V., and Jödicke, H., 2005. Is Ries crater typical for its size? An analysis based upon old and new geophysical data and numerical modelling. Geological Society of America Special Papers, 384, 67–83.

Yilmaz, T.I., Prosser, G., Liotta, D., Kruhl, J.H., and Gilg, H.A., 2014. Repeated hydrothermal quartz crystallization and cataclasis in the Bavarian Pfahl shear zone (Germany). Journal of Structural Geology, 68(A), 158–174.

Young, G.M., 2002. Stratigraphy and geochemistry of volcanic mass flows in the Stac Fada Member of the Stoer Group, Torridonian, NW Scotland. Transactions of the Royal Society of Edinburgh, Earth Sciences, 93(1), 1–16.

Zhao, Y.S., Feng, Z.C., Liang, W.G., Yang, D., Hu, Y.Q., and Kang, T.H., 2009. Investigation of fractal distribution law for the trace number of random and grouped fractures in a geological mass. Engineering Geology, 109(3–4), 224–229.

Appendix One: Impact-induced fracture patterns and fragment size distribution (FSD)

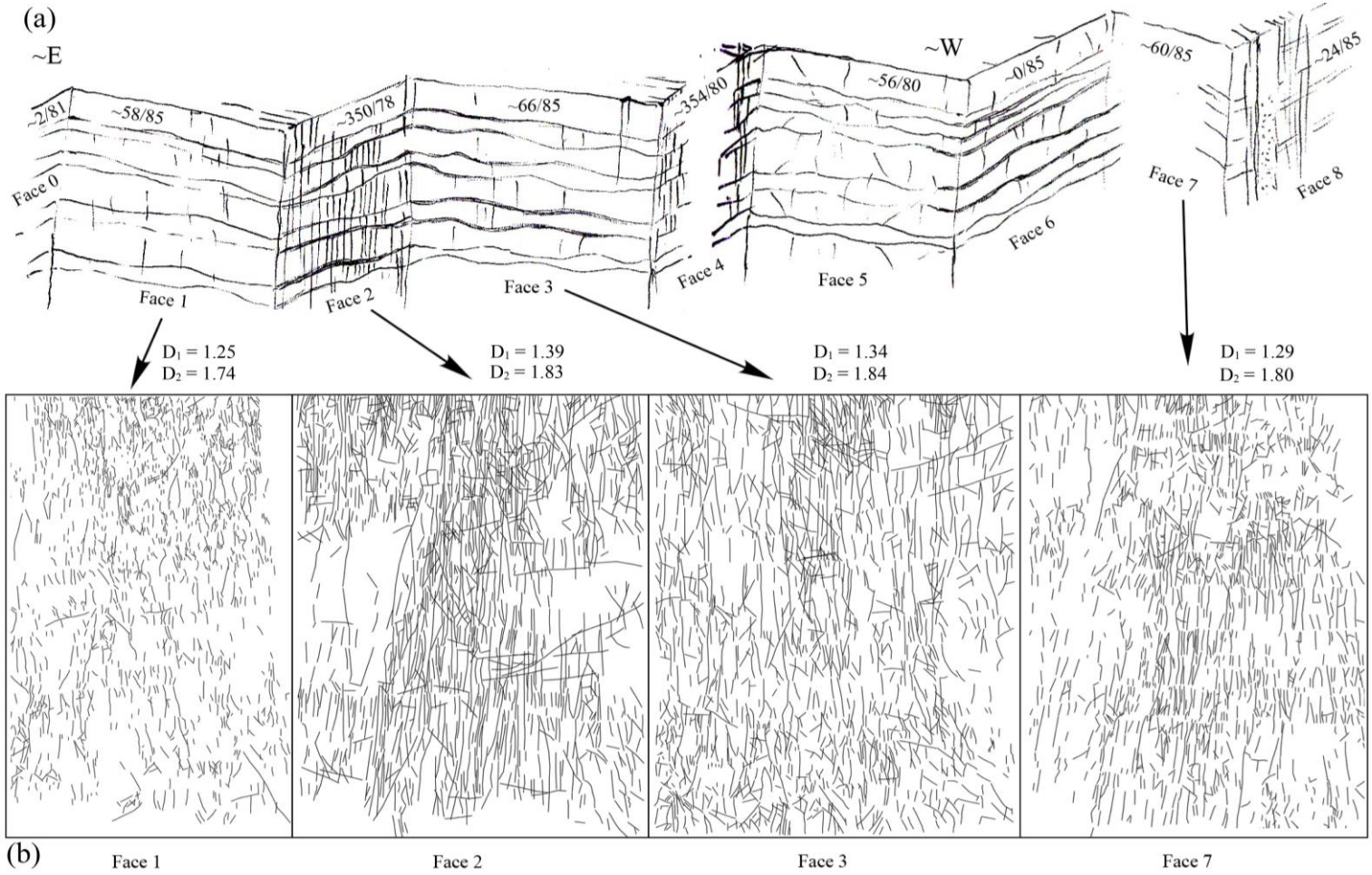

Figure App. 1.1: Impact-induced small-scale fracture patterns in the Eireiner quarry, ~13 km E of the Ries crater centre. (a) Schematic sketch illustrating an E-W oriented vertical section consisting of multiple faces (sub-sections) approx. orthogonal to each other. Each face is numbered and orientation is measured (not to scale). (b) Binary image of fractures in the face 1, 2, 3 and 7. Each face has an area of roughly 2.59 × 3.75 m. The fractures are manually drawn on the basis of the field photographs. Fractality (*D*-value) of the fracture patterns in each face is quantified by 2D box counting using the Benoit software. Two fractal dimension values are indicated by D_1 and D_2.

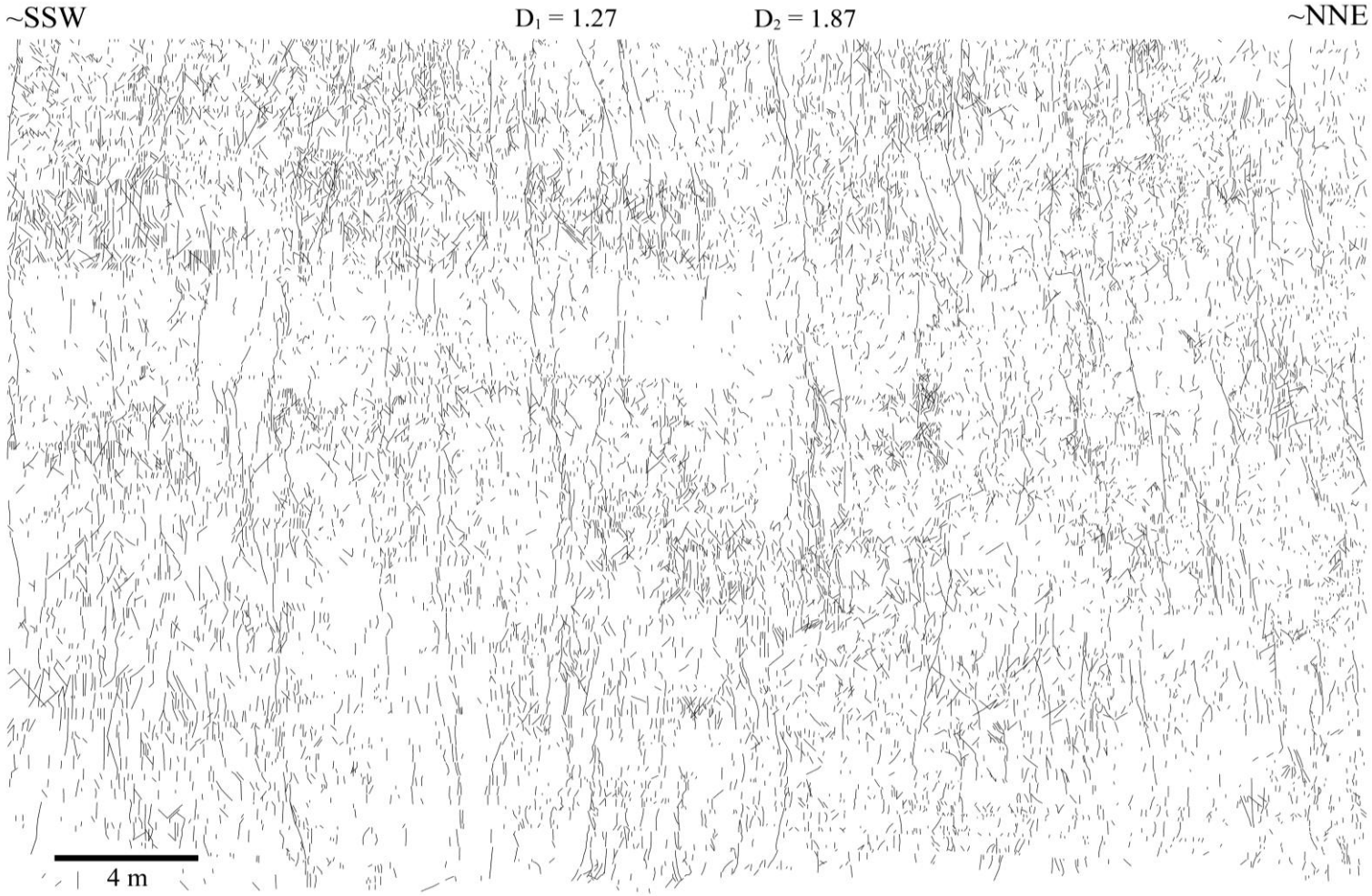

Figure App. 1.2: Binary image of fracture patterns in a vertical section in the Solnhofen quarry (~30 km E of the crater centre) after merging, digitizing and processing of 3 high-resolution digital field photographs. The vertical section is oriented at ~N20E. One pixel in the binary image = 1.98 mm on the ground. The fractures were manually drawn on the basis of the digital field photographs. Fractality (*D* -value) of the fracture patterns is quantified by 2D box counting using the Benoit software. Two fractal dimension values are indicated by D_1 and D_2 (on top).

Table App. 1.1: Published *D*-values on fragment size distribution (FSD) analyses measured for different deformation modes and materials. LM: light microscope image of thin section, SEM: scanning electron microscope image, manual: analogue box counting, digitizer: instrument for digital analysis of photomicrographs, digital: analysed with computer, Coult. count.: laser diffraction particle size analysis, CIAS: crack image analysis system. SAF: San Andreas Fault, USA. Modified after Keulen et al. (2007) and Buhl et al. (2013).

Location	Type of deformation	Material	Method of Analysis	2D Fractal dimension	References
Natural deformation with low strain rate					
Lopez Canyon	Fault zone	Granite	LM & SEM, manual	1.60	Sammis et al., 1987
	Fault zone	Granite	Manual	1.60	Sammis and Biegel, 1989
SAF, Canyon Pass	Fault zone	Granite, gneiss	LM, digitizer	0.8-2.1	Blenkinsop, 1991
Drillhole	Fault zone	Arkose	LM, digitizer	1.6-2.0	
SAF, Tejon Pass	Fault zone	Granite	Sieve & Coult. Count.	1.4-2.6	An and Sammis, 1994
San Gabriel	Fault zone	Gneiss	Sieve & Coult. Count.	1.6-1.9	
Lopez Canyon	Fault zone	Tonalite	Sieve & Coult. Count.	1.5-1.9	
Qinling Mountain	Fault zone	Schist and gneiss	LM & SEM, manual	1.60	Shao and Zou, 1996
Tanakura	Fault zone	Granite	LM, manual	1.70	Monzawa and Otsuki, 2003
It.-Shimotsutaki	Fault zone	Granite	LM, manual	2.10	
Koi	Fault zone	Granite	LM, manual	2.10	
Nojima	Fault zone	Granite	LM, manual	2.30	
	Fault zone	Carbonate		0.88-2.49	Storti et al., 2003
	Fault zone	Carbonate		1.09-1.93	Billi and Storti, 2004
SAF, Punchbowl	Fault zone	Granite	LM & TEM, manual	2.00	Chester et al., 2005
	Fault zone	Shale		2.30	Ma et al., 2006
Nojima Fault Zone	Fault zone	Granitoids	SEM, digital	1.6-2.4	Keulen et al., 2007
	Fault zone	Tonalite		1.80	Pittarello et al., 2008
	Fault zone	Sand		1.64-2.02	Balsamo and Storti, 2011
	Fault zone	Dolostone		1.49-1.56	Fondriest et al., 2012
Pfahl shear zone	Fault zone	Hydrothermal quartz	Fabric analyser, CIAS	2.08-4.02	Yilmaz et al., 2014
Experimental deformation with low strain rate					
Ottawa	Hydrostatic load 20MPa	Quartz sand (porous)	SEM, manual	1.40	Marone and Scholz, 1989
	Hydrostatic load 100 MPa	Quartz sand (porous)	SEM, manual	1.80	
	Shear test	Quartz sand (porous)	SEM, manual	1.60	
	Shear test	Artifical gouge		1.60	Biegel et al.,1989
	Shear test	Westerly granite		1.60	
Masillon, Ohio	Tri axial compression	Quartz sandstone	LM, digitizer	1.9-2.5	Hadizadeh and Johnson, 2003
Verzasca	Tri axial compression	Granitoids	SEM, digital	1.4-2.3	Heilbronner and Keulen, 2006
Verzasca	Tri axial compression	Granitoids	SEM, digital	1.4-2.3	Keulen et al., 2007
	Rotary shear	Granitoids		1.54-2.26	Stünitz et al., 2010
	Tri axial compression	Granite		1.13-2.28	Dyer et al., 2012
Experimental deformation with high strain rate					
	Impact	Basalt		1.4-1.62	Fujiwara et al., 1977
	Chemical explosion			1.42	Schoutens, 1979
	Nuclear explosion			1.50	
	Impact	Basalt		1.44-1.71	Lange et al., 1984
Seeberger, Layer 3	Crater	Sandstone	SEM & BSE, digital	0.84-1.74	Buhl et al., 2013
	Shock recovery	Sandstone		2.42	
Natural deformation with high strain rate					
	Natural impact	Sudbury Breccia		1.2-1.8	Rousell et al., 2003
	Natural impact	Sandstone		1.55	Key and Schultz, 2011
Ries crater	Natural impact	Limestone	Scan image, manual	1.21	Hossain and Kruhl, 2014a
Ries crater	Natural impact	Granite		1.21-2.99	Hossain and Kruhl, 2014a

Appendix Two: Quantification of fracture patterns and fracture frequency

Appendix 2.1: Quantification of the Ries-impact induced fracture patterns using 1D Cantor's-dust method

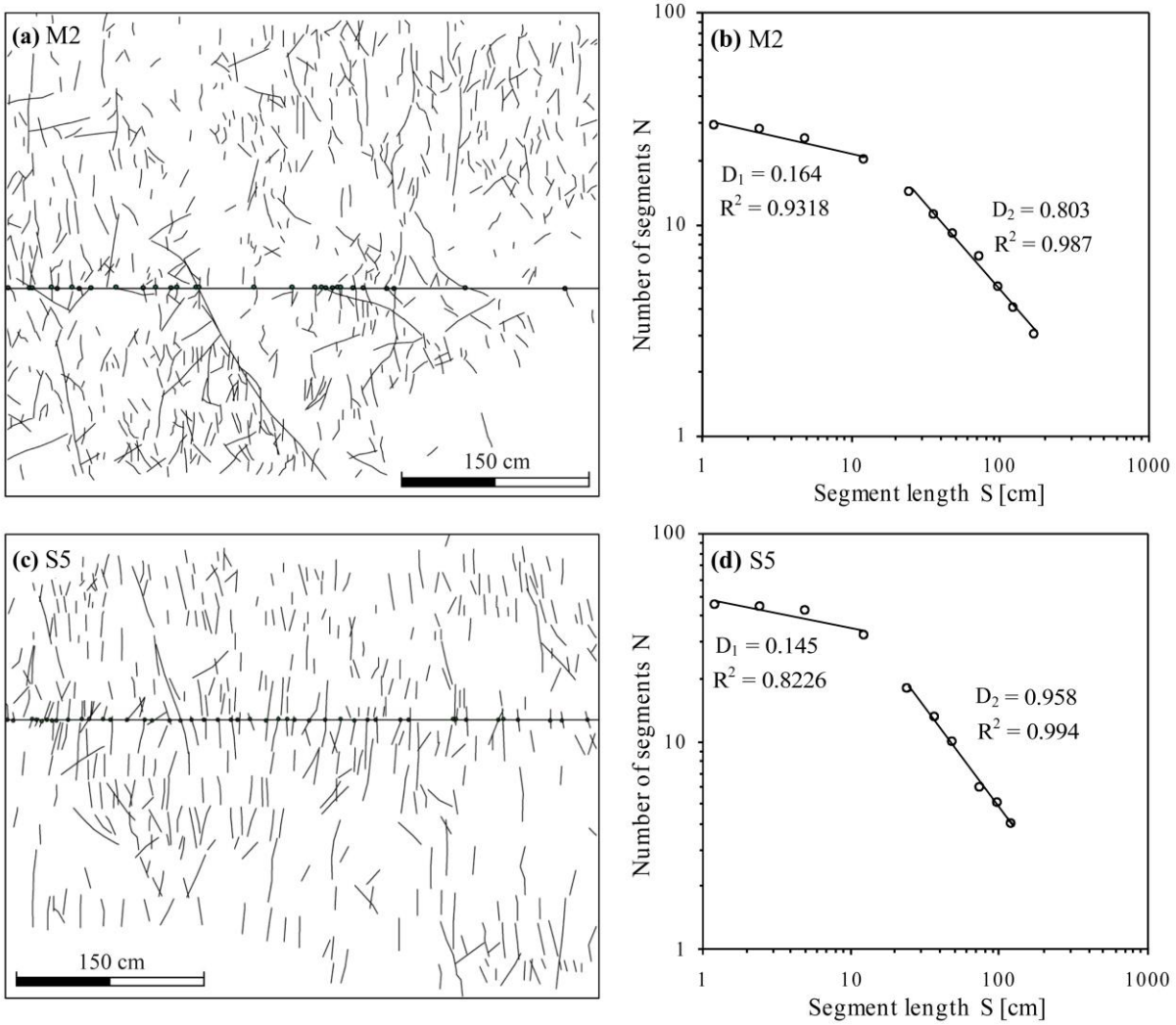

Figure App. 2.1: 1D Cantor's-dust method applied to sub-sections M2 (a + b) and S5 (c + d) of section-1 (Chapter three, Fig. 3.2). (a + c) Binary fracture patterns based on field photographs of sub-sections M2 and S5. Points on horizontal scan-lines mark intersections with fractures. (b + d) Cumulative frequency distributions of fracture spacing along scan-lines, presented in log-log plots. Two intervals of linear point arrangement with two different fractal dimensions D_1 and D_2 occur. R^2: correlation coefficient.

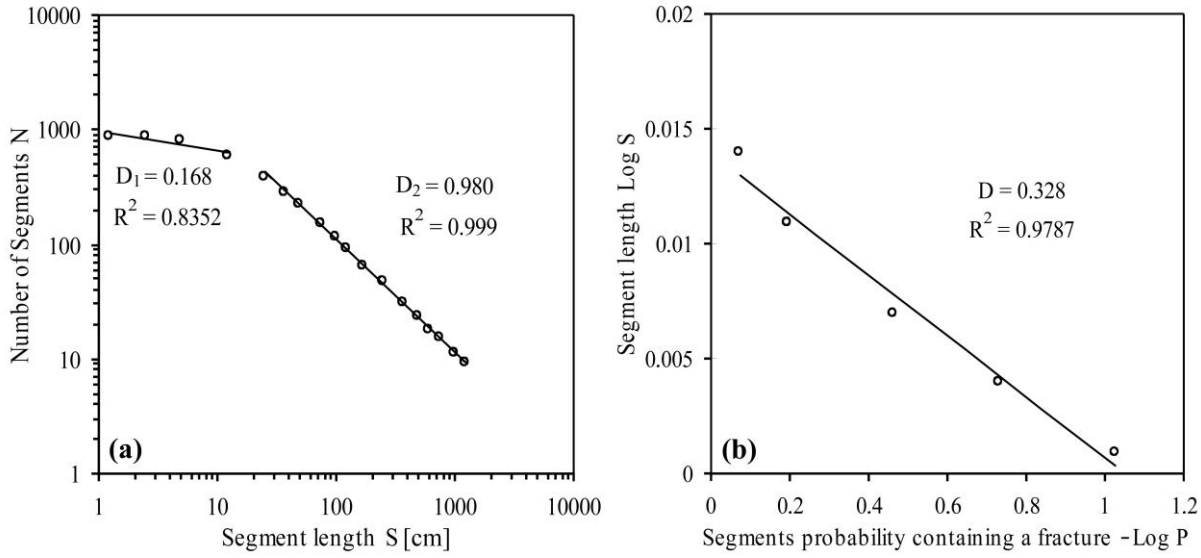

Figure App. 2.2: 1D Cantor's-dust method applied to section-1 in the Eireiner quarry (chapter three, Fig. 3.2). (a) Cumulative frequency distribution of fracture spacing along a horizontal scan-line, placed roughly in the middle of the section. Since the section's elevation is slightly decreasing from N to S the scan-line is divided into several horizontal parts decreasing from ca. 5.5 m above the quarry bottom in the N to ca. 3 m in the S. Interval counting technique after Velde et al. (1990). Two intervals of linear point arrangement with two different fractal dimensions D_1 and D_2 occur. R^2: correlation coefficient. (b) Probability of segments containing a fracture P versus segment length S for the total length of section-1. Spacing population technique after Merceron and Velde (1991). The approximate linear point arrangement is represented by a fractal dimension of D = 0.328. R^2: correlation coefficient.

Appendix 2.3: Matlab script for time series analysis of the impact-induced fracture frequency data

Appendix 2.3a: Autospectral analysis of the fracture frequency data

```
% First, load data from the Eireiner quarry with the name 'fouriertransformei.txt' (text file)

load fouriertransformei.txt
x_distance=fouriertransformei(:,1);
y_variable=fouriertransformei(:,2);

figure (1), plot(x_distance,y_variable)
xlabel('Section width [cm]'),ylabel('Fracture number [every 12.5 cm]')
title('Frequency plot')

% To zoom the plot at specific interval, plot only 50 data points out of 89 (Eireiner data set)

figure (2), plot(x_distance(1:50),y_variable(1:50),'b.-');

                %%      Calculation of Fourier coefficients by using fft function

% Now compute the Fourier coefficients of the y variable using fft function, the fft is know as the
% first Fourier transformation. For discrete data (Eireiner, 89), 1st component of Y-axis (y1), is
% simply sum of data point, which can be removed.
```

```
Y = fft(y_variable);
Y(1)=[];

% To visualize the Fourier coefficients of the y variable, plot it as

figure (3), plot(Y,'ro')
title('Fourier Coefficients in the Complex Plane');
xlabel('Real Axis');
ylabel('Imaginary Axis');

                    %%      Draw Periodogram based on Nyquist Frequency

% The complex magnitude squared of Y is called the power, and a plot of power versus frequency is
% called ‘periodogram‘. Here frequency (1/12.5) is calculated from data interval (12.5 cm),
% Nyquist=1/2 of sample frequency 88 data points for Eireiner (1 less than actual 89 data points)

n=length(Y);                        % 88 Data points
power = abs(Y(1:floor(n/2))).^2;    % abs is the absolute value
nyquist = (1/12.5)*1/2;             % 1/12.5 is frequency and 1/2 of it is Nyquist
freq = (1:n/2)/(n/2)*nyquist;
figure (4), plot(freq,power,'r')
xlabel('Frequency [1/12.5 cm]')
ylabel('Power')
title('Autospectrum')

% The scale in cycles/12.5 cm is somewhat inconvenient. It is possible to plot in length (12.5 cm)/
% cycle and to estimate the length of one cycle. Length of power and freq vector are 90 (from above)

figure (5), plot(freq(1:90),power(1:90))
xlabel('cycles/0.5 m'),ylabel('Power')

                    %%      Now plot Power data against Period (1/frequncy)

% Plot power versus period for convenience (where period=1./freq). Here period actually indicate
% the distance along x axis in cm. As expected, there is a strong cycle with a length of about 375 cm.
% X-axis is 1200 cm long for the Eireiner quarry.

period=1./freq;                     % convert frequency to period
figure (6), plot(period,power);
axis([0 1200 0 2e+4]);              % 1200 cm use to see cyle in the entire range
ylabel('Power');
xlabel('Period [Distance in cm]');
```

```
%%      Marks the strong cycle location and its value on the figure

% It is possible to fix the cycle length a little more precisely by picking out the strongest frequency.
% Red dot on the figure locates this point.

hold on;
index=find(power==max(power));
mainPeriodStr=num2str(period(index));
figure (6), plot(period(index),power(index),'r.', 'MarkerSize',25);
text(period(index)+2,power(index),['Period = ',mainPeriodStr]);
hold off;

%%      End of the time series analysis

%%      Spectral analysis of the 1-D data (Distance or time)

% First load the data and read the variables from the text file

load fouriertransformei.txt
x_dist=fouriertransformei(:,1);
y_freq=fouriertransformei(:,2);
y_variable=detrend(y_variable);          % Eliminate long term trend from the signal
plot(x_dist,y_freq)
title('Distance versus Fracture Frequency')

% Now compute evolutionary power spectrum for a window of 48 data points with a 40 data points %
overlap. The short time Fourier transform (STFT) is computed for nfft = 128 (neraerst power 2 % of
89 of our actual data points), and frequency = 1/12.5

figure(7)
[Pxx,f] = periodogram(y_freq,[],128,1/12.5);
plot(f,Pxx)
xlabel('Frequency [1/12.5 cm]')
ylabel('Power')
title('Autospectrum')

figure (8)
spectrogram(y_freq,48,40,128,1/12.5)   % 48 data points, 40 overlap, 128 nfft
title('Evolutionary Power Spectrum')
xlabel('Frequency [1/12.5 cm]')
ylabel('Distance [cm]')

% Due to linear tendency of the data, the highest peak is concentrated or appear near 0 frequency. It is
% possible to solve this problem by smoothing the data using different smoothing command and then
% using detrend function
```

```
%%      Smoothing of the data points and replot Peridogram and Spectram

% Use three kinds of smoothing tools for raw data smoothing (y_dist): simple smooth by using
% smooth, and more efficient smoothing by using rloess and loess functions. However it is necessary
% to check with given data which method is best. For this first load data and read variables again

load fouriertransformei.txt
x_dist=fouriertransformei(:,1);
y_freq=fouriertransformei(:,2);

% Now smooth data in y_dist (to check what % is best fit to the real data). Here, 7% smooth for
% the Eireiner quarry is appears better.

s1 = smooth(y_freq(:));                 % simple smoothing, very poor
s2 = smooth(x_dist,y_freq,0.07,'rloess');   % Here smooth 7% (0.07)
s3 = smooth(x_dist,y_freq,0.07,'loess');    % Here smooth 7% (0.07)

% Now plot all data together to see which smoothing give best result

figure (9)
plot(x_dist,y_freq,'r',x_dist,s1,'b',x_dist,s2,'gr',x_dist,s3,'r--')
title('Section width vs. Fracture Frequency Plot')

% After smoothing, it is necessary to elimanate the long trend (if any) from the data set, responsible
% for the 0 centered frequency. For this, use detrend function on smooth variable s3

s4=detrend(s3);

% Now, compute Peridogram and Evolutionary spectrum for a window of 64 data points with a 50
% data points overlap. The STFT is computed for nfft=128 (neraerst power 2 of 89 of real data points)
% for the Eireiner quarry, frequency=1/12.5

figure(10)
[Pxx,f] = periodogram(s4,[],128,1/12.5);
plot(f,Pxx)
xlabel('Frequency [1/12.5 cm]'),ylabel('Power'),grid on
title('Power Spectrum [after smoothing & removing linear vector trend]')

% Spectrum window need to adjusted based on data series in each analysis. Here window of 40 data
% points with 36 data points overlap give best result

figure (11)
spectrogram(s4,40,36,128,1/12.5)
title('Evolutionary Power Spectrum [after smoothing & removing linear trend]')
xlabel('Frequency [1/12.5 cm]')
ylabel('Section width [cm]'),grid on,colorbar
```

Appendix 2.3b: Wavelet transform of the fracture frequency data

```
% In case of Wavelet transform, rad did not analysed. First data were smoothed and then smooth data
% has been used as smooth data give good results during autospectrum and evolutionary power
% spectrum analysis. Therefore, first it is necessary to load the actual data

load fouriertransformei.txt
x_dist=fouriertransformei(:,1);
y_freq=fouriertransformei(:,2);

% Now smooth data in y_dist (to check what % is best fit the real data). As it is observed before,
% 7% smooth using loess function give best smoothness for the section-1.

s3 = smooth(x_dist,y_freq,0.07,'loess');              % Here smooth 7% (0.07)

% After smoothing, now elimanate the long trend in the data that responsible for the 0 centered
% frequency by using detrend command

s4=detrend(s3);

% Now scale the data and do the wavelet analysis. The scaling may causes shift up-down of the
% wavelet power spectrum.

scales = 1 : 100;

% Now compute the wavelet transform for 50 scales using the function cwt and a Morley mother
% wavelet commnad on s4 smooth variable of the fracture frequency data set

coefs = cwt(s4,scales,'morl'); % morl is Morley mother wavelet

% Use scal2freq function to convert the scales to pseudo-frequencies, using the Morley mother
% wavelet and sampling period of 12.5 (data interval)

f = scal2frq(scales,'morl',12.5);

% Next use a filled contour plot to portray the power spectrum, i.e. the absolute value of the
% wavelet coefficients (for non-smoothing data)

figure (4)
contour(x_dist,f,abs(coefs),'LineStyle','none','LineColor',[0 0 0],...
'Fill','on')
xlabel('Section Width [cm]')
ylabel('Frequency [1/12.5 cm]'),grid on,colorbar;
title('Wavelet Power Spectrum')

% A clear wavelet spectrum is visible at frequency 0.0026 which is equivalent to ca.380cm.
```

Appendix Three: Supplementary materials of the chapter three those are published in online version

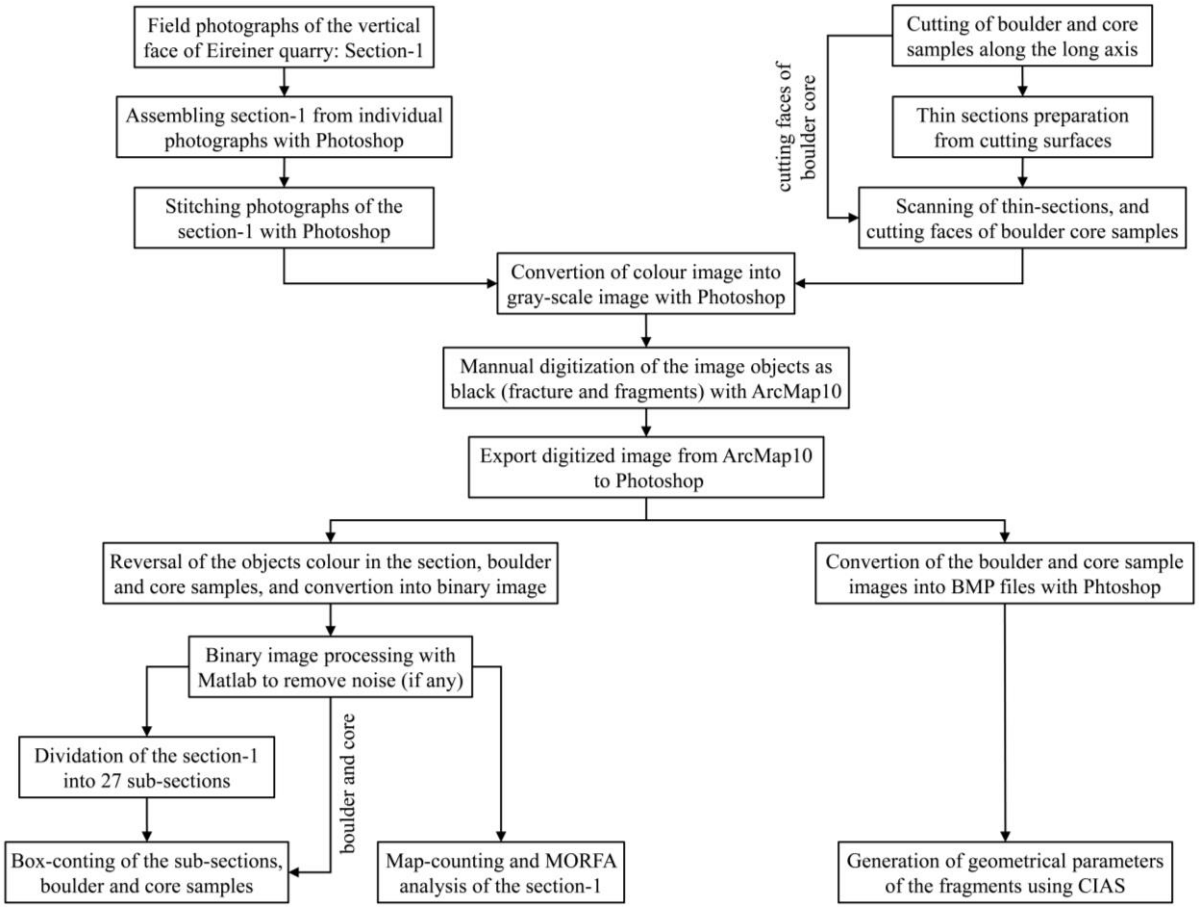

Figure App. 3.1: Illustrates the work steps undertaken from image acquisition to final processing by using different methods.

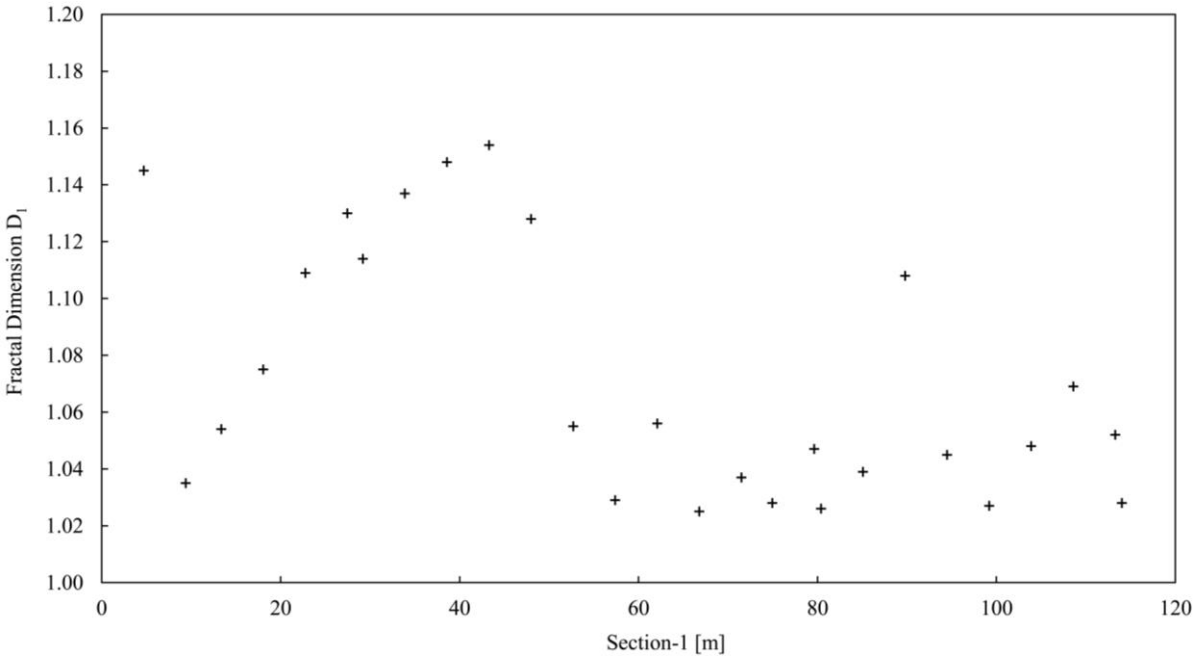

Figure App. 3.2: Variation of fractal box-counting dimension D_1 for 27 sub-sections along the section-1 in the Eireiner quarry.

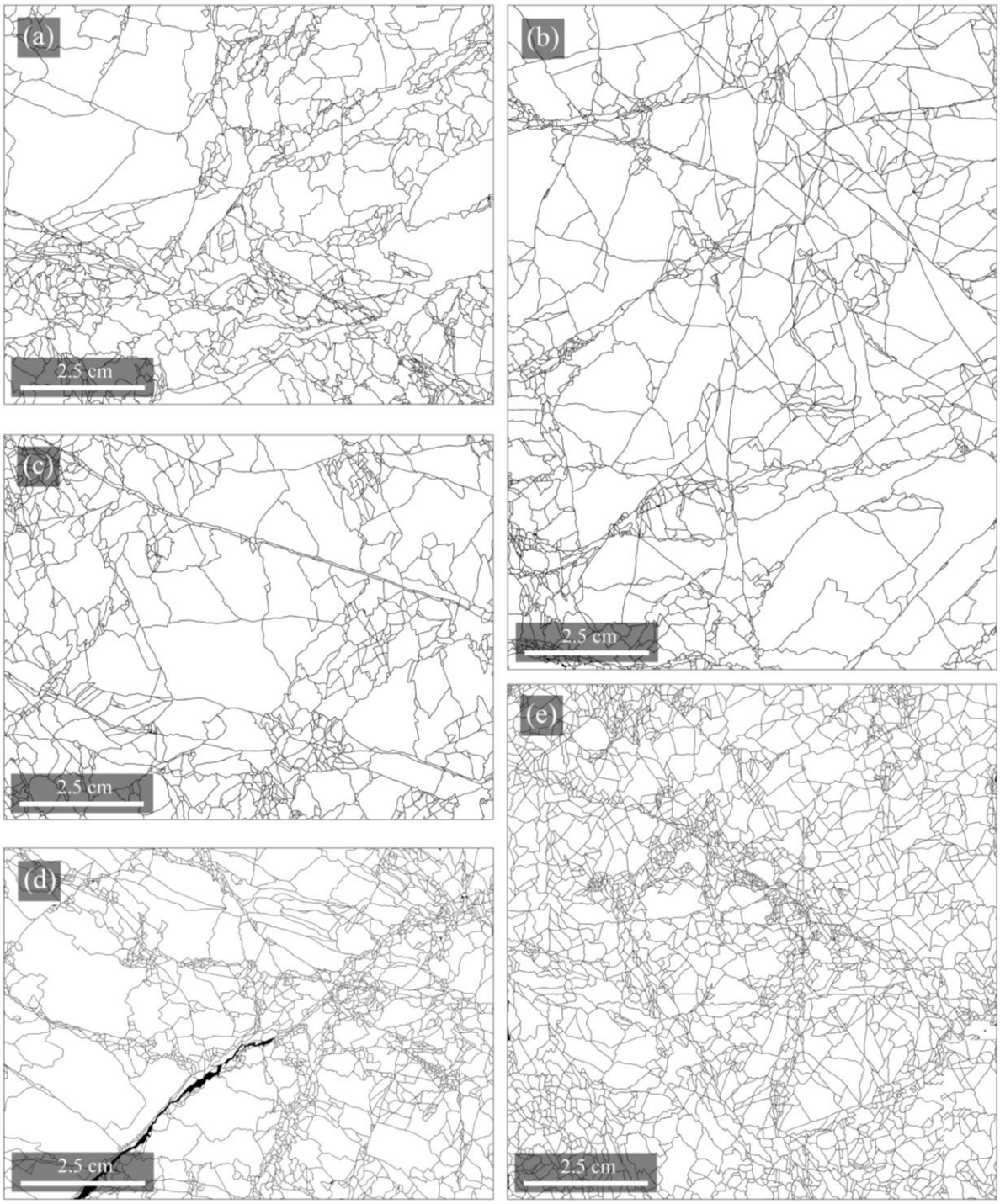

Figure App. 3.3: Binary image of fractures (black lines) and regions of sub-microscopically fragmented material (small black areas) from vertical cut of granitoid rock samples from the Ries Research Borehole 1973. One pixel = 0.025 mm on the rock surface. Depth of the core samples: (a) 604.60 m, (b) 679.20 m, (c) 766.25 m, (d) 773.30 m and (e) 1169.50 m. Results of the fracture patterns quantification by box-counting method and fragment size distribution are given in Fig. 3.11 in chapter three. Note: These binary images of fracture patterns are not published as supplementary material in the online version of the article.

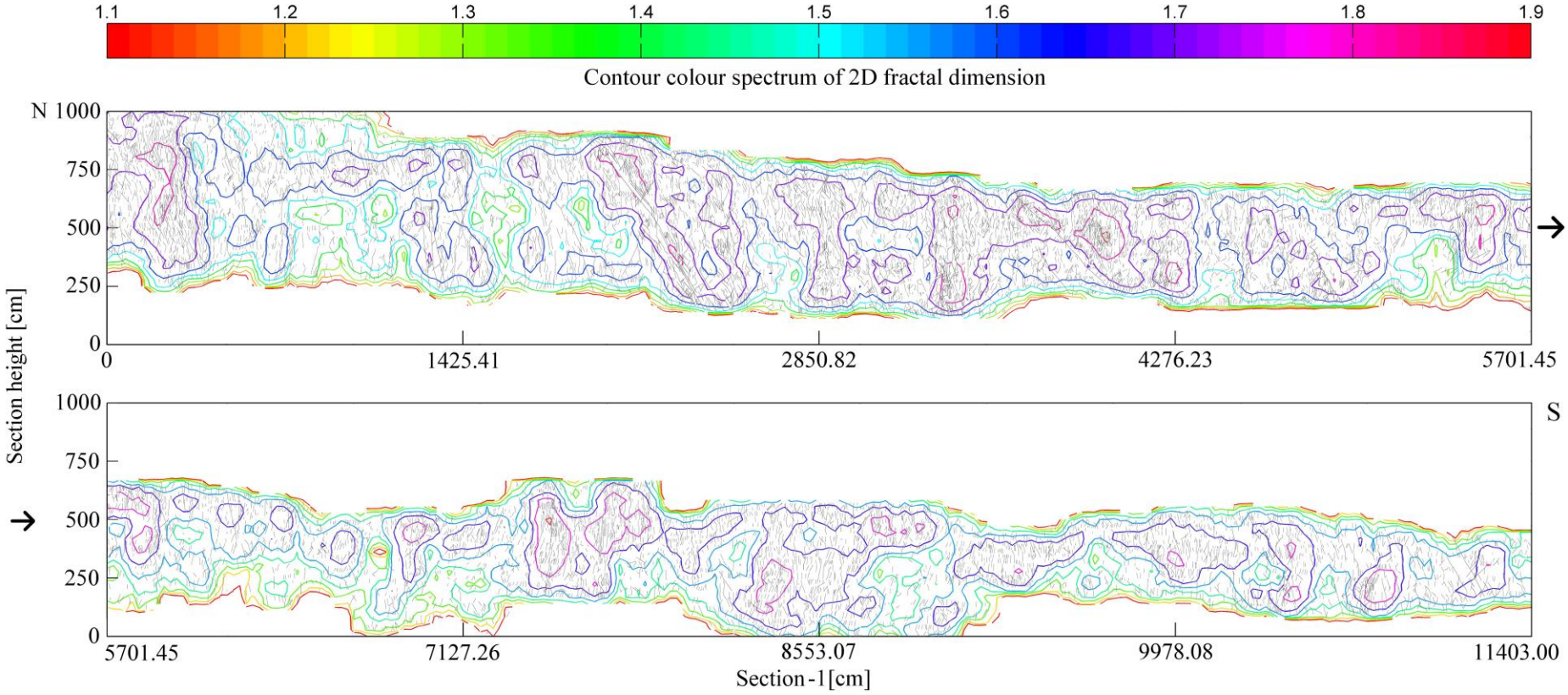

Figure App. 3.4: Contour diagram of the 2D box-counting dimension using map-counting method applied to the fracture pattern of section-1 in the Eireiner quarry. See text for description of the map-counting method. The contour color spectrum represents the intensity of inhomogeneity of the fracture pattern's complexity in term of 2D box-counting dimension, with 1.1 = low complexity (light yellow) and 1.87 = high complexity (blue). Black lines are the original fractures superimposed on top of the contour diagram. Note: Very low *D*-value contour at the margin is the artifacts due to partial data fillings of the sub-image window.

Appendix Four: Supplementary figures, metadata and data of chapter four

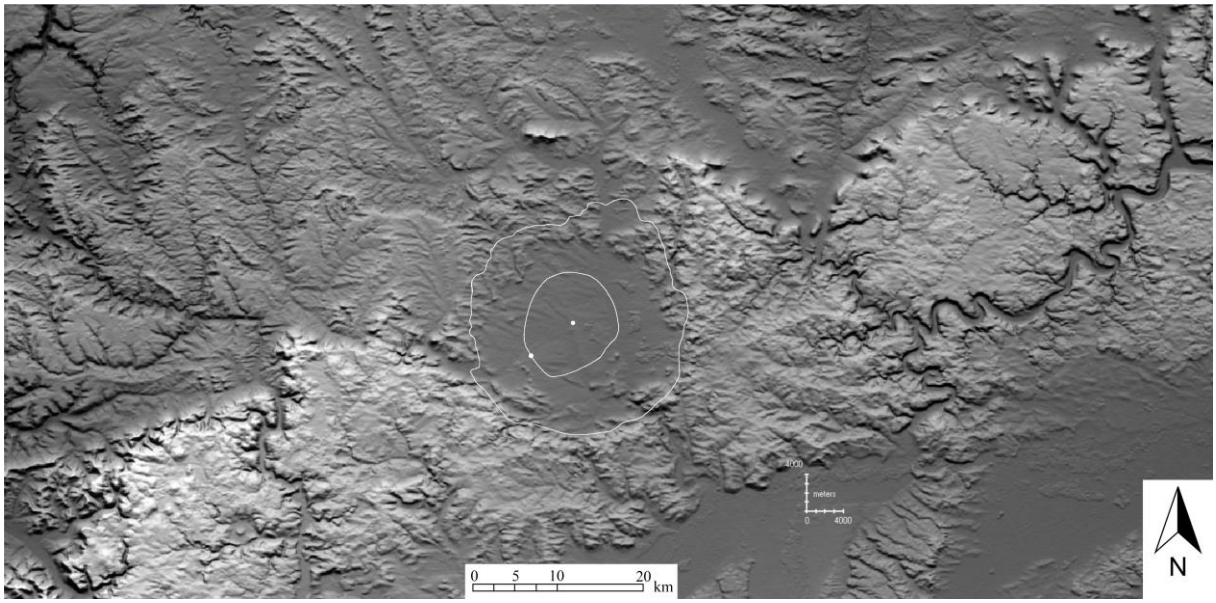

Figure App. 4.1: Topographic relief image of the Ries impact area. Image is based on Shuttle Radar Topography Mission (SRTM) data with grid resolution ca. 60 m (north illumination, magnification 1:5). Crater outlines are marked by white lines (outer line: outer crater rim; inner line: inner crystalline ring) at the centre of the image.

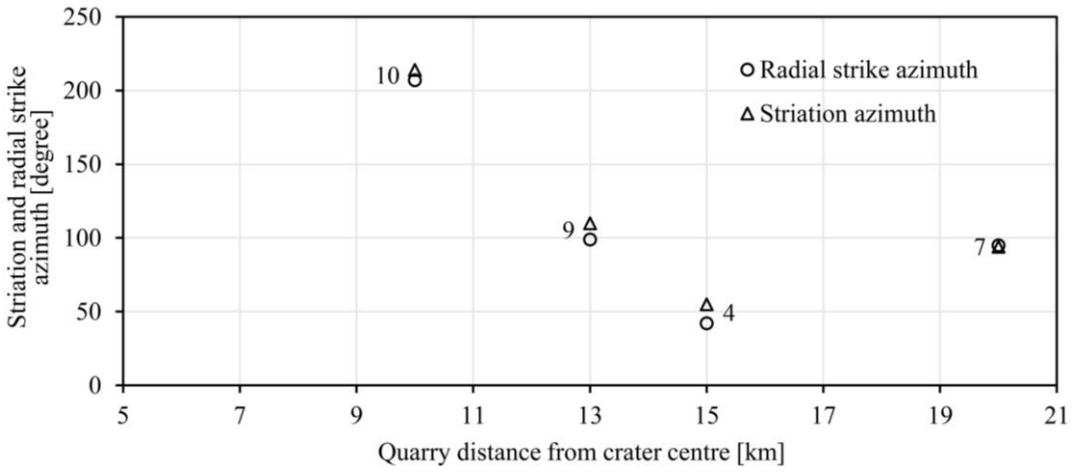

Figure App. 4.2: Relationships between mean striation azimuth (developed by the radial outward-directed flow of the Bunte Breccia) and the measured mean radial strike in four different quarries. The quarries are numbered 4, 7, 9 and 10 (see Fig. 4.4 in chapter four for quarry locations).

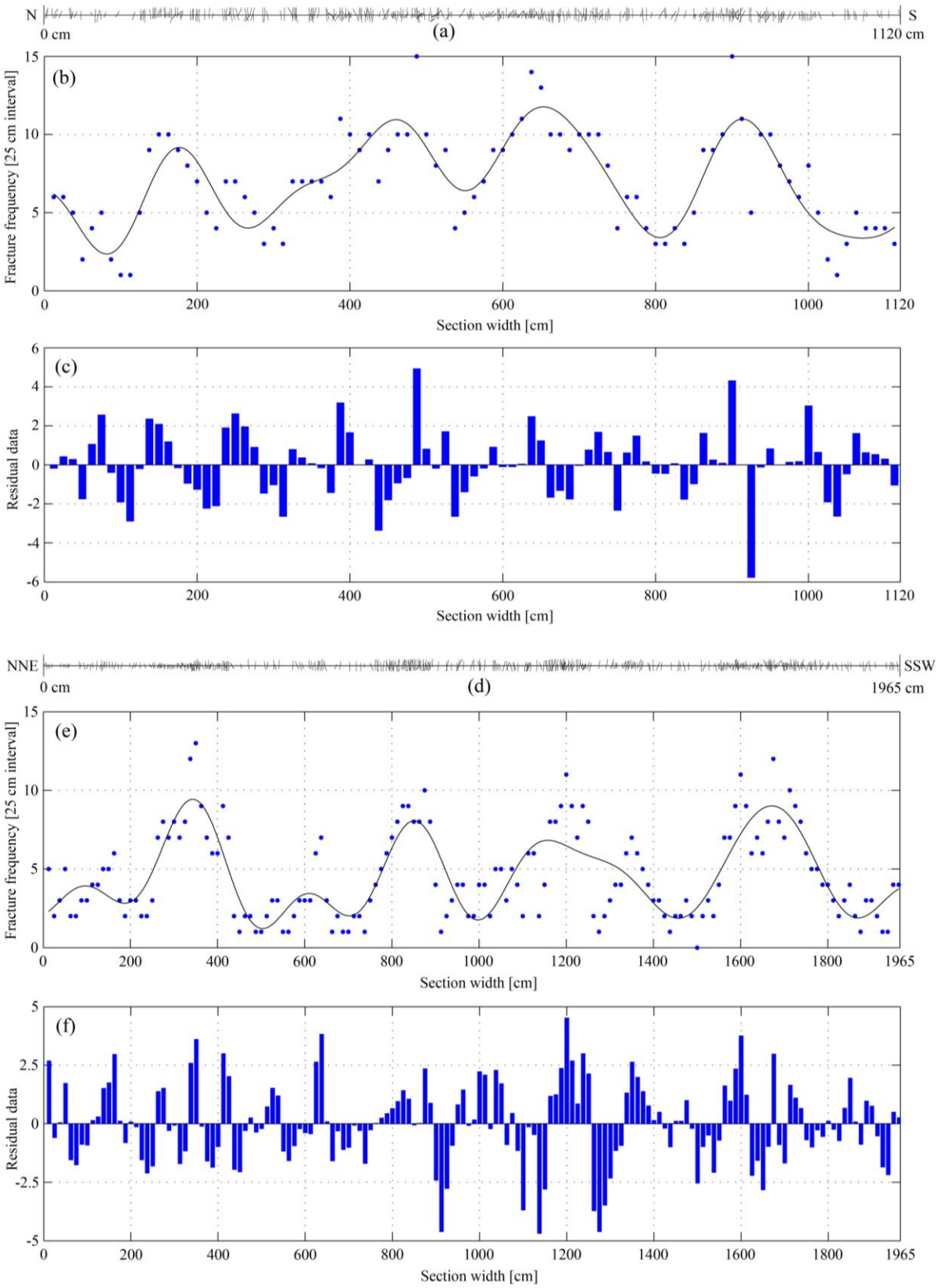

Figure App. 4.3: Fracture frequencies of an approximately N–S-oriented 1120 cm vertical section in the Eireiner quarry and a 20°-oriented 1965 cm vertical section in the Solnhofen quarry (see Fig. 4.4 in chapter four for quarry locations). (a) Horizontal scan-line approximately at medium altitude of the section, along which the number of fracture intercepts is recorded for each 25-cm interval. (b) Fracture frequency diagram. Dots are the number of fracture counts every 25-cm interval, with 50% overlap, plotted against the section length. Solid

curve: eighth-order Fourier fit of the fracture frequency data points. The fit appears to be the best representative of most of the data points (based on the maximum correlation coefficient value, $R^2 = 0.741$). (c) Residual bar diagram: Residual values appear random for most of the data, although a pattern is still visible indicating that additional cycles might be present. Similarly, the horizontal scan-line, fracture frequency diagram and residual bar diagram for the Solnhofen section are provided in figure (d), (e) and (f), respectively. Solid curve (e): seventh-order Fourier fit of the fracture frequency data points.

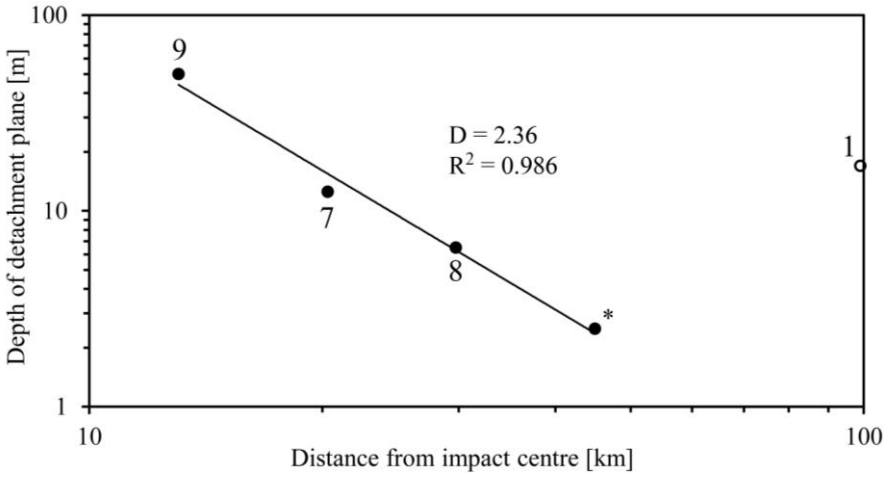

Figure App. 4.4: Relationship of depth of near-surface deformation to distance from the impact centre in five different quarries. Double logarithmic plot of quarry distance versus depth of near-surface deformation (target delamination) in each quarry shows a power-law relationship, i.e. fractality ($D = 2.36$) for the four nearest quarries. Four quarries are numbered 1, 7, 8 and 9 (see Fig. 4.4 in chapter four for quarry locations). The quarry marked with an asterisk [*] is located ~10 km north of Eichstätt, i.e. ~46 km E of the Ries impact centre (the quarry name is unknown).

Table App. 4.1: Metadata of the studied quarries in and around the Ries impact crater. Quarry numbers 1 to 16 are based on increasing azimuth values with respect to geographic N.

Ries impact crater centre (latitude: ~48.884443, longitude: ~10.557868)						
Quarries in and around the Ries crater				Geographic coordinates		Tectonic region
Quarry number	Quarry name/location	Distance from Ries centre [km]	Azimuth [degree]	Latitude [decimal degrees]	Longitude [decimal degrees]	
1	Bärnereuther	99.09	30	49.654317	11.243121	NNE
2	Wolfgang	98.8	31	49.655074	11.237839	
3	Oberndorf	99	33	49.625694	11.310762	
4	Neumarkt	89.28	61	49.270592	11.629940	
5	Stahlmühle	14.86	58	48.956019	10.728874	ESE
6	Wiesenhofen	65.92	74	49.043487	11.425143	
7	Gundelsheim	20.33	83	48.906783	10.833058	
8	Solnhofen	29.75	89	48.889878	10.963426	
9	Eireiner	13.04	102	48.860608	10.731941	
10	Holheim SE	9.93	224	48.819843	10.464336	WSW
11	Holheim SW	10.68	226	48.818305	10.452246	
12	Dehlingen	15.07	235	48.805792	10.390657	
13	Lauchheim	24.7	261	48.849791	10.225251	
14	Heumann	47.18	310	49.156853	10.063259	NNW
15	SHF-Bettenfeld	59.28	327	49.330059	10.112187	
16	Bad Windsheim	71.81	352	49.522982	10.411463	

Table App. 4.2: Strike of the Radial fracture set related to the Ries impact crater (see details in chapter four). Note: NaN means no data (used to process data in Matlab).

Tectonic region	Northern part of Fränkische Alb **(NNE)**				Southeastern part of Fränkische Alb **(ESE)**					Eastern part of Schwäbische Alb **(WSW)**				South-German Schichtstufenland **(NNW)**		
Quarry name/location	**Bärnereuther**	**Wolfgang**	**Oberndorf**	**Neumarkt**	**Stahlmühle**	**Wiesenhofen**	**Gundelsheim**	**Solnhofen**	**Eireiner**	**Holheim SE**	**Holheim SW**	**Dehlingen**	**Lauchheim**	**Heumann**	**SHF-Bettenfeld**	**Bad Windsheim**
Quarry azimuth	**30**	**31**	**33**	**61**	**58**	**74**	**83**	**89**	**102**	**224**	**226**	**235**	**261**	**310**	**327**	**352**
Quarry number	**1**	**2**	**3**	**4**	**5**	**6**	**7**	**8**	**9**	**10**	**11**	**12**	**13**	**14**	**15**	**16**
Strike of the radial fracture [degree]	172	209	198	225	212	260	96	290	291	12	230	248	260	136	175	176
	248	197	213	218	215	260	88	250	293	22	204	247	288	132	174	137
	249	191	192	231	220	260	94	288	310	30	189	219	242	128	180	139
	176	195	198	236	220	259	85	260	315	0	234	237	250	137	184	156
	177	199	198	215	225	261	105	260	312	26	197	231	300	135	190	151
	194	193	207	223	231	258	116	280	282	20	204	249	268	133	191	156
	193	186	203	207	230	255	75	280	280	26	217	240	265	140	185	165
	190	207	189	210	NaN	257	97	281	265	36	231	222	243	133	166	182
	173	187	193	216	NaN	260	88	260	281	67	221	235	246	130	175	145
	181	185	194	221	NaN	262	112	288	293	NaN	223	238	290	140	182	142
	174	193	200	202	NaN	258	93	298	286	NaN	222	232	244	139	194	148
	216	174	194	198	NaN	262	83	277	300	NaN	210	243	NaN	132	176	143
	211	211	215	201	NaN	259	98	262	289	NaN	222	213	NaN	143	183	136
	182	171	216	204	NaN	265	100	265	256	NaN	240	214	NaN	137	187	142
	213	200	200	268	NaN	267	77	254	246	NaN	NaN	240	NaN	135	180	NaN
	185	205	NaN	217	NaN	261	118	258	248	NaN	NaN	252	NaN	143	178	NaN
	190	190	NaN	212	NaN	255	80	272	248	NaN	NaN	237	NaN	139	190	NaN
	180	208	NaN	201	NaN	250	87	250	260	NaN	NaN	240	NaN	148	NaN	NaN
	195	198	NaN	215	NaN	NaN	118	276	272	NaN	NaN	226	NaN	135	NaN	NaN
	214	206	NaN	267	NaN	NaN	NaN	258	264	NaN	NaN	230	NaN	NaN	NaN	NaN
	189	179	NaN	211	NaN	NaN	NaN	262	268	NaN	NaN	241	NaN	NaN	NaN	NaN
	166	203	NaN	218	NaN	NaN	NaN	275	294	NaN	NaN	NaN	NaN	NaN	NaN	NaN
	197	186	NaN	228	NaN	NaN	NaN	271	250	NaN	NaN	NaN	NaN	NaN	NaN	NaN
	NaN	212	NaN	223	NaN	NaN	NaN	267	267	NaN	NaN	NaN	NaN	NaN	NaN	NaN

Table App. 4.3: Strike of the tangential fracture set related to the Ries impact crater (see details in chapter four). Note: NaN means no data (used to process data in Matlab).

Tectonic region	Northern part of Fränkische Alb **(NNE)**				South eastern part of Fränkische Alb **(ESE)**					Eastern part of Schwäbische Alb **(WSW)**				South-German Schichtstufenland **(NNW)**		
Quarry name/location	**Bärnereuther**	**Wolfgang**	**Oberndorf**	**Neumarkt**	**Stahlmühle**	**Wiesenhofen**	**Gundelsheim**	**Solnhofen**	**Eireiner**	**Holheim SE**	**Holheim SW**	**Dehlingen**	**Lauchheim**	**Heumann**	**SHF-Bettenfeld**	**Bad Windsheim**
Quarry azimuth	**30**	**31**	**33**	**61**	**58**	**74**	**83**	**89**	**102**	**224**	**226**	**235**	**261**	**310**	**327**	**352**
Quarry number	**1**	**2**	**3**	**4**	**5**	**6**	**7**	**8**	**9**	**10**	**11**	**12**	**13**	**14**	**15**	**16**
Strike of the tangential fracture [degree]	103	118	112	129	140	195	186	215	128	302	258	315	300	48	50	70
	104	101	119	149	142	175	178	204	220	330	274	288	300	50	92	100
	110	134	103	192	125	190	185	203	143	299	280	326	336	55	80	71
	96	122	100	160	135	198	178	205	152	285	349	350	350	51	92	22
	120	156	107	158	132	200	180	190	240	345	314	315	300	52	96	69
	82	102	116	175	140	191	174	155	176	260	300	332	350	40	59	72
	98	112	110	192	138	194	179	170	158	262	302	272	300	48	91	83
	88	NaN	105	174	137	192	172	190	148	NaN	325	274	302	46	97	NaN
	142	NaN	107	158	168	170	173	200	172	NaN	319	339	350	48	NaN	NaN
	143	NaN	109	172	191	180	178	190	164	NaN	313	338	354	50	NaN	NaN
	120	NaN	110	160	170	178	182	192	158	NaN	314	300	350	50	NaN	NaN
	118	NaN	117	NaN	185	172	182	190	176	NaN	280	304	300	40	NaN	NaN
	89	NaN	148	NaN	128	171	170	190	158	NaN	322	303	350	47	NaN	NaN
	156	NaN	112	NaN	126	NaN	172	195	162	NaN	298	288	353	67	NaN	NaN
	133	NaN	NaN	NaN	132	NaN	168	168	155	NaN	300	304	340	72	NaN	NaN
	98	NaN	NaN	NaN	183	NaN	175	167	143	NaN	NaN	313	330	75	NaN	NaN
	112	NaN	NaN	NaN	180	NaN	181	170	146	NaN	NaN	316	342	39	NaN	NaN
	110	NaN	NaN	NaN	185	NaN	184	184	186	NaN	NaN	NaN	NaN	63	NaN	NaN
	80	NaN	NaN	NaN	182	NaN	183	185	190	NaN	NaN	NaN	NaN	48	NaN	NaN
	NaN	NaN	NaN	NaN	181	NaN	186	191	177	NaN	NaN	NaN	NaN	62	NaN	NaN
	NaN	NaN	NaN	NaN	191	NaN	193	195	NaN	NaN	NaN	NaN	NaN	50	NaN	NaN
	NaN	NaN	NaN	NaN	171	NaN	187	201	NaN	NaN	NaN	NaN	NaN	77	NaN	NaN
	NaN	NaN	NaN	NaN	189	NaN	204	198	NaN	NaN	NaN	NaN	NaN	85	NaN	NaN
	NaN	NaN	NaN	NaN	NaN	NaN	NaN	182	NaN	NaN	NaN	NaN	NaN	NaN	NaN	NaN
	NaN	NaN	NaN	NaN	NaN	NaN	NaN	181	NaN	NaN	NaN	NaN	NaN	NaN	NaN	NaN
	NaN	NaN	NaN	NaN	NaN	NaN	NaN	181	NaN	NaN	NaN	NaN	NaN	NaN	NaN	NaN

Appendix Five: Relationship of the straight cave section orientation to the regional tectonic structures

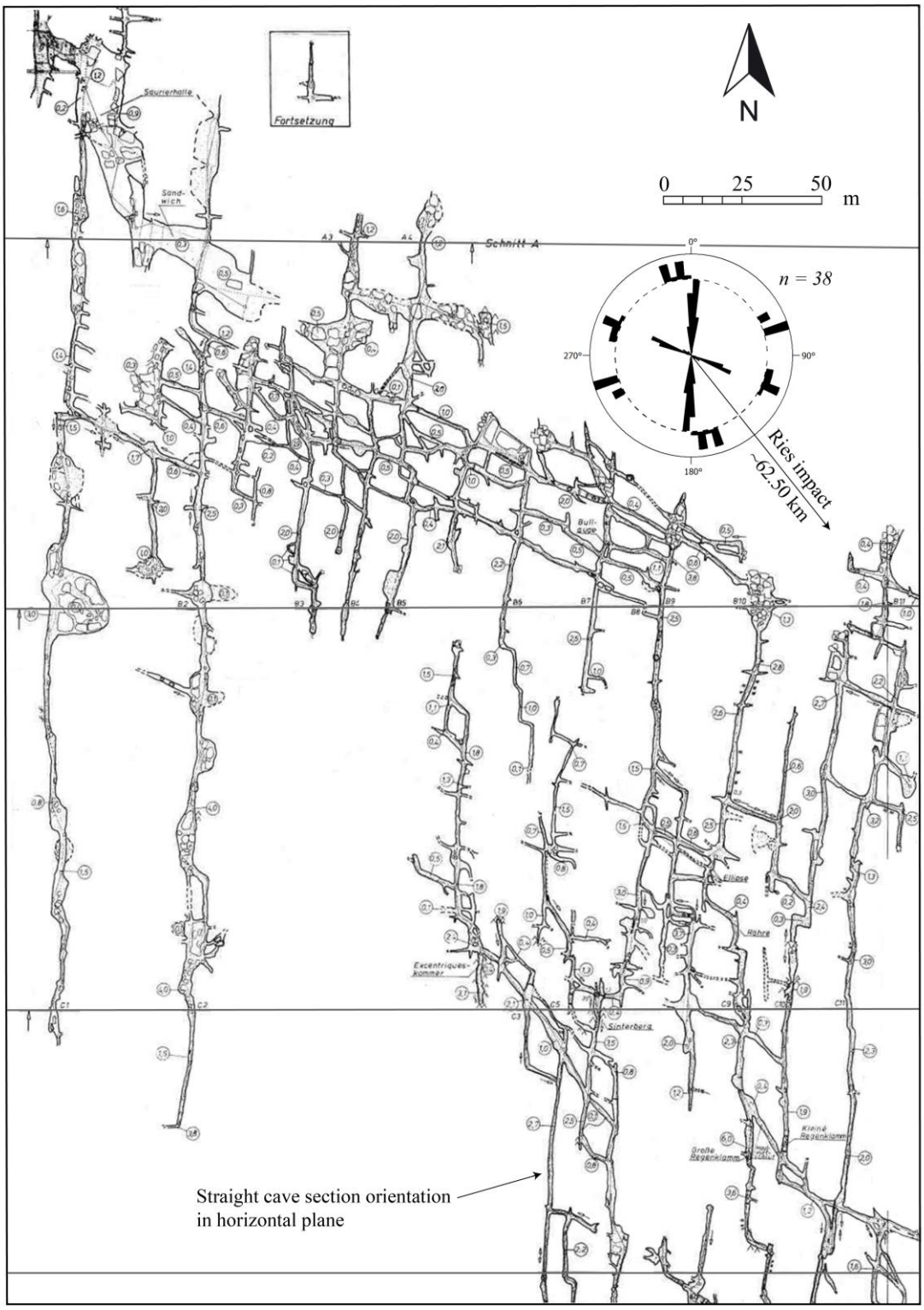

Figure App. 5.1: Plan view of an Eastern Swabian Alb cave (Fuchslabyrinth) situated at a distance of approximately 62.5 km from the Ries impact centre (www.argestuttgart.homepage.t-online.de/hoehlen.htm). The orientation data of the nearly straight sections of the cave in the horizontal plane is presented as rose diagram (inside broken circle). Number of the orientation measurement is given by *n*. Lineaments strike related to regional tectonics in the Eastern Swabian Alb region (Strasser et al., 2011) is presented as outer ring to the rose diagrams of the cave. Orientation of the straight cave sections show strong similarities to the orientation of the regional tectonic structures (lineaments) (see chapter five for details).

Appendix Six: The kinematic data of the 'suevite' at the Stoer impact area, NW Scotland

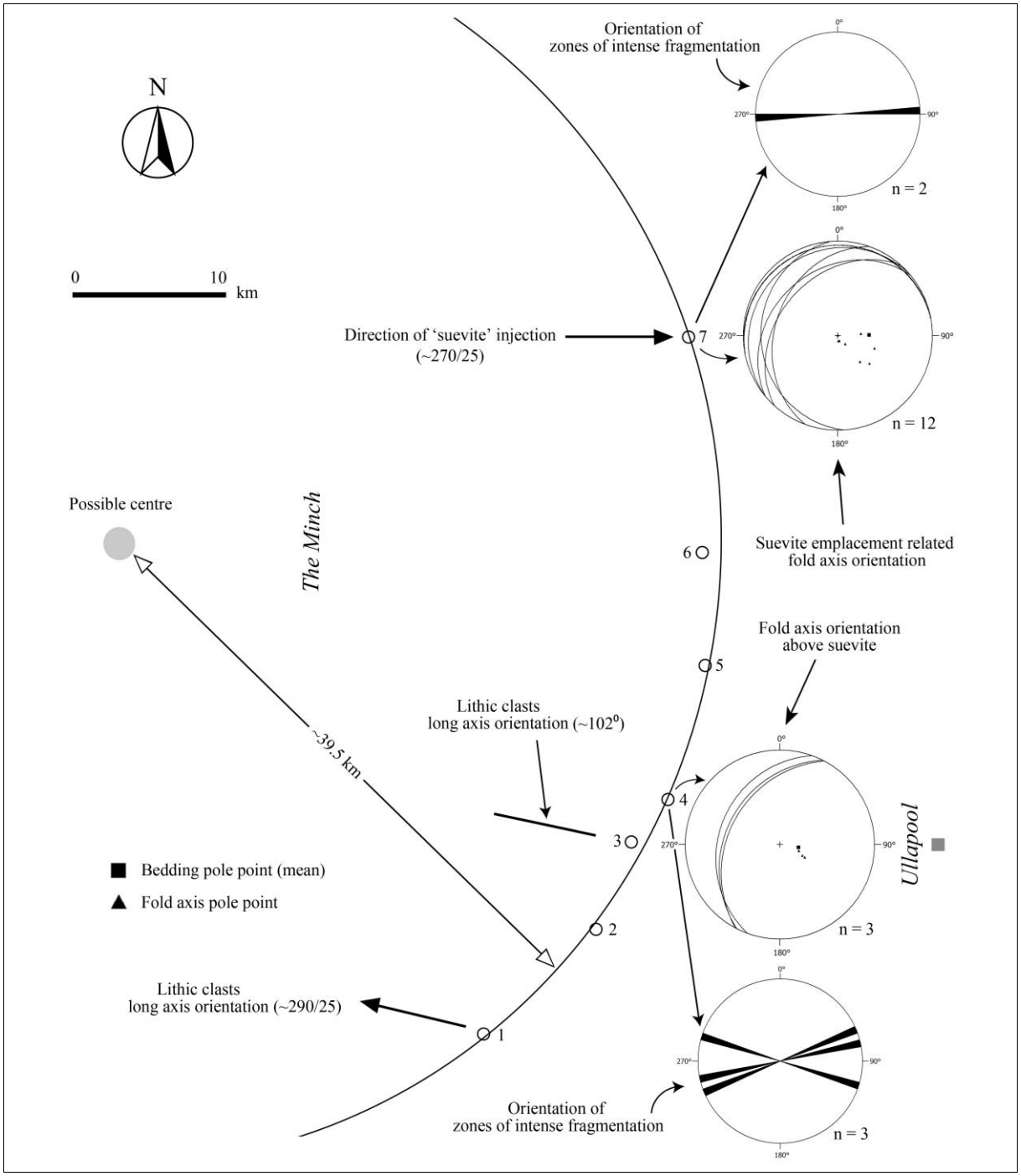

Figure App. 6.1: Possible location of the Stoer impact centre based on (i) distribution of the SFM or 'suevite' exposures, (ii) fold axis orientation related to the 'suevite' emplacement, (iii) orientation of the zones of intense fragmentation (Hossain and Kruhl, 2015) beneath the 'suevite' and (iv) direction of the 'suevite' injection within the sandstone bedding planes. The exposed SFM locations (see Figs. 6.1 and 6.2 in chapter six) form a chord like distribution which is possibly part of the impact crater. A circle has been drawn using all exposure locations as the chord section. The radius of the circle fitted with the chord shape is ~39.5 km which in turn indicate possible radius of the 'Stoer impact crater'. All data sets indicate direction of the possible impact centre, but not the exact location of the crater centre. However, this figure is just only an intuition not an actual scientific argument. Moreover, it is worth to mention here that most of the earth impact is oblique (Gilbert, 1893; Shoemaker, 1962) and therefore the resultant crater rim is not necessarily circular (Kenkmann et al., 2014).